IMPERIAL

Imperial College London

Department of Physics

Mode transforming vortex laser with optical levitation

Abdul-Haseeb Munj

20, December, 2024

Submitted in part fulfilment of the requirements for the degree of Doctor of Philosophy in Physics of Imperial College London and the Diploma of Imperial College London.

Declaration of Originality

I, Abdul-Haseeb Munj, declare that the work in this thesis is my own. The work of others has been appropriately referenced. A full list of references is given in the bibliography.

Copyright

The copyright of this thesis rests with the author. Unless otherwise indicated, its contents are licensed under a Creative Commons Attribution-NonCommercial 4.0 International Licence (CC BY-NC).

Under this licence, you may copy and redistribute the material in any medium or format. You may also create and distribute modified versions of the work. This is on the condition that: you credit the author and do not use it, or any derivative works, for a commercial purpose.

When reusing or sharing this work, ensure you make the licence terms clear to others by naming the licence and linking to the licence text. Where a work has been adapted, you should indicate that the work has been changed and describe those changes.

Please seek permission from the copyright holder for uses of this work that are not included in this licence or permitted under UK Copyright Law.

Acknowledgements

I must begin by recognising the key efforts of those around me, without whom this work would not have been possible. Firstly, I'd like to thank my supervisor Dr. William Kerridge-Johns for his immense patience and exceptional guidance that was instrumental in shaping my research journey. We have come a long way since my struggles at aligning a laser cavity for the first time all those years ago. I will be forever grateful for this opportunity.

Thank-you to Prof. Mike Damzen for his seemingly endless insights into laser fundamentals and vortex beams which provided clarity and direction particularly when I got stuck in theory. Thank-you to Dr. Ara Minassian for everything lab-related and showing me the ways of elegant optical design. And a collective thank-you to both for our lively discussions over coffee in the level 8 common room on everything from space lasers to current events.

I would like to thank Prof. Roland Smith for collaborating with us on our work on optical levitation and for accepting me into his group meetings. His enthusiasm for scientific discovery was inspirational and what drove me to go the extra mile in the pursuit of the unknown.

To my group members, both past and present, thank you for making the office an energetic and supportive space. I am truly grateful to all — mentor and friend alike — for an incredible four years.

Finally, it would not be complete without expressing my gratitude to my family and relatives who have supported me through my journey. To my grandparents, aunts, uncles and cousins who have been cheering along the way. And most importantly, to my parents and siblings, who I hope to have done proud, and who have encouraged me through these years to follow my passion for research.

Abstract

The work in this thesis spans two primary fields of inquiry. The first focuses on the development of a novel laser system capable of direct optical vortex (OV) emission, while the second aims to demonstrate its application in the optical levitation of reflective hollow microspheres.

We first present the non-standard use of a wedge-plate shearing interferometer (WPSI) as a TEM_{00} Gaussian to LG_{01} OV mode conversion device. A detailed description of its geometric configuration and interferometric process is presented. It gives an idealised power conversion of 99.6 % in favour of the of the LG_{01} OV-mode. However, since the OV is generated in its face-reflection, the incident power conversion is equal to only its Fresnel reflectance. Power scaling potential is improved through intracavity use of the WPSI. A unidirectional ring cavity was used with a 20:1 power imbalance in favour of clockwise propagation which enhanced incident power to enable watt-level OV output power (1.15 W). The unconverted power is recycled back into the cavity. In this configuration we demonstrate the generation of OV beams with high beam-quality ($M^2 = 1.94, 2.09$) and high LG_{01} mode-purity (97.8 %).

In the second part, we demonstrate the use of this system in optical levitation. This work was motivated by the desire to levitate metallic (possible reflective) hollow-sphere (shells with low internal refractive index) targets for experiments with high-intensity, high-energy laser systems particularly in the generation of high-density plasmas, point X-ray sources, and charged-particle acceleration. We demonstrate the optical levitation of shells 20 to 110 µm in diameter (masses of 25 ng to 230 ng) at long focal length ($f = 40$ mm) and measure <5 µm spatial stability in air and low vacuum.

List of Publications

Journal articles

A-H. Munj, W. R. Kerridge-Johns, Unidirectional ring vortex laser using a wedge-plate shearing interferometer. *Optics Express* 31.3 (Jan. 2023), 4954-4963 DOI:10.1364/OE.482849.

Conference presentation

A-H. Munj, R. A. Smith, W. R. Kerridge-Johns, Optical levitation using an LG01 vortex beam. *Optical Manipulation and Structured Materials Conference* (Sep. 2023).

A-H. Munj, **W. R. Kerridge-Johns**, Ring Cavity Vortex Laser using a Wedge-Plate Shearing Interferometer. in *Proceedings of the 2022 Conference on Lasers and Electro-Optics Pacific Rim*, CThP1H-03

Conference poster

A-H. Munj, R. A. Smith, W. R. Kerridge-Johns, Optical levitation of reflective shells using an LG01 vortex beam. in *2023 Conference on Lasers and Electro-Optics Europe and European Quantum Electronics Conference, CLEO/Europe-EQEC 2023*, CG-P2

List of Figures

2.1 Intensity profile, phase map and wavefront structure of $l = 0, 1, 2$ LG modes. 8
2.2 Two identical cylindrical lenses separated by 2f used to convert HG mode to LG mode 10
2.3 (Top) Decomposition of HG mode oriented at 45°. (Bottom) HG modes rephased to form LG mode. Figure from Ref. [34] 10
2.4 Spiral phase plate of step height h. Figure from Ref. [28] 11
2.5 (a) $q = 1/2$ and $\alpha_o = 0$ used to generate OAM $l = \pm 1$. Both (b) $q = 1$ and $\alpha_o = 0$ and, (c) $q = 1$ and $\alpha_o = \pi/2$ used to generate $l = \pm 2$. Figure from Ref. [31] 12

3.1 WPSI operation illustrating TEM_{00} to LG_{01} mode conversion. 20
3.2 (a) Side view of WPSI with nominal thickness t_0 and wedge angle α. It is illuminated by a Gaussian beam with incidence angle θ_i. Front and rear surface reflections at θ_{r1} and θ_{r2}. (b) Top view of WPSI with reflected rays parallel in the horizontal plane 23
3.3 Mode reflectance as a function of angle of incidence 27
3.4 WPSI mode collage 27
3.5 WPSI beam waist corrected mode generation 29
3.6 (a) WPSI reflectance for shifts in incident wavelength relative to 1064 nm are shown. TEM_{00} and LG_{01} mode reflections found when constructive and destructive interference conditions are satisfied respectively. (b) Reflectance plot zoomed in to near reflectance minimum. The red vertical lines indicate the position of cavity longitudinal modes. The WPSI spectrum (blue) can be adjusted in position via Δy-control 32

4.1 Electron transitions for 3-level laser gain medium. Solid lines denote the laser transitions with dotted arrows indicating spontaneous processes. . . . 35
4.2 Electron transitions for 4-level laser gain medium. 36
4.3 Notable pump and laser electron transitions in Nd:YVO4. Adapted from [77] and [78] 39
4.4 (a) Linear resonator with curved mirrors R1 and R2 separated by length L. (b) Unfolded cavity with replaced lens. Beam propagates from left to right. 39
4.5 Linear Optical Resonator Stability curve 42

4.6 Pump diode laser power curve. Inset shown the top-hat profile of the pump beam 47
4.7 Optical tranmsittance of the pump power through 0.5 % doped Nd:YVO_4 . 48
4.8 (a) Laser spot size w_2 at the PR and w_3 at the thermal lens. w_2 maximised when L2=89 mm and ceases at L2=192 mm. w_3 monotonically increases with L2 and approaches asymtote near L2=192 mm. (b) MATLAB cavity mode simulation at maximum L2. 49
4.9 Linear cavity setup with WPSI for OV generation. The back-mirror (BM) and partial reflective mirror (PR) enclosed the gain medium (GM). An aperture (AP) was used to block the back-reflection from the WPSI. 50
4.10 (a) Intensity profile of OV generated by the linear cavity. Although the intensity profile of the ring is good, the phase singularity has non-zero intensity (b) Intensity cross-section of OV along the horizontal axis (indicated by the red dotted line in (a)) 50
4.11 FP setup to analyse the laser emission spectrum. The fringe orders have been identified as $s' - s = 1$ and $s' - s = 2$ in orange and red respectively. Each fringe is shown to possess a dual ring structure denoting bi-modal laser emission. 51
4.12 FP rings for emission at (a) lasing threshold and (b) ~ 0.8 W lasing power. At threshold we immediately see multimode emission with a line width of $\Delta\nu = 6$ GHz measured using an FP with FSR = 10 GHz. Above threshold the line width becomes too broad to measure using this FP as indicated by overlapping fringe orders. 52
4.13 Optical setup of the ring cavity vortex laser. It is comprised of the gain medium (GM) optically pumped at 808 nm. High-reflectance mirrors (HR) and partial-reflectance mirror (PR) form the remained of the cavity. A retro-reflective (RR) mirror is used of seed a portion of the ACW power leaked through the back into the cavity in the opposite direction. This biases the internal mode in the CW direction. The WPSI is used as a VOC to sample the intracavity mode and generate an OV in its reflection. Lens (f) used for internal mode size control. 53
4.14 FP ring for SLM laser emission. Rings' separation matches the FSR of the FP. Emission linewidth was measured to be at least 50 MHz. 54
4.15 (a) Reference (b) OV and (c) fork interferogram used in the phase retrieval algorithm. 56
4.16 (a) The intensity of the OV signal and (b) associated phase profile. (c) The intensity and (d) phase reconstructed from the fork interferogram. (e) Modal decomposition shows 97.7 % $LG_{0,-1}$ mode purity with trace contributions from other LG_{pl} modes. 58
4.17 The ring cavity lases at a threshold of 0.06 W and an efficiency of 22.6 % . . 59
4.18 Pump powers at laser threshold for varying PR reflectances. 59

5.1 Top view of the optical bench setup comprised of the laser cavity, active power modulation components, the levitation system and levitation diagnostics itself comprised of levitating shell imaging and position sensing. . . 61
5.2 Top-illuminated microscope image of silver-coated shells. 63
5.3 Internal shell structure. (Not to scale) 63
5.4 (a) Fine line fractures seen on the surface of the shells. Shell on top-right has smaller shell protrusions on its surface. (b) Discoloured shell observed with distinct reddish-orange colour. (c) Egg-shaped shell 65
5.5 Frequency distribution of successfully levitated microspheres between 20 µm - 110 µm. The shell counts appears to be tending towards a uniform distribution upto the 60 µm range with a slight preference for shells in the 70 µm range. The gap in the 80 µm range is currently unaccounted for. 66
5.6 Distribution of microshell sizes from sample images. 66
5.7 (a) Side view schematic of the levitation system with OV input, focusing optic f and trapped microsphere inside draft collar (b) Close-up of draft collar with trapped microsphere. IR light appears purple on the camera . . 67
5.8 Half-wave plate and Faraday rotator used to protect the laser cavity from back-scatter. Modulation system consists of two Pockels cells connected to an HV-driver and signal generator. Pi5-ADC may be connected to generate custom time-signals. 68
5.9 Beam delivery to the vacuum chamber levitation system. A by-pass was installed to avoid transmission lossed for when power modulation was not desired. The chamber was stationed on a portable optical bench. A periscope after the second AP was used to bring the beam to the appropriate level. . 69
5.10 (a) Top view schematic of the trapping diagnostics consisting of a Red HeNe back illumination source, microscope objective and camera fitted with a 633 nm bandpass filter. (b) shows similar for an incoherent green LED illumination source. 70
5.11 Image of microsphere (diameter = 110 µm) taken using the HeNe back-illuminated diagnostics microscope. Inhomogeneous background due to speckle interference 71
5.12 Collage of microsphere imaged produced using LED back-illumination. (a) Poor image contrast (b) Aberration in shell image due to misalignment of delivery lenses with microscope (c) Smooth background but weak contrast (d) High contrast. 72
5.13 (a) Back illuminated image of wire ($d = 0.6$ mm). (b) Intensity cross-section used to calibrate magnification. 72
5.14 Measured position along the (a) vertical and (b) horizontal axes shows a linear response scorss the full length of the sensor. 74
5.15 Frequency response of PRP90A sensor for frequencies between 10 Hz to 10 kHz 75
5.16 Frequency response of PRP90A sensor for frequencies between 10 Hz to 10 kHz 77

5.17 Frequency response of ADC-Pi5 (a) with and (b) without active feedback routine and ADC-Pi5 with the v14 PD sensor head (c) with (d) and without active feedback routine. 78

5.18 Circuit diagram of the position sensing PSD head showing the sensor, transimpedance and voltage amplification stages with integrated RC filters for high frequency noise reduction. 79

5.19 Noise characterisation of various signal types fed into the ADC and ADC+v14 sensor head. The response of the ADC was directly measured by firstly passing a DC voltage signal using a low-noise 3.3 battery. This characterises the noise associated with an unchanging signal (blue). Then the noise response of a time varying signal was characterised by producing a fixed 60 Hz sinewave using a signal generator and passing it directly into the ADC (green). Similar was done with the ADC+v14 sensor head where the voltage sources were connected to an LED. This replicated the steady (orange) and time varying (red) brightness response of the sensing system. Finally the noise associates with fluctuations in the laser power was recorded (purple). 81

6.1 (Left) Transmissive target trapped in a Gaussian beam with an attractive restoring force acting to pull the target towards the beam center. (Right) Reflective target held in an annular beam. Reflected rays produce a repulsive force away from the bright ring perimeter. The target is held in the intensity minimum at the beam center. 83

6.2 Ray picture of scattering of light incident at M on shell located at origin O. Azimuthal angle ϕ is measured from x to when it meets For rays parallel to $+z$ incident at point M, the incidence and reflection angle are $\theta_i = \theta_r = \theta_1$ relative to the surface normal, n. P is the projection of M onto the $xy-$plane. Since M is located on the lower hemisphere, its spherical coordinates are defined as $(r, \phi, 180 - \theta_1)$ for θ taken relative to the $+z$ axis. For divergent rays incident at P, we have $\theta_i = \theta_2$ to the normal. The divergence half-angle is $\theta_2 - \theta_1$ 85

6.3 Damping curves for 50 µm shell at $T = 300\,\mathrm{K}$ and constant dynamic viscosity within the pressure range. (Red) Stokes' law assuming constant γ with pressure. (Blue) KTG-γ varying with pressure. 10 % deviation in γ at 3×10^3 Pa. 93

6.4 One must imagine Sisyphus happy 97

6.5 Microshell is illuminated in the $+z$-direction. It has $d = 100\,\mu\mathrm{m}$ with 0.1 µm thick silver (Ag) layer, and 0.85 µm total wall thickness. 99

7.1 (a) Radial temperature distribution extending to 2.5x shell radius. Shell boundary indicated by the solid line (b) Full simulation domain with zero flux boundary at 5 mm radial distance from the shell center. 105

7.2 Average surface temperature-time plots for 34 µm shell for various static pressures. We find rapid increase in average surface temperature as pressure decreases due to increased reliance on radiative heat loss. 106

7.3 Simulated temperature distribution over shell surface against radial position. The shell is centered at 0 and heated from below. 107

7.4 Simulated temperature distribution of shell interior from $-r$ to r. Shell layer boundaries indicated by the red vertical lines. 108

7.5 (a) Simulated surface temperature distribution of shell under 10^4 Pa of pressure. (b) Internal shell temperature distribution. 108

7.6 (a) Simulated surface temperature distribution of shell under 10^3 Pa of pressure. (b) Internal shell temperature distribution. 109

7.7 Diagnostics setup for the vacuum chamber levitation system. Imaging and position sensing arms were installed on a raised breadboard platform. . . . 114

7.8 Vertical stability shown as (a) position time series data over 106 s duration and (b) position histogram for 37 µm shell. 115

7.9 Vertical position distributions shown in (a) Linear-linear axes histograms with fitted Gaussians and (b) the same fittings plotted on Log-linear axes with an additional sum fit to show the combined profile contributions. . . . 116

7.10 Horizontal stability shown as (a) position time series data over 106 s duration and (b) position histogram for 37 µm shell. 117

7.11 Horizontal position distributions in (a) Linear-linear axes histograms with fitted Gaussians. (b) The same fittings plotted on Log-linear axes. 118

7.12 Power spectral density of 37 µm shell using 10^6 samples collected over 106 s. Brownian (green) and rough oscillatory motion (orange) modelled applied to fit the spectrum. Low frequency oscillations at 2 Hz oscillation with higher harmonics indicating complex oscillation structure. 119

7.13 Vacuum chamber setup. 120

7.14 Levitating shell inside the draft collar of the vacuum chamber. The shell is back illuminated using a green LED. 120

7.15 Position-histogram and PSD results for 90 µm shell levitated at (a) 10^5 Pa (b) 7×10^4 Pa (c) 4×10^4 Pa (d) 8×10^3 Pa (e) 1×10^3 Pa. 10^6 samples were obtained at a rate of $f_{Nyq} = 3.6$ kHz. In all cases the PSD fit shows f_c around the Hertz level or lower. 122

7.16 (a) Position-histogram and (b) PSD results for 80 µm shell levitated at 500 Pa pressure. 123

7.17 Power modulation setup. Due to low driving voltage range of the HV-drivers, two Pockels cells were used in series to get 10 % swing. 124

7.18 Peak oscillation amplitudes in the FFT power spectra of the respective modulation frequencies is plotted. 125

7.19 (a) Two 67 µm trapped shells with a third vertically and radially separated. Deep-red spots on the lower surfaces denote scattering of the trapping beam. (b) The lone shell was observed to loop underneath and attached itself to join the cluster. 126
7.20 (Left to right) Images of two 50 µm shells initially separated by 15 µm then combine to form shell cluster. Cluster is observed to change orientation over time. When laying flat the shells sat higher in the trap. 127
7.21 Two 30 µm levitating shells vertically separated by 20 µm 127
7.22 (a) Optically levitated 4-shell cluster (b) cluster rotated. (c) Vertical stack of three 60 µm shells. (d) Top-heavy stack. (e) The Mickey Mouse cluster comprised of three 43 µm shells (f-g) cluster rotated. 128
7.23 Plot taken from [164]. It compares force and acceleration sensitivity with radius of levitated silica particle at 1 kHz trap frequency. γ_{sc} denotes photon recoil heating 129

8.1 (a) Same as Fig. 7.15(d) it shows the PSD of a 90 µm shell levitating at a pressure of 10^3 Pa. (b) Corresponding force sensitivity as per Eq. 8.4. Red dotted line denote the thermal noise limit per measurement bandwidth. . . 137

List of Tables

4.1 Comparison of physical and optical properties of Nd:VO_4 and Nd:YAG laser crystals. Data from ref. [69, 70] 37
4.2 Pump emission wavelength and optical transmission for varying heat sink temperatures. 48

5.1 Table shows a range of microsphere diameters with corresponding wall-thicknesses. Note: these values are not from direct measurement but obtained from the Cospheric who estimates values using true particle densities. 64

6.1 Knudsen numbers for varying ambient pressures. Values calculated correspond to a trapped shell diameter of 50 µm and gas particle size of 3.7×10^{-4} µm [134]. 92

7.1 Comparision of results for expected variance based on a thermally driven oscillator, variance computed directly from position data and variance computed from the sum of the PSD over the frequency domain. It is often more intuitive to work in terms of standard deviation and so corresponding values are included. 117
7.2 Similar to Tab. 7.1 the entries show the expected and computed spatial variance and standard deviation in the horizontal axis data. 118

Contents

1 Introduction **1**

1.1 Project overview 2

2 Optical vortex generation **5**

2.1 Motivations 5

2.2 Laguerre-Gaussian optical vortex 6

2.3 OAM in electro-magnetic fields 7

2.4 Optical vortex generation techniques 9

2.4.1 Extracavity optical vortex generation 9

2.4.2 Intracavity optical vortex generation 12

2.5 Interferometric mode generation 13

2.5.1 Experimental implementation 14

2.6 Optical vortex diagnostics 15

2.6.1 Determining helical phase profile and handedness 15

2.6.2 Beam quality 16

2.6.3 Modal decomposition 17

2.7 Summary 18

3 The Wedge-Plate Shearing Interferometer **20**

3.1 Motivations 21

3.2 Addition of two Gaussian beams 21

3.3 WPSI configuration 23

3.4 WPSI for vortex generation 25

3.5 Angle of incidence 26

3.6 Beam waist correction 27

3.7 WPSI operation 28

3.8 Vortex output coupler 30

3.9 Intracavity phase control 30

3.10 Summary 32

4 Solid state laser cavities **34**

4.1 Selection of laser gain media 34

4.1.1 Rare-earth doped laser gain media . . . 36
4.1.2 Nd:YVO_4 . . . 37
4.2 Linear resonator . . . 38
4.2.1 Linear resonator stability . . . 39
4.2.2 Internal and thermal lenses . . . 41
4.2.3 Gaussian cavity mode propagation . . . 43
4.2.4 Longitudinal modes and non-ideal effects . . . 43
4.3 Four-mirror ring resonator . . . 44
4.3.1 Ring resonator stability . . . 44
4.3.2 Ring resonator longitudinal modes . . . 45
4.3.3 Unidirectional ring resonator . . . 45
4.4 Linear vortex laser . . . 46
4.4.1 Pre-laser characterisation . . . 46
4.4.2 OV generation in a linear cavity . . . 49
4.5 Ring vortex laser . . . 53
4.5.1 Unidirectional laser cavity . . . 54
4.5.2 Beam quality measurement . . . 54
4.5.3 OV modal decomposition . . . 55
4.6 Power efficiency . . . 56
4.7 Summary . . . 56

5 Optical levition system & Diagnostics 60
5.0.1 Motivations . . . 60
5.1 Reflective shell targets . . . 62
5.2 Levitation system . . . 65
5.3 Beam delivery . . . 67
5.4 Vacuum chamber integration . . . 68
5.5 Imaging system . . . 69
5.6 2-D position detector . . . 73
5.6.1 Thorlabs PDP90A Lateral effect sensor . . . 73
5.7 1-D position detector . . . 76
5.7.1 Electrical response of PD system . . . 76
5.7.2 Asynchronous data aquisition . . . 80
5.7.3 Spatial noise . . . 80

6 Levitation optomechanics 82
6.1 Introduction . . . 82
6.2 Optical trapping mechanisms . . . 83
6.3 Ray optics force model . . . 84
6.4 Harmonic oscillator model . . . 88
6.4.1 Mathematical prelude . . . 89
6.4.2 Power spectral density of levitated oscillator . . . 90

6.5 System damping . . . 91
6.5.1 Pressure dependent damping . . . 92
6.5.2 Damped oscillator . . . 93
6.6 Thermally driven oscillator . . . 94
6.6.1 Brownian dynamics . . . 94
6.6.2 Thermal noise power density . . . 95
6.7 Parametric oscillator . . . 96
6.8 Photophoresis . . . 97
6.8.1 Photophoretic force . . . 97
6.8.2 Photophoresis on coated hollow shells . . . 98
6.9 Summary . . . 101

7 Levitated reflective microshells 103
7.1 Thermal study on laser induced heating . . . 103
7.1.1 Simulation setup . . . 104
7.1.2 Thermal simulations . . . 105
7.1.3 Photophoresis: briefly revisited . . . 110
7.2 Discrete Fourier analysis . . . 110
7.2.1 Signal widowing . . . 112
7.2.2 DFT summary: worked example . . . 112
7.3 Analysis of shell oscillations . . . 113
7.3.1 Spatial variance of an oscillating shell . . . 116
7.4 Optical levitation at low pressure . . . 118
7.5 Vertical position stabilisation . . . 123
7.6 Trapping power modulation response . . . 124
7.7 Multi-shell levitation . . . 125
7.7.1 Spatially separated shells . . . 126
7.7.2 Shell clusters . . . 127
7.8 Summary . . . 128

8 Conclusions & future works 131
8.1 Thesis conclusion . . . 131
8.2 Future work . . . 133
8.2.1 Laser stability . . . 133
8.2.2 Active feedback stabilisation . . . 134
8.2.3 Levitation at low pressure . . . 134
8.2.4 High-intensity laser experiments . . . 135
8.2.5 OAM transfer . . . 135
8.2.6 Force sensing applications . . . 136
8.2.7 Final remarks . . . 137

References 138

Chapter 1

Introduction

Since their inception, lasers have played an integral role in revolutionising the modern world with applications spanning from surgical medicine [1] to material processing and fabrication [2]. The generation of high optical irradiance, fine-tuning of its chromatic output, and structuring of its beam profile have been key areas of laser development that has facilitated their wide-ranging applications. The delivery of highly concentrated optical energy has allowed researchers to create extreme laboratory conditions to study systems previously inaccessible due to energy limitations. In particular laser-induced high-density plasma physics has itself stemmed research covering laboratory astrophysics [3] particle acceleration [4] and high energy radiation generation [5]. The development of frequency stable laser systems through the use of reference cavities and frequency combs have been used to probe fine electron transitions in intricate atomic systems to achieve unprecedentedly low measurement uncertainties [6, 7]. Large laser interferometer facilities with high finesse oscillators have demonstrated incredible feats of metrology [8]. And undoubtedly optical manipulation of matter ranging from biological cells to trapped atoms [9] has demonstrated a rich history of discovery.

Maiman's work in 1960 [10] demonstrated for the first time the operation of a working laser using a flash lamp to pump a rod of synthetic ruby. The field of laser development subsequently experienced rapid growth. Later designs explored variations in operational parameters, including advancements in continuous-wave (CW) [11] and Q-switch [12] operation, the introduction of fiber-based systems [13, 14] and the development of more efficient gain media to enhance output power and wavelength tunability. Typically, lasers oscillate at the TEM_{00} transverse mode, which is an intensity profile that follows a Gaussian distribution. This is also referred to as the fundamental mode as it is the simplest solution to the Helmholtz wave equation that governs optical propagation and within the laser cavity under the paraxial wave approximation. It is possible to generate higher-order modes whose intensity profiles exhibit greater spatial complexity. The separation of variables when solving the paraxial wave equation in cartesian coordinates yields higher order solutions in the Hermite-Gaussian (HG) modes, and their cylinderical analogues the

Laguerre-Gaussian (LG) modes under their respective coordinate basis. Of these, it is the latter which will be of relevance to the work presented in this thesis.

The Laguerre-Gaussians are a set of modes with annular geometries characterised by the their radial index, p, and azimuthal index, l, often expressed as LG_{pl}. For $p = 0$ and $l \neq 0$ these modes form a series of ring-like intensity profiles with an intensity minimum at their center referred to as the phase singularity. The azimuthal index, sometimes referred to as the topological charge, or simply the charge of the vortex, denotes the number of times the beam winds itself around its axis. Any beam that possesses an azimuthal phase profile carries within itself a discretised component of orbital angular momentum (OAM) of $l\hbar$ per photon [15]. This is distinct from spin angular momentum (SAM) that arises from the polarisation state of the optical field. As the beam propagates, the wavefronts form a helical structure as the phase rotates about its optical axis. As the charge of the beam increases, the helical structure becomes tighter and thus carries greater OAM. Although the term "optical vortex" may generally refer to rotation inducing beams, the work in this thesis exclusively relates to the generation of only OAM carrying optical vortex beams of which we focus on the simplest amongst them, the first order LG_{pl} when $p = 0$ and $l = 1$.

1.1 Project overview

This thesis reports on the development of a compact laser cavity capable of direct LG_{01} vortex beam generation using interferometry and then demonstrates its application in the optical levitation of reflective hollow-spherical targets. The structure of the thesis is as follows.

Chap. 2 provides the theoretical framework necessary for the existence of optical vortex beams. It introduces the Laguerre-Gaussian modes which are the primary focus of the type of optical vortex used in this work, followed by an overview of current generation techniques. It also introduces the idea of interferometric mode conversion and discusses previously demonstrated examples. Finally in-lab techniques to diagnose optical vortex beams are presented, used to characterise these beams in terms of beam quality, confirm phase helicity and determine its modal content.

Chap. 3 introduces the Wedge-Plate Shearing Interferometer (WPSI) as the primary tool for vortex beam generation in this work. It provides a detailed frame-work describing interferometric mode conversion taking the simple example of two TEM_{00} Gaussian beams in superposition and deriving the satisfying conditions under which its transformation to an LG_{01} vortex is possible. This frame-work is then applied to the specific geometry of the WPSI which takes a single Gaussian beam to produce an LG_{01} beam in its reflection. The chapter will describe the WPSI's configuration and provide operational procedures such as mode generation parameters, mode corrective mechanisms and realisations towards intracavity use for enhanced performance.

Chap. 4 begins discussing aspects of solid-state laser development including the choice

of laser gain-medium and its spectroscopic properties, and resonator stability for linear and ring configurations. Building upon the idea of intracavity optical vortex generation, it shows experimental demonstrations of vortex lasers in linear and ring cavity arrangements. We find severe limitations in the linear case due to broadband emission with incompatible coherence length for interferometric mode conversion leading to non-optimal vortex beam generation. This is resolved using a ring cavity arrangement with the WPSI acting as a vortex output coupler. This system was capable of watt-level vortex output (1.15 W) with 98 % LG_{01} mode purity. A full system characterisation is presented implementing techniques that have been mentioned in previous chapters.

The combination of watt-level power and annular beam geometry is seldom seen as research groups often have limited access to systems with such capabilities. This provides a suitable domain for experimental explorations, namely in the optical levitation of large reflective spherical targets ($\sim 100\,\mu m$). Chap. 5 presents the optical setup for the vortex beam levitation system including beam delivery, properties of our trapping targets and the optical trap itself with integrated vacuum chamber and accompanying diagnostics. Particular attention is given to the operation of position sensors that were developed in-house by our collaborator Prof. Roland Smith that were tested in this work.

The larger goal of this work is in the context of levitating targets to be used as firing targets for high-repetition rate, ultra high-power laser systems. There is a strong desire to levitate targets with high-atomic number materials, such as those of metallic composition, as this enables the production of higher-density plasmas, and high energy radiation as compared with dielectric targets. However, prior to this work, there is a current lack of methods to facilitate the levitation of suitably sized metallic targets.

Chap. 6 delves into the theoretical background of optically levitated targets. A ray-optics model is used to describe the optical forces acting on a reflective spherical target to achieve optical levitation. When trapped, the target can be modeled as a mechanical oscillator and Fourier-based analytical tools are used to describe its expected time dynamics. This chapter aims to catalogue a collection of analytical tools that can be used to understand the characteristics of our system. Various models are compiled investigating the effects of a thermally driven system exhibiting Brownian-like motion, the influence of various damping regimes and explore the effects of photophoretic forces.

Chap. 7 presents experimental findings on the optical levitation of reflective targets. These are used to characterise the degree of spatial confinement using the position time series measurements made using the newly developed position sensors. We have observed high spatial stability ($<5\,\mu m$). A thermal study is conducted looking at the evolution of surface and internal heating at various pressures. We find there to be a fixed difference in temperature between the poles of the targets due to asymmetric heating by the laser. However this difference remains fixed as a function of the thermal conductivities of the target and surrounding medium. Fourier analysis is used to inspect spectral features of trapped target dynamics. Measurements have been made at pressures from 1 atm down

to $1/100^{th}$ atm. We generally find good match at low frequencies with that expected of a thermally driven system however, these results could benefit from greater resolution to better resolve these features. There is generally poor matching at high frequencies as other spectral features unaccounted for in our model begin to dominate. A major concern was found in the coupling of induced rotation of the trapped target being interpreted as position changes by the sensors thus invalidating the reliability of these measurements. For this reason position stabilisation using active feedback was unsuccessful. Finally, non-spherical target trapping is demonstrated with several cases of irregular target geometries that could allude to interesting application where bespoke target geometries are required.

Having starting this thesis from an empty optical bench, by this stage we have now covered the development of the entire optical system from scratch - from OV generation using a WPSI and its implementation as a VOC to explorations in optical levitation. This work has been highly developmental and exploratory meaning the route to progress wasn't always straightforward. Chap. 8 provides some reflections on select areas that warrant further investigation, either towards the enhancement of current capabilities or to explore research that was cut short.

Chapter 2

Optical vortex generation

The literature surrounding OV generation spanning the last three decades has seen a broad array of methodologies demonstrating the rich breadth of research that has gone into their development and implementation. This chapter will provide a general overview of OV generation beginning with the theoretical framework underpinning the LG modes in particular and their carrying of OAM. We will proceed to discuss contemporary OV generation techniques, the various mechanisms through which this is achieved and discuss their function and limitations. We then present interferometric mode conversion of a fundamental Gaussian mode for OV generation which forms the core focus of our OV generation research. At this stage only a generalised view will be presented as further details on our implementation will be given in Chap. 3. This chapter will then come to a close by bridging the theoretical realisations of OVs to how they are diagnosed experimentally through table-top characterisation and profiling measurements.

2.1 Motivations

Allen *et al.*'s discovery (1992) revealed any beam possessing an azimuthal phase profile, such as an LG-mode OV, will innately carry a well-defined component of orbital angular momentum (OAM) [15]. Other works have demonstrated their intensity profiles to be propagation stable and exhibit self-healing capabilities [16]. These properties have since garnered significant interest within the scientific community at large and have been exploited widely for various applications. Uses have been found in quantum information and cryptography with the observation of entangled photon OAM states [17] and the development of methods to measure the OAM of single photons [18]. OAM liberates a new degree of freedom to which information can be encoded [16] and preserved in free-space optical communications [19, 20]. Material processing has made use of OAM in the manufacture of micro- and nano-chiral needles [21, 22]. OV-based phase masks have been used to aid astronomical observations in the form of vortex coronagraphs to improve dynamic and angular resolution of dim objects such as exoplanets [23, 24]. And finally, the OV intensity

profile has facilitated super-resolution in microscopy [25, 26] and metamaterial processes [27]

The harnessing of OVs and their OAM in such wide-ranging applications has naturally led to the development of just as numerous OV generation techniques. The current landscape of OV generation techniques will be explored later in this chapter, with popular examples including mode converting lenses, spiral phase plates [28], computer generated holograms [29], diffractive optics [30], q-plates [31, 32], and spatial light modulators [33]. Each method can be evaluated based on value and trade-offs that must be considered for their long-term viability within a particular niche or the sphere of OV generation in general. Some points to consider include, ease of access to relevant hardware and setup, the quality of the generated optical vortex, power scaling potential and system tunability in wavelength, handedness or charge selection. Of course these do not encapsulate the entire range of experimental considerations as one must evaluate the requirements specific to their system or application.

2.2 Laguerre-Gaussian optical vortex

Laguerre-Gaussian modes are characterised by their azimuthal index, l, and radial index, p. The naming convention for l may vary depending on the context in which is it used. In the context of OVs and their physical properties, azimuthal index refers to the helical phase structure of the OV whereas, the charge may be associated with the quantised OAM states of its photons. These are however manifestations of the same phenomenon, and so may be used interchangeably.

Only those LG modes with $l \neq 0$ possess OAM to be considered OVs. These are comprised of a set of ring-like modes with bright perimeters and an intensity minimum at its center referred to as the phase singularity. The simplest of these is the first-order LG_{01}. The complex amplitude of a Laguerre-Gaussian propagating in the z-axis can be described mathematically in cylindrical coordinates as the following [15],

$$E_{pl}^{LG}(r,\phi,z) = u_{pl}^{LG}\exp(i(kz-\omega t)) \tag{2.1}$$

where the u_{pl}^{LG} is the field amplitude

$$\begin{aligned} u_{pl}^{LG}(r,\phi,z) = \frac{C_{pl}}{w(z)}\left(\frac{r\sqrt{2}}{w(z)}\right)^{|l|} L_p^{|l|}\left[\frac{2r^2}{w(z)^2}\right] \\ \times \exp\left(-\frac{r^2}{w^2(z)}\right)\exp\left(-ik\frac{r^2}{2R(z)}\right)e^{-i\psi(z)}e^{-il\phi} \end{aligned} \tag{2.2}$$

where $C_{lp}^{LG} = \sqrt{\frac{2p!}{\pi(p+|l|)!}}$ normalises eq. 2.2 to $\iint |u_{pl}^{LG}|^2\,dx\,dy = 1$. The Guoy phase term is given by $\psi(z) = (2p+|l|+1)\tan^{-1}(\frac{z}{z_R})$ where z_R is the Rayleigh length, and $L_p^{|l|}[...]$ are the

Laguerre polynomials which take the form,

$$L_p^{|l|}(x) = (-1)^{|l|} \frac{d^{|l|}}{dx^{|l|}} L_{p+|l|}(x). \tag{2.3}$$

As we are interested in the cases of $p = 0$, eq. 2.2 may be simplified accordingly.

$$u_{01}^{LG} = \sqrt{\frac{2}{\pi w(z)^2}} \left(\frac{r\sqrt{2}}{w(z)}\right) \times \exp\left(-\frac{r^2}{w^2(z)} - ik\frac{r^2}{2R(z)} - 2i\tan^{-1}\frac{z}{z_R} - i\phi\right) \tag{2.4}$$

The LG modes form a complete set of basis functions that span the set of solutions to the paraxial wave equation. Meaning, any allowed mode can be decomposed into a linear combination of one or more of these basis functions. An arbitrary field U(x, y) may be decomposed into its constituent parts as,

$$U(x,y) = \sum_{p=0}^{\infty}\sum_{l=0}^{\infty} K_{pl} u_{pl}^{LG} \tag{2.5}$$

$$c_{pl} = \iint_{-\infty}^{\infty} \left(u_{pl}^{LG}\right)^* U(x,y)\, dx\, dy \tag{2.6}$$

where K_{pl} is the complex expansion coefficient such that $\sum_{p,l} K_{pl} = 1$ when $\iint |U|^2\, dx\, dy = 1$. Therefore $|K_{pl}|^2$ represents the relative power of each constituent LG mode.

The higher-order modes still obey standard Gaussian beam propagation with parameters such as radius of wavefront curvature R, the beam radius at position z along the propagation axis $w(z)$, and the Rayleigh length z_R,

$$R(z) = z + \frac{z_R^2}{z} \tag{2.7}$$

$$w(z) = w_0\sqrt{1 + \frac{z^2}{z_R^2}} \tag{2.8}$$

$$z_R = \frac{\pi w_0^2}{M^2\lambda} \tag{2.9}$$

2.3 OAM in electro-magnetic fields

Orbital angular momentum (OAM) emerges from the helical structure of the optical phase causing the wavefronts to twist about the optical axis. Allen [15] demonstrated any beam that carries such a phase structure carries a well defined component of orbital angular momentum (OAM). What is surprising here is the OAM states are quantised in units of $\hbar$ just as spin angular momentum (SAM) - the difference here being that OAM states are not restricted to $\pm\hbar$ but instead take $l\hbar$ per photon. The sign determines the handedness of rotation and $l \in \mathbb{Z}$ is the topological charge of the beam. This also results in the field possessing a distinct annular intensity profile. Fig. 2.1 shows the intensity profile, phase and wavefronts for LG modes with $l = 0, 1, 2$.

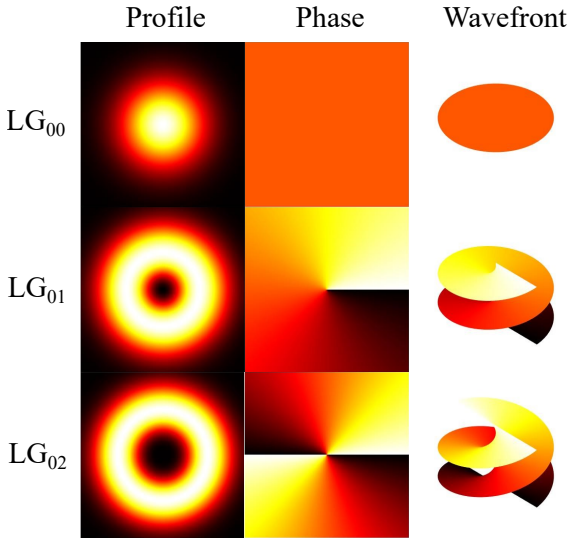


Figure 2.1: Intensity profile, phase map and wavefront structure of $l = 0, 1, 2$ LG modes.

A linearly polarised transverse electromagnetic field cannot carry OAM unless there is an azimuthal component to its Poynting vector. This can only be achieved if the wave is finite in extent either through aperturing effects of measurement apparatus or enforced by the field's own geometric constraints [34]. The total angular momentum density of an electromagnetic field, u, in free space can be written as $\boldsymbol{j} = \boldsymbol{r} \times \boldsymbol{p}$ where $\boldsymbol{r}$ is the radial component of the field, $\boldsymbol{p} = \epsilon_0 \boldsymbol{E} \times \boldsymbol{B}$ is the linear momentum density using the electric and magnetic field components, $\boldsymbol{E}$ and $\boldsymbol{B}$, and ϵ_0 is the electric constant. For a linearly polarised field u we can write,

$$\begin{aligned} \boldsymbol{p} = \epsilon_o \boldsymbol{E} \times \boldsymbol{B} &= \frac{\epsilon_o}{2} \left(\boldsymbol{E}^* \times \boldsymbol{B} + \boldsymbol{E} \times \boldsymbol{B}^* \right) \\ &= i\omega \frac{\epsilon_o}{2} \left(u \nabla u^* - u^* \nabla u \right) + \omega k \epsilon_o |u|^2 \hat{\boldsymbol{z}} \end{aligned} \tag{2.10}$$

The angular momentum density of an optical field u_{pl} per unit power is given by [15],

$$\boldsymbol{j} = \boldsymbol{r} \times \boldsymbol{p} \tag{2.11}$$

$$\boldsymbol{j} = \frac{l}{\omega} \frac{z}{r} |u_{pl}|^2 \boldsymbol{r} + \frac{r}{c} \left[\frac{z^2}{(z^2 + z_R^2)} - 1 \right] |u_{pl}|^2 \boldsymbol{\phi} + \frac{l}{\omega} |u_{pl}|^2 \boldsymbol{z}. \tag{2.12}$$

The total angular momentum $\boldsymbol{J} = \int \boldsymbol{j} dV$ is symmetric in $\boldsymbol{r}$ and $\boldsymbol{\phi}$, leaving only the $\boldsymbol{z}$ component $J_z = l/\omega$. For N photons of energy $\hbar\omega$, the angular momentum of a single photon is then $l\hbar$. This is the OAM of the field since the Poynting vector $c^2 \boldsymbol{p}$ traces a spiral in z. However, OAM is not always the only source of angular momentum. We can separate $\boldsymbol{J}$ into parts $\boldsymbol{L}$ and $\boldsymbol{S}$ by taking the vectorial picture on $\boldsymbol{B}$ in terms of potential $\boldsymbol{A}$ [35],

$$\begin{aligned} \boldsymbol{J} &= \epsilon_0 \int dV \left[E_i \left(\mathbf{r} \times \nabla \right) A_i + \mathbf{E} \times \mathbf{A} - \nabla_i \left(E_i \mathbf{r} \times \mathbf{A} \right) \right] \\ &= \epsilon_0 \int dV \left[E_i \left(\mathbf{r} \times \nabla \right) A_i + \mathbf{E} \times \mathbf{A} \right] - \epsilon_0 \int (\mathbf{r} \times \mathbf{A}) \mathbf{E} \cdot d\mathbf{S}, \end{aligned} \tag{2.13}$$

Field localisation ensures $\boldsymbol{A}$ decays rapidly in r so the surface integral falls to 0. We can then identify $\boldsymbol{L} = \epsilon_0 \int dV \left[E_i \left(\mathbf{r} \times \nabla\right) A_i\right]$ as the OAM part through analogy of the quantum mechanical orbital angular momentum operator and $\boldsymbol{S} = \epsilon_0 \int dV \mathbf{E} \times \mathbf{A}$ as the SAM part through its vectorial dependence, and so the polarisation, of the field [35].

For a field u of arbitrary polarisation we can write [15],

$$\boldsymbol{p} = i\omega \frac{\epsilon_o}{2} \left(u \nabla u^* - u^* \nabla u\right) + \omega k \epsilon_o |u|^2 \hat{\boldsymbol{z}} + \omega \sigma_z \frac{\epsilon_0}{2} \frac{\partial |u|^2}{\partial r} \hat{\Phi} \tag{2.14}$$

where σ_z is the polarisation state of the field with $\sigma_z = 0$ denoting linear polarisation and $\sigma_z = \pm 1$ denoting left and right-handed circular polarisation. The axial component of the angular momentum is then modified as,

$$j_z = \frac{l}{\omega} |u_{pl}|^2 + \frac{\sigma_z r}{2\omega} \frac{\partial |u_{pl}|^2}{\partial r}. \tag{2.15}$$

and the total angular momentum per photon is then $J_z = L_z + S_z = \hbar(l + \sigma_z)$. Here we have only considered the OAM of LG modes, however other beam families have also been demonstrated to possess OAM such as Bessel [36] and Mathieu beams [37].

2.4 Optical vortex generation techniques

This section a brief overview of common OV generation techniques is presented. These can be categorised into two classes; extracavity techniques where an external laser is used to illuminate an OV generating device, and intracavity techniques where a laser cavity is capable of direct OV emission. There is overlap in some cases where the OV component can be simply integrated into the laser cavity setup for direct emission capabilities.

2.4.1 Extracavity optical vortex generation

Cylindrical mode converters

Allen *et al.*'s work [15] relied on the use of cylindrical-mode converters for OV generation. HG modes form a complete set of solutions to the paraxial approximated Helmholtz equation when solved in Cartesian coordinates; when the coordinate basis is changed to cylindrical coordinates the solutions return the LG modes. One can easily transform between HG and LG modes using a cylindrical lens telescope of which there are two types, $\pi/2$- and π-mode converters. Their construction is simple; two identical cylindrical lenses are separated by either $\sqrt{2}f$ in the case of the $\pi/2$-mode converter or $2f$ for the π-mode converter. Each acts to modify the phase of the axial component of the beam as shown in figure 2.2. A subsequent paper to Allen's 1992 work was later published presenting a more detailed demonstration of the use of cylindrical lenses as mode converters [38]. An analogy was drawn between the transformation of SAM and OAM states. The $\pi/2$-mode converter transforms an HG mode into an LG mode by introducing a $\pi/2$ spatial phase shift, just as a quarter-wave plate is used to transform linear polarisation into circular

polarisation by introducing a $\pi/2$ phase shift to the linear polarisation state. Likewise a π-mode converter can be used to reverse the handedness of rotation on an incident OV, just as a half-wave plate reverses the polarity of a circularly polarised beam.

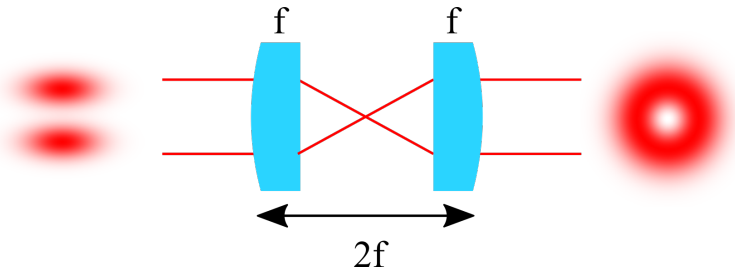


Figure 2.2: Two identical cylindrical lenses separated by 2f used to convert HG mode to LG mode

An HG mode oriented at 45° may be expressed in terms of a pair of HG modes which, when rephased, can be combined to instead form a new LG mode. The cylindrical lenses influence how the Gouy phase of the input modes are transformed depending on their respective indices. For example, the $\pi/2$-mode converter with an HG_{mn} mode input, oriented at 45° to the cylindrical lens axis, will be converted to an LG_{lp} mode where $l = m - n$ and $p = min(m, n)$ (figure 2.3). In contrast, the π mode converter is used to produce a mirror image of the input beam. The operation of these lenses is limited only by the efficiency of their anti-reflective coatings and provides a high-damage threshold mode conversion mechanism suitable for high-power applications. Misalignments in the incident beam and imperfections in the lens' manufacturing can introduce aberrations that can interfere with the mode conversion quality.

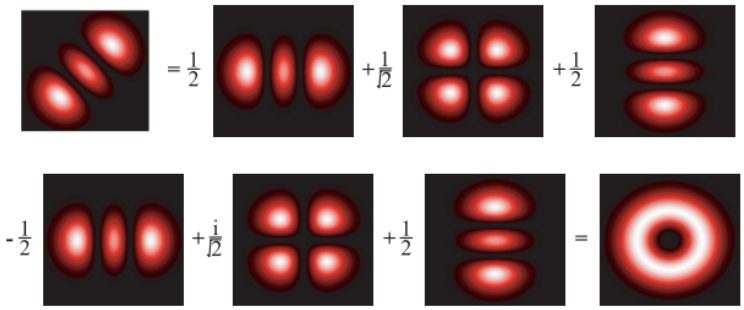


Figure 2.3: (Top) Decomposition of HG mode oriented at 45°. (Bottom) HG modes rephased to form LG mode. Figure from Ref. [34]

Spiral phase plate

Spiral phase plates (SSPs) are optical devices, available in reflection or transmission variants, whose thickness varies as a function of azimuthal angle as shown in Fig. 2.4. This affects the optical path of an incoming beam so that a helical phase is imparted into its output. The transformation of an incident field u is given by $u' = u\exp(i\Delta l\phi)$, where u' is the resultant field and $\Delta l = \frac{\Delta nh}{\lambda}$ is the height of the step, h, in terms of wavelengths

and Δn is the difference in the refractive indices of the SPP and external medium [28]. The resultant mode isn't a pure mode but instead a superposition of LG modes. Hence SPP can suffer from lower mode purity as compared with other techniques. This is due to the fact the SPP only adds the $\exp(il\phi)$ phase shift but neglects matching the intensity profile of the incident field to that of the desired mode. However mode purity increases as higher-order modes are transformed using the SPP as can be seen in Beijersbergen *et al.* 1994. The same paper demonstrates early techniques in improving the performance of the SPP by submersing it in a fluid bath. Adjusting the temperature of the bath, grants control of the index matching the SPP thereby improving the quality of the imparted phase. Since Beijersbergen's 1994 paper, further advancements in SPPs have been made. Precise

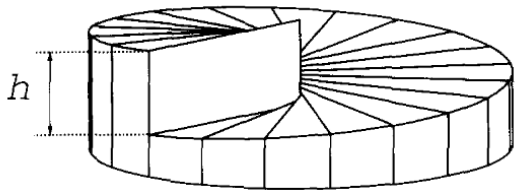


Figure 2.4: Spiral phase plate of step height h. Figure from Ref. [28]

control of the spiral surface is required to minimise wave front distortions from the SPP. Sueda *et al.* (2004) developed a multilevel SPP using electron beam deposition to stack layers of film to coat each division [39]. The optical path through the SPP was controlled by varying the thickness of the film. The use of femtosecond laser photopolymerization has been used to produce SPPs with continuous phase gradients with surfaces accuracies of $\lambda/15$ [40] and potential to reach $\lambda/20$ [25, 26]. OAM beam generation using SPPs has also been shown for mm-wavelength light [41] and x-rays [42].

Q-plates

Q-plates [31, 32] are devices used to convert circularly polarised light, with well-defined SAM, into light that carries OAM with no net angular momentum transfer to the medium. This is due to properties of the q-plate relating to the Parcharatnam-Berry (PB) phase [43, 44] in inhomogeneous, anisotropic media. The q-plate is essentially a liquid crystal cell sandwiched between two glass faces used to create a birefringence plate whose optical axis varies as a function of azimuthal angle,

$$\alpha(r,\phi) = q\phi + \alpha_o. \tag{2.16}$$

The q-plate derives its name from the q denoting its topological charge as per convention in this case, however for purposes of preserving continuity, we will continue to use l as already defined in the remainder of this thesis. The transformation of circularly polarised light incident on a the q-plate can be described using Jones notation.

$$\boldsymbol{M} = \boldsymbol{R}(-\alpha)\begin{pmatrix}1 & 0\\ 0 & -1\end{pmatrix}\boldsymbol{R}(\alpha) = \begin{pmatrix}\cos(2\alpha) & \sin(2\alpha)\\ \sin(2\alpha) & -\cos(2\alpha)\end{pmatrix} \tag{2.17}$$

$\boldsymbol{M}$ is the Jones matrix denoting the transformation and $\boldsymbol{R}(\pm\alpha)$ are 2x2 rotation matrices. Then, for left circular polarised light $\boldsymbol{E}_{in} = E_o \times [1, i]$ into the q-plate, the electric field out of the q-plate is as follows,

$$\boldsymbol{E}_{out} = \boldsymbol{M} \cdot \boldsymbol{E}_{in} = E_o e^{i2\alpha} \begin{bmatrix} 1 \\ -i \end{bmatrix} = E_o e^{i2l\phi} e^{i2\alpha_o} \begin{bmatrix} 1 \\ -i \end{bmatrix} \tag{2.18}$$

The output is right circular polarised light as expected from a half-wave plate, but with a spatial phase, $e^{i2l\phi}$, acquired due to the PB-effect. The q-plate transforms the polarisation state of the photon from $+1\hbar$ to $-1\hbar$. For an $l = 1$ q-plate, the spatial phase corresponds to the beam acquiring an OAM of $2\hbar$ per photon with the handedness determined by the initial spin state. Thus total angular momentum is conserved and no torque is applied to the medium, instead the q-plate acts as a coupler between the SAM and OAM states.

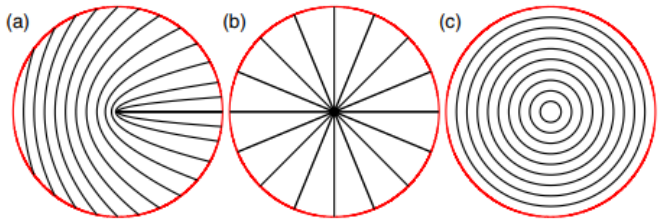


Figure 2.5: (a) $q = 1/2$ and $\alpha_o = 0$ used to generate OAM $l = \pm 1$. Both (b) $q = 1$ and $\alpha_o = 0$ and, (c) $q = 1$ and $\alpha_o = \pi/2$ used to generate $l = \pm 2$. Figure from Ref. [31]

Other methods

Early approaches to OAM generation methods included diffractive optics such as (computer generated) holograms [45, 29] forked and Fresnel spiral diffraction gratings. Forked gratings were generated as the sum of the desired phase distribution and a linear phase ramp. These could be used to replicate any refractive optic but limited to single wavelength operation.

Spatial light modulators (SLMs) have become perhaps the most popular method of OAM generation in recent years. SLMs are electronic pixelated devices that use liquid crystals to manipulate the properties of incident light. Unlike SPPs and diffractive optics, SLMs offer great flexibility in controlling the amplitude, phase and polarisation of an incident beam and are able to generate different topological charges by simply programming a different hologram onto the interfacing device. However SLMs can be expensive and have limited power scaling due to the energy threshold of the liquid crystals making it impossible for high power applications.

2.4.2 Intracavity optical vortex generation

Intra-cavity OV generation offers an alternative approach whereby the vortex is generated directly within the laser itself. This is an appealing prospect as it negates the need for additional optical systems to be assembled and doesn't require precise alignment of

the laser onto external systems. Alignment sensitivity is reduced due to the lasers' natural affinity towards low-loss regimes. Cavity generated OVs, or vortex lasers, have been demonstrated through various methods. As already mentioned there is some overlap in functionality of the mode conversion devices discussed in the previous section for intracavity use. Intra-cavity SPPs [46, 47] q-plates [48] and SLMs [49] have been demonstrated. However, specific intracavity methods also exist that rely on the self-adaptive nature of laser cavities to preferentially select the desired mode. In most cases this involves the suppression of lower-order modes to allow high-order LG modes to gain dominance. This can be achieved by directly inducing losses in lower-order mode through spot-defect mirrors [50]. Annular pumping geometries to create inversion that preferential favours higher-order modes [51]. Coupled-cavities [52] whereby gain is artificially depleted from the center of the inversion region so that the excited emission is annular in profile, resulting in LG mode emission. Off-axis pumping that directly excites higher-order mode generation has been shown. Ref. [53] demonstrates the production of HG cavity modes that require external mode conversion to LG external to the laser cavity whereas refs. [54, 55] present a monolithic ring-cavity that excites the LG mode in its emission for direct OV generation.

2.5 Interferometric mode generation

Using interferometry as a means of OV generation at first seems counter-intuitive. The process requires the input of two fundamental Gaussian beams, that are brightest at their center, to generate a beam with, what is effectively, a hole in the middle and a bright outer ring perimeter. Of course we will come so see experimental verification of this in later sections, however the aim of this section is to provide a brief introduction to the concept and provide a mathematical basis to validate the mode conversion mechanism does truly generate an LG_{01} OV.

Interferometric OV generation has been previously demonstrated using Mach-Zehnder [56], Sagnac [57, 58], and Wedge-plate [59] interferometer setups. Irrespective of the type of interferometer chosen, the key principles in interferometric mode conversion remains the same; two interfering Gaussian beams are spatial misaligned, with a shear offset, d_x, and angular offset θ_y acting in directions orthogonal to one another. Suppose the spatial offset is a horizontal separation along the x-axis, and the angular offset is a separation in the vertical oriented y-axis. Then the canonical condition in eq. 2.19 bounds the upper limit of these offsets relative to the incident beam parameters so that an OV is generated. The origins of this condition will be derived in Chap. 3 but for now we will take this condition to be true. These beam parameters are w_0, the beam waist, and θ_0, the beam divergence.

$$\epsilon = \frac{d_x}{w_o} = \frac{\theta_y}{\theta_o} << 1 \tag{2.19}$$

The canonical condition sets the offset ratio relative to the beam waist and divergence to remain less than unity. We found ϵ-values around 0.2 to be ideal for optimal mode

symmetry and beam quality without the expense of the high precision offset alignment required for when $\epsilon = 0.1$. Additionally, there must be a relative π-phase shift between the two beams so that the interference is destructive. The canonical condition is calculated based of the values of these offsets as measured at the beam waist defined at $z = 0$, and within one Rayleigh range.

2.5.1 Experimental implementation

The Mach-Zehnder interferometer (MZI) is a simple and commonly used optical system consisting of two mirrors and two beam-splitters. A single Gaussian beam is split into two parts at the first BS, each following its own optical path. Ideally there is no relative phase accumulation between the beams except that due to the optical path difference between the two arms. The arms of the MZI are traversed only once by one beam, meaning each beam can be controlled independently, without affecting the other. Turning mirrors are used to introduce spatial and angular offsets as measured at $z = 0$ which is the beam waist location that also coincides with the point of recombination. A tilted AR-plate may be used to vary the optical path in one of the arms to satisfy this condition.

The MZI offers the benefit of simple alignment however is prone to vibrational instability along the length of its arms that can be problematic for the offset sensitive process of interferometric mode conversion implemented here. On the other hand the Sagnac interferometer is a common-path system where both arms travel the same path. This enhances robustness against vibrations instabilities but leads to increased alignment complexity as the shared optomechanical components results in coupling of the alignments controls. The output of the Sagnac is destructive by default which is favourable for OV generation. An AR-plate may also be used here to enable handedness selection during laser operation. Integrating the Sagnac into an existing laser system gives realisation to the vortex output coupler (VOC) - a device used to modify existing laser cavities for direct vortex beam generation by converting a portion of the the intracavity TEM_{00} mode and recycling the remaining power for the next cycle [57]. This approach holds the record for the highest cavity generated OV power [58].

The Wedge-plate shearing interferometer (WPSI) is a single component glass optic similar to an etalon but with a small wedge-angle along one axis. When a tilted WPSI is illuminated by a TEM_{00} beam, Fresnel reflection off the front and rear faces produce two Gaussian beams with shear offset determined by the tilt angle and angular offsets determined by the wedge angle. The relative phase of the two reflections is determined by the double-pass the transmitted beam takes through the optic. A detailed breakdown of the WPSI mode conversion and operational features will be provided in Chap. 3. However, it is clear to see at this stage, the power conversion of the OV is poor due to the low Fresnel reflection coefficient of glass or similar transparent uncoated media. For extracavity use a watt-level source would be needed to generate tens of milliwatts of OV power. However its simple design and fixed geometry allow for easily obtained OV without the need for

precise alignment. The work of this thesis will expand on WPSI OV generation by demonstrating its use inside a laser cavity for OV generation. The high transmission losses are problematic in the extracavity case, whereas the transmitted power when used intracavity can be recycled back into the resonator just as was demonstrated for the Sagnac. This allows the WPSI to operate as a VOC with OV generation in its reflection and output coupling power determined by its face reflectance. Watt-level OV power can be expected due to the high intensity of the intracavity flux.

2.6 Optical vortex diagnostics

This section outlines the methodologies employed for the measurement of key properties used to identify an OV. This is a necessary step in the accurate characterisation our beams to effectively distinguishing between OAM carrying beam and those exhibiting similar traits, such as vector beams with SAM or annular beams lacking phase helicity. Helicity can be shown using an interferogram where the generated fringe pattern reveals the phase structure of the beam; beam quality, that is, how diffraction limited a beam is can be determined through M-squared (M^2) measurement, and mode purity can be determined using modal decomposition. While any one of these measurements could potentially suffice in revealing whether or not a beam is truly an OV that carries OAM, a thorough characterisation combining all three measurements provides a comprehensive understanding of its properties.

2.6.1 Determining helical phase profile and handedness

The interference of two plane waves produces a highly recognisable interference pattern consisting of a series of fringes, from which properties of one beam (the signal) can be inferred provided sufficient information regarding the other (the reference) is known. If one of these plane waves is replaced with an OV, a fork in the fringe pattern is observed indicating the presence of a phase dislocation. This is only possible if one of the beams contained a phase singularity. As the separation between the signal and reference is reduced so too do the number of fringes as they increase in size. This can distort contrast when imaging and make features difficult to resolve. A MZI can be used to separately handle the signal and reference beams so that the generated fringes are appropriately spaced with high contrast.

A difference in wavefront curvature, obtained by introducing a lens in the signal arm, produces a spiral interferogram. Similar to the fork interferogram, a spiral interferogram can also be used to infer the presence of a helical phase profile in the signal beam, with the phase dislocation located at the origin of the spiral arms with the number of arms indicating the topological charge of the OV.

The topolgical charge, or azimuthal index, l, of the OV can be inferred using both forms of the interfergram - its value corresponds to the number of prongs observed at the fork

or the number of arms in the spiral respectively. The handedness of the OV can be inferred using the orientation of the interferogram although it is predominantly a matter of convention. A fork interferogram can only give a relative indication as there is no reference to assign handedness and so its usage is less obvious. It requires predefining the convention used; say, an upwards pointing fork is "right-handed" then the downwards is "left-handed". Handedness selection may be more obvious through the spiral interferogram where the direction of the spiral can indicate the handedness of the underlying OV.

2.6.2 Beam quality

A beam is said to be diffraction limited as it approaches the principle limit in achieving its smallest possible beam width at a given wavelength. The fundamental TEM_{00} Gaussian mode can be brought to the smallest beam width for all wavelengths of light, its size limited only by diffraction. Typical lasers however, will not be resonant on a purely single transverse mode, instead they will often generate a superposition state of resonant modes. It is therefore useful to define a metric to characterise how closely a given beam matches its propagation to that of an ideal TEM_{00} mode. We use the beam propagation factor, M^2, to define the quality of beam propagation expressed as a ratio of the fundamental mode which has $\mathrm{M}^2 = 1$.

The ISO 11146 standard for beam quality measurement is a widely used metric that requires the measurement of beam widths as it is propagated through a focus. This technique defines the beam width by taking the second moment of the beam's intensity distribution as seen in a given plane. The intensity of a Laguerre-Gaussian mode with complex field amplitude $u_{pl}LG$ can be expressed as,

$$I(x,y) = \frac{1}{2Z_0}|u_{pl}^{LG}|^2. \tag{2.20}$$

where $Z_0 = \frac{|E|}{|B|}$ is the impedance of free space. Then the beam widths are found by computing the following [60],

$$\sigma_x^2 = 2\frac{\iint (x-\bar{x})^2 I(x,y)\,dx\,dy}{\iint I(x,y)\,dx\,dy} \tag{2.21a}$$

$$\sigma_y^2 = 2\frac{\iint (y-\bar{y})^2 I(x,y)\,dx\,dy}{\iint I(x,y)\,dx\,dy} \tag{2.21b}$$

Lasers will typically generate modes with some inherent simple astigmatism due to the resonator design or thermal lensing effects. This can result in differences in mode evolution in the $x-$ and y-directions as the beam propagates. We define σ_x as the second moment radius, i.e. $\sigma_x = w_x(z)$, with $\bar{x}$ denoting the centroid location, and similar for the y-axis expression. For the fundamental mode, defining beam width as the $1/e^2$ point of the maximum intensity returns measurements consistent with the above, however this becomes invalid for higher-order modes. It is therefore recommended to use the second-moment

definition for beam width and beam quality measurements.

Once beam widths through the focus have been sufficiently sampled, the M^2 parameter can be found by fitting the following to eq. 2.21 and optimising for M^2 [61].

$$w(z)^2 = w_0^2 + (M^2)^2 \left(\frac{\lambda}{\pi w_0}\right)^2 (z - z_0)^2 \tag{2.22}$$

We see the M^2 factor only modifies the beam propagation term and thus is consistent with Gaussian propagation relation given in eq. 2.8. For astigmatic beams, eq. 2.22 is applied to both expressions in eq. 2.21 and an averaged M^2 is be calculated.

We expect a pure beam of an ideal LG_{01} mode to return a beam propagation factor of $M^2 = 2$ as given by eq. 2.23 for appropriately normalised $|c_{pl}|^2$. Beam quality measurements can be helpful in diagnosing defects in optical setup. The deterioration of beam quality, or lack thereof, when comparing the M^2 before and after an optical component is inserted can indicate the presence of poor surface quality or aberrations inherent to the optic.

$$M^2 = \sum_{p=0}^{\infty} \sum_{l=0}^{\infty} (2p + |l| + 1)|c_{pl}|^2 \tag{2.23}$$

Cavity adjustments can also be steered in the direction of optimal M^2 to produce high-quality resonant modes. This is particularly important in the generation of OVs through interferometric addition as the resultant beam quality is contingent on the quality of the underlying constituent Gaussian modes. Beam quality measurements can also indicate the presence of unwanted higher-order transverse modes resonant within a laser cavity. The degree of their contribution is proportional to their respective power fraction $|c_{nm}|^2$.

2.6.3 Modal decomposition

In Sec. 2.6.2 we saw how beam quality measurements can be used to reveal the dominant mode content of a given beam. However, determining the exact modal breakdown can be problematic due to ambiguity in knowing the precise combination of $|c_{pl}|^2$ that results in any M^2 value. Modal decomposition is a powerful tool to discriminate the contents of any transverse mode into its constituent parts. The OV used in this work is a superposition state weighted in favour of the $LG_{0,\pm1}$ mode, however unwanted higher-order modes may seep in if the mode-conversion is non-optimal or the underlying Gaussian itself is non-ideal. Surface defects can introduce wavefront distortions for improper phase handling and WPSI misalignment can dissatisfy the canonical condition to instead generate impure superposition states. There is a high degree of interferometric tunability inherent to our system due to the nature of the mode transformation mechanism and operation of the WPSI that can make precise alignment of the WPSI difficult to achieve. Therefore, the ability to diagnose instances of non-ideal mode generation is highly desirable.

The WPSI parameters, in the first instance, can be set based on predicted values as will be

seen in Chap. 3. Finer adjustments can then be guided by modal analysis to compensate for any experimental variation in input parameters. Modal decomposition can be used to indicate the quality of the mode conversion process by comparing the modal content of the superposition state to the expected case for Gaussian beam interference.

Modal decomposition was performed computationally using a Fourier phase retrieval algorithm developed by Dr William Kerridge-Johns based on work by Takeda et al. [62]. A fork interferogram was generated using a tilted plane wave reference and an OV signal beam. Through analysis of the fringes produced by the fork interferogram, both the intensity and phase of the OV input could be reconstructed to be used to obtain the full electric field description of the OV. Any field, u, can be expressed as a superposition of u_{pl}^{LG} states, such that $u = \sum_{p=0}^{\infty}\sum_{l=-\infty}^{\infty} c_{pl}u_{pl}^{LG}$ where $\iint |u|^2 dxdy = 1$. Then $|c_{pl}|^2$ is the fractional power stored in each component since $\sum|c_{pl}^2|= 1$. These components can be weighted against the mode reconstruction to evaluate the modal content of the OV.

2.7 Summary

This chapter provides an introductory overview of OVs. These are optical fields that carry OAM intrinsic to their helical phase profile. Generation techniques vary based on application requirements and ease of access, but generally require the insertion of mode conversion optics to transform an incident beam into one with annular geometry. Cylinderical mode converters can be used to transform an incident HG mode under a $\pi/2$ Guoy phase shift to produce a pure equivalent LG mode. Alternatively, an SPP alters the planer wavefronts of an incident Gaussian mode by imprinting a helical step in phase to match that of the desired annular mode. However it fails to match the expected intensity profile of an ideal OV of similar topological charge. Q-plates and SLMs use liquid crystal cells to convert an incident beam to an OV. Q-plates exploit non-linear effects to convert SAM to OAM where as SLMs offer programmable capabilities to modify a variety of beam characteristics. They can be used to produce holograms to generate optical fields of the desired geometry, including OVs.

Interferometry to generate OV is the primary focus of this work. The mechanism relies on the addition of two TEM_{00} modes in superposition to generate higher-order modes. To avoid the generation of fringes as seen in plane wave interference, the parameters for interference are constrained to satisfy the canonical condition in eq. 2.19. When the interference is between two fundamental Gaussian modes, the result is a first-order LG mode, provided the spatial and angular offsets have been set appropriately. Here both the phase and intensity match that of the expected OV facilitating the production high-purity OVs with wavelength tunability and loss mitigation dependant on the quality of the coatings applied to the respective optics.

Finally methods to characterise OVs in a lab setting are presented. Fork and spiral interferograms produced by interfering an OV with a plane wave or curve wavefront reference

respectively, and are used to confirm the helicity of the OV wavefronts to distinguish OVs from other beams with annular profiles. The interferograms can be used to measure charge and handedness, indicated by the number of fork or spiral arms observed and their orientation. Beam quality measurements can reveal the dominant mode content of an OV and diagnose the presence of defects such as abberations that would affect its propagation. Modal decomposition methods may be more appropriate where the goal is to obtain a complete breakdown of its constituent parts and their respective power contributions. Due to the properties of the LG basis set, an OV, or any arbitrary optical field for that matter, can be decomposed and expressed as a linear combination of u_{pl}^{LG} modes as a means to measure the mode purity of the optical field.

Chapter 3

The Wedge-Plate Shearing Interferometer

This chapter introduces the Wedge-plate shearing interferometer (WPSI) as an interferometric mode converter to produce an LG_{01} type OV as shown in Fig. 3.1. We will first provide a mathematical basis for the interferometric mode conversion process by considering the generalised case of adding two Gaussian beams. We will then explore the function of the WPSI, describing its geometric configuration and introduce key parameters relevant to OV generation. This will lead us to presenting the mode conversion mechanism in the context of the WPSI specifically, and reveal some operational sights for its use in a lab setting. We will end with realisations of WPSI implementation as a vortex output coupler (VOC) for intracavity OV generation.

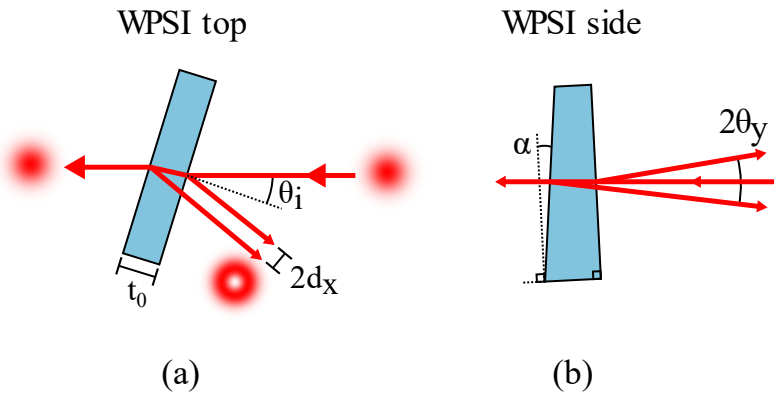


Figure 3.1: Incident TEM_{00} is converted into an LG_{01} by introducing a shear displacement and angular misalignment in the reflected beam. (a) Top view: the tilted faces of the WPSI are parallel separated by t_0. An incident beam at θ_i is reflected with a shear separation of $2d_x$. (b) Side view: Wedge angle α reflects the incident beam in opposing directions resulting in a total angular separation of $2\theta_y$.

3.1 Motivations

In the previous chapter we were introduced to interferometric mode conversion taking a TEM_{00} input for OV generation. The Mach-Zehnder interferometer is a common interferometer setup consisting of two beam-splitters and two mirrors with a phase tuning shear-plate placed in one of the arms. This setup is simple in its design, easy to align thanks to its two independently controllable arms however it can be prone to vibrational instability. The Sagnac interferometer negates the effect of vibrational instability through its common-path design. Its two arms share the same optomechanical components at the expense of greater complexity in alignment due to coupled controls. The WPSI is a monolithic wedged-glass device that greatly reduces the complexity of the aforementioned interferometric setups. The lack of movable parts substantially enhances vibrational stability and its simple design removes the need to align multiple optomechanical components. Beam propagation is limited to the region confined by the device interfaces resulting in a highly compact and stable interferometric setup. For these reasons we find the WPSI to be a promising tool for OV generation.

3.2 Addition of two Gaussian beams

This section will provide a mathematical picture describing the interferometric addition of two TEM_{00} Gaussian beams. The aim here is to guide the reader through the theoretical framework to arrive at the realisation of interferometry based spatial mode conversion. We will find, through the careful selection of spatial offsets and phase conditions applied to the input modes, we can produce a single charge vortex in the form of a high-purity LG_{01} mode in the output. We begin by expressing the field relating to a single Gaussian beam,

$$E_g(r,z) = E_0 \frac{w_0}{w(z)} \exp\left(\frac{-r^2}{w(z)^2}\right) \exp\left(-ikz - \frac{ikr^2}{2R(z)} + i\psi(z)\right) \tag{3.1}$$

where E_0 is the field amplitude, $w(z)$ and w_0 are the beam radii at position z and $z = 0$ along the propagation axis, r is the radial coordinate, and $\psi(z)$ is the Gouy phase. We can substitute the radial coordinate with $r^2 = x^2 + y^2$ to describe the beam's spatial profile in Cartesian coordinates. This is useful as we are now about to introduce spatial offsets that are best applied in this coordinate basis. First we apply a lateral offset in the x-direction so that the Gaussian beam is displaced by d_x. We then introduce a vertical tilt of θ_y in the y-direction which requires adjustment of the $\exp(-ikz)$ propagation term by $\exp(iky\sin\theta_y)$. The tilt angle is small so that we can apply the small angle approximation $\sin\theta_y \approx \theta_y$. A second Gaussian beam is introduced, identical to the first, but with equal and opposite offsets, so that the total shear displacement between the two beams is $2d_x$ and the total angular separation is $2\theta_y$. The result is two beams $E_1(x,y,z)$ and $E_2(z,y,z)$

as given below,

$$\begin{aligned} E_1(x,y,z) =& E_0 \frac{w_0}{w(z)} \exp\left(-\frac{(x-d_x)^2+y^2}{w(z)^2}\right) \\ & \times \exp\left(-ikz - ik\frac{(x-d_x)^2+y^2}{2R(z)} + iky\theta_y + i\psi(z)\right) \end{aligned} \tag{3.2a}$$

$$\begin{aligned} E_2(x,y,z) =& E_0 \frac{w_0}{w(z)} \exp\left(-\frac{(x+d_x)^2+y^2}{w(z)^2}\right) \\ & \times \exp\left(-ikz - ik\frac{(x+d_x)^2+y^2}{2R(z)} - iky\theta_y + i\psi(z)\right) \end{aligned} \tag{3.2b}$$

We allow the two beams to interfere with relative phase $e^{i\phi}$ and find the resultant field,

$$E_{total}(x,y,z) = E_1(x,y,z) + E_2(x,y,z)e^{i\phi} \tag{3.3}$$

$$\begin{aligned} E_{total}(x,y,z) = & E_0 \frac{w_0}{w(z)} \exp(-ikz + i\psi(z)) \\ & \times \left[\exp\left(-\frac{(x+d_x)^2+y^2}{w(z)^2} - iky\theta_y - ik\frac{(x+d_x)^2+y^2}{2R(z)}\right)\right. \\ & \left. + \exp\left(-\frac{(x-d_x)^2+y^2}{w(z)^2} + iky\theta_y - ik\frac{(x-d_x)^2+y^2}{2R(z)}\right)e^{i\phi}\right] \end{aligned} \tag{3.4}$$

First we consider the case of destructive interference when $e^{i\phi} = -1$ at $z = 0$.

$$\begin{aligned} E_{total}(x,y,z=0) = & E_0 \left[\exp\left(-\frac{(x+d_x)^2+y^2}{w_0^2} - iky\theta_y\right)\right. \\ & \left. - \exp\left(-\frac{(x-d_x)^2+y^2}{w_0^2} + iky\theta_y\right)\right] \end{aligned} \tag{3.5}$$

$$= E_0 \exp\left(-\frac{x^2+y^2}{w_0^2}\right) \exp\left(-\frac{d_x^2}{w_0^2}\right) \times \left[\exp\left(-\frac{2d_x x}{w_0^2} - ik\theta_y\right) - \exp\left(\frac{2d_x x}{w_0^2} + ik\theta_y\right)\right] \tag{3.6}$$

$$= E_0 \exp\left(-\frac{x^2+y^2}{w_0^2}\right) \exp\left(-\frac{d_x^2}{w_0^2}\right) \times \left[-2\sinh\left(\frac{2d_x x}{w_0^2} + ik\theta_y\right)\right] \tag{3.7}$$

Finally we apply the small angle approximation we declared earlier to get,

$$E_{total} \approx E_0 \exp\left(-\frac{x^2+y^2}{w_0^2}\right) \exp\left(-\frac{d_x^2}{w_0^2}\right) \times \frac{4}{w_0}\left[\frac{d_x}{w_0}x - i\frac{\theta_y}{\theta_0}y\right] \tag{3.8}$$

This result is the LG_{pl} mode profile as given in Eq. 2.2 when $p = 0, l = 1$ at $z = 0$. We also note the condition to ensure the x and y terms are equal in magnitude is satisfied when

$$\epsilon = \frac{d_x}{w_0} = \frac{\theta_y}{\theta_0} \tag{3.9}$$

where θ_0 is the beam divergence half-angle. We call this the canonical condition and use it to constrain the magnitude of the offsets with respect to the input beam parameters to generate a OV in the output. The ratio of the shear displacement to beam waist and the angular separation to beam divergence must remain small, i.e. $\epsilon << 1$ so the small angle approximation remains valid.

The LG result was derived by applying a relative π-phase shift between the two interfering Gaussian modes so that they add destructively. We now revisit Eq. 3.3, this time applying the constructive phase condition. If we set the phase to be an integer multiple of 2π we get constructive interference. This produces a sum of exponential terms in Eq. 3.4 rather than the subtraction we saw previously. Once again setting $z = 0$, we now find a sum of exponentials within the [...] brackets,

$$E_{total} = E_0 \exp\left(-\frac{x^2+y^2}{w_0^2}\right) \exp\left(-\frac{d_x^2}{w_0^2}\right) \times \left[\exp\left(-\frac{2d_x x}{w_0^2} - ik\theta_y\right) + \exp\left(\frac{2d_x x}{w_0^2} + ik\theta_y\right)\right] \tag{3.10}$$

which reduces to a cosh term so that the total field is,

$$E_{total} = E_0 \exp\left(-\frac{x^2+y^2}{w_0^2}\right) \exp\left(-\frac{d_x^2}{w_0^2}\right) \times \left[2cosh\left(\frac{2d_x x}{w_0^2} + ik\theta_y\right)\right] \tag{3.11}$$

Under the small angle approximation, the cosh term is 1 under Taylor expansion to the first order. The resultant field is then Gaussian like that of the initial incident beam.

3.3 WPSI configuration

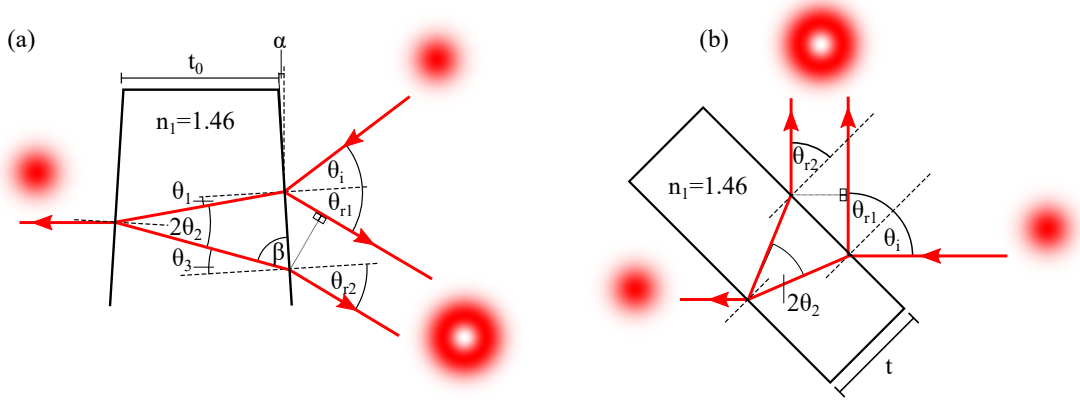


Figure 3.2: (a) Side view of WPSI with nominal thickness t_0 and wedge angle α. It is illuminated by a Gaussian beam with incidence angle θ_i. Front and rear surface reflections at θ_{r1} and θ_{r2}. (b) Top view of WPSI with reflected rays parallel in the horizontal plane

The WPSI is a glass (UV-Fused Silica) optic with nominal thickness, t_0, and is wedged along one axis with wedge angle, α. Its monolithic design significantly improves stability as the interference arms are contained within the confines of the optic. Its simple design

facilitates all necessary offsets for OV generation to be set purely by the geometry of the WPSI itself. A ray diagram showing the internal and surface reflection angles is shown in Fig. 3.2. A TEM_{00} fundamental Gaussian beam incident on the WPSI with angle θ_i is reflected off the front face with a secondary beam reflected off the rear face. The front face reflection angle is simply $\theta_r = \theta_i$. To find the rear face reflection we begin by applying Snell's law which gives the refraction angle,

$$\theta_1 = \sin^{-1}\left(\frac{1}{n}\sin\theta_i\right) \tag{3.12}$$

We only consider the first order internal reflection. The optical path through the WPSI creates a triangle with $\beta = 180 - (90 - \theta_i + 2\theta_2)$ and θ_2 is the internal surface reflection angle,

$$\theta_2 = \alpha + \theta_1. \tag{3.13}$$

The angle β is complementary to the internal angle of incidence to the front face giving,

$$\theta_3 = 2\alpha + \theta_1. \tag{3.14}$$

Now, to find θ_{r2} we apply Snell's law once but in reverse so that,

$$\begin{aligned} \theta_{r2} &= \sin^{-1}(n\sin\theta_3) \\ \theta_{r2} &= \sin^{-1}(n\sin(2\alpha + \theta_1)). \end{aligned} \tag{3.15}$$

In the small angle approximation this gives,

$$\theta_{r2} \approx 2\alpha n + \theta_i. \tag{3.16}$$

For purposes of ease we restrict deflections in the y-direction to only be due to the wedged-face reflections and so set θ_i here to be 0. The total angular separation between the front and rear reflected beams is $2\alpha n$, or equivalently, we define,

$$\theta_y = n\alpha \tag{3.17}$$

Tilting the WPSI around the wedge axis reflects the beams in the horizontal plane as shown in Fig. 3.2(b). Here $\theta_i = \theta_{r1} = \theta_{r2}$ with the front and rear reflected beams laterally separated by,

$$d_x = \frac{t\theta_i}{n} \tag{3.18}$$

for WPSI thickness, $t = t_0 + \alpha\Delta y$ where Δy is the height of the beam along the wedge-angle. The final condition is to meet the require phase for destructive interference. The phase control is set by varying the optical path difference between the reflected beams using a vertical translation stage to vary the WPSI thickness. The phase difference between the

two reflected beams is,

$$\Phi = 2nkt\left(1 - \frac{\theta_i^2}{2n^2}\right) + \pi. \tag{3.19}$$

An additional π phase term is included to account for the rear-face reflection. Typical wedge angles for the WPSI will be a few tens of arcseconds, in our case we have $\alpha = 40$" (for calculation purposes we express the wedge angle in radians, so $\alpha = 0.19mrad$). It can then be seen a 1 mm translation results in submicron thickness variation, and so, translation using a micrometer translation stage facilitates remarkably precise phase tunability.

The above summarises the WPSI configuration used in the rest of this work. The key takeaway is the wedge-angle points vertically so that we have vertical angular separation (θ_y) and horizontal shear and incidence angle, (d_x and θ_i respectively). This will continue to be the case for the remainder of this thesis.

3.4 WPSI for vortex generation

This section will combine the principles of interferometric mode conversion presented in Sec. 3.2 for the specific case of the WPSI using the geometry presented in Sec. 3.3.

Suppose a beam falls incident upon the front face of the WPSI (at $z = 0$) with a Rayleigh distance such that $z_R >> t_0$ so to ensure the reflected beams share a common beam waist location, within reasonable approximation. The incident beam takes the form $E_g = E_0 \exp\left(-\frac{x^2+y^2}{w_0^2}\right)$. Fresnel reflection off the front face results in a portion of the beam being reflected back. We call this E_1. The transmitted portion of the beam encounters a surface reflection off the rear face. We call this E_2. We neglect higher-order reflections for now and assume the remainder exits the WPSI by transmission through the rear face. The reflected beams can then be expressed as follows,

$$E_1 = r_1 E_0 \exp\left[-\frac{(x-d_x)^2 + y^2}{w_0^2}\right] e^{-iky\theta_y} \tag{3.20a}$$

$$E_2 = r_2 E_0 \exp\left[-\frac{(x+d_x)^2 + y^2}{w_0^2}\right] e^{+iky\theta_y} e^{i\phi} \tag{3.20b}$$

where $r_1 = r$ is the reflection amplitude from the front face and $r_2 = rt^2$ is the reflection amplitude from the second face. Note the double-pass coefficent which is the product of the transmission amplitude, t, from the front face and the reflection amplitude due to the second-face rt. We assume linear polarisation of the optical fields, which has been dropped in this derivation for purposes of simplicity. The polarisation state does not influence the formulation presented here. The addition of these Gaussian fields under destructive interference produces a result similar what was seen previously in Eq. 3.8.

$$E \approx 2E_0 \exp\left(-\frac{x^2+y^2}{w_0^2}\right) \exp\left(-\frac{d_x^2}{w_0^2}\right) \left[\frac{2\rho}{w_0}\left(\frac{d_x}{w_0}x - i\frac{\theta_y}{\theta_0}y\right) + \delta\right] \tag{3.21}$$

where $\rho = \frac{r_1+r2}{2}$ and $\delta = \frac{r_1-r_2}{2}$. When the canonical condition is met, the field can be written in terms of E_g and converted to polar coordinates, substituting for $r = \sqrt{x^2+y^2}$ and azimuthal angle $\phi = \arg(x+iy)$.

$$E \approx 2E_g \left[\frac{2\rho\epsilon}{w_0} r e^{-i\phi} + \delta\right] \tag{3.22}$$

The field is a super position of the reflected transverse modes and so needs to be expressed in terms of their respective normalised powers to clearly see the form of the resultant field. When $E_g = LG_{00}$ then these take the form $LG_{00} = \sqrt{2w_0/\pi}\exp(-r^2/w_0^2)$ and $LG_{01} = \sqrt{2}r/w_0 \exp(-i\phi)LG_{00}$.

$$E \approx 2\sqrt{2}\rho\epsilon LG_{01} + 2\delta LG_{00} \tag{3.23}$$

We see from Eq. 3.23 the superposition state generated by the WPSI mode conversion is that of a dominant LG_{01} mode accompanied by a comparitavely weak LG_{00} mode due to $\delta \neq 0$. The power of each mode can be found by taking the square of the field amplitudes $R_{01} = 8\rho^2\epsilon^2$ and $R_{00} = 4\delta^2$. Taking the WPSI to be made of UV-fused silica with refractive index $n = 1.46$ the reflection and transmission coefficients are $R_{01} = 1.01\,\%$ and $R_{00} = 4.17 \times 10^{-3}\,\%$. This gives an idealised power fraction of 99.6 % in favour of the LG mode.

So far we have only considered mode conversion from a single internal reflection. Higher order reflections can be neglected due to their comparatively weaker amplitudes that scale with increasing factors of r_1^2. The WPSI face reflectances can be tuned to vary the power in the reflected field components shown in Eq. 3.23. It is discussed in Ref. [59], that the use of surface coatings to increase face reflectance can improve output OV power but only with larger ϵ. This comes at the cost of lower mode purity. Although this hinders its use in applications where high mode purity or rotation symmetry in the beam profile is required, this may be a fair trade-off for other applications where higher output power is prioritised. Whereas the uncoated WPSI converts $\approx 1\,\%$ of the incident power, it was shown reflective surface coatings could enable 14 % power conversion while retaining 95 % mode purity [59].

3.5 Angle of incidence

The primary control when operating the WPSI is setting the correct angle of incidence. Its effect can be seen in Fig. 3.3 which plots the reflected power as a function of incident angle. An OV is said to be canonical when eq. 2.19 is met while also satisfying the case for destructive interference ($e^{i\phi} = -1$). Otherwise modes are generated where a singularity may be present but the intensity profile is not that of a true LG_{01} mode. We observe oscillatory behaviour in the reflected power as we cycle through constructive and destructive phase conditions given by eq. 3.19. For large θ_i the horizontal separation in the reflection dominates, generating modes resembling HG_{10} modes. As $\theta_i \to 0$ so too does the horizontal separation and vertically oriented HG_{01}-like modes are generated. The range

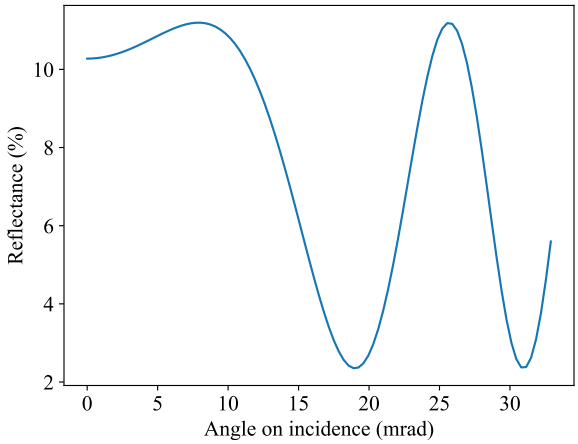


Figure 3.3: Percentage of reflected power for varying angle of incidence. OV generation found at troughs corresponding to destructive interference.

of generated modes are depicted as a montage in Fig. 3.4

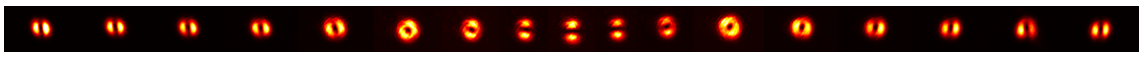


Figure 3.4: Collage of WPSI modes generated in reflection by scanning between large $\pm\theta_i$.

3.6 Beam waist correction

We assume the offsets described in Sec. 3.3 are applied at the waist of the incident Gaussian beam. If however, the WPSI is positioned elsewhere, away from the beam waist, the quality of the mode conversion worsens and in some cases can be invalid. Suppose the WPSI is placed at some distance z away from the beam waist. As the WPSI's position is translated, the horizontal shear isn't affected as the beams run parallel to one another - shearing is independent of WPSI location. However the angular misalignment must originate at the waist or else for a given location along the reflected beams' propagation, the spatial separation between the two beams grows. We can define the term d_y as the shear in the vertical direction which refers to the amount by which the beams have vertically separated at the beam waist.

$$d_y = \theta_y z = n\alpha z. \tag{3.24}$$

This additional shear at the beam waist invalidates the previously set offsets resulting in improper OV generation and so must be eliminated. This can be done by simply introducing a vertical tilt correction, $\theta_{y,i}$, to counteract the shear and return the system to ideal alignment.

$$\theta_{i,y} = \frac{nd_y}{t}. \tag{3.25}$$

To test the reliability of this method, beam correction was tested at $z = 0, z_R$ and $2z_R$. The WPSI was mounted on two goniometers for vertical and horizontal tilt control and a vertical translation stage for phase tuning. The whole system was then mounted onto a larger axial translation stage for z-position adjustment. A telescope was used to predictably

bring a 1064 nm Gaussian beam to a focus which coincided with the WPSI interface at $z = 0$. The waist spot size was measured to be 0.39 mm x 0.43 mm and expected to generate an OV with offset ratio $\epsilon = 0.16$ - 0.17 at an incident angle $\theta_i = 1.0°$ - $1.2°$. The Rayleigh length in each axis was expected to be in the range of z_r =11 cm - 13 cm.

Fig. 3.5(a) shows a montage of modes generated by scanning through vertical and horizontal angles of incidence in a raster fashion. We can see for shallow angles of incidence the modes resemble HG_{01} modes which become vortex-like with increasing θ_i. Accurately locating the "zero-point" in the tilt controls was difficult due to limited viewing angles but reliance on the quality of the generated modes could be used to dictate a suitable starting point, since offsets can be detected in the form of lob-sided intensity profiles, tilt or directional symmetry. The ideal OV mode at $z = 0$ was identified at (1.6°, 0°). The discrepancy in the horizontal tilt was attributed to a slight offset in the "zeroing" of the scale. No vertical tilt correction was required. At z_r we see no change in the horizontal-tilt correction as expected and we see a change in vertical-tilt of 1.2° which was in agreement with the expected 1.15° tilt accommodating for experimental errors. The optimal mode was found at (1.6°, -1.2°). Expecting a linear relation between z and $\theta_{i,y}$, at twice the distance, we should expect twice the correction. At $2z_r$ the hypothesis was confirmed in locating the best mode which was a further 1.2° in the vertical-tilt at (1.6°, -2.4°). Deterioration of the modes seen at z_r and $2z_r$ was attributed to astigmatisms present in the incident beam. Given these results we can say the corrections are valid for all z provided the necessary angles are experimentally obtainable.

3.7 WPSI operation

We have described the physical characteristics of the WPSI, the appropriate selection of incident beam and WPSI parameters, and the mechanism by which the OV mode is generated. We will now provide some operational insights on how best to implement WPSI OV generation in a lab setting.

Although the WPSI is operational in any orientation, preference is given to those that have desirable output trajectories. For example, in our case, we wish to prevent all possibility of vertically deflected beams as this poses an occupational hazard, especially for high-power use. Additionally, guidance of such beams using available optomechanics could become overly complex. In order to keep the optical system in-plane and parallel to the bench the wedge angle was oriented vertically so that the exit angle of the OV is tilted in the horizontal plane. This eliminates the risk of vertical beam deflection. Small vertical tilts introduced due to a misplaced beam waist relative to the WPSI can be easily compensated through tilt controls of mirrors mounts down-beam

It is important to consider the working constraints defined by the physical properties of the WPSI. The WPSI is rigid in its parameters as they stem from its physical characteristics - variability in these will require physical modification or replacement. Such parameters

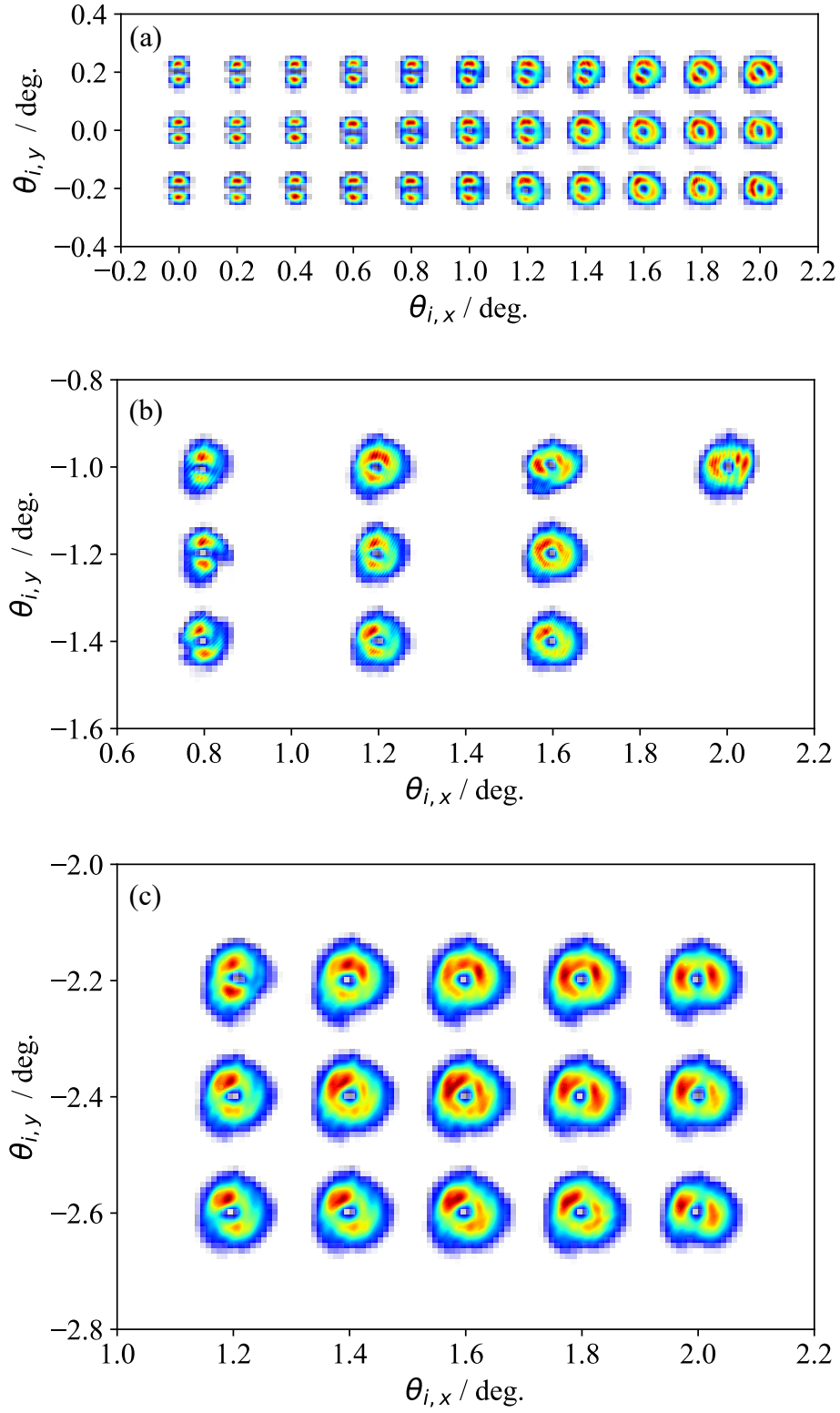


Figure 3.5: (a) Montage of generated modes scanning from near $\theta_{i,x} = 0°$ until ideal OV mode is found. Non-zero $\theta_{i,y}$ values also shown to illustrate effect of vertical tilt when locating OV. Optimal OV at (1.6°, 0°). (b) Modes when WPSI translated to z_r. Optimal OV at (1.6°, -1.2°). (c) Modes when WPSI translated to $2z_r$. Optimal OV at (1.6°, -2.4°).

include, face reflectance, nominal thickness and wedge angle. Beam parameters are case dependent based on extra- or intra-cavity use. For extracavity use, an incident beam can be easily manipulated to alter beam focus, waist location, and if another source is available, wavelength. The offset ratio can be determined using the face reflectances of the WPSI by $\epsilon = \sqrt{R_{01}/8\rho^2}$. For an uncoated WPSI using Fresnel reflection, R_{01} is usually on the order of a few percent. We can then find the beam waist of the required Gaussian beam as $w_0 = \epsilon\lambda/\pi n\alpha$ which in turn helps us determine the incident angle given by Eq. 3.26. Now all other parameters can be calculated where needed, the angular beam separation is set by the wedge-angle of the WPSI, the shear separation is found using the incident angle and the beam divergence is set by the imaging of the beam waist onto the WPSI interface. Finally, the destructive phase condition can be tuned through translation of the WPSI along the wedge direction.

Intracavity use is expected to be more restrictive as the incident beam parameters, w_0 and θ_0, relate to those of the intracavity mode whose characteristics are determined by the geometry of the laser cavity. Cavity beam propagation simulations can be used to assist in the search for a stable lasing configuration that satisfies the beam requirements for a given WPSI. The angular separation θ_y is fixed by the physical constraints of the WPSI leaving only d_x which depends on the angle at which it meets the incident beam. This leads to an an additional restriction in the cavity dimensions needing to accommodate the WPSI (and attached optomechanics) and provide sufficient clearance for beam exit while still maintaining a stable oscillator. It is therefore recommended to work in terms of the incident angle calculated using Eq. 3.26 and build the surrounding system based on the exit trajectory of the beam.

$$\theta_i = \frac{n\epsilon w_0}{t_0} \tag{3.26}$$

3.8 Vortex output coupler

The operational considerations for WPSI use inside a laser cavity leads to the possibility of it being used as a vortex output-coupler (VOC) for direct OV emission from the laser. The OV is not resonant within the oscillator, instead the OV is output-coupled by the WPSI face reflections while the remaining power is recycled back into the next round-trip. Where as previously, the extracavity conversion efficiency was merely the reflected power, the VOC configuration effectively achieves zero conversion losses due to the returned power. Power scalability is substantially improved, with the potential to achieved watt level OV powers. This is due to the WPSI sampling the incident power of the high intracavity flux that can easily reach several tens of watts.

3.9 Intracavity phase control

The principle of interference relies on the careful setting of relative phase between the two reflected beams so that the desired output can be generated. It can be seen from Eq. 3.19

that the phase between the front and rear-reflected beams relies, in part, on the laser wavelength resulting in a sinusoidal relationship between wavelength and WPSI reflectance as computed in Fig. 3.6(a). The reflectance is maximised under constructive interference where a TEM_{00} mode is generated in its output. A minimum in reflectance is observed under destructive interference and generates a LG_{01} mode. The oscillating reflectance resembles that of a low-finesse Fabry-Perot etalon. A vortex laser must operate at the minima as indicated by the inset. Due to the loss avoiding nature of the laser oscillator, the laser adapts its wavelength to minimise the reflectance of the WPSI and operate in the destructive interference condition. This makes WPSI operation in the laser simple as the phase condition in principle should be met by default, as much as is possible.

A further consideration for the laser wavelength is that the cavity is restricted to certain longitudinal modes, M. The concept of longitudinal modes within an optical resonator will be expanded upon in Chap. 4. For now we can treat them as operational states relating to the laser wavelength that depend on the optical path the internally propagating mode takes around the laser oscillator. With the inclusion of the WPSI, these are given by

$$M = \frac{L + nt}{\lambda} \tag{3.27}$$

where L is the total cavity optical path length excluding the WPSI, t is the thickness of the WPSI with index n, and M is the resonant longitudinal mode order which must be of integer value. An example longitudinal mode pattern for the laser in this work is shown in Fig. 3.6(b), where the red lines indicate the position of the longitudinal modes. Due to the relative thickness of the WPSI and the length of the cavity, it is possible that there isn't a valid longitudinal mode at the correct location for destructive interference. This can be easily corrected using the vertical translation control of the WPSI to change its thickness until the appropriate phase condition is met. The minute wedge-angle of the WPSI enables thickness variation on the order of 0.2 µm over a vertical translation of 1mm. This enables fine-tuning of the optical path at sub-wavelength sensitivity. Once the path is set the laser will naturally operate at the ideal phase condition for OV generation.

Disturbingly, there appears to be coupling of the phase control and laser wavelength selection. Translating the WPSI in principle changes the total optical path length in the cavity, which in turn will also cause the longitudinal mode spectrum to spectrally shift. If there is spectral drift in the laser cavity or its initially mode selection is non-ideal then the effect of the spectral shift due to the phase correction will need to be negligible for the laser to correctly operate. For the cavity in this work, the spectral shift due to phase correction was computationally compared. The longitudinal mode pattern was found to move by a factor of 1/50 compared to the WPSI spectrum. Its effect in this case was deemed negligible as a result.

In practice, the necessary adjustments were easily made. A 2π phase change was achieved through vertical translation distance of 0.5 mm. It should also be noted that if the cavity

perimeter were larger, or the WPSI thinner, the spectra would be much more likely to have a valid longitudinal mode at the destructive interference condition, making these considerations and adjustments unnecessary.

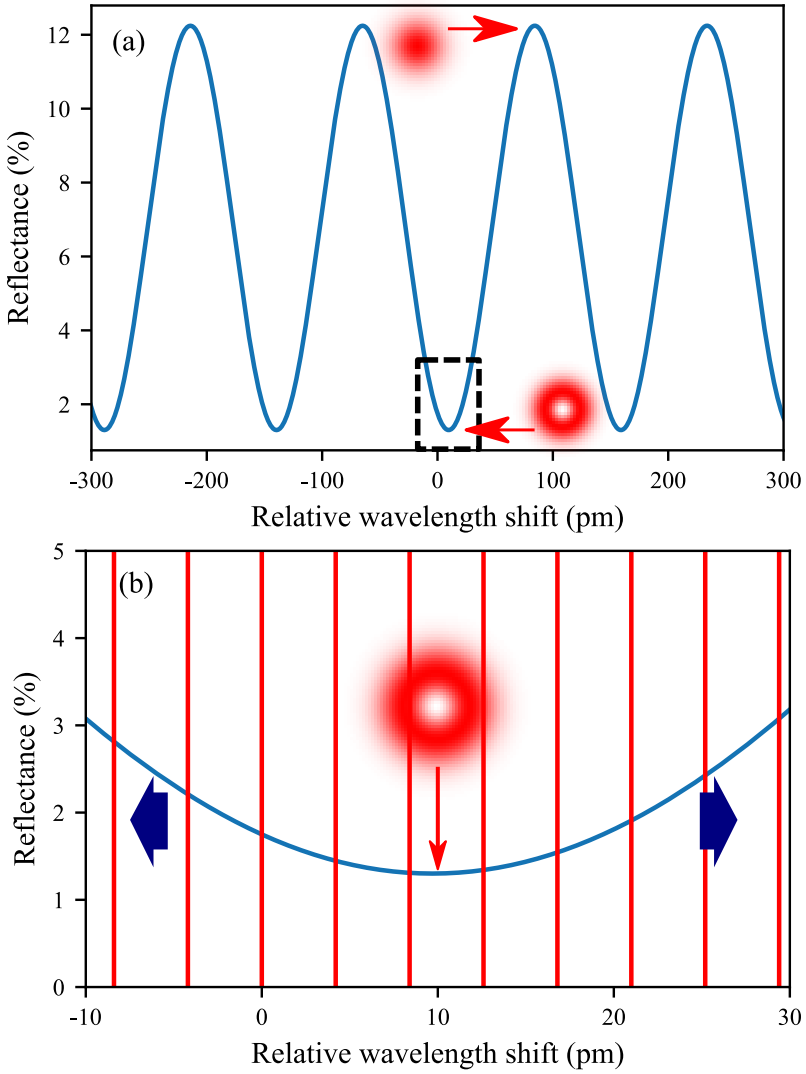


Figure 3.6: (a) WPSI reflectance for shifts in incident wavelength relative to 1064 nm are shown. TEM_{00} and LG_{01} mode reflections found when constructive and destructive interference conditions are satisfied respectively. (b) Reflectance plot zoomed in to near reflectance minimum. The red vertical lines indicate the position of cavity longitudinal modes. The WPSI spectrum (blue) can be adjusted in position via Δy-control

3.10 Summary

This chapter presents the non-standard use of a WPSI as a mode-converting device for OV generation. We began by providing a mathematical picture of OV generation through the principle of interferometric mode conversion by considering the general case of interfering two Gaussian beams. We find that by applying a shear and angular separation along orthogonal axes at the beam waist, we can derive the conditions under which an OV is

generated in its output. We refer to this as the canonical condition and it is used to limit the magnitude of these offsets based on the parameters of the input beam.

We then apply this framework to the geometry of the WPSI and find it yields an OV with high (99.6 %) LG_{01} mode purity. We provide operational insights on how to apply the WPSI in a laboratory setting and describe its functional features. Its primary control is through tilting it relative to the incoming beam. In our configuration, OV generation is controlled via the horizontal tilt control while the vertical tilt can be used to correct for axial misplacement of the beam waist relative to the WPSI interfaces.

The primary drawback to the WPSI is its poor power conversion efficiency which is equal to only the Fresnel surface reflectance of the WPSI medium. The remaining power is lost in transmission. We realise the option for intracavity operation through application of the WPSI as a VOC. This way, the transmission losses instead recycle the "lost" power back into the laser cavity while the face-reflections act as an output coupling mechanism for direct OV emission.

Chapter 4

Solid state laser cavities

A laser oscillator is comprised of two basic components - a laser gain medium to provide amplification and a resonator for optical feedback. The laser oscillator acts to increase the total photon flux at the end of each round trip by selecting operational modes that minimise losses. The lasing threshold is satisfied when the gain exactly balances the round-trip losses at which point the gain is clamped and laser action reaches steady state. Losses can occur due to poor resonance of the oscillating field due to diffraction and component insertion losses which act to diminish the photon intensity. High losses reduce the efficiency of the laser as larger gain is required to maintain the same level of output. Laser action ceases when the losses exceed the maximum gain that can be extracted from the gain medium.

The performance of a laser oscillator is dependent on the correct setup of both the amplifier and resonator. The laser oscillator will always operate at optimal efficiency for a given optical configuration but this does not necessitate the optical configuration itself will be optimal for laser performance. Developing an operational understanding of a laser oscillator and where its limitations lie is therefore necessary to ensure best performance. In this chapter we discuss the workings of the laser gain medium and optical resonator. The former will provide a generalised overview of laser action and explain the choice of laser gain medium used in this work by discussing its physical and spectroscopic characteristics. The latter will discuss the geometric requirements for resonator stability, in firstly a linear resonator configuration, how this is modified through the introduction of additional optics such as lenses, and describe the mechanism by which transverse and longitudinal mode resonance is achieved. Similar will follow for a ring resonator.

4.1 Selection of laser gain media

There are particular requirements the electron structure of the gain medium must satisfy that determine whether laser action can occur. Consider a lone gain medium with a background level of incident photons. It will undergo spontaneous excitation and decay

processes with energies determined by the electronic structure of its active species. Due to the random nature of these processes, it forms a base noise floor of weak photon emission with no appreciable coherence or power at this stage. The intensity of emission at a particular energy can be enhanced by raising the number of electrons in the excited state of that particular transition. This can be achieved by pumping the gain medium at a particular absorption energy to artificially create a top heavy distribution of excited to ground state electrons from which gain can be extracted. This is referred to as a population inversion. In order to maintain a population inversion to sustain lasing, the decay rate of excited state electrons must be greater than the absorption rate of ground state electrons. If the energies of the absorption and emission cross-sections are equal, the same pump photons used to excite ground state electrons will also act to deplete the excited state population through stimulated emission. For this reason a simple two-level system is incompatible for steady lasing.

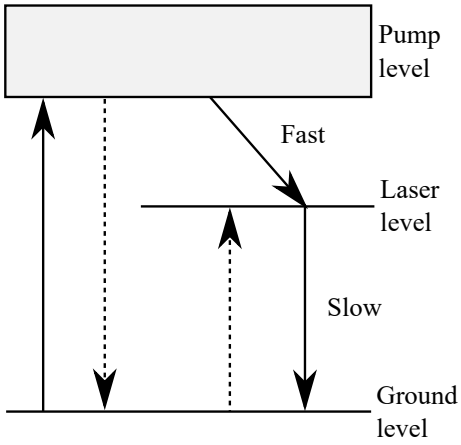


Figure 4.1: Electron transitions for 3-level laser gain medium. Solid lines denote the laser transitions with dotted arrows indicating spontaneous processes.

Three-level systems appear to solve this problem through an additional non-radiative transition that restricts the decay of excited electrons by the pump due to a separation in their respective absorption and emission transition energies. This is shown in Fig. 4.1. Rapid decay of the excited state to the laser state facilitates the creation of a population inversion between the ground and laser states. As ground state electrons are pumped to the excited state, they readily decay to the laser state. The lifetime of the laser state is long enough for the laser state population to build-up before an incident photon can stimulate laser emission and demote the electron back to the ground state. However, three-level systems are prone to reabsorption of laser photons as there is a direct pathway for electron excitation. As a result, intense pumping is required to bleach the ground state. The high flux of pump photons floods the ground state to statistically reduce the likelihood of reabsorption. Nevertheless, with sufficient pumping, a population inversion can still be sustained with positive gain to enable lasing.

The high-threshold of a three-level system is detrimental to operating efficiency due to the high power requirements for the pump. Instead we can use a four-level system. Just as

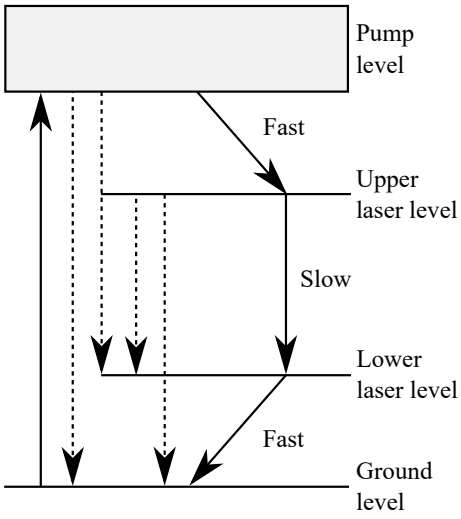


Figure 4.2: Electron transitions for 4-level laser gain medium.

before, optical pumping is used to promote electrons from the ground state to the upper excited state. The electron is released through rapid phonon decay to the upper laser state where stimulated emission produces a laser photon. However here, instead of falling to the ground state, the electron falls to a lower laser level. As this state is also short-lived, it prevents the build-up of any appreciable population while also mitigating the chance of self-absorption. This way, the lasing threshold can be greatly improved with less pump power. The electron falls back down to the initial ground state through rapid phonon decay. The cycle then continues.

4.1.1 Rare-earth doped laser gain media

In solid-state laser systems, laser gain media come in a variety of chemical compositions. they can be categorised into families of crystalline oxides such as sapphire (Al_2O_3) [63, 64], garnets such as YAG ($Y_3Al_5O_12$) [65], fluorides such as YLF (YLiF) [66] and vanadates (VO_4) such as Nd:YVO_4 [67] with transition metal (TM) or rare-earth (RE) metal dopants added to host media which act as the active species. Glasses and ceramics are also used. Laser transitions generally occur between the 4f-4f and 4f-5d orbitals for RE doped gain media and 3d-3d orbitals for TM granting direct photon generation capabilities spanning the NIR, visible and UV spectral regions.

RE dopants in particular are notable for their strong yet narrow emission lines originating from their 4f orbital. They are nearly always trivalent ions with examples in Nd^{3+}, Y^{3+}, Yb^{3+}, Gd^{3+}, which replace similar valance ions within the host lattice. Interaction of the 4f orbital with the surrounding crystal field results in further splitting of degenerate $^{2S+1}L_J$ electron levels due to the Stark effect. The specific energy configuration this yields may vary depending on the combination of dopant and host, however this interaction is relatively weak ($100\,\mathrm{cm}^{-1}$) due to shielding by the outer 5s and 5p orbitals reducing its effect [68]. As a result, similar spectral characteristics are seen for RE dopants in different host crystals. An example of this is seen in Nd:VO_4 and Nd:YAG which share a common

Nd^{3+} ion with notable emission lines at 0.9 µm, 1.06 µm and 1.3 µm.

4.1.2 Nd:YVO_4

Table 4.1: Comparison of physical and optical properties of Nd:VO_4 and Nd:YAG laser crystals. Data from ref. [69, 70]

	Nd:VO_4		
Property	c-axis	a-axis	Nd:YAG
Crystal structure	tetragonal		cubic
Mass density (g/cm^3)	4.22		4.56
Moh hardness	5-6		8-8.5
Thermal conductivity ($Wm^{-1}K^{-1}$)	5		10-14
Thermal expansion coefficient ($10^{-6}K^{-1}$)	11	4.4	7-8
dn/dT ($10^{-6}K^{-1}$)	3	8.5	7-10
Absorption cross-section at 808 nm ($10^{20}cm^2$)	60		7.7
Emission cross-section at 1064 nm ($10^{20}cm^2$)	114		28
Nd density for 1% at. doping ($10^{20}cm^{-3}$)	1.24		1.38
Fluorescence lifetime (μs)	90		230
Gain bandwidth (nm)	1		0.6

Neodymium-doped Yttrium Othovanadate (Nd:YVO_4) is a widely used RE-doped laser gain medium particularly known for its ability to lase with high gain and low threshold [67]. Although it can lase with flashlamp pumping for pulsed operation, its popularity grew significantly with the advent of high-power diode pump lasers becoming readily available. Compared to Nd:YAG - another popular Nd-doped gain medium - Nd:YVO_4 offers enhanced pump absorption coefficient and gain efficiency giving it an edge over Nd:YAG for low threshold lasing and has similar performance for CW operation. For pulsed operation Nd:YAG allows higher pulse energies due to its longer fluorescence lifetime, however the high laser cross-section of Nd:YVO_4 makes it well suited for high repetition rate systems. A list of key properties comparing Nd:YVO_4 and Nd:YAG is presented in Tab. 4.1.

Nd:YVO_4 is a crystalline laser gain with Nd^{3+} as the active ion for laser emission and Yttrium Vanadate (YVO_4) as its host crystal. Here the trivalent Nd^{3+} ion replaces the similarly sized Yttrium without significant modification to the host's lattice structure thereby preserving its thermoconductive properties. It has tetragonal lattice structure of the D_{4h} space group. The anisotropy in lattice structure makes Nd:VO_4 naturally birefringent with asymmetric properties along its a- and c-axis. In some instances Nd:YVO_4 is seen as inferior to Nd:YAG due to its lower thermal conductivity and Moh hardness leaving Nd:YVO_4 susceptible to thermal strain. However its lower dn/dT reduces thermal lensing effects.

Nd:YVO_4, as with other Nd-doped laser gain media such as Nd:YAG, is a classic choice for laser emission as 1064 nm. The Nd^{3+} active species has its highest absorption cross-section at 808 nm where it exhibits strong 4-level behaviour within its 4f orbital. The $^4I_{9/2}$ and

$^4F_{5/2}$ manifolds act as the lower and upper pump levels. Nd:YVO_4 has strongest emission peak at 1064 nm which corresponds to the laser transition between the $^4F_{3/2}$ and $^4I_{11/2}$ manifolds. Vibronic transitions link the respective pump and laser manifolds to complete the 4-level system. Thermal interaction allows the respective populations to distribute themselves following the Boltzmann probability distribution, permitting us to assume upper vibronic states to be in thermal equilibrium as are the lower vibronic states due to the short-lived relaxation time relative to the lifetime of the metastable $^4F_{3/2}$ and ground levels.

Additional weaker yet notable laser transitions are available at 914 nm and 1340 nm [71, 72] which have implications for watt-level second-harmonic generation into the visible. However, there is considerable reabsorption of the laser light associated with the former. This due to a high thermal population of the lower laser level. The latter suffers from a high quantum defect resulting in greater thermal loading and excited state absorption which reduces efficiency as compared to emission as compared to 1064 nm where it is negligible [73].

One of the primary drawbacks of Nd:YVO_4 is its poor thermo-mechanical properties as compared to Nd:YAG which limits high-power performance. The apparent solution to this would seem to be to reduce the thermal load applied to the crystal by the pump. In-band pumping excites ground state electrons directly to the emitting level, subverting the need for excitation of the upper pump state and subsequent phonon decay which dissipates as heat. As the respective electron levels are less energetically separated, the quantum defect is improved and shown to improve lasing threshold and slope efficiency [74]. The $^4I_{9/2}$ to $^4F_{3/2}$ transition corresponding to absorption of 879 nm is the strongest absorption line in Nd:YVO_4 with an absorption cross-section half that of 808 nm with a reported decrease in thermal load of 27 % and enhanced emission at 914 nm [75].

The spectroscopic properties for other Nd^{3+} active gain media may vary depending on the specific crystal field interactions with its host and how this influences the resultant energy structure [73]. Another example of this is Nd:$GdVO_4$ [76] which shares the same crystalline structure, and similar transition energies. It has greater pump absorption yet lower laser emission cross-section and is known for its larger gain bandwidth.

4.2 Linear resonator

The linear resonator is the simplest and most common optical resonator configuration used in laser systems. Its optical setup is fairly simple, it consists of two end mirrors enclosing a gain medium between which the laser light oscillates; a dichroic back-mirror (BM) transmissive at the pump wavelength and highly reflective at the emission wavelength, and an output coupling end reflector (OC). The transmission through the OC can be tuned to vary laser output. A higher transmission percentage effectively increases cavity losses through the OC for greater laser output, however at the cost of a higher lasing threshold.

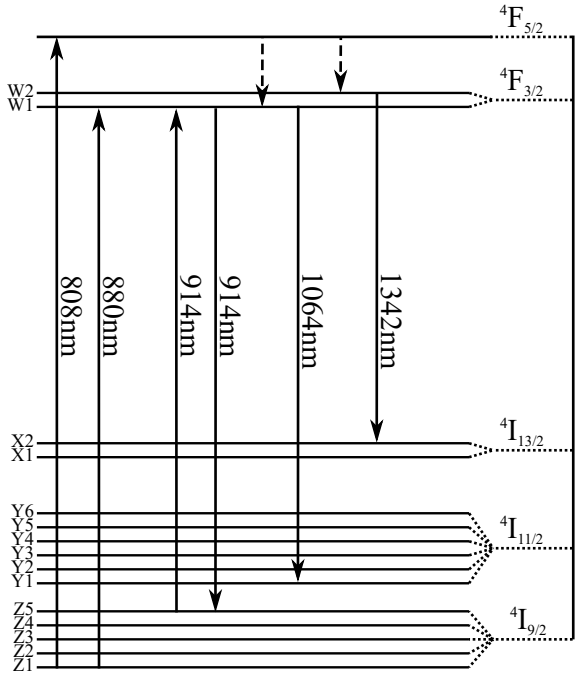


Figure 4.3: Notable pump and laser electron transitions in Nd:YVO4. Adapted from [77] and [78]

This is usually not a problem for high-gain media such as Nd:YVO_4 but may be problematic for low-gain media which require access to higher pumping powers to accommodate the high cavity losses. Decreasing the OC transmission can improve the lasing threshold as fewer photons are lost each round trip, however laser output is diminished for the same reason. One must balance losses appropriately to maximise performance, accounting for the properties of the gain medium and the intended use of the laser power.

4.2.1 Linear resonator stability

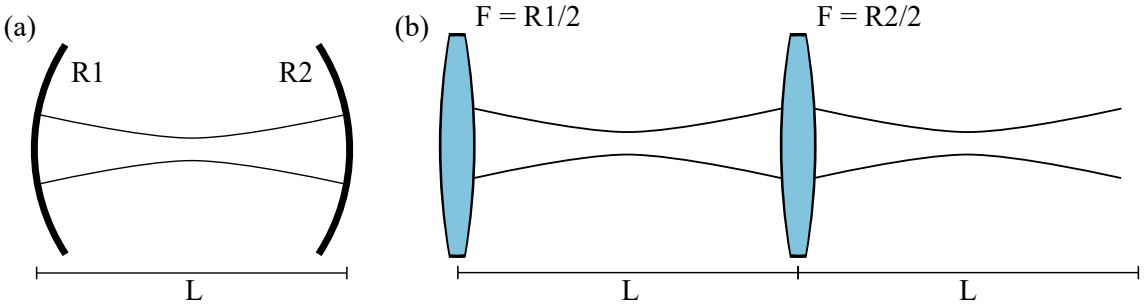


Figure 4.4: (a) Linear resonator with curved mirrors R1 and R2 separated by length L. (b) Unfolded cavity with replaced lens. Beam propagates from left to right.

The stability of a resonator describes how readily it can entrap a optical field to resonant within its bounds. When discussing resonator stability we consider a "cold" resonator, that is, a resonator without an active gain medium driving the field from within. When the resonator is "hot" as with active laser cavities, round trip gain can replenish the optical decay from component losses, resulting in zero effective loss when the laser is in steady-

state. A lossy laser cavity may still be functional but with poor efficiency and higher threshold. When these losses cannot be fully compensated by the gain alone, instability in the laser resonator ensues with sporadic power fluctuations or complete extinction of the laser mode. To account for the gain contributions from the laser crystal adds a great deal of complexity when modeling the behaviour of the internal mode. It is therefore useful to use the "cold" resonator model for the initial stability considerations.

A two mirror optical resonator consists of two oppositely faced end mirrors used to steer the propagation of an enclosed optical field. The space bound by the end mirrors is often referred to as the optical cavity. The field inside the cavity must be reproducible at any arbitrary reference plane after each round trip to ensure stable resonance. If this condition is not met, even small error accumulations in phase or amplitude can rapidly build-up with each round trip and be detrimental to the interference between the forward and back-reflected fields. If the points of destructive interference are led to drift along the propagation axis each round trip, resonance will be impossible and the resonator will be incapable of confining the optical field.

A stable resonator can confine a set of transverse modes which within the paraxial limit is satisfied by the fundamental TEM_{00} Gaussian and higher-order Hermite-Gaussian modes. A Gaussian mode at an arbitrary reference plane located at z can be described using its complex beam parameter,

$$\frac{1}{q} = \frac{1}{R(z)} + i\frac{\lambda}{\pi w(z)^2}. \tag{4.1}$$

Its state after a single round trip, q', is determined using a Ray Transfer Matrix (RTM) to describe the beam as it is manipulated by cavity propagation and internal optical components [79].

$$q' = \frac{Aq+B}{Cq+D} = q \tag{4.2}$$

Consider a linear resonator comprised of two end mirrors of curvature, R_1 and R_2, separated by distance, L. We can unfold the round-trip optical path into a single path as shown in Fig. 4.4 by replacing the mirrors with lens of appropriately set focal lengths. Then we express the free-space propagation RTM by left-multiplying the ABCD matrices of the respective components in reverse order to the optical path.

$$\begin{aligned} M &= \begin{pmatrix} 1 & 0 \\ -\frac{2}{R_2} & 1 \end{pmatrix} \begin{pmatrix} 1 & L \\ 0 & 1 \end{pmatrix} \begin{pmatrix} 1 & 0 \\ -\frac{2}{R_1} & 1 \end{pmatrix} \begin{pmatrix} 1 & L \\ 0 & 1 \end{pmatrix} \\ &= \begin{pmatrix} 1-\frac{2L}{R_2} & 2L-\frac{2L^2}{R_2} \\ -\frac{2}{R_1}-\frac{2}{R_2}+\frac{4L}{R_1R_2} & 1-\frac{2L}{R_2}-\frac{4L}{R_1}+\frac{4L^2}{R_1R_2} \end{pmatrix} = \begin{pmatrix} A & B \\ C & D \end{pmatrix} \end{aligned} \tag{4.3}$$

By substituting the elements of Eq. 4.3 into Eq. 4.2 we can solve for q'. To ensure $q' \in \mathbb{C}$ we are bound by the condition

$$0 < \frac{1}{4}(A+D+2) < 1. \tag{4.4}$$

This can be conveniently be expressed in the form,

$$0 < g_1 g_2 < 1. \tag{4.5}$$

where we have defined parameters, g_1 and g_2 such that

$$g_1 = 1 - \frac{L}{R_1} \quad \text{and} \quad g_2 = 1 - \frac{L}{R_2}. \tag{4.6}$$

These g-parameters are complex eigenvalue pair conjugates of M used to define the stability criterion for any two mirror resonator. A high stability resonator will be able to confine the oscillating field over many round-trips with minimal losses, whereas a low stability system may lose the field after a few round trips due to losses induced from poor field reproducibility or be incapable of enclosing field oscillations altogether. The stability criterion in Eq. 4.5 is used to quantitatively classify the suitability of an optical cavity for stable resonance. Any two mirror resonator can be characterised by its g-parameters and represented as a point on Fig 4.5. A resonator is stable for all values within the shaded area. If the product of the g-parameters exceeds $g_1 g_2 = 1$ or lies beyond the axes, the resonator falls out of the stable region. Then the cavity can no longer contain a stable mode due to poor re-imaging of the optical field. In the paraxial limit of a laser oscillator, laser action ceases as high round trip losses exceed the maximum gain that can be extracted from the population inversion.

4.2.2 Internal and thermal lenses

An intracavity lens may be used for greater control of the transverse mode size and better spatial matching with the inversion region. This prevents higher-order modes being generated, improving beam quality and overall efficiency. When lasing above threshold, optical pumping can generate a transverse thermal gradient in the gain medium where it is hottest along the beam axis and cools radially creating a temperature dependent change in local refractive index. We can express the focal length of the resulting lens as follows,

$$f^{-1} = \frac{dn/dT}{2\kappa A} P_{heat} \tag{4.7}$$

where dn/dT is the thermooptic coefficient of the gain medium, κ is its thermal conductivity, A is the area of the pump spot size, and P_{heat} is the power dissipated as heat primarily due to the quantum defect of the laser energy transition.

Thermal effects can also exert mechanical strain on the crystal resulting in physical distortion or bulging at its surface. These effects contribute to thermal lensing which too acts to vary the internal mode size as would an internal lens, although in this case it is often considered undesirable. As such, a power varying thermal lens may be treated as would an internal lens when modeling resonator stability. If both lensing effects are present and spatially separated then one may re-derive the stability criterion for this setup using the

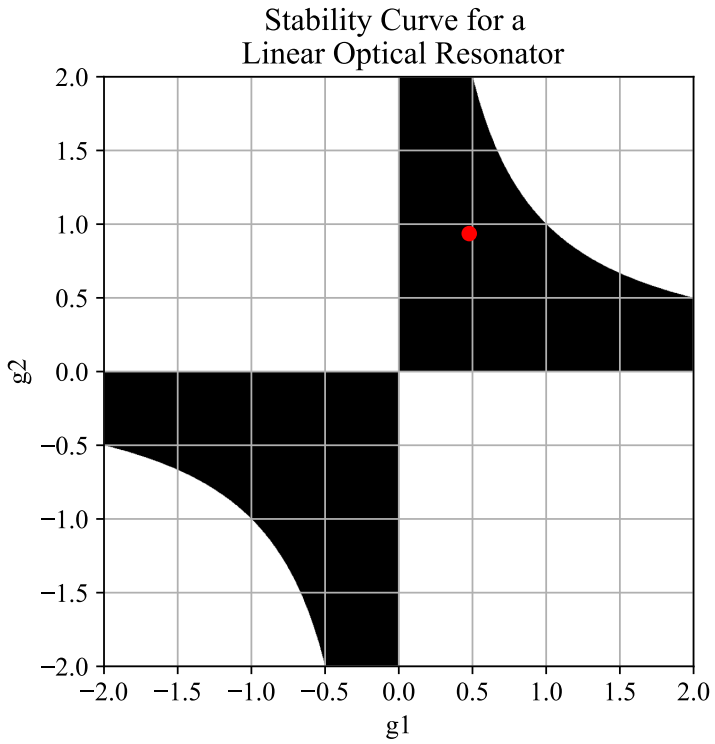


Figure 4.5: Stability curve for a linear two-mirror optical resonator. A stable resonator can be denoted as a point (red) on the plot based on its g-parameters. The shaded area indicates regions of stable resonance bound by $g_1, g_2 = 0$ and $g_1 g_2 \leq 1$. As the point approaches these limits instability in the resonator can be induced. Once past these limits, there is no stable solution that satisfies the cavity dimensions and field resonance ceases.

appropriate RTM.

For now lets take the example of a single internal lens between two mirrors of curvature R_1 and R_2. As before we can unwrap the round trip path but we will need to account for the double pass through the lens. This modifies the resonator's g-parameters as follows,

$$g_1 = 1 - \frac{L'}{R_1} - \frac{L_2}{f} \quad \text{and} \quad g_2 = 1 - \frac{L'}{R_2} - \frac{L_1}{f}. \tag{4.8}$$

Here we have defined an effective resonator length [80],

$$L' = L_1 + L_2 - L_1 L_2 / f \tag{4.9}$$

where L_1 and L_2 are the distances to the end mirrors on either side of the lens and f is its focal length. Again, the field reproducibility condition requires $q' = q$ for an indefinitely resonant Gaussian field. Additionally, the curvature of the field must match that of the end mirrors for it to maintain its shape through propagation. The beam size and mirror locations can be calculated as before using the appropriate g-parameter values.

4.2.3 Gaussian cavity mode propagation

We can describe Gaussian beam propagation through the resonator in terms of known g_1 and g_2. In particular, it is useful to determine the spot size at each end mirror, which must remain smaller than the end mirror diameters to prevent aperture losses.

$$w_1^2 = \frac{L'\lambda}{\pi}\sqrt{\frac{g_2}{(g_1(1-g_1g_2)}} \quad \text{and} \quad w_2^2 = \frac{L'\lambda}{\pi}\sqrt{\frac{g_1}{(g_2(1-g_1g_2)}} \tag{4.10}$$

Another useful reference point is the transverse mode size at the thermal lens [81].

$$w_3^3 = \frac{2\lambda}{\pi}\max(L_1, L_2) \tag{4.11}$$

we can use these to describe the propagation of the internal Gaussian mode. To promote stable laser operation, the location of the end mirrors can be expressed in terms of the resonator g-parameters as follows,

$$z_1 = \frac{g_2(1-g_1)}{g_1+g_2-2g_1g_2}L \quad \text{and} \quad z_2 = \frac{g_1(1-g_2)}{g_1+g_2-2g_1g_2}L \tag{4.12}$$

4.2.4 Longitudinal modes and non-ideal effects

An optical field must form a standing wave for it to see stable oscillation within a linear resonator of length, L. This discretises the possible states within the resonator only allowing certain spectral modes whose round trip optical path is an integer multiple of its wavelength. The resonance condition for a linear resonator describes the possible allowed states, referred to as longitudinal modes, and can be expressed in terms of wavelength, λ, or frequency, ν, as follows,

$$2L = j\lambda = \frac{jc}{\nu} \tag{4.13}$$

with mode spacing,

$$\Delta\nu = \frac{c}{2L} \tag{4.14}$$

The overlap of the possible modes modulated by the gain spectrum of the gain medium determines which mode reaches threshold first. Once a mode reaches threshold, it clamps the gain to suppress all other modes granting it sole dominance. This process maximises lasing efficiency as it allows the laser to always find the lowest-loss case to maximise gain extraction for a given configuration.

In practice, non-ideal effects can complicate the mode selection processes. Spatial hole burning occurs when the interference between counter propagating quasi-monochromatic light generates periodicity in the gain medium in half-wavelength intervals. Local regions of saturated gain are created preferentially at the antinodes of the standing wave which distorts the spatial distribution of the gain spectrum. This induces losses in the lasing mode and gives way to other modes to compete for gain dominance. Spatial hole burning

can prevent the laser from operating at a single longitudinal mode as gain extraction alternates between multiple laser modes. Laser power stability can be greatly affected as the emission will alternate between competing modes. This can be especially problematic for single frequency applications such as spectroscopy or doppler measurements.

4.3 Four-mirror ring resonator

Although there are similarities between ring and linear resonators in what has already been discussed, there are some particulars regarding ring resonators that make them unique. Ring resonators come in a variety of configurations where the optical paths follow a closed loop around the cavity. Examples of these include circular paths along the perimeter of 3- and 4-mirror cavities or more complicated folded arrangements such as bow-tie cavities. A key property of these systems is the ability to accommodate unidirectional oscillation that prevent spatial hole burning effects in the crystal. Single-frequency oscillation is more easily obtained by eliminating these non-ideal effects largely attributed to standing-wave internal modes seen in the linear resonator.

4.3.1 Ring resonator stability

Just as we saw in sec. 4.2.1, the stability of a resonator can be determined by calculating the RTM of a unfolded representation of the internal optics. However unlike a linear resonator, the path through a ring resonator is single pass. Consider a rectangular ring resonator comprised of four high-reflectance planer mirrors, an internal fixed power cavity lens for mode size control and an active gain medium which will act as a power variable thermal lens. The two lenses are symmetric in position separated by distance, L. The optical path RTM is calculated as follows,

$$\begin{aligned} M_{ring} &= \begin{pmatrix} 1 & L \\ 0 & 1 \end{pmatrix} \begin{pmatrix} 1 & 0 \\ -\frac{1}{f_1} & 1 \end{pmatrix} \begin{pmatrix} 1 & L \\ 0 & 1 \end{pmatrix} \begin{pmatrix} 1 & 0 \\ -\frac{1}{f_2} & 1 \end{pmatrix} \\ &= \begin{pmatrix} 1 - \frac{L}{f1} - \frac{2L}{f_2} + \frac{L^2}{f_1 f_2} & 2L - \frac{L^2}{f_1} \\ -\frac{1}{f_1} - \frac{1}{f_2} + \frac{L}{f_1 f_2} & 1 - \frac{L}{f_1} \end{pmatrix} \end{aligned} \tag{4.15}$$

As before, we can substitute elements A and D into the stability condition in Eq. 4.4 which returns our new g-parameters,

$$g_1 = 1 - \frac{L}{2f_1} \quad \text{and} \quad g_2 = 1 - \frac{L}{2f_2} \tag{4.16}$$

4.3.2 Ring resonator longitudinal modes

The ring resonator is a peculiar class of optical resonators which lack a standing-wave resonance solution. The lack of a back-reflection mechanism means there is no boundary condition requiring the node locations to be fixed at the end mirrors. Instead the cavity produces two counter-propagating traveling-wave modes with resonance instead achieved through the accumulation of round trip phase around a closed loop being restricted to integer multiples of 2π. This allows node locations to drift each round trip, the rate at which the nodes drift governs the degree to which spatial hole burning takes effect. As we will see in the next section, a unidectional intracavity mode can be enforced by weakening the contributions of the counter-propagating mode so that local gain saturation in the crystal is prevented. When the resonator is not unidirectional, multimode oscillation may be observed. To avoid spatial hole burning we exclusively operate in unidirectional oscillation so that there is no standing wave pattern at all.

The accumulated round trip phased due to free space propagation through cavity length, L, is expressed as,

$$\Delta\phi = 2kL - \phi \tag{4.17}$$

The round trip phase is still an integer multiple of 2π so that it is self-replicating. By making the substitution $k = 2\pi\nu/c$ and solving for when $\Delta\phi = 2n\pi$ for integer n, we get the ring cavity resonant frequencies as follows [82],

$$\nu = \frac{c}{2L}\left[n + \frac{\phi}{2\pi}\right] \tag{4.18}$$

4.3.3 Unidirectional ring resonator

A ring laser will generally lase with two counter-propagating modes in the clockwise (CW) and anticlockwise (ACW) directions. Their longitudinal mode content is identical as their allowed frequencies are determined by the same cavity mirrors. However, as the ring resonator lacks a back-reflection mechanism, these internal modes form two travelling waves that propagate independent of one another [83]. As the CW and ACW modes are optically uncoupled and compete for gain. The counter propagating modes have similar thresholds, so due to transient perturbations and gain clamping the oscillator will rapidly switch from CW to ACW emission. This also effectively halves the emission power available in a given direction. The interference of these travelling waves can create a standing wave as seen in a linear resonator, leading to the same limitation. The advantage of the ring resonator however, is its ability to operate in single-pass in either direction, through the use of direction selective optics which otherwise would not be possible in linear resonators configurations.

Unidirectional propagation of the internal mode can be imposed through the suppression of one of the travelling wave modes such that, say the CW mode, is preferred. A simple example of how this can be achieved is through a Faraday rotator used in conjunction with a half wave-plate which acts to block backwards propagation. By forcing travelling

wave resonance, the spatial distribution along the axial direction in the active medium is homogeneous so that gain saturation is mitigated. This allows further pumping without inducing unwanted competition so that the system operates at a single frequency at narrow line-width. Gain extraction is uncontested allowing the single-pass travelling-wave mode to fully exploit the available gain and single frequency operation is more easily achieved.

Another less common method to impose a unidirectional internal mode is through an external feedback mirror [84, 83, 85, 86]. Whereas the Faraday rotator acts to impede one mode without appreciably affecting the other, the feedback mirror strengthens the desired mode at the expense of the other. Suppose we have a ring cavity with two counter-propagating modes of equal power density competing for gain amplification, yet we desire the singular CW mode to be dominant. We can introduce losses of equal magnitude in both modes using a slightly transmissive cavity mirror. Then using a retro-reflective mirror we can feedback the CW mode that exits the resonator back into the cavity. This increases the power density in the CW direction upon re-entry. By biasing the internal power in the CW direction, the unbalance in mode power allows the share of gain to shift in its favour and the ACW direction is suppressed due to unrecovered losses. The share of power held in the desired mode can be expressed as a ratio comparing the total power contained in the respective modes. Expressed as a ratio, unidirectional powers of 2500:1 have been reported for Nd:YVO_4 based ring laser systems [86].

4.4 Linear vortex laser

In Chap. 3 we were introduced to the concept of OV mode transformation using a WPSI. In this chapter so far we have looked at key considerations towards the development of an efficient laser oscillator in a linear and ring configuration. We will now combine these ideas to show the development of a OV laser cavity using the WPSI as a VOC. This is demonstrated through two examples. Our initial attempt implemented a linear cavity configuration selected due to its simple optical set up where the WPSI would sample the intracavity power for OV conversion. In the end this configuration was deemed unsuccessful due to limitations which will be discussed in this section. The second implimentation was in a ring cavity configuration which will be presented in the next section.

4.4.1 Pre-laser characterisation

Before proceeding with the construction of the laser cavity, we must characterise the output of the pump laser-diode and the thermal lensing it induces in the laser gain medium as these factors will determine key properties of the laser such as power efficiency and cavity dimensions.

Pump laser emsission

The pump beam was produced using a K808DA5RN-60.00W fibre coupled diode laser from BWT Beijing. It possessed a top-hat profile with nominal emission at 808 nm to

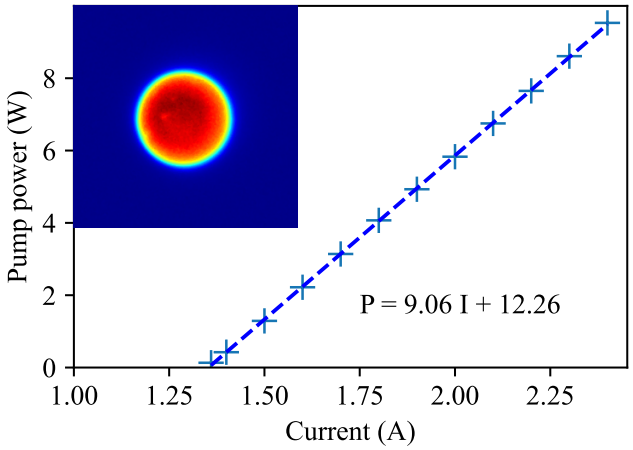


Figure 4.6: Pump diode laser power curve. Inset shown the top-hat profile of the pump beam

coincide with the Nd:YVO_4 $^4I_{9/2}$ to $^2F_{5/2}$ absorption line which promotes ground state electrons in the gain medium to the upper pump state. The pump laser was characterised to serve as a point of reference for input power delivered to the laser cavity should there be any alterations to the optical system or performance in the future. A power curve for the pump diode laser is shown in Fig. 4.6 at a fixed temperature of 25.0 °°C using a Coherent 0114J05 LM-10 10 W power meter.

The pump beam was focused using a $f = 20$ cm lens to a focal spot size of 0.6 µm at the laser crystal. The laser gain medium was 0.5 % doped Nd:YVO_4. Its pump absorption fraction was calculated by measuring the optical power transmitted through the crystal. The optical tranmsission data is shown in Fig. 4.7. The data was collected as single-pass transmission with no back reflections from external mirrors or surface coatings to prevent induced lasing. The optical pump power were kept low to minimise fluorescence of the gain medium inflating the power detected by the power meter.

We found the absorption to be lower than expected at 78 %. The gain medium had been damaged from previous use which could affect its performance, however measures were taken to avoid placing the pump directly on to the fracture lines. We expected the emission wavelength of the pump sat outside of the gain medium's optimal acceptance range. This could be offset due to the temperature setting of the liquid cooled heat sink that was connected to both the laser-diode module and the Nd:YVO_4 gain medium. Data collected in Tab. 4.2 shows the shift is pump emission wavelength and associated transmission through the laser crystal for varying heat sink temperatures.

Absorption of the optical power improved with temperature however a significant reduction in absorption was observed at 25 °C compared to what was obtained in Fig. 4.7. Vibrations due to the cooling units on the optical bench became severe beyond 27.5 °C. Despite operating off the nominal 808 nm wavelength, we opted to set the heat sink to 27.5 °C to

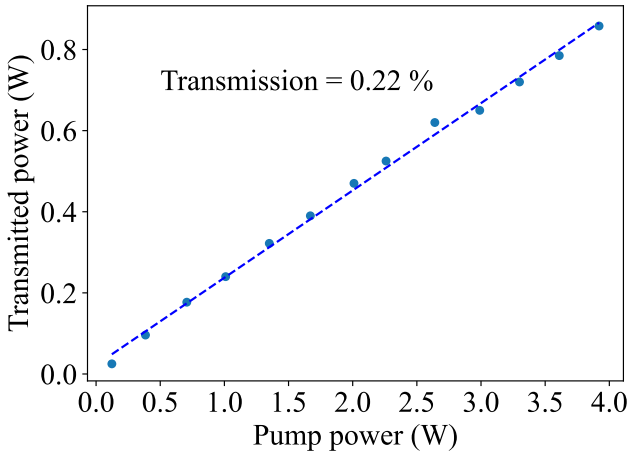


Figure 4.7: Optical tranmsittance of the pump power through 0.5 % doped Nd:YVO_4

Table 4.2: Pump emission wavelength and optical transmission for varying heat sink temperatures.

Temperature (°°C)	Pump wavelength (nm)	Transmission (%)
17.5	802.76	53.2
20.0	803.31	47.2
22.5	803.90	38.7
25.0	804.25	29.8
27.5	805.07	19.2
30.0	805.44	11.5
32.5	806.21	10.0
35.0	807.03	10.5
37.5	807.62	7.8

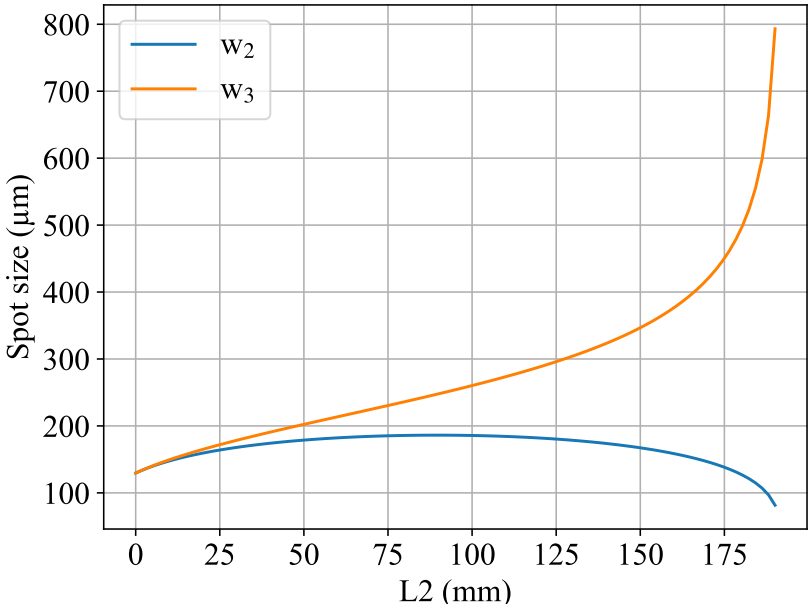
minimise vibrations which could have adverse affect on laser stability down the line. Of course the compromise with improved vibrational stability is the reduced overall power efficiency of the laser but this is of lesser importance at this stage.

Thermal lens

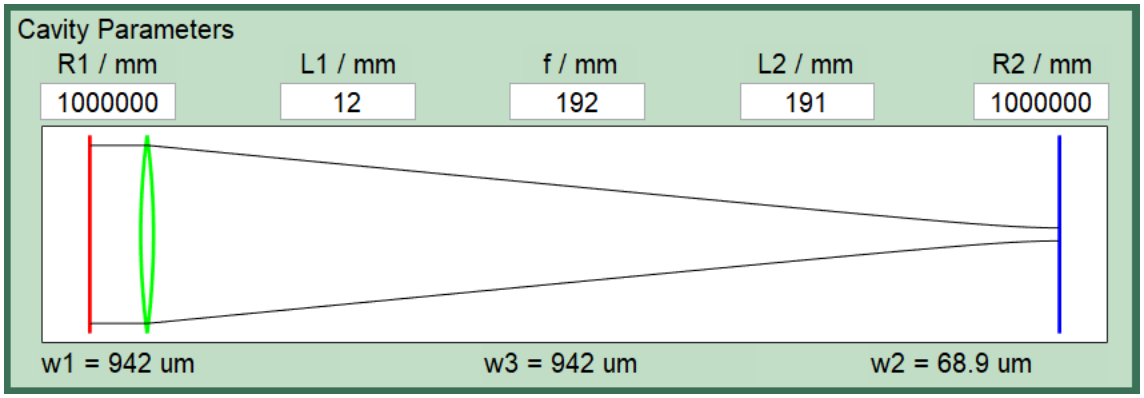
The thermal lens induced by optical pumping of the laser gain medium was measured. The PR was mounted on to a translation stage so that the cavity length could be increased while the laser was operational. L1 is the distance from the BM to the laser crystal and was fixed at 12 mm from the laser crystal. L2 is the distance from the laser crystal to the PR. Lasing ceased when the total cavity length exceeded the distance required to reimage the intracavity mode on the PR. This was found when L2 = 192 mm for 5 W of optical pump power.

The evolution of the laser spot size was calculated using an optical cavity simulator on MATLAB (developed by Dr Kerridge-Johns) based on equations formulated by *Magni et*

al.[81]. The spot sizes at the thermal lens and PR were calculated for varying L2. This allows us to examine cavity length parameters to find the optimal setting based on the strength of the thermal lens. The laser has optimal power output when L2 was set just shy of 100 mm. This corresponds to when w_2 is maximised in Fig.4.8 and possibly indicating optimal overlap of w_3 with the pump induced inversion.



(a)



(b)

Figure 4.8: (a) Laser spot size w_2 at the PR and w_3 at the thermal lens. w_2 maximised when L2=89 mm and ceases at L2=192 mm. w_3 monotonically increases with L2 and approaches asymtote near L2=192 mm. (b) MATLAB cavity mode simulation at maximum L2.

4.4.2 OV generation in a linear cavity

The linear cavity was constructed with the WPSI placed between the cavity mirrors as shown in Fig. 4.9. An immediate drawback to this setup was the inability of the OV reflection angle to extend beyond the PR so that direct WPSI output coupling could be

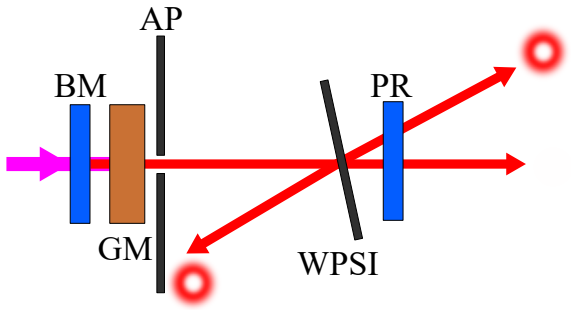


Figure 4.9: Linear cavity setup with WPSI for OV generation. The back-mirror (BM) and partial reflective mirror (PR) enclosed the gain medium (GM). An aperture (AP) was used to block the back-reflection from the WPSI.

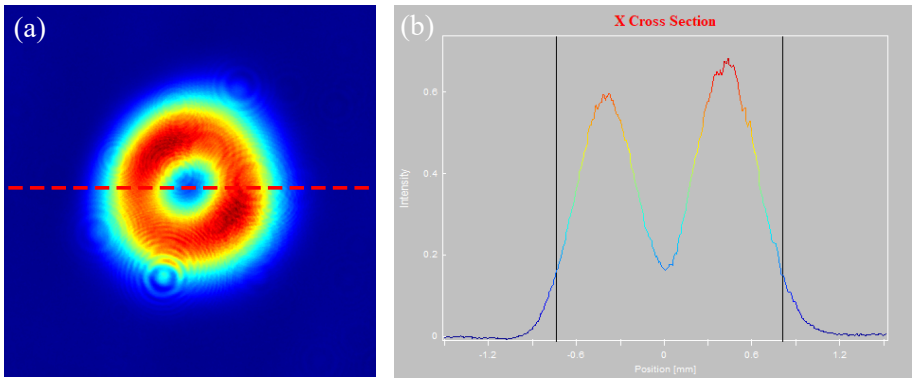


Figure 4.10: (a) Intensity profile of OV generated by the linear cavity. Although the intensity profile of the ring is good, the phase singularity has non-zero intensity (b) Intensity cross-section of OV along the horizontal axis (indicated by the red dotted line in (a))

achieved. Avoiding the PR required an incident angle too large for any annular shaping of the reflected mode let alone to produce a canonical OV. Instead an OV could only be produced when the exit angle was through the PR which greatly diminished the OV output power. This was more so a limitation of this particular setup and not linear cavities in general. Since the exit angle is determined by the dimensions of the WPSI a custom built WPSI or access to a greater selection of WPSI sizes could easily resolve this compatibility issue. In fact, Ref. [87] successfully demonstrated the use of a linear cavity with the WPSI functionality replicated using microscope slides.

The transverse mode generated by the intracavity WPSI was found to possess traits indicative of improper mode conversion. The phase singularity was observed to have non-zero intensity and the resultant mode had poor phase control sensitivity. Fig. 4.10 shows the intensity profile and cross-section for such an OV. The performance of the WPSI was significantly affected by the broad line width of the incident radiation. Interferometry relies on the incident light maintaining coherence over the entire optical path difference, which here corresponds to the dual-pass distance through the WPSI. A broad line width, indicating a short coherence length, limits the ability of the light waves to interfere after traveling this distance. As a result, the interference becomes washed out, disrupting the intended mode conversion and reducing its efficiency.

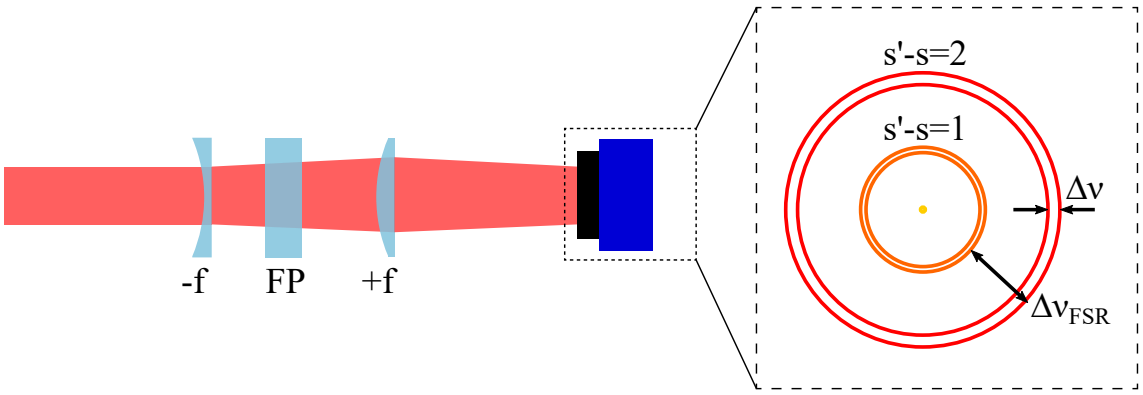


Figure 4.11: FP setup to analyse the laser emission spectrum. The fringe orders have been identified as $s'-s=1$ and $s'-s=2$ in orange and red respectively. Each fringe is shown to possess a dual ring structure denoting bi-modal laser emission.

The broad spectral line width was thought to be due to a combination of spatial hole burning effects which permitted the lasing of multiple longitudinal modes and the intracavity WPSI acting as an frequency selection tool, similar to an etalon. As a result, the laser spectrum adjusted to minimise losses across longitudinal modes which were modulated by the WPSI depending on its orientation within the cavity. This is further complicated through coupling of WPSI orientation and the geometry of the transverse mode reflected out the cavity. We can characterise the suitability of the incident radiation for interference through its coherence length, L_c which is the distance over which the light waves remain coherent. The point of incoherence is generally defined as the point when self-interference sees a $1/e$ decay in fringe visibility.

$$L_c = \frac{c}{n\Delta\nu} \tag{4.19}$$

For effective interference, the coherence length must exceed twice the WPSI thickness. The coherence length, in turn, depends on the bandwidth of the laser emission spectrum. To measure this bandwidth, we used a spectral diagnostics setup incorporating a Fabry-Perot (FP) etalon. Commercial spectrometers can typically be found capable of providing spectral resolutions of around 0.1 nm. However for laser line width measurement finer resolutions are required. This can be achieved through the use of a FP spectral analyser as shown in Fig. 4.11, that can provide an order of magnitude improvement in this regard. This method separates the spectral components of the incident radiation through the FP transmission function given in Eq. 4.20 depending on the incident angle, θ, of the incoming wave fronts.

$$T_{FP} = \left[1 + \frac{4R}{(1-R)^2}\sin\left(\frac{2\pi\nu L\cos\theta}{c}\right)\right]^{-1} \tag{4.20}$$

The transmission function is maximised when $2\pi\nu L\cos\theta/c = s\pi$ for integers s with the highest order fringe occurring at normal incidence when $s' = 2L\nu/c$ for FP length L. The incident angles are produced by passing a sample of the laser emission through a negative lens placed before the FP. The FP transmission is brought to a focus and imaged

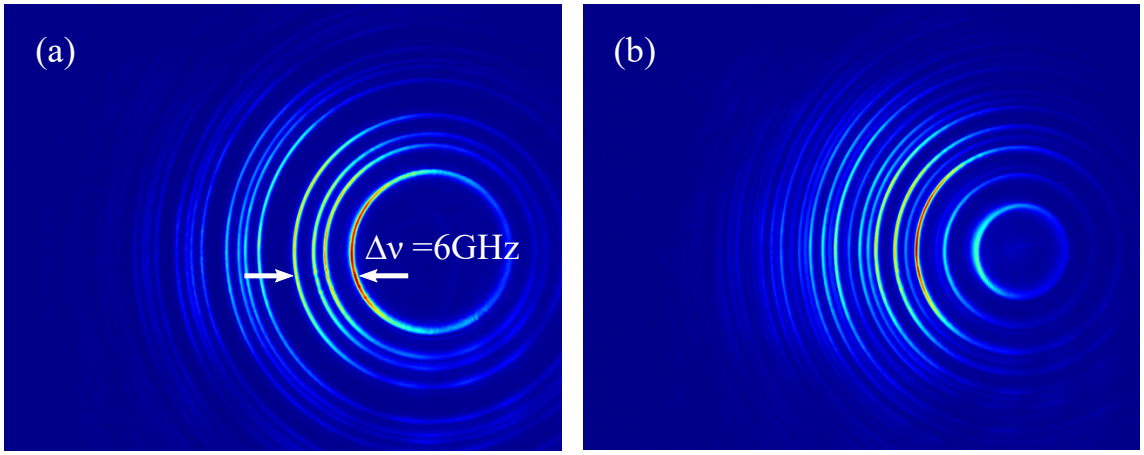


Figure 4.12: FP rings for emission at (a) lasing threshold and (b) $\sim 0.8\,\mathrm{W}$ lasing power. At threshold we immediately see multimode emission with a line width of $\Delta\nu = 6\,\mathrm{GHz}$ measured using an FP with FSR = 10 GHz. Above threshold the line width becomes too broad to measure using this FP as indicated by overlapping fringe orders.

onto a camera to reveal a pattern of concentric ring fringes as shown in Fig. 4.11. Each fringe increasing in radial position decreases in fringe order, each order is separated by the free spectral range (FSR) of the FP given by $\Delta\nu_{FSR} = c/2L\cos\theta$. The transmission function then grants the ability to decompose the laser spectrum by mapping the spectral content of the incident beam to radial coordinates on the image plane. The incident angle corresponding to a fringe order can be approximated by,

$$\theta_s^2 \approx 2\frac{s' - s}{s'} \tag{4.21}$$

The resolution of the spectral features is determined by the finesse of the FP, $\mathcal{F} = \pi\sqrt{R}/(1-R)$ for face reflectance R.

Multi-mode emission is identified when multiple rings occupy the same fringe order with the repeating unit separated by the FSR of the FP as illustrated in Fig. 4.11. Experimental measurements are shown in Fig. 4.12. Fig. 4.12(a) shows the case where the broad emission spectrum is still within the FSR of the FP. In cases where the emission spectrum exceeds the FSR of the FP, the friges are no longer clearly seperated and begin to overlap as shown in Fig. 4.12(b). The overall width of the fringe equates to the spectral linewidth. The coherence length of the linear OV laser at threshold was calculated to be $L_c = 3.4\,\mathrm{mm}$ which is less than the dual-pass distance through the WPSI. Hence we have incoherent mode conversion.

It is not uncommon to see multimode emission spectra in linear cavities. This is can simply be corrected through the use of an intracavity etalon that applies stronger modal selection that the cavity or, in this case, the combined effect with the WPSI. The FSR of the WPSI is 39.5 GHz. A FP with an FSR of 3.4 GHz was used to clear the laser spectrum and was proven to be successful rear threshold. At higher powers, the laser spectrum was improved from Fig. 4.12(b) to dual-mode lasing, however coherence length issues still persisted.

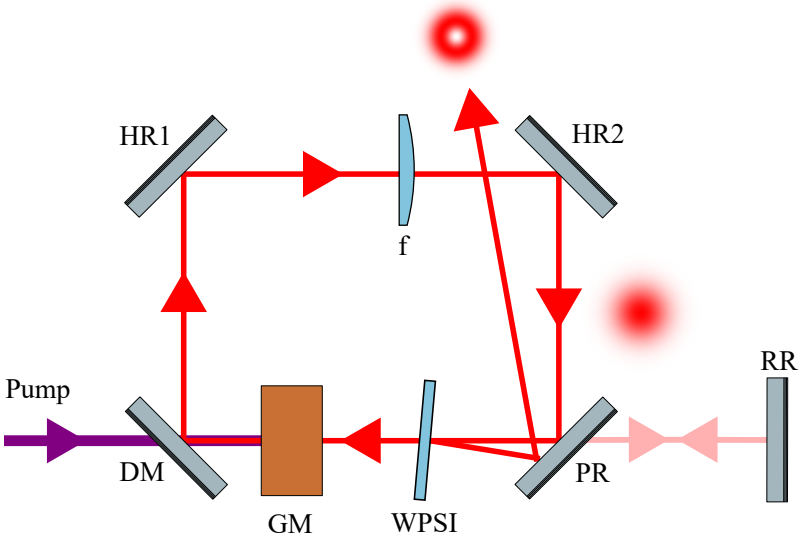


Figure 4.13: Optical setup of the ring cavity vortex laser. It is comprised of the gain medium (GM) optically pumped at 808 nm. High-reflectance mirrors (HR) and partial-reflectance mirror (PR) form the remained of the cavity. A retro-reflective (RR) mirror is used of seed a portion of the ACW power leaked through the back into the cavity in the opposite direction. This biases the internal mode in the CW direction. The WPSI is used as a VOC to sample the intracavity mode and generate an OV in its reflection. Lens (f) used for internal mode size control.

4.5 Ring vortex laser

In the previous section we found the linear cavity to be unsuitable for efficient OV generation due to limitations in incoherent mode conversion and poor OV power efficiency. As we discussed, the incompatible exit angles could easily be resolved through better selection of WPSI dimensions. Issues in poor interferometric conversion due to the broad laser line width were inherent to the linear configuration and persisted despite attempts at spectral filtering. To an extent, even this could be resolved though better WPSI selection by using a thinner WPSI so that its thickness matched the coherence length of the incident radiation. This leaves the back-reflected OV still unresolved. This isn't necessarily problematic especially where coupled dual-OV generation is desirable, however in our pursuit for a watt-level OV laser, the standing wave internal oscillation halves the emission power available to the VOC.

All of these issues were resolved by opting for a ring cavity configuration. This section will relay the characteristics of the ring cavity OV laser that successfully demonstrated watt-level OV generation using the WPSI as a VOC. Near perfect beam quality and mode purity was achieved highlighting the efficiency of the mode transformation method implemented. Additionally single longitudinal mode operation was achieved with narrow line width in agreement with similar Nd-doped vanadate ring lasers.

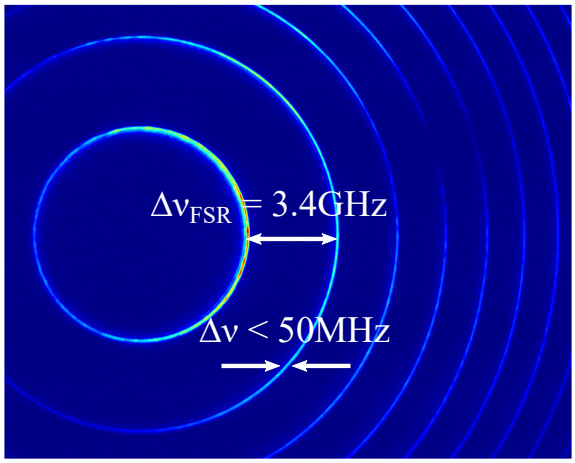


Figure 4.14: FP ring for SLM laser emission. Rings' separation matches the FSR of the FP. Emission linewidth was measured to be at least 50 MHz.

4.5.1 Unidirectional laser cavity

As mentioned in 4.3.3, a retroreflective mirror (RR) can be used to bias a ring cavity to a preferred lasing direction so to ensure the intracavity mode is unidirectional. The optical setup of the ring cavity is shown in Fig. 4.13 implementing the RR mirror feedback. The PR has measured transmission of $T = 1.3\,\%$. The RR was used to direct the ACW power back into the laser cavity to enforce CW bias. Power leakage through HR1 was used to measure the power bias in the CW and ACW directions. This was found to be 20:1 in favour of the CW direction.

Power bias in the internal mode produces a traveling wave oscillation of the optical field around the resonator. Effects such as spatial hole burning and gain saturation no longer occur or are greatly reduced which eliminates multi-mode lasing. Instead single longitudinal mode lasing is achieved with narrow line width. Spectral analysis on the laser emission was again conducted using the FP spectral diagnostics used previously. The FP transmission spectrum in Fig. 4.14 shows a series of single ring fringes. The linewidth measurement was limited by the resolution of the FP but confirmed to be at least less that 50 MHz. This is in line with similar Nd-doped vanadate ring lasers [86].

4.5.2 Beam quality measurement

The M^2 value is a dimensionless metric set by the International Organisation of Standards (ISO) used to measure the quality of a beam. Higher-order modes such as the LGs are measured to how closely they match a diffraction limited TEM_{00} Gaussian. It is important to distinguish between what would be called a Gaussian in a lab setting and what is truly a diffraction limited beam. Experimental factors such as aberrations in the beam delivery optics can affect the quality of the beam. Similarly undesired processes within the laser cavity such as thermal lensing, cavity mirror misalignment, spatial hole burning and mode matching can lead to distortions that adversely affect the quality of the generated

Gaussian.

To measure the beam quality one must ensure the beam is initially collimated. It is then propagated through a focus by a lens with minimal aberrations. As the beam propagates along the z-axis, beam size measurements are to be taken as various points through its propagation. We can measure the beam size in terms of the 2^{nd}-moment, which is, the beam diameter at four times the standard-deviation of the beam intensity distribution. This is also referred to as the D4σ method. For Gaussian beams the 2^{nd}-moment agrees with its $1/e^2$ value, however this is not true for higher-order modes. It is therefore strongly recommended to use the former. It is important to not use too tight of a focus so position measurements near the focus can be made with a reasonably high degree of accuracy. It is recommended to take at least ten measurements up to two Rayleigh lengths from the focus with half contained within one Rayleigh length of the focus. The measurements are then fit to the following expression and solved for M^2,

$$w^2(z) = w_0^2 + (M^2)^2 \left(\frac{\lambda}{\pi w_0}\right)^2 (z - z_R)^2$$

In this work, beam quality measurements were made using a camera that was translated along the beam axis using a camera rail. Beam size and quality calculations were automated using the *RayCi Pro* software package by Cinogy. The ring cavity was capable of producing OVs with an $M^2_{x,y} = 1.94, 2.09$ which agreed well with the theoretical ideal of $M^2_{x,y} = 2$. Differences in the $x, y-$components indicate astigmatism in the OV which could be due to asymmetric lensing effects within the cavity or beam delivery components. The beam quality of the internal cavity mode was also measured and found to be $M^2 = 1.03$. The high beam quality of the internal mode potentially rules out cavity lensing and inherent asymmetries in the underlying Gaussian.

4.5.3 OV modal decomposition

Modal decomposition is a powerful tool that can be used to determine the constituent components of a of an unknown signal. This was performed using a Fourier-based phase retrieval algorithm (developed by Dr Kerridge-Johns) based on methods first proposed by *Takeda et al.* [62].

An interferogram is produced by combining an OV (signal) with a titled plane wave (reference) as shown in Fig. 4.15. Fourier-manipulation of the fringes is used to reconstruct the phase of the underlying OV. One then obtains the intensity through input of the reference. To ensure best alignment of the images, the signal and reference should be as kept as they were to generate the interferogram and then the signal is simply blocked to allow only the reference to be imaged. This is to ensure the algorithm is provided the correct overlap information to correctly analyse the fringe pattern.

Results of the modal decomposition are shown in Fig. 4.16. We see strong agreement of the original and reconstructed intensity and phase profiles. The complex field associated with

the OV can then be reconstructed to estimate the modal content of the OV as described previosuly in Chap. 2. We see a high $LG_{0,-1}$ purity (97.7 %) with trace contributions from other modes up to $p+|l|=3$. This is in agreement with previous modal analysis of the WPSI [59] and the idealised case seen in Chap. 3. This result also confirms the high mode transformation efficiency of the WPSI.

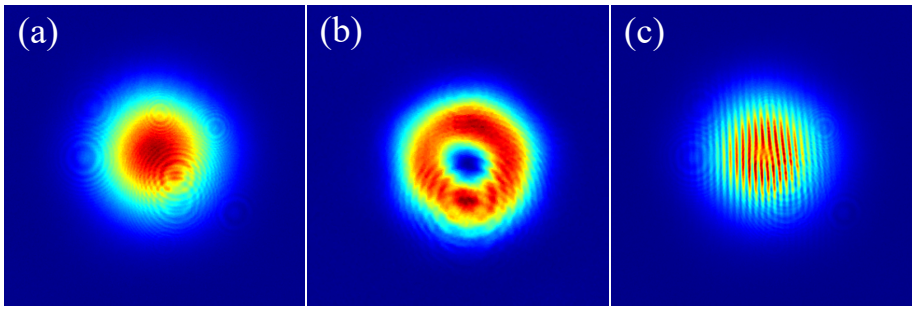


Figure 4.15: (a) Reference (b) OV and (c) fork interferogram used in the phase retrieval algorithm.

4.6 Power efficiency

The OV output power plotted against absorbed pump power is shown in Fig. 4.17. The laser began lasing at 0.06 W and was capable of generating a 1.15 W beam from 4.73 W of absorbed pump power, given a slope efficiency of 22.6 %. There is potential for further power scaling by increasing the input pump power. The intracavity flux at maximum power was calculated to be 50 W based on the known transmittance of the PR ($T = 1.3\,\%$). Despite the high internal oscillating power, no measurable degradation in WPSI performance was observed demonstrating its high damage threshold and low loss characteristics. The output coupling of the WPSI can then be calculated comparing the internal power with the portion output coupled by the WPSI. This returned $R_{01} = 2.3\,\%$. The intracavity and output vortex modes were vertically polarised.

Findlay-Clay analysis was used to investigate cavity losses by relating the pump power at laser threshold for varying PR reflectances as shown in Fig. 4.18. PR reflectances at R =90 %, 95 %, 98 %, and HR with 99.4 % were tested. The x-intercept gives the total cavity losses. Neglecting the 2.3 % WPSI reflectance, a total round-trip loss of 4 % was measured. This includes combined mirror losses of 1.5 % with the remainder due to imperfections in the laser crystal AR coating due to hair-line fractures present from prior work. Eliminating these losses would further increase laser performance.

4.7 Summary

The development of a native OV laser requires the construction of a suitable laser oscillator to which the WPSI can be used as a VOC. This chapter presented the development of a solid-state free-space laser oscillator with discussions on the choice laser gain medium

for high gain extraction, and stable resonator configurations to confine a TEM_{00} internal mode. Two resonator arrangements are explored. The linear resonator is the more common of the two, known for its simple setup with dual-pass pumping for high gain extraction. However, the internally propagating mode forms a standing-wave that can cause inhomogeneous gain saturation within the gain medium and lead to multimode spectral features in the laser emission if left uncorrected. The ring configuration has the option to operate in single pass with a traveling-wave internal mode that alleviates much of these issues.

Both systems were demonstrated experimentally with attempts at intracavity OV generation using the WPSI as a VOC. As expected the linear cavity suffered from coherence length issues due to poor spectral performance that resulted in the incoherent combination of its interfering beams. This produced a poor quality OV in its output. The ring cavity on the other hand was successful in demonstrating a intracavity OV generation. The laser operated at a single-longitudinal mode with a narrow laser emission linewdith of at least 50 MHz which is comparable to similar Nd-doped systems. The WPSI was used as both the mode conversion device and output coupler, with 2.3 % output coupling fraction. The WPSI was shown to operate at 50 W of incident intracavity power with no detected degradation in performance or surface damage due to its high optical and thermal damage thresholds. It produced high OV beam quality ($M^2_{x,y} = 1.94, 2.09$) and 97.7 % LG_{01} mode purity.

Now that we have access to high quality OV at high power, we propose possible applications in optical levitation where the enhanced radiative force can be used to support the weight of large, massive targets. Additionally, the ring-like shape of the OV grants is the ability to capture opaque and reflective targets that are traditionally not possible standard Gaussian breams. We will explore this possibility in the following chapters.

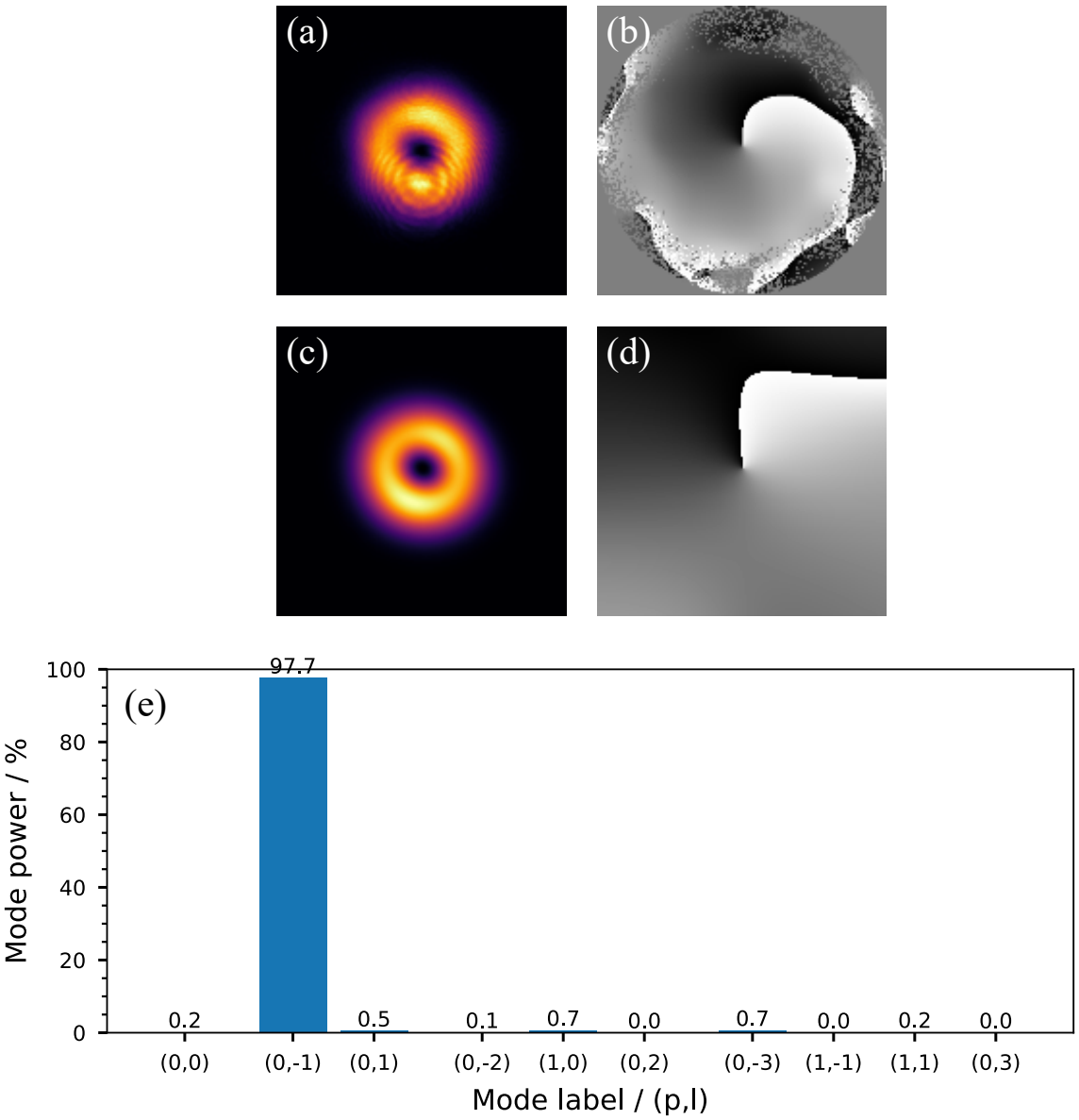


Figure 4.16: (a) The intensity of the OV signal and (b) associated phase profile. (c) The intensity and (d) phase reconstructed from the fork interferogram. (e) Modal decomposition shows 97.7 % $LG_{0,-1}$ mode purity with trace contributions from other LG_{pl} modes.

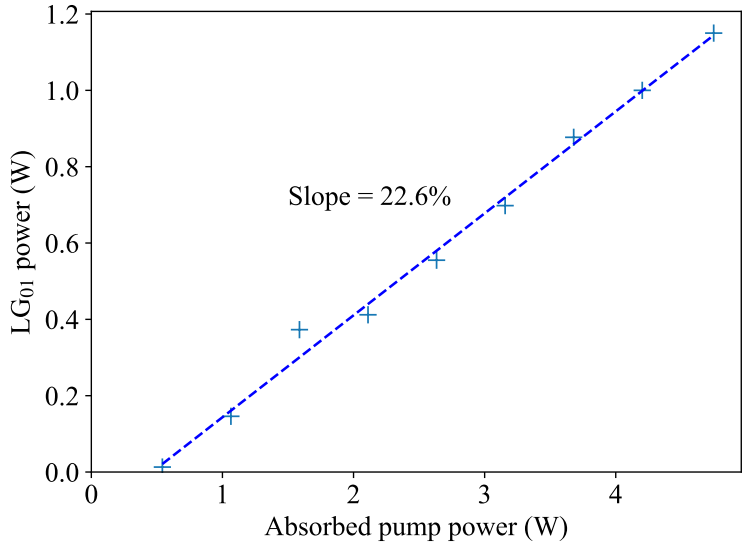


Figure 4.17: The ring cavity lases at a threshold of 0.06 W and an efficiency of 22.6 %

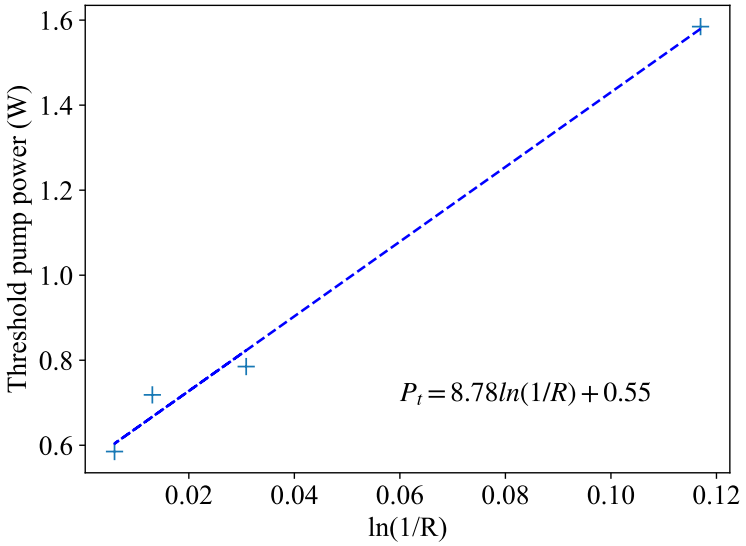


Figure 4.18: Pump powers at laser threshold for varying PR reflectances.

Chapter 5

Optical levition system & Diagnostics

The optical vortex (OV) laser which we have discussed so far forms the first stage of a larger optical system intended for experiments in optical levitation. The design of the levitation system is influenced by our goal to levitate reflective and possibly metallic, hollow microspheres (or shells) to be used as end-targets for terrawatt (or petawatt) class high-energy laser systems. This work forms the foundations of a fully functional system with integrated OV laser and optical trap. Previous work within the group on OV optical levitation used fiber delivery of a TEM_{00} mode to a spiral-phase plate (SPP) to produce the trapping beam. Although an SPP may be used to easily produce an OV trapping beam, mode impurities leave a degree of uncertainty as to the quality of the beam profile in a given plane. We expect the improved beam geometry produced by our OV laser to improve trapping performance.

The layout of its main components is illustrated in Fig. 5.1. It is comprised of the OV laser source, active power modulation components, the optical levitation system and its diagnostics. Later, a vacuum envelope to the levitation system is applied and will be discussed separately. This system demonstrates the trapping of large shells in excess of 100 µm in diameter at long range (40 mm from the final focusing optic), we have achieved high spatial stability with position standard deviation of <5 µm, explored levitation at $1/100^{th}$ atmospheric pressure, and observed intriguing and unexpected behaviour in trap dynamics and target geometries that could present obstacles to overcome and avenues for further investigation in later generations of this work.

5.0.1 Motivations

Optical levitation has successfully demonstrated applications ranging from force sensing [88, 89, 90] to biophysics [91, 92, 93, 94]. This is often undertaken with transmissive dielectric objects trapped in fluid, air or vacuum. We expect our system to be capable of

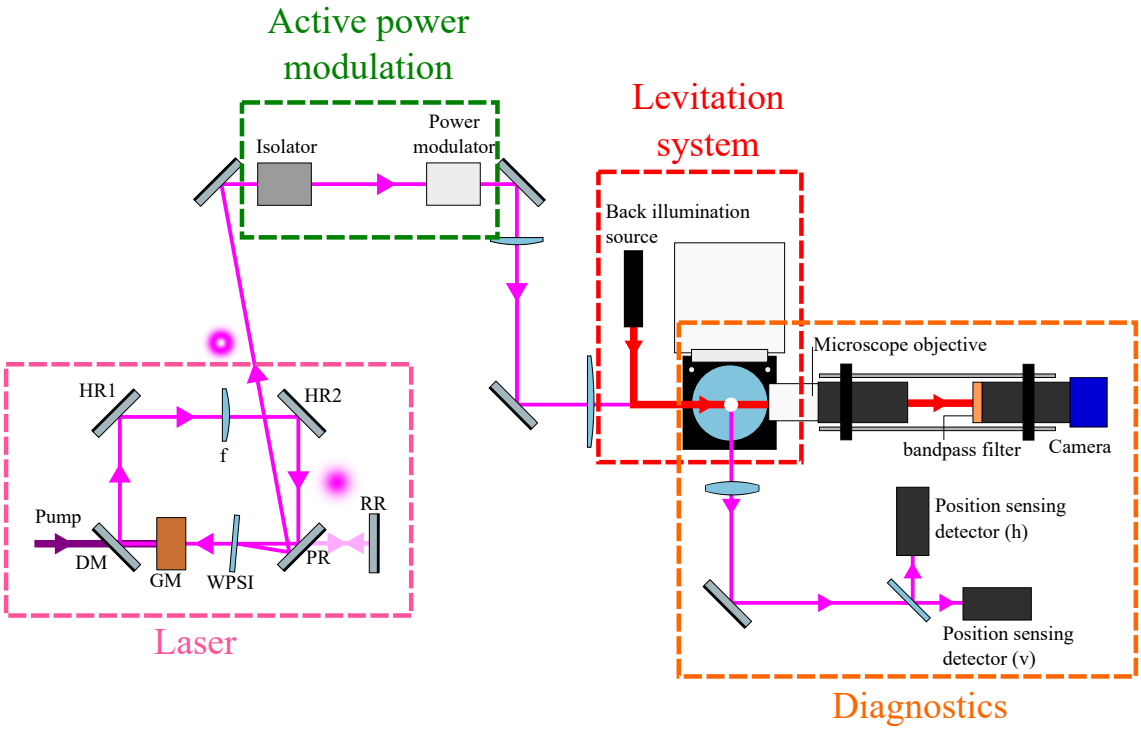


Figure 5.1: Top view of the optical bench setup comprised of the laser cavity, active power modulation components, the levitation system and levitation diagnostics itself comprised of levitating shell imaging and position sensing.

similar feats. However, access to watt-level power from our OV laser provides comfortable headroom for power scaling to capture large-mass targets. A rough calculation for 1 W beam at normal incidence exerts a radiative force of $F \sim 2P/c = 3/3 \times 10^8 = 6.7\,\text{nN}$. Given our choice of trapping beam geometry, the kinds of target compositions now extends to the capture of highly reflective targets such as those with metal-coating and polished surfaces, and thin-walled "shell" (low refractive index interior) targets.

Levitating metal-coated targets is of particular interest to active areas of research in high-energy density plasma physics and table-top radiation generation. Access to high-intensity pulsed laser fields exceeding $10^{19}\,\text{W cm}^2$ [95] have granted university-scale laboratories new capabilities in the generation of energetic electrons [96] protons [97] and gamma radiation [98]. The production of laser-induced plasma has also emerged as a pivotal technique in the generation of table-top X-ray sources [99, 100].

Intense laser interactions with metal-coated nanoparticles have reported 13-fold enhancement to hard X-ray yield as compared to uncoated targets expected to be due to surface plasmon and “lightning rod” effects enables by the metallic surface [101]. Typically, X-ray energies scale with the density of the irradiated material ($E_\gamma \propto Z^2$ - for atomic number Z). However hard X-rays ($50-150\,\text{keV}$) have been generated from liquid microdroplets [100] due to these targets being considered to be "mass-limited", that is, the interaction region is contained within the confines of the target and does not extend to connected apparatus such as suspension wires or mounts. Since heating is confined to the target region, higher

temperatures can be achieved as compared with solid targets of greater atomic number (Z) [102]. Unwanted radiation generation through hot (electrons ejected from plasmon resonance) and thermal (thermal energy exceed the materials work function) electron transfer to surrounding material is also reduced. Additionally, the lack of return paths for ejected electron currents reduces the effects of electromagnetic pulses that can otherwise leave nearby sensitive electronics susceptible to intense RF field damage.

Mass-limited targets are most commonly found as liquid micro-droplets sprayed into an experimental chamber or as liquid jets. The fast moving targets make them unsuitable for low-repitition rate lasers where individual shots are expensive in cost and time thus requiring the hit to be guaranteed. Electrostatic trapping has been used to produce mass-limited targets for solid dielectric micro-beads with greater spatial confinement [103, 104]. But the applied charges may be unsuitable for liquid droplets where Coulomb repulsion approaching the Rayleigh limit could lead to deformation or break-up [105]. Configurations such as the Paul trap also have limited access to viewing angles for diagnostics. Optical levitation techniques aims to resolve a number of these issues with greatly improved viewing angles and demonstrated use with neutral oil droplets spatially held with micron stability for reliable shot accuracy using high-intensity low and high repetition rate lasers [106]. Expanding to solid targets is then conceptually trivial as the optical trapping and levitation of transmissive dielectric targets can be found widely in the literature. There may be concerns with more complex solid target geometries with frozen-in asymmetries and differet thermal transport mechanisms. Problems also arise if we wish to levitate large reflective targets with a Gaussian beam profile as these generate repulsive radial forces on such targets.

Our motivations aim to expand optical trapping capabilities to now include reflective target levitation with performance characteristics suitable for integrating into larger experimental facilities for high-intensity high-energy laser interactions. The suspension of isolated metal-coated particles allows one to combine various target enhancing properties such as high Z materials, that are mass limited and highly confined. Additionally, if the target is thin-walled, applications in forward ion acceleration can potentially be realised [107]

5.1 Reflective shell targets

The levitation targets shown in Fig. 5.2 are silver-coated hollow glass microspheres (or shells) ranging between 10 µm-125 µm in diameter from Cospheric - Product Code: M-60-0.18 10-125um. These are thin-walled nominally spherical targets - their structure is illustrated in Fig. 5.3. Exact wall thicknesses of individual shells are not well documented, however estimates from similar product lines were obtained from the manufacturer based on true particle densities. These are presented in Tab. 5.1. Unfortunately, corresponding statistical data could not be obtained.

The wall-thickness estimates assume a silver-coating of 100 nm which we take to be con-

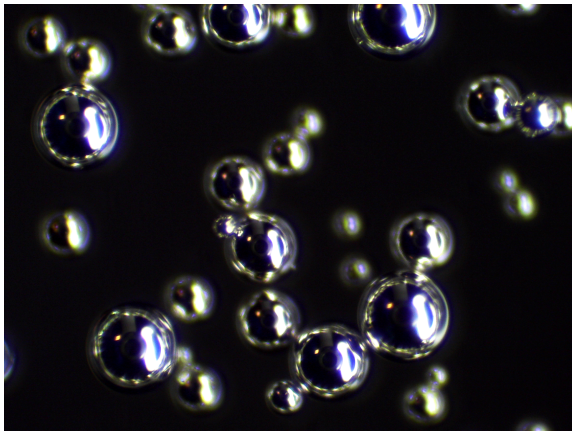


Figure 5.2: Top-illuminated microscope image of silver-coated shells.

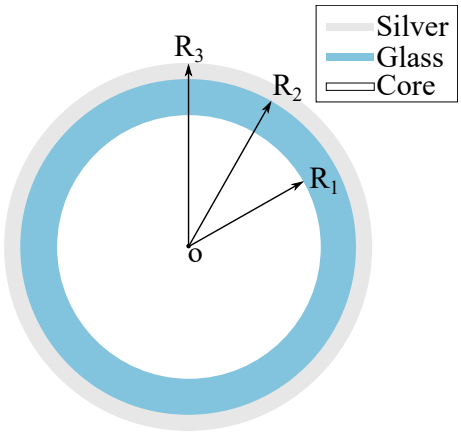


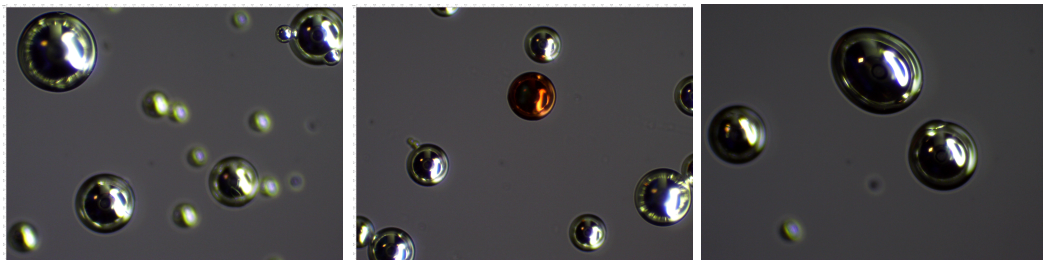
Figure 5.3: Internal shell structure. (Not to scale)

stant across all shell sizes. We were assured this to be the case as the coating is applied using an immersion deposition process. Again, statistical data of coating variation was not available but may be obtained using electron microscopy. Assuming a shell diameter of 50 µm, with densities $\rho_{Ag} = 10{,}490\,\mathrm{kg/m^3}$ and $\rho_{gl} = 2200\,\mathrm{kg/m^3}$, the mass of a single microshell is estimated to be $\sim 20\,\mathrm{ng}$. The interior is gas filled and its composition is a function of the proprietary glass composition. No further information could be obtained however we expect the gas component to have negligible effect on the mass calculation.

The silvered exterior is highly reflective under 1064 nm illumination with a calculated reflectance of 99.7 % based on its r_s and r_p reflection coefficients [108]. The surface quality of the coatings was inspected under a table-top microscope. Top-illuminated images reveal a high-quality smooth mirrored surface as shown in Fig. 5.4. Some hair-line fractures were observed upon close inspection of the surface coating. It is unclear exactly to what extent these defects affect ease of shell trapping, and what role they play in cases where we observe peculiar scattering dynamics. More notably, instances of smaller shells and part-hemispheres attached to a larger host have been observed which, due to their asymmetry, would destabilise the optical forces acting on the combined body. Such shells have been observed to exhibit intriguing behaviour including spontaneous flips in orientation

Microsphere dimensions			
Item code	Shell diameter range (μm)	Assumed diameter (μm)	Estimated wall thickness (μm)
M-60-0.31 10-20um - 1ml	$10-20$	15	0.3
M-60-0.35 10-27um - 5ml	$10-27$	18.5	0.47
M-60-0.26 27-32um - 5ml	$27-32$	29.5	0.64
M-60-0.23 32-38um - 5ml	$32-38$	35	0.68
M-60-0.21 38-45um - 5ml	$38-45$	41.5	0.77
M-60-0.19 45-53um - 5ml	$45-53$	49	0.85
M-60-0.17 53-63um - 10ml	$53-63$	58	0.93
M-60-0.16 63-75um - 10ml	$63-75$	69	0.99
M-60-0.16 75-90um - 10ml	$75-90$	82.5	1.38
M-60-0.15 90-106um - 10ml	$90-106$	98	1.58
M-60-0.17 106-125um - 10ml	$106-125$	115.5	2.3

Table 5.1: Table shows a range of microsphere diameters with corresponding wall-thicknesses. Note: these values are not from direct measurement but obtained from the Cospheric who estimates values using true particle densities.



(a) (b) (c)

Figure 5.4: (a) Fine line fractures seen on the surface of the shells. Shell on top-right has smaller shell protrusions on its surface. (b) Discoloured shell observed with distinct reddish-orange colour. (c) Egg-shaped shell

perhaps to a more energetically stable position and undergo highly regular periodic motion - both oscillatory and rotational. In later Chap. 7 we will present instances of asymmetric trapped-target arrangements and cases where stable trapping was observed.

On rare occasions, discoloured shells with a red-orange hue were observed as in Fig. 5.4(b). We suspect this is due to defective coating application resulting in a thinner layer of silver than intended having been applied to the shell surface. The could result in thin-film interference to produce the reddish colour observed. Alternatively this could be due to reaction of the coating layer with atmospheric nitrogen compounds.

The diameters of the first 69 successfully trapped microspheres was recorded and is shown in Fig. 5.5. The distribution appears to be somewhat uniform up to the 60 µm range before peaks in the 70 µm's. This may indicate a selective pressure for microspheres in this range dependant on the trapping power used at the time. There is an anomolous gap in the 80-90 µm range which is puzzling given the significant number of encounters >90 µm. This could indicate a gap in the distribution of the microsphere sample itself.

To investigate this further, 22 back-illuminated table-top microscope images of the microshells were analysed collecting 300 distinguishable microsphere diameter measurements. Their size distribution is plotted Fig. 5.6. As we can see there are large gaps present in the distribution. This could be a symptom of low sampling and requires more data to better represent the true distribution. Furthermore, the larger sizes are severely underrepresented compared to the trapped microshell distribution. We deem the nature of the 80 µm gap in the trapped microshells distribution inconclusive.

5.2 Levitation system

A schematic of the levitation apparatus is shown in Fig. 5.7. The levitation tower is built to accommodate 2-inch optical components with an up-expanded collimated OV input. The beam is brought to a focus using a 2-inch $f = 40$ mm lens. Although the OV is propagation invariant and holds its shape through focus, poor lens quality can introduce aberrations to distort the beam profile near best focus. This in turn affects the shape of the trapping

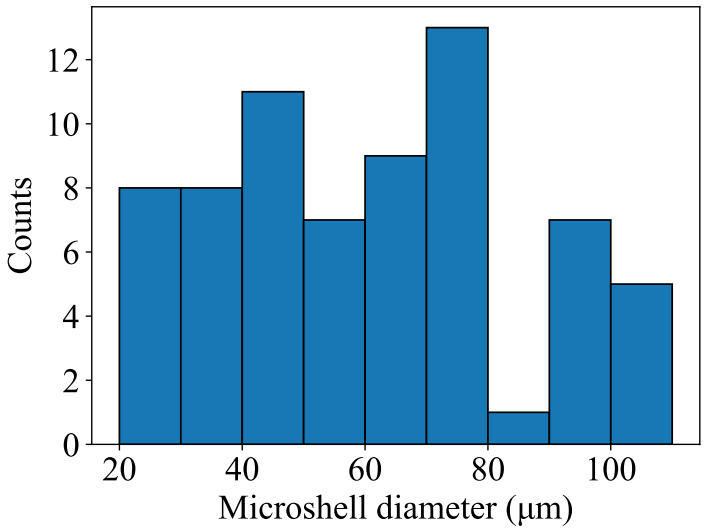


Figure 5.5: Frequency distribution of successfully levitated microspheres between 20 µm - 110 µm. The shell counts appears to be tending towards a uniform distribution upto the 60 µm range with a slight preference for shells in the 70 µm range. The gap in the 80 µm range is currently unaccounted for.

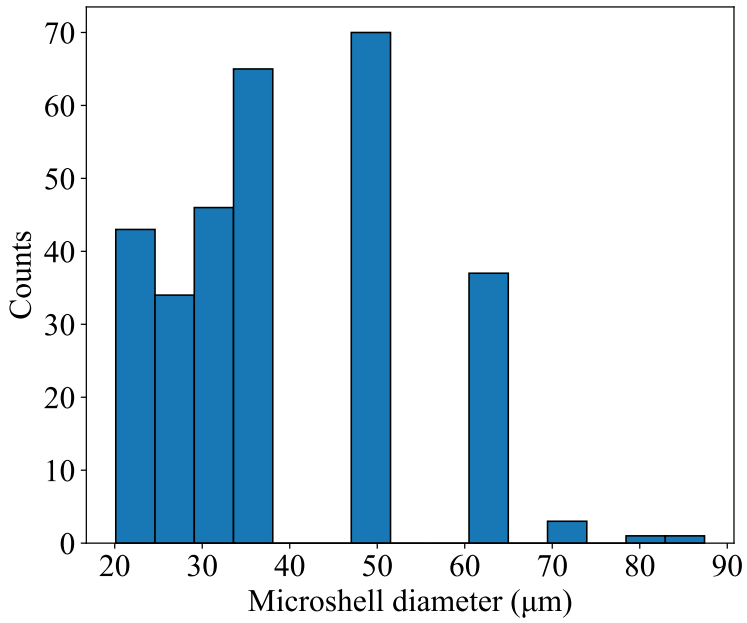


Figure 5.6: Distribution of microshell sizes from sample images.

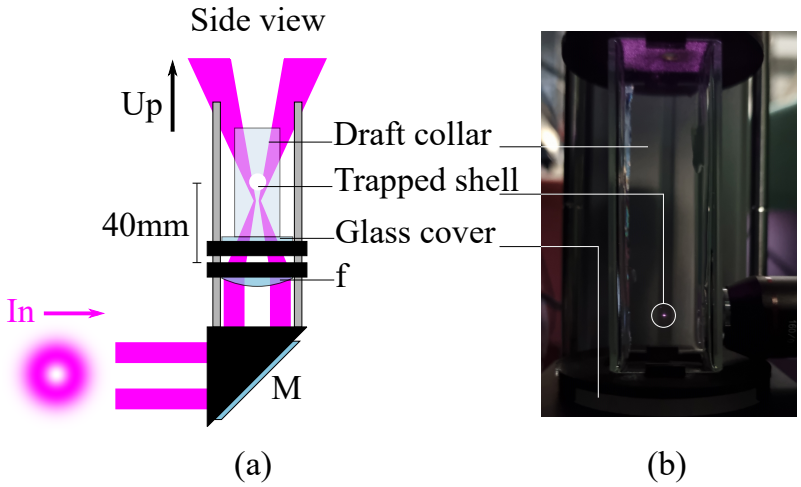


Figure 5.7: (a) Side view schematic of the levitation system with OV input, focusing optic f and trapped microsphere inside draft collar (b) Close-up of draft collar with trapped microsphere. IR light appears purple on the camera

potential leading to unexpected or unoptimal trapping performance. To minimise lens distortion and compensate for low system NA, an aspheric lens (Thorlabs AL5040-C) was used to ensure a high-quality focal spot was produced. Its performance was verified by inspecting the beam profile when passed through its focus using a magnifying imaging system attached to a translation stage to to allow sampling along the beam axis. High symmetry in the trapping beam ensures the optical forces are distributed evenly over the target for improved stability. The trap is loaded by injecting a plume of shells into the draft collar from above. The draft collar acts as a container to isolate the shells from air currents that would knock the shells out of the trap. The shells are let to fall under gravity into the trapping zone. Shells that were not captured by the beam were collected on a glass cover that protects the optics beneath from the falling debris. The cover glass was AR coated for improved optical transmission.

5.3 Beam delivery

A 10x expansion telescope was used to magnify the OV beam before delivery to the levitation tower. A standard Keplerian configuration was used with two plano-convex lenses, a primary 1-inch $f = 75\,\text{mm}$ and secondary 2-inch $f = 750\,\text{mm}$. The telescope was found to be highly sensitive to beam alignment and contributed to significant beam distortion observed near best focus inside the trap if not well aligned. Although initial guesses would point to the primary lens as the cause due to strong lensing effects, the true culprit was in fact the secondary lens due to poor size matching with the expanded beam. Future iterations of the setup should look to replace the lenses with an aspheric or bestform or use a larger diameter optic. The aspheric lens inside the levitation tower was found to be quite robust against beam misaligment although effects on beam profile can be seen for large misalignments.

Power modulated beam delivery was implemented to induce driven oscillations in the trapping dynamics. This was intended as a precursor to developing end-target stabilisation capabilities by varying trapping power dependant on trapped shell displacement. The complete power delivery system is shown in Fig. 5.8. A Faraday rotator was used to isolate beam propagation to only the forward direction to shield the cavity from optical feedback. Due to the polarisors attached to the end faces of the Faraday isolator, a waveplate-Faraday pair was used to act as a first-stage manual power controller. Power modulation was achieved using Pockels cells activated by a high-voltage driver. The Pockels cell was limited to 5 % modulation depth limited by the range of the high-voltage driver (±200 V). By connecting two in series the desired depth of 10 % modulation was achieved. A secondary waveplate was used for optimal polarisation matching with the Pockells cells.

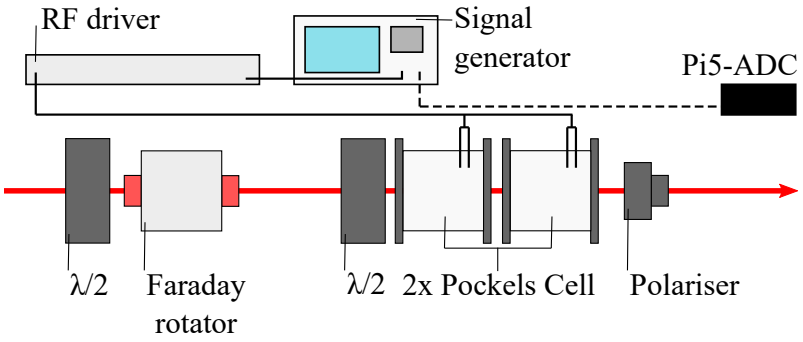


Figure 5.8: Half-wave plate and Faraday rotator used to protect the laser cavity from back-scatter. Modulation system consists of two Pockels cells connected to an HV-driver and signal generator. Pi5-ADC may be connected to generate custom time-signals.

5.4 Vacuum chamber integration

Many applications of optically levitated particles, be it high-intensity laser targets or levitated force sensors require low pressure conditions to isolate the levitated targets from their environment. This helps reduce external influence from affecting the experiment but can introduce additional challenges with loading and pressure dependent interactions with the trapping target. It is therefore highly desirable to demonstrate the feasibility of this system to achieve optical levitation at low pressure. A vacuum chamber was installed and a replica of the in-air levitation system was constructed inside. A rotary pump was used to pull vacuum. Mechanical valves at either ends of the piping connecting the pump to the chamber were used to isolate the pressure at their respective points in the system. At these points gauges were used to measure the local pressure. A release valve attached to the chamber was used to repressurise the chamber after use. A secondary release-intake value was installed for finer pressure control during live experiment or measurement.

The right-face port of the chamber seen in Fig. 5.9 used a semi-permanent flange fixture to access the internal optical system. The flange was was attached using removable 3-D

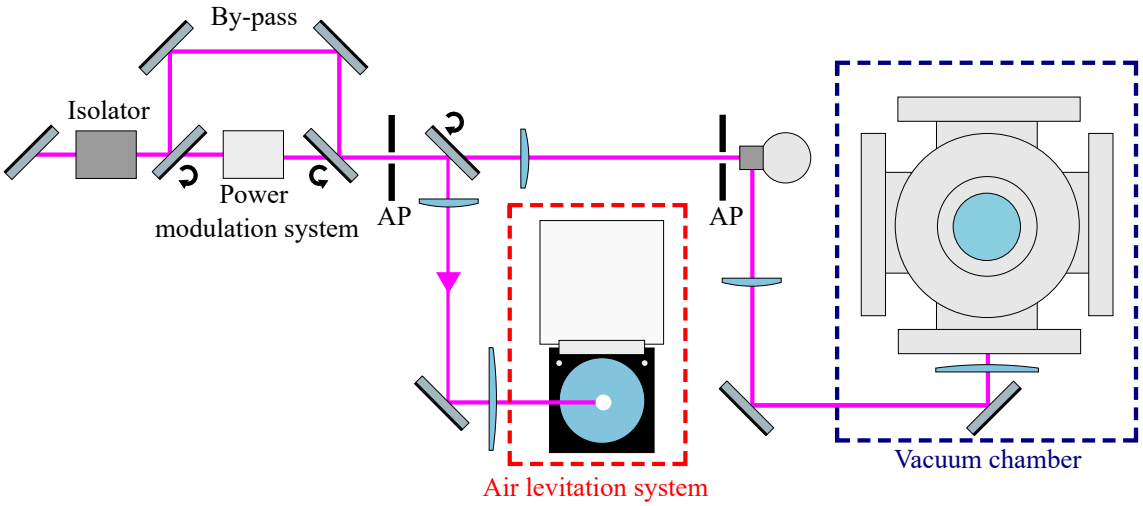


Figure 5.9: Beam delivery to the vacuum chamber levitation system. A by-pass was installed to avoid transmission lossed for when power modulation was not desired. The chamber was stationed on a portable optical bench. A periscope after the second AP was used to bring the beam to the appropriate level.

printed fixtures and a rubber-lip gasket provided sufficient sealing especially once negative pressure was applied. It was initially used as an access point to load the levitation system. However attachment of the flange after loading would often agitate the trap causing the shell to fall out due to mechanical disturbance. Instead a similar access point was created through the top-face port as this was less cumbersome to reattachement. All other ports were permanently sealed using copper gaskets created a knife-edge seal with their flanges. The chamber was tested to provide seals sufficient for pressures down to 0.1 Pa.

Beam delivery was through a flip mirror used to divert the beam away from the air levitation system as shown in Fig. 5.9, to the vacuum chamber. Although this meant the two systems could not operate simultaneously, each system was granted access to the full power of the OV source. The beam lines shared common components to enable power modulation capabilities. A beam by-pass was installed to avoid transmission losses for when constant power operation was desired instead. Apertures (AP) were put in place to maintain common beam alignment of both systems. A corrective collimation lens was used to minimise divergence over the additional propagation distance. A separate 10x telescope was used for beam expansion. A vertically tilted elliptical mirror was used to feed the beam into the chamber coupled through a viewing window. Two additional viewing windows on the front and rear faces allow access for diagnostics which were mounted onto raised platforms.

5.5 Imaging system

Once the levitation system is successfully loaded with a shell, the imaging system is used to produce a live video feed to observe the trapped shell in real time. This is extremely useful for slow dynamics measurement but was unable to capture faster that 20 Hz. Fig. 5.10(a)

illustrates the initial imaging setup used in the in-air levitation system. It consists of a 633 nm HeNe back illumination and a microscope-camera fitted with a bandpass filter to prevent unwanted signal affecting the image. The trapped microsphere, when in line-of-sight of the microscope objective, casts a shadow onto the illuminated camera sensor. The microsphere is identified by its silhouette. The magnification of the imaging system is calibrated using known distances so that is can be used to make size and slow (<10 Hz) spatial measurements. The position measurements are useful where there is slow drift perpendicular to the illumination axis due to laser power or pressure variation.

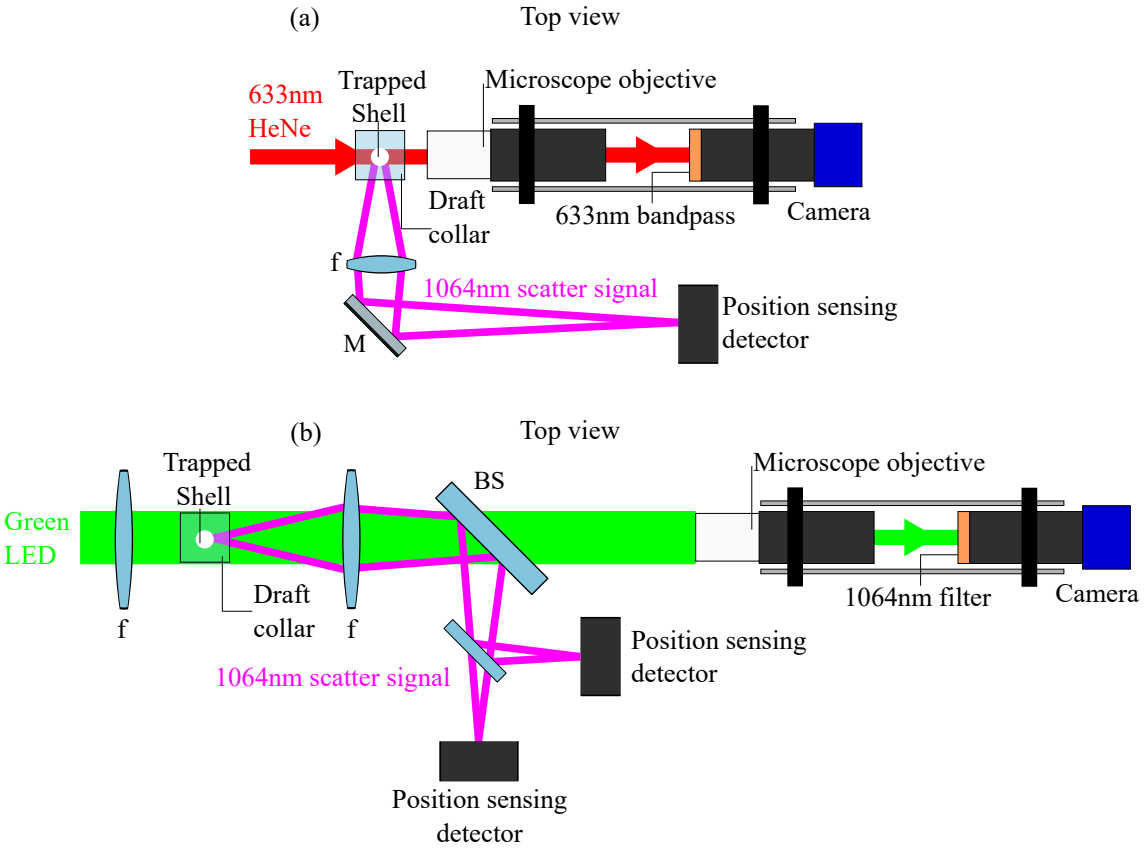


Figure 5.10: (a) Top view schematic of the trapping diagnostics consisting of a Red HeNe back illumination source, microscope objective and camera fitted with a 633 nm bandpass filter. (b) shows similar for an incoherent green LED illumination source.

Illumination source

The use of the HeNe as an illumination source provided good brightness and contrast to identify microspheres against the background when in focus, but suffered severely from speckle interference. The high coherence of the laser light diffracting off impurities that would eventually build up on the inside faces of the draft collar was detrimental to the quality of images produced. The strong similarlity between the speckle background and a defocussed trapped microsphere was particularly problematic when trying to locate the correct image-plane for the first time using a camera that is initially off-plane. It was not practical to clean the draft collar consistantly to the level require to mitigate this. However

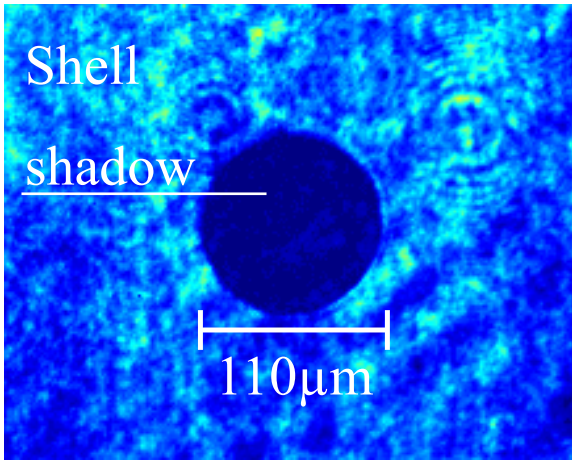


Figure 5.11: Image of microsphere (diameter = 110 µm) taken using the HeNe back-illuminated diagnostics microscope. Inhomogeneous background due to speckle interference

once in focus, the contrast was sufficient to distinguish the shell from the background. An example of this is shown in Fig. 5.11.

The image quality could be improved by removing coherence, achieved through the use of an LED as the illumination source. Fig. 5.10(b) illustrates the second iteration of the imaging setup. This layout was used once the levitation system was moved to the vacuum chamber. Although not to scale, the relocation came with some constraints in footprint and viewing angles limitation which is accounted for in the arrangement of the microscope and position sensor signals lines.

The LED was driven using a 2V USB connection. Due to its large divergence, 2-inch collecting optics were required to captupre and collimate (or focus) the light. The divergence could be somewhat reduced by lapping the plastic end-cap off the LED flat. However, like the two new heads of a Hydra that replaces the one severed, the coherence was removed but the lens system ended up imprinting the structure of the diode emitter into the beam profile such that the background was still structured and very much visible. Some parts in fact worsening the image quality. Such can be the nature of experimental work and attempts to resolve seemingly mundane problems. Regions of uniform intensity could still be found but required expansion of the beam and required a turning mirror to direct smooth regions of the expanded beam to illuminate the image at the cost of reduced brightness and overall contrast in the live-view. Fig. 5.12 shows a collection of these images. A fair bit of tunability could be achieved through LED beam size tuning at the trapping site, aberration reduction using the turning mirror and the smoothness of the illuminating region.

Image calibration

The imaging setup was calibrating using reference imaging of a wire of known width and comparing its size in the image plane. This is shown in Fig. 5.13 which was used to

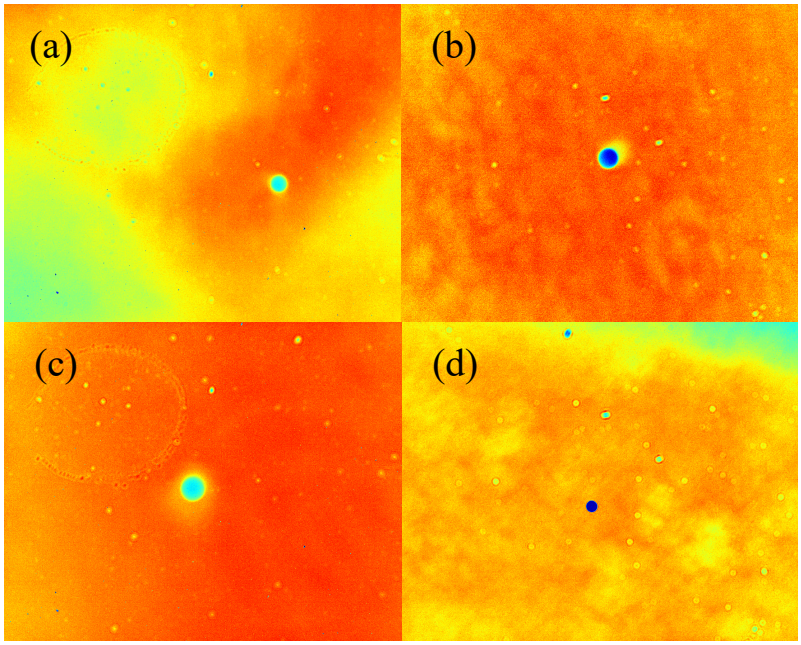


Figure 5.12: Collage of microsphere imaged produced using LED back-illumination. (a) Poor image contrast (b) Aberration in shell image due to misalignment of delivery lenses with microscope (c) Smooth background but weak contrast (d) High contrast.

calibrate the setup in Fig. 5.10(b). A wire is of thickness 0.6 mm measured using electronic calipers. From Fig. 5.13(b) we see the wire is 4.43 mm wide on the sensor. This gives a true magnification of 4.43 times. A CinCam Nano-RT CMOS sensor is used that has a pixel size of 5.3 µm. With this magnification we can expect to resolve features on the order of 1.2 µm in the object plane which is sufficient for the size range of our microsphere sample.

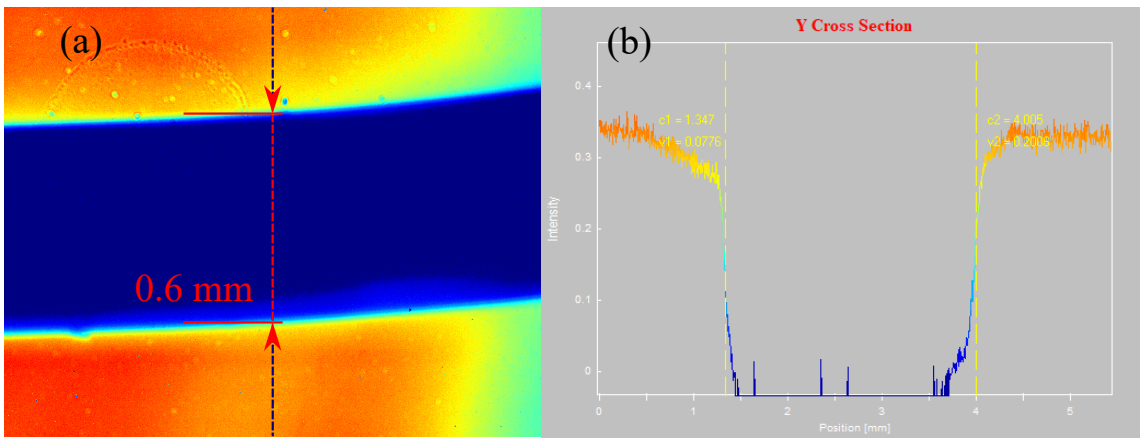


Figure 5.13: (a) Back illuminated image of wire ($d = 0.6$ mm). (b) Intensity cross-section used to calibrate magnification.

5.6 2-D position detector

We now pivot our focus to the position sensors which were intentionally neglected in the last section as they require a dedicated section to themselves. The trapped microspheres produce a strong scattering of the 1064 nm trapping beam due to their highly reflective surface coating. We can approximate the signal to be point-like and so use it as an indicator of the microsphere's position using biased photodiode sensors. With appropriate signal normalisation the centre-of-mass of the bright source is treated as the true position of the target which we can track in a 2D-plane perpendicular to line-of-sight. This allows us to track its position inside the trap and apply metrics to stability measurements and the magnitude of these displacements. Relating this to its use case as a firing target for ultra-high power laser systems, it is of paramount importance to know the location of its target or the amount by which it has been displaced, if at all, to the order of the laser spot-size - around 10 µm. Otherwise, we risk missing the target. This can be not only costly in physical resources powering the system but also in time, as such systems may only be able to fire a few shots a day spaced by lengthy cool-off periods.

We can collect the scatter signal and image it onto a position detector (PD). These are voltage biased photodiodes that generate a voltage differential based on the location of the signal's focal spot on the active region. As you can see between Figs. 5.10(a) and (b) two PD configurations are used. We will now elaborate on their use here.

5.6.1 Thorlabs PDP90A Lateral effect sensor

The first of the setups as shown in Fig. 5.10(a) makes use of a single PD in the form of a Thorlabs PDP90A Lateral effect sensor. This is a 2D sensor capable of simultaneous x-y position data handling. The active sensor region proportionally distributes the photocurrent generated by the signal using a single resistive layer with four anodes corresponding to the $\pm x, \pm y$ regions of lengths L_x and L_y, and share a common cathode to generate the bias. The PD signal differentials and SUM channels are calculated as,

$$\Delta x = (A+D)-(B+C)$$
$$\Delta y = (A+B)-(C+D)$$
$$SUM = (A+B+C+D)$$

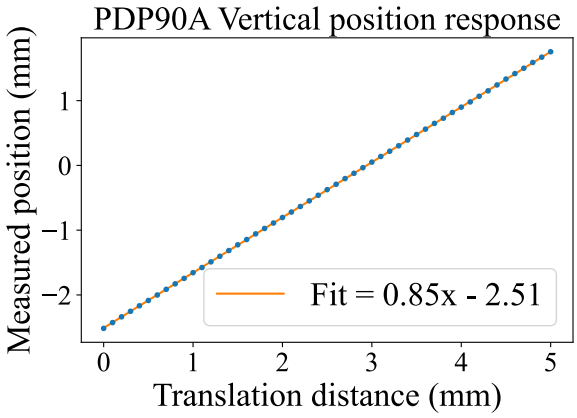
The true position must be normalised to the SUM channel accounting for the length of the sensor.

$$x = \frac{L_x \Delta x}{2SUM} \tag{5.1}$$
$$y = \frac{L_y \Delta y}{2SUM} \tag{5.2}$$

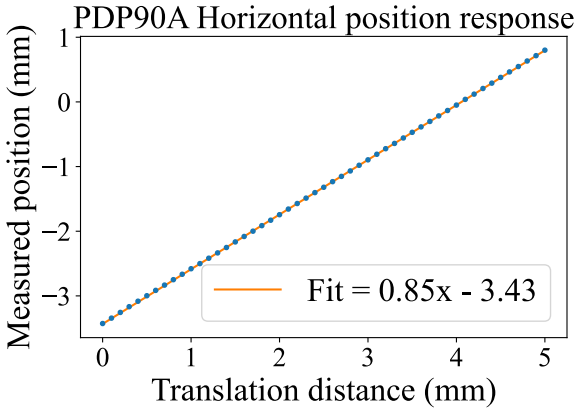
The PDP90A was used in tandem with the Thorlabs KPA101 K-Cube. Typically this

pairing would be used to measure small position changes detected by the PD and fed into the K-cube to drive a corrective response to align components such as a motorised mirror stage. Instead we fed the output of the K-cube directly into a connected oscilloscope to record the position-time signal produced by the PD.

The electrical response of the PD may become non-linear towards the extremes of the active region as neighbouring anodes approach one another. This can be problematic for position sensing where large non-linearities can negatively affect the accuracy of the measurements leading to unreliable results. This was measured by scanning a small spot produced by a HeNe laser across the sensor's active region and recording the position output. Data for both the vertical and horizontal axis are shown in Fig. 5.14



(a)



(b)

Figure 5.14: Measured position along the (a) vertical and (b) horizontal axes shows a linear response scorss the full length of the sensor.

We found the responses to in fact be linear across the length of the sensor. The total length quoted in its documentation is state to be 10 mm, but only an edge-to-edge distance of 5 mm was translated which concides with the linear response region. The zero on the y-axis denotes the center of the sensor along the respective axes. The offset is not important as the position measurements are relative not absolute. Additionally the plots serve a secondary purpose in calibrating the measured position to the known translation distance. The translation distance was determined using a micrometer stage onto which the sensor

was mounted. In both cases the position was underestimated by 15 % of its true value.

The PDP90A is a rated to a bandwidth of 15 kHz. The frequency response of the sensor was characterised by conducting a frequency sweep of the sensor using an LED for flat illumination, connected to a signal generator. The oscilloscope for readout was operated at 125 kHz as before so to negate the effect of poor sampling affecting the characterisation. The result is shown in Fig. 5.15.

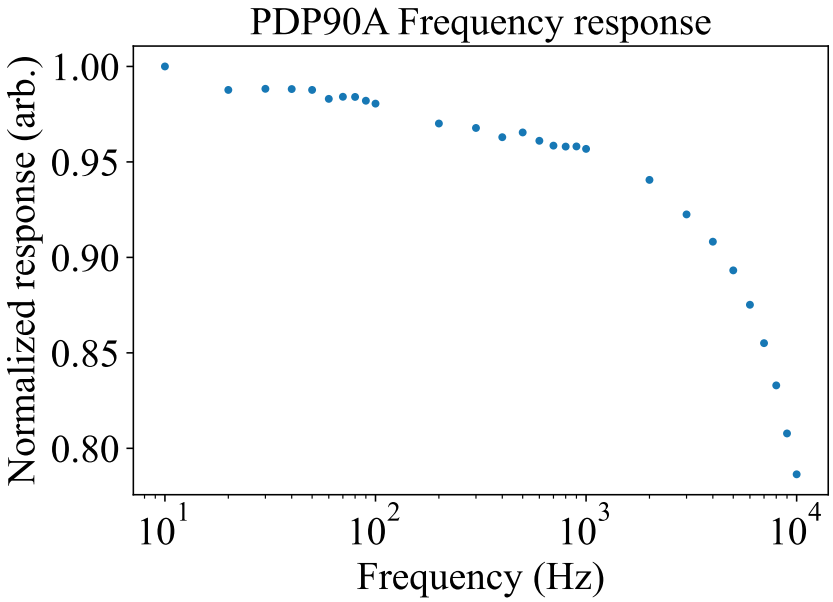


Figure 5.15: Frequency response of PRP90A sensor for frequencies between 10 Hz to 10 kHz

The response begins to drop-off with increasing frequency which is expected, however this is only a 20 % drop over the tested range and confirms its rated performance up to 10 kHz. The full range up to 15 kHz was not tested for two reasons. The first being the upper limit far exceeds the frequency sensitivity for our purpose. Trapped shell dynamics were expected to be <1 kHz. Secondly the range of the PDP90A was intended to be tested against a second, in-house built, position sensor. An upper limit common to both sensors was imposed.

The Thorlabs PDP90A offers an off-the-shelf position sensing solution but requires additional hardware in the form of the K-cube to digitise its analogue signal and an oscilloscope for signal readout and data export. Integrating this system into our intended application case however comes with a number of drawbacks. Due to the required proximity of the sensors to the high-energy targets, this system will be highly susceptible to electronic disturbances from intense electro-magnetic pulses and charged radiation that will potentially damage the internal electronics. The cost of replacement for each experiment will quickly add up. Instead we can opt for a low-cost and disposable solution in the form of in-house built PDs using inexpensive components that can easily be replaced.

5.7 1-D position detector

For the remainder of the thesis all results presented will be of those collected using the in-house built 1-dimensional position detectors. These detectors were designed and built by our collaborator Prof. Roland Smith, with my contributions in the experimental testing and characterisation. The system consists of a single Hamamatsu S4584-06 based sensor head - which includes a low-noise transimpedence and voltage gain stages - interfaced with an AB Electronics Raspberry Pi5 minicomputer connected to a 12-bit ADC board as the operating module. These are duplicated where 2-D position sensing is required with the second sensor head fitted orthogonal to the first. The development of this system was an iterative processes with incremental improvements in hardware electronics and operational software tools. This section will highlight some key developmental stages and system characterisation.

5.7.1 Electrical response of PD system

Multiple identical copies of the sensor heads and ADC-Pi modules were constructed for various operational and developmental tasks. For example two copies were made for experimental x-y position sensing while additional copies were made for various undergraduate projects and further development. We assume the copies to be near identical in performance and so only one set of each characterisation is presented.

Sensor head

The sensors heads are 1-dimensional in that they are limited to measuring position change only along a single spatial axis at a time. The advantage here being increased speed and lower complexity for feedback control along the vertical axis where most instabilities occurs. The sensor itself is a single 3.5 mm Silicon photodiode with a resistive layer that forms the active region. A pair of output anodes are stationed at either end for signal readout with a common cathode producing the bias. Electric charge is generated when a spot of light strikes the sensor and is extracted by the anodes as a photocurrent. The photocurrent is divided inversely proportional to the distance to each anode. The position of the spot on the sensor is calculated based on the portion of the signal at each anode over the total photocurrent accross the sensor. When a spot is centered on the sensor the signal is zero. The position would then be calculated as follows,

$$x = \frac{L}{2} \times \frac{I_2 - I_1}{I_2 + I_2} = \frac{L}{2} \times \frac{V_2 - V_1}{V_2 + V_1} \tag{5.3}$$

However the current to voltage conversion has non-ideal effects relating to the operation of the transimpedance amplifier that converts the photocurrent to a voltage. It has a maximum output of V_{max} when the sensor is saturated and a constant offset V_{min} corresponding to minimum output such that $V_{1,2} = V_{max} - I_{1,2}G + V_{min}$ for gain, G. The

position calculation is modified to,

$$x = \frac{L}{2} \times \frac{(V_{max} + V_{min} - V_2) - (V_{max} + V_{min} - V_1)}{(V_{max} + V_{min} - V_2) + (V_{max} + V_{min} - V_1)}$$

$$x = \frac{L}{2} \times \frac{V_2 - V_1}{V_1 + V_2 - 2(V_{max} + V_{min})} \tag{5.4}$$

The position response of the 1D-PD is shown in Fig. 5.16. We see a slight improvement compared to the PDP90A in the measured position which is off (overestimated) by 13 %. The performance is slightly non-linear with an S-shaped response curve and deviations at the sensor edges. However these features are small and so should not significantly affect the reliability of its measurements. The flats at the extremes of the plot is signal fall off as the HeNe spot translation exceed the length of the sensor. The corresponding position measured here is due to background offset.

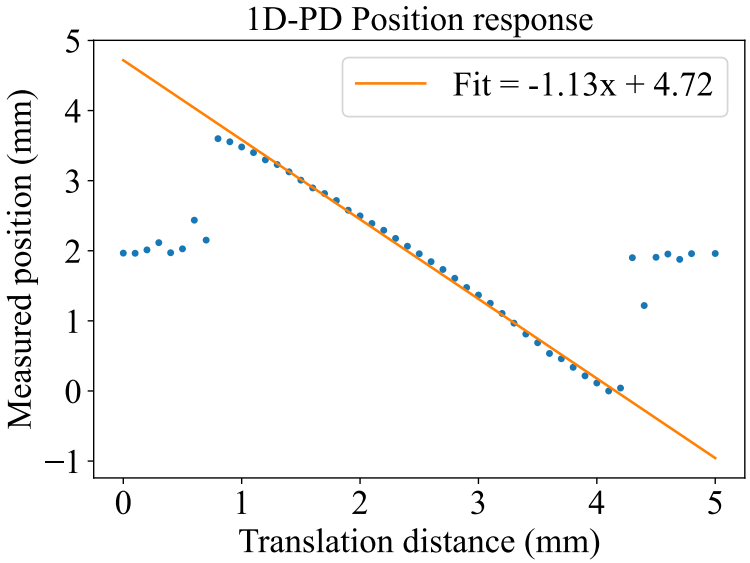


Figure 5.16: Frequency response of PRP90A sensor for frequencies between 10 Hz to 10 kHz

Integrated ADC-Pi module and sensor head

The 1D-PD runs off an AB Electronic ADC-Pi 5 module responsible for the digitisation of the analogue PD signal and hosting the Linux based operating system. Data acquisition routines are initiated in Python.

The Hamamatsu S4584-06 is rated to have a rise time of 5 µs (200 kHz). This is significantly faster than the run speed of the Python code which presents a bottleneck in performance based on the complexity of the Python routines. Simple ADC-channel readout was found to run at ≈ 14 kHz however this is reduced by approximately half when implementing active position feedback routines. We characterise the frequency response by again conducting a frequency sweep and recording the response. The response curves of the ADC-Pi5 with and without feedback routines are shown in Fig. 5.17. This was repeated for the ADC-Pi5

with version 14 of the PD sensor head to characterise the complete integrated system. Since the PD speed is an order of magnitude faster, adding its contribution should have negligible effect as is shown. The fitting of these curves will be discussed in the following section

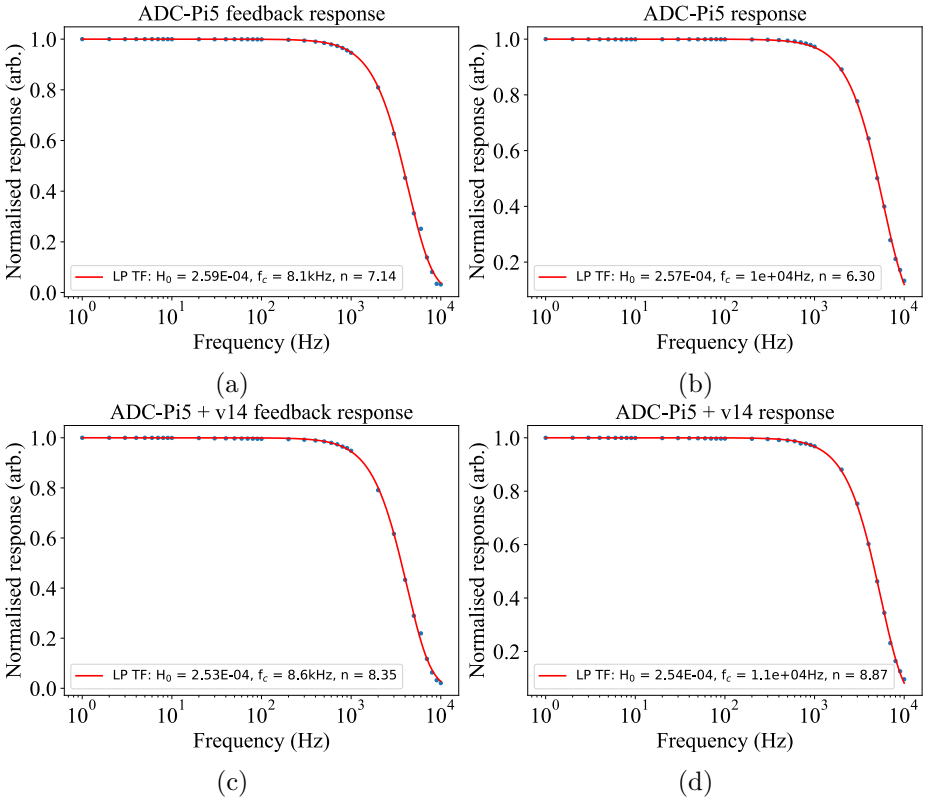


Figure 5.17: Frequency response of ADC-Pi5 (a) with and (b) without active feedback routine and ADC-Pi5 with the v14 PD sensor head (c) with (d) and without active feedback routine.

Low-pass transfer function

The circuit diagram of the position sensing system is shown in Fig. 5.18. It forms an RC circuit with frequency dependant transmission of the electronic signal produced by the PD. RC circuits are commonly used as electronic spectral filters due to the impedance response of the capacitors depending on whether they are connected in series or parallel to the input signal, corresponding to high-pass or low-pass filtering respectively. We can tell Fig. 5.18 forms a low-pass filter from the responses shown in Fig. 5.17. Lower frequencies are shown to pass with little to no attenuation and the attenuation of the signal grows with increasing frequency past resonance f_c. We can relate the output signal to the input via a transfer function H where,

$$H(\omega) = \frac{V_{out}}{V_{in}} \tag{5.5}$$

The transfer function of the low-pass filter is,

$$H(\omega) = \frac{1}{1 + i\omega RC} \tag{5.6}$$

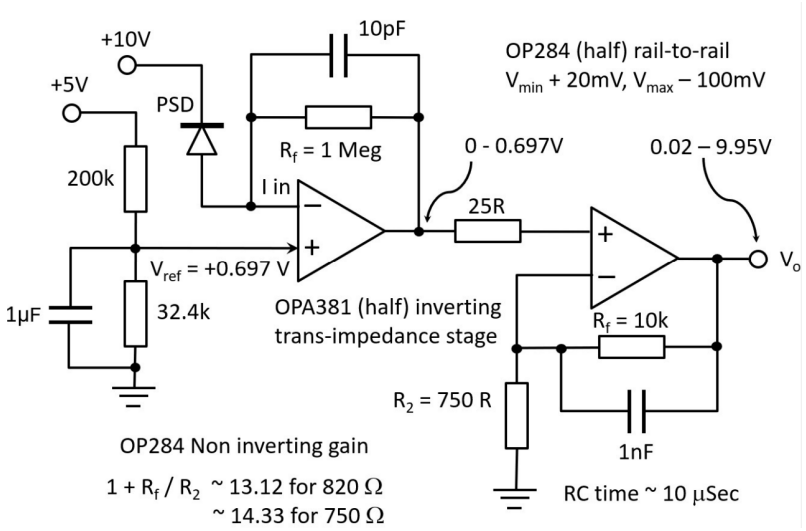


Figure 5.18: Circuit diagram of the position sensing PSD head showing the sensor, transimpedance and voltage amplification stages with integrated RC filters for high frequency noise reduction.

for resistance R and capacitance C and signal frequency $\omega = 2\pi f$. When the number of RC components increases with n, the form of the transfer function grows exponentially as,

$$H(\omega) = \frac{1}{(1+i\omega RC)^n} \Rightarrow H(f) = \frac{1}{(1+f/f_c)^n} \tag{5.7}$$

$fc = 1/2\pi RC$ is the cut-off frequency. The cut-off frequency is defined as the -3 dB point i.e. when the signal amplitude falls by $1/\sqrt{2}$ of its reference value. Higher frequencies beyond this point are then reduced by 20n dB per decade. Due to the residual capacitance stored within the circuit components in addition to the RC components themselves is it difficult to precisely account for the combined effects. The general case in Eq. 5.7 was used to approximate the behaviour of an n^{th}-order low pass filter.

We notice the frequencies in Fig. 5.17 begin to fall-off just beyond 1 kHz in all cases, however the fits predict the cut-off frequency to be between 8-10 kHz which is contradictory to the -3 dB point defined earlier. This is possibly a symptom of the non-ideal RC behaviour of the ADC-Pi5 units that isn't accounted for by Eq. 5.7. To explore this further direct measurements of the capacitance and resistances of the circuitry components may be taken to better characterise its RC behaviour. However this may be tedious if all that we require is the general effect it has on the output.

The purpose of plotting the response curves in Fig. 5.17 and the subsequent fit of Eq. 5.7 was two-fold. First, it was used to characterise the frequency sensitivity of the detection system. If the sensitivity range did not fully cover the experimental data range, particularly the frequencies in which we expect shell dynamics to occur, then the detection system would be deemed unsuitable and require further tuning. Secondly, if the filtering effects did attenuate frequencies of interest then a reliable fit to predict the response of the system could be used to scale the data accordingly so to remove the appearance of

weaker components.

5.7.2 Asynchronous data aquisition

Data was collected at fixed sampling frequencies, f_s, determined by the operating speed of the Pi5-ADC module. What could vary was the number of samples taken within a particular acquisition run and set by user input before initiation. Due to the on-going development of the Pi5-ADC units and improvements in data aquisition efficiency sampling time interval, Δt would improve. However, the ADC used for this proof-of-principles work was found to have asynchronous channel readout from the sensor head which resulted in irregularly spaced time intervals between measurements. This was eventually resolved by implementing a time-interpolated correction so that data points were time stamped on capture and were then regularly spaced using a linear interpolation routine for constant Δt. This emulates synchronous channel readout with a slight discrepancy in the expected sampling interval but still preserves the total measurement duration.

5.7.3 Spatial noise

A homogeneous illumination source shone on to the sensor's active region should in principle generate equal signal at both channel readout anodes resulting in a position detection of zero. In reality the electronics are non-idealised and so the split in signal delivered to each anode is slightly unbalanced resulting in a non-zero position measurement. This is not of major concern as the position measurements are relative, not absolute, and so we can redefine the "zero" of the position measurement scale accordingly. There is also some variation associated with the measurement due to background illumination noise, and electronic noise. We define as the positional noise of the system as the combined effect of these sources, and use it to define the lower limit in positional stability we can reliably measure.

We can construct a noise picture by isolating key components and noise contributions to characterise the spatial sensitivity of the sensing system. A DC voltage supplied to the ADC using a high-stability NiCd battery pack with voltage-reference chip to reveal the electronic imbalance in the presence of a constant signal. We then begin to replicate experimental conditions through the introduction of the sensor head. We firstly take a dark field exposure to record the thermal response of the sensor head. Then a flat illumination source such as an LED is used to isolate the signal balance between the anodes across the photosensitive region. The connected signal generator then replicates the signal detected from an oscillating body. The final stage is to introduce noise due to the trapping beam. The beam is directed to a stationary target so that signal fluctuations here are dominated by power variation in the laser output. These results are summarised in Fig. 5.19

The noise threshold helps determine the minimum signal level detectable by the sensor head which sets a lower bound for the smallest change in microshell position that can be measured with confidence. The base-level response of the system in the absence of

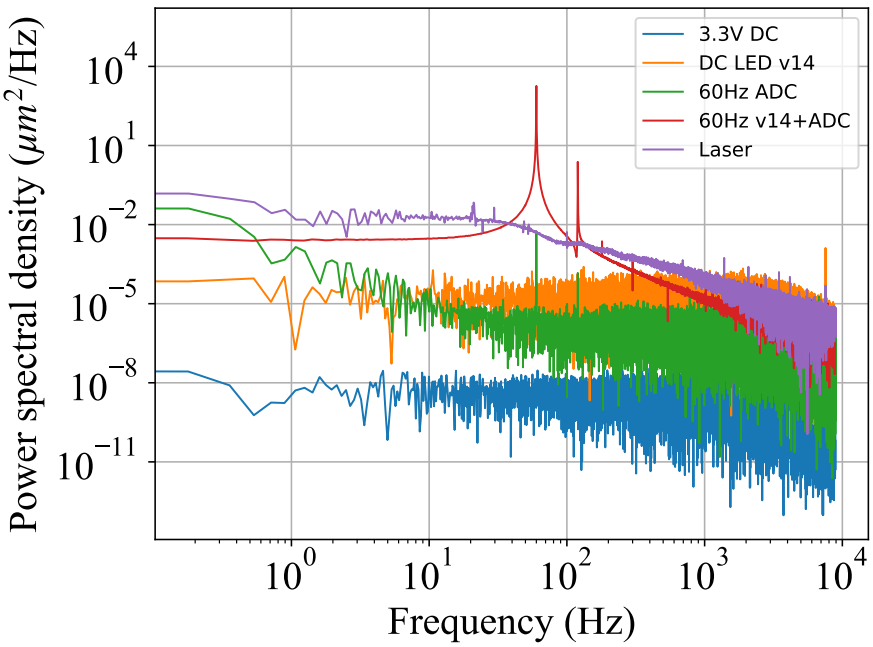


Figure 5.19: Noise characterisation of various signal types fed into the ADC and ADC+v14 sensor head. The response of the ADC was directly measured by firstly passing a DC voltage signal using a low-noise 3.3 battery. This characterises the noise associated with an unchanging signal (blue). Then the noise response of a time varying signal was characterised by producing a fixed 60 Hz sine-wave using a signal generator and passing it directly into the ADC (green). Similar was done with the ADC+v14 sensor head where the voltage sources were connected to an LED. This replicated the steady (orange) and time varying (red) brightness response of the sensing system. Finally the noise associates with fluctuations in the laser power was recorded (purple).

microshell scatter signal is referred to as the noise-floor. It is comprised of contributions from the sensor-head that itself may suffer from shot noise and thermal noise, electronic noise from the ADC and amplifier stages, and other environmental sources such as surrounding temperature, external vibrations and electromagnetic interference from nearby electronics.

This system is our first iteration of a fully operational optical system from source to end-target, granting our group new capabilities in optical vortex levitation. Improvements in beam delivery, power augmentation and end-target diagnostics were made from the ground up and as we progress through this chapter we will see how some of these stages were altered or modified to accommodate improvements in performance and functionality. We hope access to watt-level OV power made available thanks to the laser source development described in previous chapters encourages further exploration of vortex beam trapping and levitation.

Chapter 6

Levitation optomechanics

6.1 Introduction

Advancements in structured light generation within recent decades has given way to optical manipulation and trapping adopting the use of exotic beam geometries [109]. Unique access to orbital angular momentum and geometric intensity profiles provides an extra degree of freedom to probe new interactions [110, 22, 111]. Optical trapping is typically performed using fundamental TEM_{00} mode Gaussian beams due to their prevalence in access and simplicity in setup. However, as we have now demonstrated, laser systems operating on the fundamental TEM00 mode can be easily modified to enable OV production through the use of the WPSI as a VOC. The radiative force due to a single beam TEM_{00} Gaussian beam is limited to only trap transmissive dielectric targets that are continuous in medium, whereas annular beams such as those found in the Laguerre-Gaussian family when $p = 0$, permit the additional use of opaque materials and hollow or layered internal structures granting flexibility in target material and composition.

The mechanism for optical trapping and levitation can vary significantly depending on the target's properties, beam geometry and environmental parameters. The mechanics of optical trapping is well established as advances over the past 30 years have extensively documented the trapping of objects scaling across several orders of magnitude in size - from microbeads and biological cells to objects in the nano and atomic scale. Of course, the work presented in this thesis most closely relates to the former, in terms of target size and optical force models. However, even here, further distinctions can be made based on the trapping medium - whether in viscous fluid or vacuum; target material properties - whether transmissive, absorbing or reflective; and the properties of the trapping beam when considering other manipulation effects such as OAM transfer. The particular case of trapping large reflective hollow spheres using a single annular beam presents a peculiar combination of experimental parameters that is seldom seen in the literature. This chapter aims to compile methodologies for calculating optical forces acting on reflective targets in the ray optics regime and that best describe the trapping dynamics of our system. The

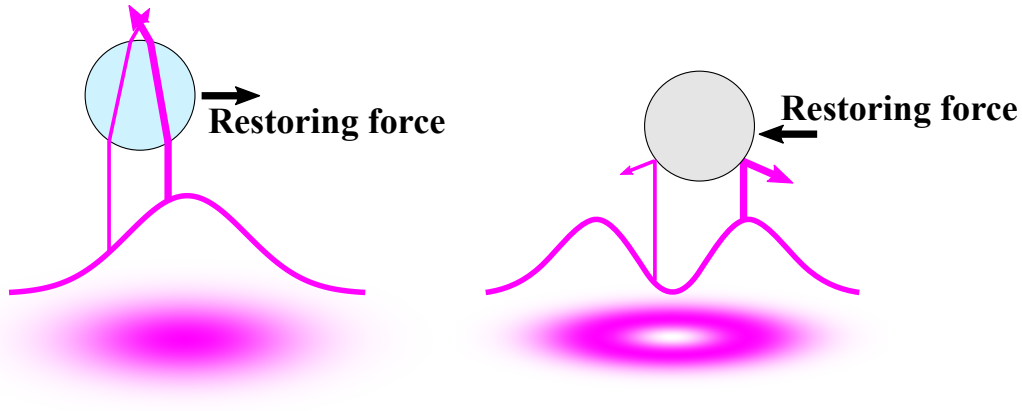


Figure 6.1: (Left) Transmissive target trapped in a Gaussian beam with an attractive restoring force acting to pull the target towards the beam center. (Right) Reflective target held in an annular beam. Reflected rays produce a repulsive force away from the bright ring perimeter. The target is held in the intensity minimum at the beam center.

purpose of this is to document our understanding of optical trapping and levitation to be used as a point of reference for future work.

6.2 Optical trapping mechanisms

A target can be trapped in an optical field with the appropriate treatment of the optical force interactions - the particulars of which depend on the scattering regime which best describes the light-particle interactions. Here we will discuss the different scattering regimes relevant to optical trapping.

Mesoscopic targets that are smaller than the trapping wavelength ($d << \lambda$), can be treated in the Rayleigh regime. Here the target acts as a polarisable object exhibiting a dipole response to an external field. The force acting on the target is the sum of the primary contributions - a conservative dipole force and a dissipative scattering force. The dipole force is due to the target's polarisability and its interaction with the intensity distribution of the optical field. It is sometimes referred to as the gradient force in reference to the gradient in the external field intensity. The scattering force accounts for radiation pressure and is due to the target index and scattering cross-section. These contributions must be balanced for stable trapping to occur. The sign of the dipole force i.e. whether it is attractive or repulsive to the intensity maximum region is determined by the detuning of the optical field in relative to the target fluorescence transition. Assuming an external Gaussian field with an intensity seeking dipole, red detuning is to be used.

As the trapping target size approaches the optical wavelength ($d \sim \lambda$) the treatment becomes non-trival. The approach requires Lorenz-Mie theory to solve Maxwell's equations with appropriate boundary conditions describing the target geometry and the associated light-particle interactions. When the trapping target size exceeds the trapping wavelength ($d >> \lambda$) the ray optics approximation suffices. As shown in Fig. 6.1 a transparent di-

electric target will experience forces dominated by the deflection of refracted rays through its medium which diminishes in strength moving radially from the optical axis. As the intensity is greatest at the beam center the intensity gradient provides an attractive mechanism to correct radial drift in the target's position. Minor reflective forces dependant on the index of the medium will oppose this. When combined with a tight focus, axial drift can be minimised, and the target can be trapped in 3-dimensional space [112]. Optical levitation is achieved by constructing such a system where the optical forces acting on the target in the axial direction counter the downwards force of gravity [113, 114, 91].

Annular beam trapping offers an intriguing alternative to traditional Gaussian beam trapping. The ring-like intensity profile of an annular beam such as LG_{0l} modes necessitates an intensity minimum due to the helical phase being undefined at its center. In the dipole approximation this leads to the realization of dark field trapping under blue detuning where targets actively seeking local intensity minima are guided to the beam center [115, 116]. This method benefits from reduced photon scattering due to the weaker interaction strength. The OAM states of LG modes also allows for unique manipulation states [117, 118]. Although this regime is out of scope, a thorough review of optical trapping using OV light can be found in Ref. [119]. Larger micron-sizes targets of lower index to their surroundings can sit in the intensity minimum of an annular beam for optical trapping as shown in Fig. 6.1. Detuning is not neccassary here due to the ray optics approximation being applied. Optical scattering forces due to reflection oppose the downward inertial forces. The gradient force for reflective targets is repulsive and acts to push targets away from the high intensity ring to the stable intensity minimum at the beam center. The reduced intensity here may be appealing for biological applications, for example, where under Gaussian illumination, the harsh intensity at best focus can be damaging to test samples [120, 121]. Additionally, annular beam trapping has shown to enhance axial trapping efficiency [122, 123, 124]. Ref. [125] reports the LG_{01} mode in particular exerts the greatest trapping force at all powers tested, when comparing the $l = 0 - 3$ states. The use of an OV beam also includes interactions through its OAM state. OAM transfer to absorbing (including weakly absorbing) targets has been observed [126, 127] leading to the realisation of the optical spanner [128, 110, 129].

6.3 Ray optics force model

In this section we derive the radiative force active on a reflective spherical target illuminated by an incident LG_{01} beam. The approach is based on work presented in Ref. [130] but with adaptations suited for a highly reflective target. A ray-optics interaction regime is employed. The target size is sufficiently large as compared to the trapping beam wavelength and so, does not need to consider wave-like interactions such as interference, diffraction and polarisation effects. Due to the metallic surface coating, we assume the absence of field propagation interior to the microshells. The following approach is well suited to account for beam divergence and arbitrary beam intensity profiles, however the vector

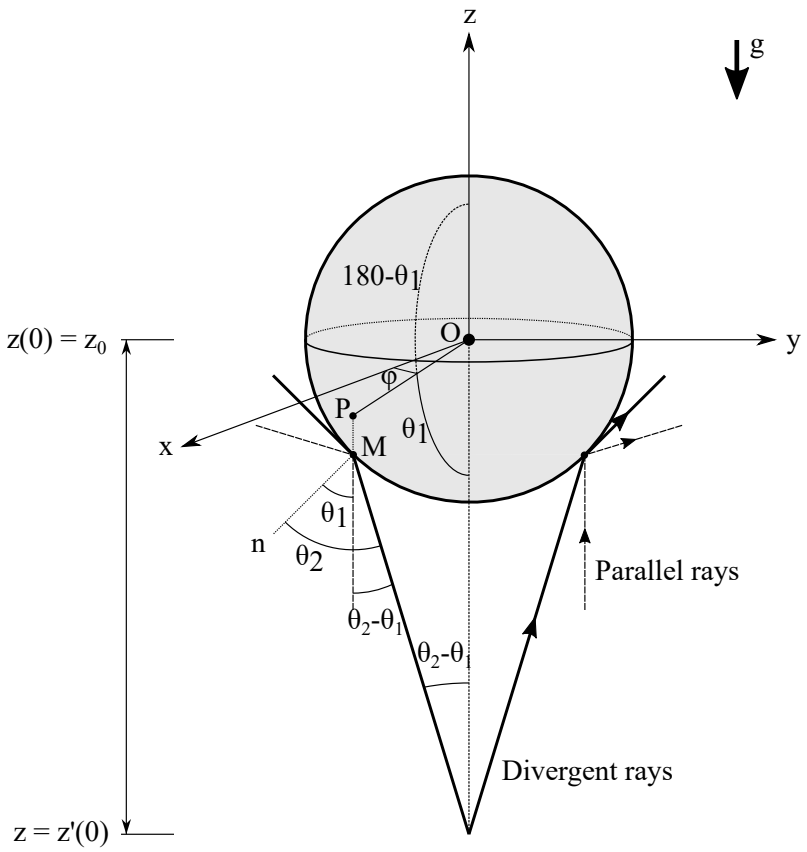


Figure 6.2: Ray picture of scattering of light incident at M on shell located at origin O. Azimuthal angle ϕ is measured from x to when it meets For rays parallel to $+z$ incident at point M, the incidence and reflection angle are $\theta_i = \theta_r = \theta_1$ relative to the surface normal, n. P is the projection of M onto the $xy-$plane. Since M is located on the lower hemisphere, its spherical coordinates are defined as $(r, \phi, 180 - \theta_1)$ for θ taken relative to the $+z$ axis. For divergent rays incident at P, we have $\theta_i = \theta_2$ to the normal. The divergence half-angle is $\theta_2 - \theta_1$

expressions increase in complexity if left generalised. For purposes of clarity and to stay relevant to our aims we will only consider those pertaining to incident plane waves and an LG_{01} profile.

We begin by describing the optical interaction at the shell target's air-surface interface using Snell's law. A ray diagram illustrating scattering off the surface is depicted in Fig. 6.2. A spherical shell of radius ρ, is stationed at the origin of the (x, y, z) coordinate space. An incoming ray originating from $z = z'(0)$, the coordinate of the beam waist relative to the shell center O, is shown to be incident at point M. It is reflected at an angle, θ_r, equal to twice its entry angle, θ_i i.e. $\theta_r = \theta_i$ relative to the surface normal $\hat{n}$. The transmission angle of light passing through the interface relative to the normal is given by Eq. 6.1, where $n_1 \approx 1$ is the refractive index of air. Transmission through opaque

media is often neglected as the field sees an exponential decay of the surface intensity parameterised by κ, the optical extinction coefficient. The refractive index of the silver coating is therefore complex due to the attenuation term and takes the form $n_{Ag} = n_r + i\kappa$ where its real component is denoted n_r. We will use $n_{Ag} = 0.04 + 7.62i$ for the refractive index when illuminated by light of wavelength $\lambda = 1064\,\text{nm}$ [108].

$$\theta_t = \sin^{-1}\left(\frac{n_1 \sin\theta_i}{n_s}\right) \tag{6.1}$$

The distance over which the field is attenuated is of interest in our case since we are dealing with thin-walled targets. We can calculate the penetration depth of the silver coating which is the distance over which the initial amplitude of the electromagnetic field at the surface falls by $1/e$. We find $\delta = \lambda/4\pi\kappa = 11\,\text{nm}$. This is an order of magnitude smaller than the expected thickness of the silver layer and so we can safely assume the transmitted component of the field to be negligible. To find the reflected component we employ the s- and p-polarised reflection coefficients for arbitrary incidence,

$$r_s = \frac{n_r \cos\theta_i - n_s \cos\theta_t}{n_r \cos\theta_i + n_s \cos\theta_t} \quad \text{and} \quad r_p = \frac{n_r \cos\theta_t - n_s \cos\theta_i}{n_r \cos\theta_t + n_s \cos\theta_i} \tag{6.2}$$

Then the reflectance is the mean square of these quantities,

$$R = \frac{|r_s|^2 + |r_p|^2}{2}. \tag{6.3}$$

Using the above information, we find the target to have a reflectance of $99.7\,\%$ at $\lambda = 1064\,\text{nm}$. For completeness, the absorption through $100\,\text{nm}$ of silver is $0.27\,\%$ of the total beam power. The transmission fraction is $4.34 \times 10^{-9}\,\%$ meaning the field that penetrates through is almost entirely absorbed.

We now proceed with the radiative force calculation. We assume the reflected light is scattered elastically. The force imparted on to the shell target can be expressed as the rate of change in its momentum.

$$F_{shell} = \frac{dp_{shell}}{dt} \tag{6.4}$$

Lets first consider the simple case of a single photon scattering event. Prior to scattering, the total momentum of the joint system is simply the single photon momentum,

$$\boldsymbol{p}_{\gamma i} = \hbar k \boldsymbol{v}_i \tag{6.5}$$

where $\hbar$ is the reduced plank's constant, k is the wave-number and $\boldsymbol{v}_i$ is the direction vector for the photon's propagation. We define $\boldsymbol{v}_r$ as the direction vector for the reflected photon and $\hat{\boldsymbol{n}}$ as the surface normal vector. Then reflection off the target's surface can be described in as follows,

$$\boldsymbol{v}_r = \boldsymbol{v}_i - 2(\boldsymbol{v}_i \cdot \hat{\boldsymbol{n}})\hat{\boldsymbol{n}} \tag{6.6}$$

For a generalised approach, an arbitrary incidence vector $\boldsymbol{v}_i = (v_{ix}\hat{\boldsymbol{x}} + v_{iy}\hat{\boldsymbol{y}} + v_{iz}\hat{\boldsymbol{z}})$ may be substituted appropriately. We use a tightly focused trapping beam propagating along $+z$ with a divergent light-cone expanding radially to the target. With this notation, the optical force is +ve and acts in the $+z$ direction in opposition to the weight of the target acting in the $-z$ direction. The surface normal of a sphere is $\boldsymbol{n} = r/\boldsymbol{r} = (\sin\theta\cos\phi\ \hat{x} + \sin\theta\sin\phi\ \hat{y} + \cos\theta\ \hat{z})$ which we use to get,

$$\boldsymbol{v}_r = -(\sin 2\theta\cos\phi\ \hat{x} + \sin 2\theta\sin\phi\ \hat{y} + \cos 2\theta\ \hat{z}). \tag{6.7}$$

Then the momentum of the reflected photon is the product of the momentum scalar and $\boldsymbol{v}_r$,

$$\boldsymbol{p}_{\gamma r} = -R(\theta)\hbar k(\sin 2\theta\cos\phi\ \hat{x} + \sin 2\theta\sin\phi\ \hat{y} + \cos 2\theta\ \hat{z}) \tag{6.8}$$

Note the $R(\theta)$ term is included to consider only the reflected photons imparting momentum transfer to the shell's surface. We can express the change in momentum of the photon, $\Delta\boldsymbol{p}_\gamma = \boldsymbol{p}_{\gamma r} - \boldsymbol{p}_{\gamma i}$ which gives,

$$\Delta\boldsymbol{p}_\gamma = -\hbar k(R(\theta)\sin 2\theta\cos\phi\ \hat{x} + R(\theta)\sin 2\theta\sin\phi\ \hat{y} + (R(\theta)\cos 2\theta + 1)\ \hat{z}). \tag{6.9}$$

The force acting on a small surface element dA due to a single stream of photons can be expressed in terms of the incidence rate $\frac{dN}{dt}$,

$$dF = \Delta p_\gamma \frac{dN}{dt} \tag{6.10}$$

We can define the flux of incident photons Φ such that $\frac{dN}{dt} = \Phi\cdot\hat{n}dA$. The total force is then,

$$F = \int_A \Delta p_\gamma \Phi\cdot\hat{n}dA \quad \text{where } \Phi\cdot\hat{n}dA = dP/E_\gamma, \quad dP = I(r)\cos\theta dA$$
$$F = \int_A I(r)\frac{\Delta p_\gamma}{E_\gamma}\cos\theta dA \tag{6.11}$$

$E_\gamma = \hbar\omega$ is the single photon energy. We can cancel the energy ($\hbar\omega$) and momentum ($\hbar k$) terms to give $1/c$. To correctly handle the sign of the expression, recall the incident photons are parallel to $+\hat{z}$ and so the lower pole of the sphere points in the direction of $-\hat{z}$. Since the azimuthal angle θ is taken from $+\hat{z}$ we note $\int_A dA = \int_0^{2\pi}\int_\pi^{pi/2} r^2\sin\theta d\theta d\phi = -\int_0^{2\pi}\int_\pi^{\pi/2} r^2\sin\theta d\theta d\phi$ which cancels the -ve sign in Δp_γ. We can write the integral form

of the total radiative force acting on the shell force in terms of its x, y and z components,

$$\begin{aligned} F_{rad} &= \int_A dF_{rad,x}\hat{\boldsymbol{x}} + dF_{rad,y}\hat{\boldsymbol{y}} + dF_{rad,z}\hat{\boldsymbol{z}}\ dA \\ F_{rad,x} &= \int_0^{2\pi}\int_0^{\pi/2} \frac{I(r)}{c}\cos\theta R(\theta)\sin 2\theta\cos\phi r^2\sin\theta\, d\theta\, d\phi \\ F_{rad,y} &= \int_0^{2\pi}\int_0^{\pi/2} \frac{I(r)}{c}\cos\theta R(\theta)\sin 2\theta\sin\phi r^2\sin\theta\, d\theta\, d\phi \\ F_{rad,z} &= \int_0^{2\pi}\int_0^{\pi/2} \frac{I(r)}{c}\cos\theta (R(\theta)\cos 2\theta - 1) r^2\sin\theta\, d\theta\, d\phi \end{aligned} \tag{6.12}$$

These expressions resemble results presented in Ref.[130] but differ in that we have only considered the reflective scattering components. As we saw in Chap. 2, the generalised electric field for of the LG modes is,

$$\begin{aligned} u_{pl}^{LG}(r,\phi,z) = C_{pl}\frac{w_0}{w(z)}\left(\frac{r\sqrt{2}}{w(z)}\right)^{|l|} L_p^{|l|}\left[\frac{2r^2}{w^2(z)}\right] \\ \times \exp\left(-\frac{r^2}{w^2(z)}\right)\exp\left(-ik\frac{r^2}{2R(z)}\right)e^{-il\phi}e^{i\psi(z)} \end{aligned} \tag{6.13}$$

Only the first-order LG mode is of relevance. Its intensity profile is simply the square of the field amplitude scaled by its power, P,

$$I_{01}(r,w) = \frac{2P}{\pi w^2}\left(\frac{2r^2}{w^2}\right)\exp\left(\frac{-2r^2}{w^2}\right). \tag{6.14}$$

6.4 Harmonic oscillator model

The dynamics of a levitated shell held within the optical potential of its trapping beam can be modeled as a damped driven harmonic oscillator. Stokes drag resists shell motion and is treated as the damping term dependant on the geometry of the shell and the pressure of the surrounding medium. Our experiments were initially conducted in air and so its corresponding viscous parameters are chosen. Changes in position are corrected by a restoring force applied by the potential to return the shell back to its equilibrium position. The system is driven by energy supplied by the thermal bath of the surrounding medium. Gaseous molecules colliding with the shell surface induce Brownian-like behaviour in the shell's motion, seen as random jitter in the shell's position. So long as these fluctuations are small, the system is believed to be harmonic.

This section will model the motion of a trapped shell in an optical trap. Its transformation to Fourier-space then reveals the frequency components of its oscillations. By identifying dominant spectral features such as the resonant frequency, we can characterise the behaviour of the shell while in the trap and parameterise properties of the trap itself such as its stiffness.

6.4.1 Mathematical prelude

In the parts following we employ a number of mathematical tricks (formally read theorems) to aid in our analysis. We will briefly introduce these here so to make later steps easier to follow.

Properties of the Fourier transform

The Fourier transform (FT) used to convert a continuous signal $x(t)$ into its reciprocal domain,

$$x(\omega) \equiv \frac{1}{\sqrt{2\pi}} \int_{-\infty}^{\infty} x(t) e^{-i\omega t}\, dt \tag{6.15}$$

This allow us to transform our time-series position data into a spectrum expressed in frequency space. The second is Parseval's theorem which equates the power spectra of the time and frequency domains. This is more so a necessary property of the Fourier transform so that the transformation is unitary. The integral of our initial function squared is equal to the integral of the square of its transform.

$$\int_{-\infty}^{\infty} |x(t)|^2 dt = \int_{-\infty}^{\infty} |x(\omega)|^2 d\omega \tag{6.16}$$

By equating these quantities its shows the total power in the system is conserved regardless of whether it is viewed in its original or reciprocal domains. If a signal is comprised of N components of increasing order then transforming the first M components of its reciprocal will yield the original signal accurate to the first M^{th}-order correction. This means a signal and be mostly reconstructed using its most dominant contributions. We can determine the power contributions of each component by calculating the power spectral density of the signal. For real signals we are only interested in the positive frequency components and so we define the one-sided power spectral density as follows,

$$S_x(\omega) = \lim_{t\to\infty} \frac{1}{t} 2|x(\omega)|^2 \tag{6.17}$$

A function $X(t)$ is said to be a wide-sense stationary process (WSS) when it is stochastic such as in Brownian motion, its mean is zero and auto-correlation is time invariant. The power spectral density $S_X(\omega)$ of such a process, and its auto-correlation function, $R_X(t)$, form a Fourier transform pair.

$$S_X(\omega) = \mathcal{F}\{R_X(t)\} \tag{6.18}$$

This is known as the Weiner-Khinchin theorem. The auto-correlation function defined as $R_X(t) \equiv \langle X(\tau)X^*(\tau - t)\rangle$ when evaluated at $\tau = 0$ produces the variance in $X(t)$. Generally the variance in x is $\sigma_X^2 = R_X - \mu_X^2$ but for a WSS process the mean is typically zero. In case of a deterministic time signal such as that of a sine wave of constant amplitude where the mean may be zero, rather than the power spectral density being distributed throughout the whole spectrum, the Fourier result is a delta function stationed at fixed

frequencies. As the frequency coordinate approaches the modulation frequency the power spectral density becomes divergent. We can relate the variance in the time signal of a WSS process to the one-sided power spectral density as follows,

$$\sigma_x^2(t) = \lim_{t\to\infty} \frac{1}{t} \int_{-t/2}^{t/2} |x(t)|^2 \, dt = \lim_{t\to\infty} \frac{1}{t} \int_{-\infty}^{\infty} |x(\omega)|^2 \, d\omega = \int_0^{\infty} S_x(\omega) \tag{6.19}$$

6.4.2 Power spectral density of levitated oscillator

The levitated shell targets are spherical and assumed to oscillate harmonically within the optical trapping potential. The surrounding medium applies a damping force in the form of Stokes drag dependant on the medium's viscosity and the geometry of the shell. Additional forces such as thermal forces from the surrounding medium will result in small stochastic fluctuations in the shell's position. We can generalise these forces as driving terms which act external to the trapping potential. The motion of the levitated shell can then be described by the Langevin equation given in Eq. 6.20. This equation is valid for small thermal perturbations, but will breakdown when the shell's behaviour is no longer harmonic, such as in the case of large displacements from its equilibrium position.

$$m\frac{d^2x}{dt^2} + \gamma\frac{dx}{dt} + \kappa x = F_{ext} \tag{6.20}$$

The first term on the left side denotes the inertial force of the trapped shell of mass m, with its position coordinate denoted x. The second is the damping term due to viscous drag from the surrounding medium and characterised by the damping coefficient γ. The third term is the restoring force applied by the optical potential.

To reveal the frequency components in the shell's oscillations, we begin by taking the Fourier transform of Eq. 6.20.

$$\mathcal{F}\{m\frac{d^2x}{dt^2} + \gamma\frac{dx}{dt} + \kappa x\} = \mathcal{F}\{F\} \tag{6.21}$$

We will tackle this in parts. For $\mathcal{F}\{m\frac{d^2x}{dt^2}\}$ we use the standard result $\mathcal{F}\{\frac{d^n x(t)}{dt^n}\} = (i\omega)^n \tilde{x}(\omega)$

$$\mathcal{F}\{m\frac{d^2x}{dt^2}\} = -m\omega^2\tilde{x}(\omega)$$

Similarly, for $\mathcal{F}\{\gamma\frac{dx}{dt}\}$:

$$\mathcal{F}\{\gamma\frac{dx}{dt}\} = i\omega\gamma\tilde{x}(\omega)$$

and finally,

$$\mathcal{F}\{\kappa x\} = \kappa\tilde{x}(\omega)$$

Combining these results and solving for $\tilde{x}(\omega)$ gives an expression for the oscillatory be-

haviour of the shell's position in frequency space,

$$\tilde{x}(\omega) = \frac{\mathcal{F}\{F\}}{-m\omega^2 + i\omega\gamma + \kappa} \tag{6.22}$$

The power spectral density is computed using Eq. 6.17 to give [131],

$$S_x(\omega) = \lim_{t\to\infty} \frac{1}{t} \frac{2|\tilde{F}(\omega)|^2/m^2}{\left|-\omega^2 + i\omega\beta + \omega_0^2\right|^2} \tag{6.23}$$

A factor of $1/m$ is taken out to replace κ with the oscillator's resonant frequency $\omega_0^2 = \kappa/m$, and a constant $\beta = \gamma/m$ is introduced. The power spectral density of $\tilde{x}(\omega)$ looks like the power spectral density of $\tilde{F}(\omega)$ in the limit $t \to \infty$ scaled by $1/m^2 \cdot 1/(-\omega^2 - i\omega\beta + \omega_0^2)^2$ so we can rewrite $S_x(\omega)$ in terms of $S_F(\omega)$. The denominator is simplified so the S_x takes the form,

$$S_x(\omega) = \frac{S_F(\omega)/m^2}{(\omega_0^2 - \omega^2)^2 + \omega^2\beta^2} \tag{6.24}$$

We can relate this to the positional variance of the shell using Eq. 6.19.

$$\sigma_x^2(t) = \int_0^\infty S_x(\omega)\ d\omega = \int_0^\infty \frac{S_F(\omega)/m^2}{(\omega_0^2 - \omega^2)^2 + \omega^2\beta^2}\ d\omega = \frac{\pi S_F(\omega)}{\beta\omega_0^2 m^2} \tag{6.25}$$

A nice solution to the integral is presented Ref. [132].

6.5 System damping

Many sources in the literature will demonstrate optical trapping of small microbeads suspended in aqueous solution or similar liquid media. Here the viscous force terms dominates the inertial term so that the oscillator becomes overly-damped. Drag from the surrounding medium results in kinetic energy loss in the absence of a driving mechanism. The time by which the system energy drops by a factor of $1/e$ is given by,

$$t_{char} = \frac{m}{\gamma} \tag{6.26}$$

A fused silica bead of radius 1 µm suspended in water at 20 °C will have $t_{char} = 0.5$ µs. This is an important consideration for electronic sensing to ensure the positional variations are sampled with sufficient time resolution. A position sensor operating at a modest 10 kHz would lack sensitivity by several orders of magnitude at these time scales. The assumption here for an over-damped system would therefore be valid, removing the need for the inertial force term in Eq. 6.20 as high frequency dynamics are neglected. Comparing this to the case of a shell target of radius 50 µm levitated in air at the same ambient temperature gives $t_{char} = 4.3$ ms. This is unsurprisingly far greater than the value seen above and in fact lies within the sensitivity of typical position sensors. Chap. 5 will discuss the position sensing setup and procedures used in greater detail. For now, if we take a similar example

of a position sensor operating at some 10 kHz, it would provide adequate sampling of the oscillation period with t_{char} being 65 times slower than measurement interval.

Conversely, when trapping in a less viscous medium or where the medium has been removed, such as when trapping at low pressure, the damping decreases. Since the resonant spectral features are broadened by the damping terms, as the damping term weakens, spectral features can appear sharper and more pronounced. The lack of damping however also affects the stability of the trap and often will require supplementary stabilisation mechansims that artificially modify the damping term.

6.5.1 Pressure dependent damping

The length scales over which interactions that result in Brownian motion or those that dampen oscillatory motion can be characterised by the Knudsen number. It relates the mean free path, l_m, of the surrounding air molecules of diameter d to the macroscopic interaction length scale, L, which here is the trapped shell diameter.

$$Kn = \frac{l_m}{L} = \frac{k_b T}{\sqrt{2}\pi d^2 P L} \tag{6.27}$$

The Knudsen number can be modified if the static pressure, P, is varied. When $Kn << 1$ we assume the regime of a continuous medium to describe continuous-flow molecular interactions. In the opposite extreme of $Kn >> 1$ we enter the free-molecular flow regime where the mean free path is larger than L and so interactions are discrete. Flow regimes can be classified depending on their respective Kn-number [133].

- $Kn \leq 0.01$ - Continuous flow
- $0.01 < Kn < 0.1$ - Slip flow
- $0.1 < Kn < 10$ - Transition flow
- $Kn \geq \mathcal{O}(10)$ - Free-molecular flow

Values of Kn calculated at pressures used in our experimental work are listed in Tab. 6.1. At lower pressures, the damping term accounting for large Kn can be found from kinetic

Kn vs Pressure						
Pressure (Pa)	10^5	10^4	10^3	10^2	10	1
Kn	1.36×10^{-3}	1.36×10^{-2}	1.36×10^{-1}	1.36	1.36×10^{1}	1.36×10^{2}

Table 6.1: Knudsen numbers for varying ambient pressures. Values calculated correspond to a trapped shell diameter of 50 µm and gas particle size of 3.7×10^{-4} µm [134].

theory of gases (KTG) [135] as given in Eq. 6.28

$$\gamma = 6\pi\eta a \frac{0.619}{0.619 + Kn}\left(1 + \frac{0.31Kn}{0.785 + 1.152Kn + Kn^2}\right) \tag{6.28}$$

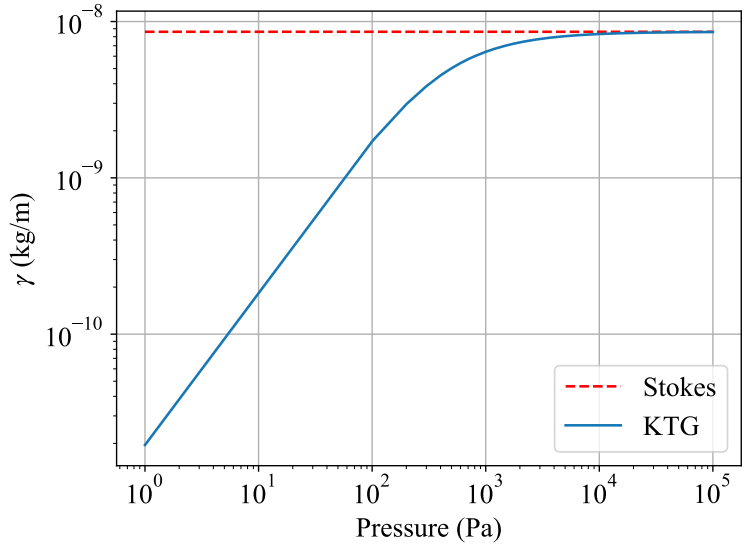


Figure 6.3: Damping curves for 50 µm shell at $T = 300\,\mathrm{K}$ and constant dynamic viscosity within the pressure range. (Red) Stokes' law assuming constant γ with pressure. (Blue) KTG-γ varying with pressure. 10 % deviation in γ at 3×10^3 Pa.

Notice in the limit $Kn << 1$ Eq. 6.28 reduces to Stokes' drag. Fig. 6.3 compares γ derived from KTG and when assumed constant with pressure using Stokes' to show when pressure considerations to damping may become significant.

6.5.2 Damped oscillator

The nature of the damping in our system is currently unclear. Literary works involving silica or polystyrene microbeads trapped in liquid suspension justifiably assume their system to be overly damped as the viscous term dominates in the limit $m \to 0$. Mediums such as water or oils are also selected for better impedence matching. The combination of a massive target by comparison trapped in a less viscous fluid would imply less damping than that seen in these examples. We follow a similar approach to the generalised case as seen in Sec. 6.4, but now for the case of an over-damped oscillator. We begin by drop the inertial force term so that the Langevin becomes,

$$\gamma \frac{dx}{dt} + kx = F(t) \tag{6.29}$$

so that we have,

$$|x(\omega)|^2 = \frac{|F(\omega)|^2}{\omega^2\gamma^2 + \kappa^2} \tag{6.30}$$

and as before, we can calculate the one-sides power spectral density using Eq. 6.17

$$S_x(\omega) = \lim_{t\to\infty} \frac{1}{t} \frac{2|F(\omega)|^2}{\omega^2\gamma^2 + \kappa^2} = \frac{S_F(\omega)}{\omega^2\gamma^2 + \kappa^2} = \frac{4k_B T\gamma}{\omega^2\gamma^2 + \kappa^2} \tag{6.31}$$

Finally the positional variance of the over-damped oscillator can be found using Eq. 6.19

$$\sigma_x^2(t) = \int_0^\infty \frac{S_F(\omega)}{\omega^2\gamma^2 + \kappa^2}\, d\omega = S_F(\omega)\frac{\pi}{2} \tag{6.32}$$

Again you may refer to Ref. [132] for the solution to the integral.

6.6 Thermally driven oscillator

When trapping a target in a viscous medium such as air we observe random jitter in its position measurement. Even under what appears to be stagnant conditions, diffusive molecules from the surrounding medium will collide with the target and apply small "kicks" to its surface. The random nature of these collision over the entire surface of the target results in motion described by Brownian dynamics dependent on the ambient temperature of the surrounding medium.

6.6.1 Brownian dynamics

The motion of a small particle in a fluid is given by [136],

$$m\frac{dv}{dt} + \gamma(t)v = \xi(t) \tag{6.33}$$

for velocity , v, mass m, friction constant γ and a random fluctuation term $\xi(t)$ that behaves as $\langle\xi(t)\rangle = 0$ and $\langle\xi(t)\xi(t')\rangle = 2k_BT\gamma\delta(t-t')$. The mean value of $\xi(t)$ is shown to be zero implying no net force is applied over a long measurement period. The auto correlation of $\xi(t)$ shows it to be a stochastic process so that the noise is time independent. In the substitution we then have solutions to the velocity of the particle in,

$$v(t) = v_0e^{-\beta t} + \frac{1}{m}\int_0^t e^{-\beta(t-t')}\xi(t')dt' \tag{6.34}$$

The positional evolution of the particle can be found by $x(t) = x_0 + \int_{t'} v(t')dt'$. Applying a substitution for displacement $s = x(t) - x_0$ the mean square displacement can be shown to be [137],

$$\langle s(t)^2\rangle = \frac{2k_bT}{\beta^2 m}(\beta t - 1 + e^{-\beta t}). \tag{6.35}$$

Applying the limits $t << 1/\beta$ and $t >> 1/\beta$ we obtain the short and long time behaviour of the particle. In $t << 1/\beta$ we have $\langle s(t)^2\rangle \approx k_bT/m \cdot t^2$ which is Ornstein's (1917) result where the particle is ballistic at its initial velocity as $\sim t^2$. When $t >> 1/\beta$ we have Einstein's (1905) result $\langle s(t)^2\rangle \approx 2k_bT/m\beta \cdot t = 2Dt$ describing uniform or "diffusive" motion as damping ensures the velocity doesn't scale with time. Instead the motion is influenced by random thermal forces. These results are collectively known as Einstein-Ornstein-Uhlenbeck (EOU) theory for the Brownian motion

6.6.2 Thermal noise power density

The time-behaviour of the particle is an important consideration when taking measurements as it influences our expectations on the form the shell's motion will take. If we consider the general case, the thermal term from EOU is treated as a small perturbation applied to the right-hand side of Eq. 6.20 where the external force is given by,

$$F_{th} = (2k_B T\gamma)^{1/2} n(t) \tag{6.36}$$

$\gamma = 6\pi\mu\rho$ is Stokes law for a spherical object of radius ρ and $k_B T$ is the thermal energy term. The thermal force is represented as white-noise resembling a random Gaussian process where $\langle 2k_B T\gamma\eta(t)\rangle = 0$ and $2k_B T\gamma\langle\eta(t)\eta(t')\rangle = 2k_B T\gamma\delta(t-t')$. The mean value of $\eta(t)$ is shown to be zero implying no net force is applied over a long measurement period. The auto correlation of $\eta(t)$ shows it to be a stochastic process so that the noise is time independant. Thus thermal noise satisfies the conditions for a WSS process. The one-sided thermal noise power spectral denity is,

$$S_{F_{th}}(\omega) = 4k_B T\gamma \cdot S_\eta(\omega). \tag{6.37}$$

Since $S_\eta(\omega)$ is unitary for white noise with $\langle\eta(t)\rangle = 0$, it has uniform distribution scaled to $4k_B T\gamma$. We can substitute this result into Eq. 6.24 to obtain the one-sided power spectral density of a thermally driven harmonic oscillator [131, 138],

$$S_x(\omega) = \frac{4k_B T\beta/m}{(\omega^2 - \omega_0^2)^2 + \omega^2\beta^2} \tag{6.38}$$

Berg-Sorensen et al. [139] demonstrates this analysis for optical tweezers where the Einstein result is taken. This is due to the high damping present in these systems that reduces the characteristic timescales over which the energy in the particle is lost to the medium and its motion equilibrates. In this case, the power spectral density takes the form of a damped oscillator as,

$$S_x(\omega) = \frac{2D}{\omega_0^2 + \omega^2} \tag{6.39}$$

where D is Einstein's coefficient. Alternatively, when the thermal force term is not explicitly given, the particle's motion may simply be equated with the thermal energy in the system via the equipartition theorem, $1/2 \cdot k_b T = 1/2 \cdot m\omega_0^2\langle s(t)^2\rangle$ [140, 141]. The mean square displacement can then be found as,

$$\langle s(t)^2\rangle = \frac{k_b T}{m\omega_0^2}. \tag{6.40}$$

6.7 Parametric oscillator

A parametric oscillator is a type of oscillator in which a varying system parameter is used to drive a response that would otherwise not occur under conditions where the parameter is stationary. An example of this is seen by modulating the trapping beam's power. A fixed frequency sine-wave passed into the beam delivery can be used to drive shell motion. Starting from equilibrium, as the power increases, the shell is forced to react to the radiative pressure by rising higher in the optical trap. As the power decreases the shell falls under gravity or partially supported by the diminishing beam intensity. The cycle then continues. The force exerted on the shell by the modulating power is,

$$F_{mod} = \pm\kappa' x \tag{6.41}$$

The modulating power directly influences the trap stiffness to produce an oscillating restoring force. We can modify Eq. 6.20 to include the modulation term so that we have,

$$m\frac{d^2x}{dt^2} + \gamma\frac{dx}{dt} + (\kappa \pm \kappa')x = F_{ext} \tag{6.42}$$

We can see the parametric behaviour directly affects the natural resonance of the oscillator driven by the modulation frequency. Rather than applying the modulation at equilibrium, the modulation can instead be timed to match the phase of the shell velocity. The force due to the modulation can be equivalently expressed in terms of the shell velocity as,

$$F_{mod} = \pm\gamma'\frac{dx}{dt} \tag{6.43}$$

The peak of the modulation corresponds to when the trap is at its stiffest; the modulation trough is when the trap stiffness is at its weakest. Matching the modulation and velocity in phase results in self-excitation as the supplied energy adds to the oscillation amplitude. Applying the modulation out of phase with the velocity ensures the shell always sees a heightened potential so to reduce its displacement amplitude as shown in Fig. 6.4. This can acts as an axial position stabilisation mechanism. However, since the natural motion of the trapped shell is driven by the thermal energy bath of its surroundings, the stochastic nature of Brownian motion then requires continuous phase correction of the modulation to coincide with when the shell is ballistic. Stabilisation of the shell beyond the Brownian level leads to the realisation of parametric cooling [142]. As demonstrated in Ref. [143] activating parametric stabilisation brings additional damping ($\delta\gamma$) and frequency ($\delta\omega$) contributions in the power spectral density as,

$$S_x(\omega) = \frac{4k_bT\gamma_0/m^2}{([\omega_0 + \delta\omega]^2 - \omega)^2 + \omega^2[\gamma_0 + \delta\gamma]^2} \tag{6.44}$$

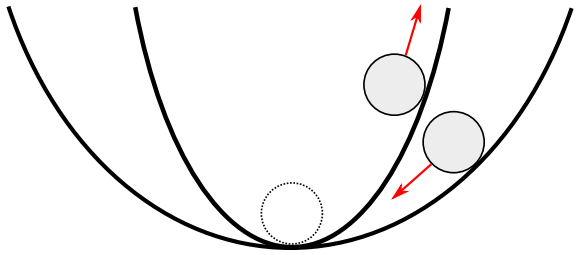


Figure 6.4: One must imagine Sisyphus happy

6.8 Photophoresis

When under direct illumination, a (weakly) absorbing target suspended in a fluid, such as water or air, will experience a peculiar class of thermally driven effects collectively referred to as photophoresis [144]. These are distinct to the Brownian fluctuations discussed previously which too are of thermal origin. Whereas Brownian motion is due to random collisions between the trapping target surface and the molecules of the surrounding medium, photophoresis results from the difference in temperature over the target surface and the surrounding medium. This causes fluid molecules to "creep" across the heated surface in the direction of the temperature gradient. For strongly absorbing particles this force can be several times greater than the radiative force and even facilitate the optical trapping of these particles in a Gaussian beam [145, 146, 147].

6.8.1 Photophoretic force

The photophoretic force comes in two types, the ΔT-force and the $\Delta\alpha$-force. One-sided illumination of the trapping target, as in single-beam optical levitation, will heat the target to produce an asymmetric temperature distribution across its surface ΔT pointing from hot to cold. Depending on the optical properties of the target medium, this will result in positive or negative photophoresis corresponding to motion directed in or against optical propagation. The second type occurs for targets with an asymmetric thermal accommodation coefficient, $\Delta\alpha$. This can be due to changes in material composition of the target surface, which even under uniform surface illumination will still result in an asymmetric temperature distribution with the force pointing from the region of higher to lower thermal accommodation coefficient. Note that while the ΔT-type is fixed relative to the side of illumination, the $\Delta\alpha$-type is body fixed. Measures can be taken to fix the latter to an external reference by gravity [148], or by an external electric/magnetic [149]/optical field to apply a torque to orient the target in the desired direction. Although we have observed hairline fractures and geometric irregularities in the shells under microscope imaging, their effects on the thermal accommodation coefficient must be large for the effects of $\Delta\alpha$-type photophoresis to be significant. Assuming a fixed coating of silver on the target surface and idealising the shells to be perfectly spherical, we will assume photophoresis occurs of the first type.

The study of photophoresis originated in the investigation of absorptive spherical aerosol

particulates and has predominantly remained so [144, 150, 151, 152]. We first see Hettner's (1926) formulation of radiometric force acting on a spherical particle in $Kn >> 1$,

$$F = \frac{3\pi\mu^2 r R \nabla T_{int}}{PM} \tag{6.45}$$

for universal gas constant R, pressure P, molecular weight M and internal temperature gradient ∇T_{int}. Where a particle is illuminated from one side, the temperature gradient can instead be given in terms of the gradient through the poles as $\nabla T_p = I/2(k_p + k_f)$ for intensity I and k_p and k_f are the thermal conductivities of the particle and surrounding fluid. This gives an order of magnitude estimate of the photophoretic effect [153]. Tong (1972) derived an more accurate expression for the photophoretic force in the free molecule and transition regimes [154] with Reed (1976) covered the $Kn << 1$ limit. Finally, Rohatschek [151] presented a unifying model using a semi-empirical approach valid for both $\Delta\alpha$ and ΔT type forces and pressure regimes.

$$F^{Kn<<1} = \frac{D_g r^2}{2k_p}\left(\frac{P}{P*}\right)^{-1} I \tag{6.46}$$

$$F^{Kn>>1} = \frac{D_g r^2}{2k_p}\left(\frac{P}{P*}\right) I \tag{6.47}$$

Here, $P*$ is the characteristic pressure $P* = 3D_g T/\pi r$, r is the trapped particle radius, and D_g is a constant determined by the state of the gas $D_g = \pi/2 \cdot \sqrt{K_{TC}\pi/3} \cdot \bar{v}\mu/T$ where K_{TC} is the thermal creep coefficient and $\bar{v} = \sqrt{8RT/\pi M}$ is the mean velocity of the gas molecules.

6.8.2 Photophoresis on coated hollow shells

Few works relate this phenomenon to particles of properties similar to those of our metal coated shells. The discrete boundary layers varying in material composition and thermal properties require a tailored approach to account for changes in thermal conductivity and heat transfer. The uncommon combination of trapping reflective shell targets, and a high-power annular trapping beam in the absence of stabilisation motivates it investigation particularly in light of the changes in target stability observed at lower pressures.

Ref. [155] presents an approach for radially varying thermal conductivity in aerosols. It was argued the thermal conductivity's dependence on θ is weak due to symmetry yet strong in r due to the aerosol formation mechanism - liquid is condensed at nucleation sites then solidifies to form a shell while its internal inhomogeniety is maintained. By applying appropriate boundary conditions to match the discrete layers of silver, glass and the gas filled core, the approach of a radially varying thermal conductivity can be adapted to model heat transfer through our hollow microspheres.

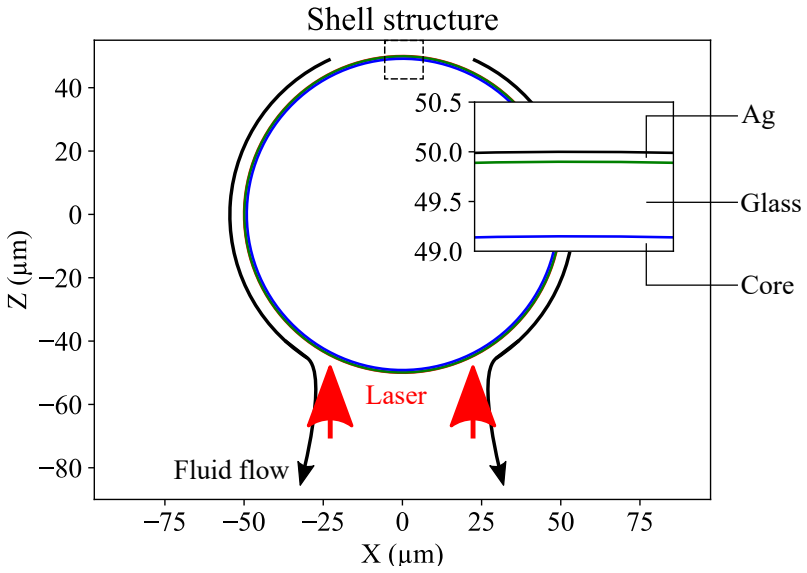


Figure 6.5: Microshell is illuminated in the $+z$-direction. It has $d = 100\,\mu\text{m}$ with $0.1\,\mu\text{m}$ thick silver (Ag) layer, and $0.85\,\mu\text{m}$ total wall thickness.

Thermal boundary conditions

We considered a multi-layered spherical geometry comprised of an outer silver shell, an intermediate glass layer, and an internal gas filled core as shown in Fig. 6.5. We assume the surrounding air to act as a thermal bath at room temperature and initially at atmospheric pressure. The Knudsen number is $Kn << 1$ so that the surrounding medium is in the gas continuum regime and we assumed thermal conduction is the primary mode of heat transfer.

The shell is illuminated in the $+z$ direction. This generates thermal energy sources q_i which we confine to only the lower hemisphere of the outer metal coating. Due to the spherical symmetry of the system, the problem becomes well-suited for solutions in spherical coordinates. Here, the heat diffusion problem is governed by Poisson's equation,

$$\nabla^2 T(r,\theta) = -\frac{J(r,\theta)}{k} \tag{6.48}$$

for temperature $T(r,\theta)$ and thermal conductivity k, and thermal source density distribution $J(r,\theta)$. We then apply the following boundary conditions, imposed by the structure of the layered interfaces [156].

$$k_1 \left.\frac{\partial T_1}{\partial r}\right|_{R_1} = k_2 \left.\frac{\partial T_2}{\partial r}\right|_{R_1} \tag{6.49a}$$

$$T_2|_{R_1} - T_1|_{R_1} = C_T K n_1 R_1 \left.\frac{\partial T_1}{\partial r}\right|_{R_1} \tag{6.49b}$$

$$k_2 \left.\frac{\partial T_2}{\partial r}\right|_{R_2} = k_3 \left.\frac{\partial T_3}{\partial r}\right|_{R_2} \tag{6.49c}$$

$$T_2|_{R_2} = T_3|_{R_3} \tag{6.49d}$$

$$k_g \left.\frac{\partial T_g}{\partial r}\right|_{R_3} = k_3 \left.\frac{\partial T_3}{\partial r}\right|_{R_3} \tag{6.49e}$$

$$T_g|_{R_3} - T_3|_{R_3} = C_T K n R_3 \left.\frac{\partial T_g}{\partial r}\right|_{R_3}. \tag{6.49f}$$

R_1 is the internal core radius, R_2 is the outer radius of the intermediary glass layer, and R_3 is the outer radius of the silver layer. The boundary conditions enforce continuity of heat flow at each interface through Eqs. 6.49a, 6.49c and 6.49e. Temperature continuity is ensured by Eq. 6.49d. Additionally, in Eqs. 6.49b and 6.49f, a thermal jump coefficient, C_T, is included to account for the finite temperature discontinuity at the solid-gas interfaces. This discontinuity arises due to rarefied gas effects, characterised by the Knudsen number, Kn, which modifies the effective heat transfer at these interfaces.

Heat transfer solution

The symmetry of this configuration relies on the z-axis alignment of the illumination source and the spherical symmetry of the shell target. The heat transfer problem is then axis-symmetric with the temperature term dependent only on r and θ. The analysis is greatly simplified by the fact there is no azimuthal dependence on the distribution. Legendre polynomials $P_n(\cos\theta)$ which form an orthogonal set over the interval $\theta \in [0, \pi]$ form an appropriate solution basis. While spherical harmonics also provide a complete basis, their solutions are unnecessarily complicated due to their ϕ dependence. The general solution to Eq. 6.48 in the literature is commonly expressed as,

$$T(r,\theta) = T_\infty + \sum_{n=0}^{\infty} T_n P_n(\cos\theta) \tag{6.50a}$$

$$T_n(r) = \frac{A_n}{r^{n+1}} + r^n B_n + \frac{1}{(2n+1)k}\left[\frac{1}{r^{n+1}}\int_{R_3} q_n(r) r^{n+2} dr - r^n \int_{R_3}^{r} q_n(r)\frac{dr}{r^{n-1}}\right] \tag{6.50b}$$

$$q_n(r) = \frac{2n+1}{2}\int_0^\pi J(r,\theta) P_n(\cos\theta)\sin\theta d\theta \tag{6.50c}$$

The temperature $T(r,\theta)$ is expressed as the sum of the distant environment temperature T_∞ and the Legendre expansion with Legendre polynomials P_n and argument $cos\theta$. A_n and B_n are boundary coefficients.

For the first layer the solution must be finite as $r \to \infty$ and with no heat sources the solution simplifies to,

$$T_1(r,\theta) = T_\infty + \sum_{n=0}^{\infty} r^n B_{1n} P_n(\cos\theta). \tag{6.51}$$

Similarly, we assume no heat sources in the glass shell layer which gives,

$$T_2(r,\theta) = T_\infty + \sum_{n=0}^{\infty}\left[\frac{A_{2n}}{r^{n+1}} + r^n B_{2n}\right] P_n(\cos\theta) \tag{6.52}$$

Since we assumed all q_i to be on the shell surface we include heat sources for the metal

coating layer,

$$T_3(r,\theta) = T_\infty + \sum_{n=0}^{\infty} T_{3n} P_n(\cos\theta) \tag{6.53}$$

$$T_{3n}(r) = \frac{A_{3n}}{r^{n+1}} + r^n B_{3n} + \frac{1}{(2n+1)k_3}\left[\frac{1}{r^{n+1}}\int_{R_3}^{r} q_n(r) r^{n+2} dr - r^n \int_{R_3}^{r} q_n(r)\frac{dr}{r^{n-1}}\right]$$

and finally for the air medium we have the following for a finite solution as $r \to \infty$,

$$T_g(r,\theta) = T_\infty + \frac{A_{gn}}{r^{n+1}} P_n(\cos\theta) \tag{6.54}$$

We are seemingly presented with an infinite set of solutions as we must determine the respective $A_{i,n}, B_{i,n}$ coefficients.

Panao et al. [156] uses this approach and shows in fact only A_{g0} and A_{g1} are required to derive an expression for the photophoretic force. Their model includes further considerations of fluid flow around a spherical body, which we will be exclude for now as it falls out of the scope of our work but the full work can be found in their paper. Their final expression is given as

$$F_{ph} = -\frac{4\pi\mu_g^2 A_{g1}(3K_s K_{kf} Kn + K_{Tc})}{(1+3K_{kf}Kn)R_3^2 T_{gS}\rho_g} \tag{6.55}$$

K_{kf} is the kinetic friction coefficient, K_{Tc} is the thermal creep coefficient. Completed expressions for the coefficient values and dependent terms can be found in their paper Ref.[156]. This model was tested by the authors and verified using CFD software. The analytical result up to the second order Legendre polynomial in Eq. 6.54 was demonstrated to agree with simulations, with negligible contribution from the third order polynomial term. We however were unable to replicate the analytical results due to time limitations.

6.9 Summary

This chapter provides background theory to various opto-mechanical and thermo-mechanical interactions that influence the behaviour of a levitating target. We begin by deriving the static radiative forces acting on a reflective spherical shell in the ray-optics regime. This is necessary to determine the balancing of inertial forces that give rise to optical levitation.

We then explore the time-dynamics of a levitating shell by modeling the system as a mechanical oscillator and apply Fourier-based tools to determine its spectral properties. Here we relate the power spectral density of the shell's positional time-series to its response in frequency-space. We assume the time-dynamics are stochastic in nature which allows us to relate the model, in the form of our power spectral density expressions, to the variance in the experimental data. We show the influence damping and pressure variation has on these results. This is of particular interest as we aim to determine the damped nature of the oscillator and how this evolves at reduced air pressure with the long term goal of

high-vacuum optical levitation.

The stochastic behaviour of the shell can be considered using Brownian dynamics realised through a thermal noise driven oscillator. This relates the mechanical properties of the oscillator to its thermal energy. In the long-term limit as $t >> 1/\beta$ the shell's motion is diffusive. From this we find a limit in the shell's spatial confinement dominated by thermal fluctuations in the absence of active stabilisation methods.

By modulating the power of the trapping beam, the oscillator becomes parametric. This directly modifies the trap-stiffness and damping of the levitation system and can be used to counter-act Brownian fluctuations. This leads to the realisation of active stabilisation in the form of "parametric cooling" to stabilise levitation targets beyond the thermal noise limit of their system.

Finally, we explore photophoretic forces. The one-sided illumination of our single beam setup generates asymmetric heating of the shell's surface. The this produces a surface temperature gradient dependent on the thermal conductivities of the shell and surrounding gaseous (or generally fluid) medium. Air molecules exhibit "creeping" over the shell surface along the temperature gradient resulting in an attractive or repulsive force relative to the heating source. Experimental observations have shown anomalous instabilities when trapping at low pressure which we suspect to be photophoresis. The form this force takes is given as seen generally in the literature. However, due to the inhomogeneous internal composition of our shells, the force expressions for this geometry is also presented.

We now have developed an understanding of key details relating to the forces and time-dependant behaviour of our optically levitated reflective shells. By comparing these models to experimental results we can find areas of agreement and instances where further development is required. We will now employ these insights to experimental results in Chap. 7.

Chapter 7

Levitated reflective microshells

This serves as the primary results chapter for our work on optically levitated reflective microshells. These consist of experimental and computational findings to provide a broad understanding of the shells' mechanical response and stability characteristics inside the optical trap. Due to the unpredictability of the trap lifetimes and inherently destructive nature of certain measurements, results are complied from several instances of shell trapping ranging a variety of shell sizes.

The goal of this chapter is to also provide key procedural insights on how results are currently obtained so that these methodologies can be further developed as our analysis and diagnostics capabilities improve.

7.1 Thermal study on laser induced heating

Laser heating of the shell surface is an important consideration, particularly in developing our understanding of photophoretic instability and how this evolves with pressure. We suspect, as pressure decreases, heat loss mechanisms become increasingly reliant on radiative heat loss. Convection and conduction heat loss requires interaction with the surrounding medium whose influence is reduced as the chamber is pumped down. Prior work has alluded to a "death-valley" zone at which the pressure becomes too low for the surrounding medium to dampen instabilities yet still high enough for molecular-surface interactions to be non-significant. We think photophoretic instability here becomes a dominating force, requiring active feedback stabilisation in order to maintain stable levitation. A thermal study was conducted looking at heat transfer across the poles of the shell surface at varying static pressures. In our current understanding, the surface temperature at these pressures and to what degree loss mechanisms contribute to surface heating is entirely unknown. Mapping the temperature distribution over the shell surface will allow us to investigate the size of the temperature gradient between the poles and thus the force differential acting on the shell because of it.

Thermal simulations were run on QuickField - a finite element analysis (FEM) package used for field modelling and analysis. We would like to acknowledge contributions of Dr. Wong from the University of Strathclyde whose expertise was enlisted to assist in the setup and running of the simulations.

7.1.1 Simulation setup

We assume the shell core to be gas filled - its true gas composition is unknown but likely to be dependent on the proprietary processes used to manufacture the hollow shells. For simplicity, we attribute it similar material characteristics to that of air, with density $\rho_{core} = 1.293\,\mathrm{kg/m^3}$, specific heat capacity $c_{core} = 1000\,\mathrm{J/(kg\,K)}$ and thermal conductivity $k_{core} = 0.025\,\mathrm{W/(K\,m)}$. Due to the thermally insulating properties of gases in general, we can expect the core to be resistant to heat transfer processes through the shell interior leading to an overall low effective thermal conductivity. Similarly, the glass composition and exact thickness of the internal walls are also unknown. One may see vast variation in material properties depending on the type of glass considered, be it soda glass, UVFS, BK7 or others. This limits the accuracy of the simulations but we can make reasonable estimates. We chose the following, $\rho_{glass} = 2320\,\mathrm{kg/m^3}$, $c_{glass} = 840\,\mathrm{J/(kg\,K)}$ and $k_{glass} = 1.38\,\mathrm{W/(K\,m)}$. For the outer silver layer we use $\rho_{Ag} = 10.490\,\mathrm{kg/m^3}$, $c_{Ag} = 233\,\mathrm{J/(kg\,K)}$ and $k_{Ag} = 430\,\mathrm{W/(K\,m)}$.

The mass of the levitating shell determines its axial equilibrium position along the trapping beam's path. The beam is also expanding as it propagates so the overlap of the shell's cross-section with the beam profile will also differ for two shells varying in size. This makes it difficult to experimentally determine the intensity overlap and the degree of heating the shell experiences. Instead, we can take a computational approach by taking the example of a $d = 50\,\mu\mathrm{m}$ shell. The outer silver layer is estimated to be $0.1\,\mu\mathrm{m}$ and the glass thickness $0.75\,\mu\mathrm{m}$ in line with wall thickness estimates given in Sec. 5.1. This gives an expected mass of 21 ng and require $2.1 \times 10^{-10}\,\mathrm{N}$ of force to balance it weight against gravity. The incident power required to generate this radiative can be roughly calculated as,

$$F_{rad} = (1+R)P/c \Rightarrow P = Fc/(1+R) = 31.56\,\mathrm{mW} \tag{7.1}$$

The power is distributed over the cross-sectional area of the shell giving an incident beam intensity of $I_{rad} = P/A_{cross-sec}$. However shell heating results only from the portion of the intensity absorbed by the shell, I_{abs}.

$$I_{abs} = (1-R)I_{rad} = 48\,\mathrm{kW/m^2} \tag{7.2}$$

The absorbed intensity was calculated to be $48\,\mathrm{kW/m^2}$. I_{abs} was used as input parameter defining the direct heat flux applied to the shell surface.

The vacuum chamber that housed the optical trap is not thermally isolated from the surrounding laboratory environment. As a result the air inside does not follow typical

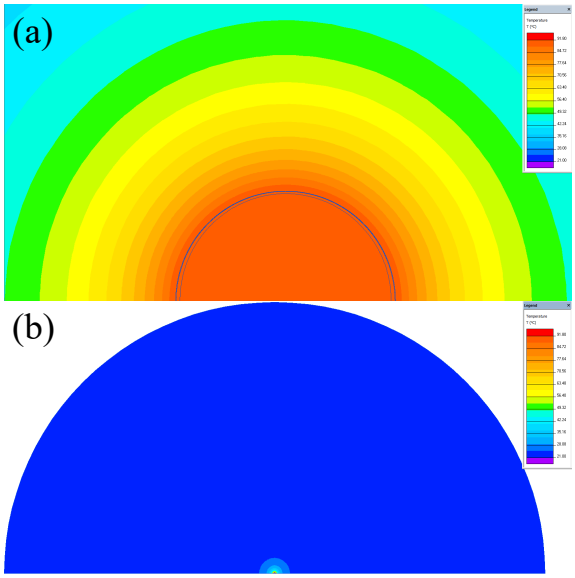


Figure 7.1: (a) Radial temperature distribution extending to 2.5x shell radius. Shell boundary indicated by the solid line (b) Full simulation domain with zero flux boundary at 5 mm radial distance from the shell center.

ideal gas law's relating pressure and temperature. The chamber was pumped slowly over a period of several minutes, granting the internal temperature time to thermalise with the external environment. This heat exchange allows us to assume the average internal temperature is approximately steady with room temperature. Simulating heat transfer across the entire chamber would be computationally inefficient, especially since most of the volume remains thermally inactive. Instead, a boundary was applied to enclose the shell and its immediate surroundings to define the simulation domain. A zero heat flux condition was applied at the boundary to ensure heat transferred from the shell to the surroundings did not reflect off back into the system which would otherwise lead to artificial heating of the domain. It also prevented thermal energy from escaping the system, avoiding any unphysical loss of heat. These conditions were applied by placing the boundary sufficiently far away so heating did not extend past this point thereby justifying the assumption of an ambient temperature, $T_\infty = 293\,\mathrm{K}$. The boundary was placed at 5 mm from the shell's center. Fig. 7.1 shows an example run of the heat transfer simulation with the boundary in place.

7.1.2 Thermal simulations

The poles of the shell are oriented horizontally and heating was applied from the right-hand side of the shell in Fig. 7.1(a). The transient heat transfer computation was rotationally symmetric about the horizontal axis. A heat flux of $48\,\mathrm{kW/m^2}$ was applied to the shell surface, in accordance with Sec. 7.1.1. Despite the radial distribution of the beam intensity, for simplicity the flux was applied uniformly as a first-order approximation at the beam center.

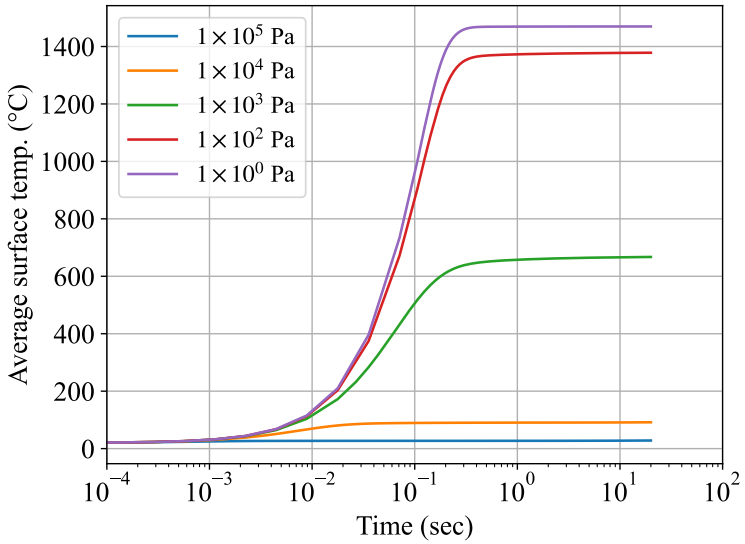


Figure 7.2: Average surface temperature-time plots for 34 µm shell for various static pressures. We find rapid increase in average surface temperature as pressure decreases due to increased reliance on radiative heat loss.

Simulations were run at static pressures of 10^5 Pa, 10^4 Pa, 10^3 Pa, 10^2 Pa and finally 1 Pa as an extreme case. The thermal conductivity of the surrounding air medium was adjusted to compensate for reduced pressure. However, the thermal conductivity was fixed within each simulation. Future work could allow variable thermal conductivity within the simulation to better replicate the properties of increasing component temperatures as they heat up. Each simulation computed 20 sec of heating. This was determined based on the time-frame over which the heating leveled off as seen in Fig. 7.2. Heat loss was primarily considered through conduction and radiation. Convective heat loss was neglected due to the physical conditions of the system namely, the shell is suspended in near-static air, with slight motion arising from shell oscillations or low-level creeping flow.

At 10^5 Pa we see heating of the shell surface up from room temperature to just below 50 °C. Fig. 7.3 shows the surface temperature distribution at equilibrium as a function of polar angle θ where $\theta = 0$ is normal to laser incidence. We have an average surface temperature of 49.43 °C with a polar temperature difference of 0.46 °C. Recall from Sec. 6.8, the temperature gradient between the poles due to asymmetric heating of a particle in a fluid can be expressed as function of the illuminating intensity over the thermal conductivities of the particle and the surrounding medium, $\nabla T = I/2(k_s + k_f)$. We can then obtain the absolute difference in temperature between two points by scaling the gradient by their separation, Δr, which in this case would be the shell diameter. We assign k_s as the thermal conductivity of the shell and k_f as that of the fluid or air. We can then solve for k_s to give an effective thermal conductivity of 2.58 W/(K m).

Fig. 7.4 shows the internal temperature distribution from pole to pole. The layer boundaries are indicated by the red vertical lines. The temperature distribution through the

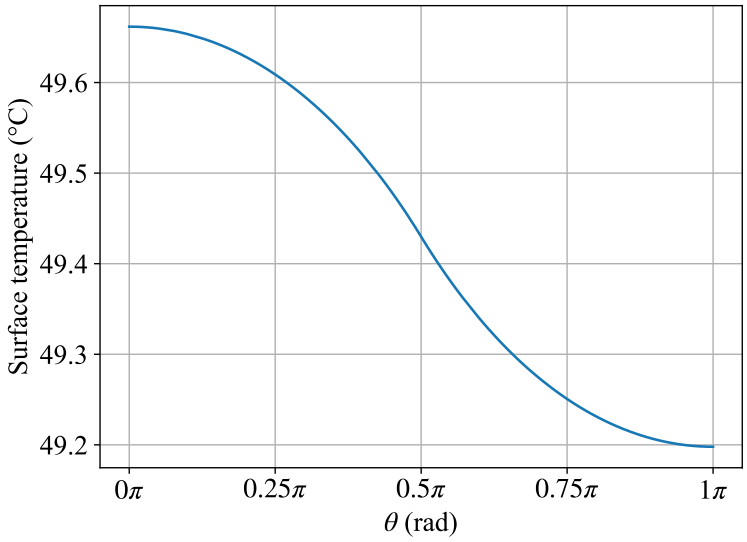


Figure 7.3: Simulated temperature distribution over shell surface against radial position. The shell is centered at 0 and heated from below.

solid layers is near uniform. In contrast, the core exhibits a slight radial non-linearity in temperature with radial position. This results in a 6 % deviation in the value of the gradient when obtained through calculation of ∇T to that obtained directly from Fig. 7.4. The gradient is negative in the direction of the upper pole. This indicates the core to be in fact hotter on average than the upper hemisphere which was unexpected; it was initially thought thermal sources would readily form over the entire outer layer due silver's high thermal conductivity. However, the result obtained is not unreasonable. The core can be considered to be surrounded by thermal sources distributed over the shell surface but whose density diminishes with polar angle, so heat flowing into the core from the illuminated lower hemisphere escapes only through the "dark" upper surface.

As pressure decreases, conductive heat loss to the surrounding air is hindered, resulting in an increase in shell temperature. This is confirmed in Fig. 7.5 which shows a rise in shell temperature at 10^4 Pa to 312 °C. However, both the surface and radial temperature distributions are similar to those seen previously. Interestingly, despite the higher average surface temperature, the temperature difference between the poles remains comparable at 0.46 °C - confirming its dependence on the thermal properties of the shell and fluid medium used above. As the temperature difference remains the same but the average surface temperature is increasing, this indicates a relative homogenising of the temperature distribution at lower pressures.

At 10^3 Pa the pressure has now dropped by 90 % of its initial value. In experiment, we begin to see a rise in the shell's vertical position and perhaps our first indicator of possible photophoretic forces influencing shell behaviour. The shell continues to rise until settling again at 10^2 Pa. On the other hand, the simulations show intense heating as simulated surface temperatures reach 1526 °C. This far exceeds the melting point of the

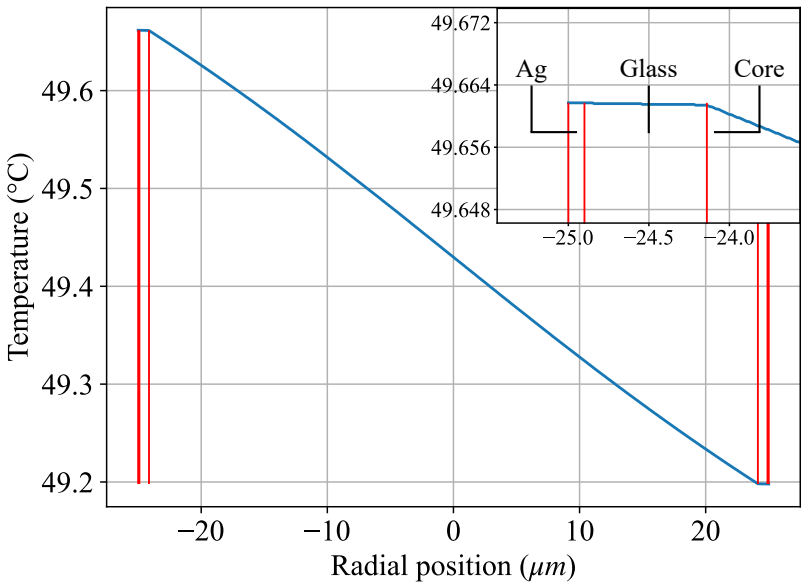
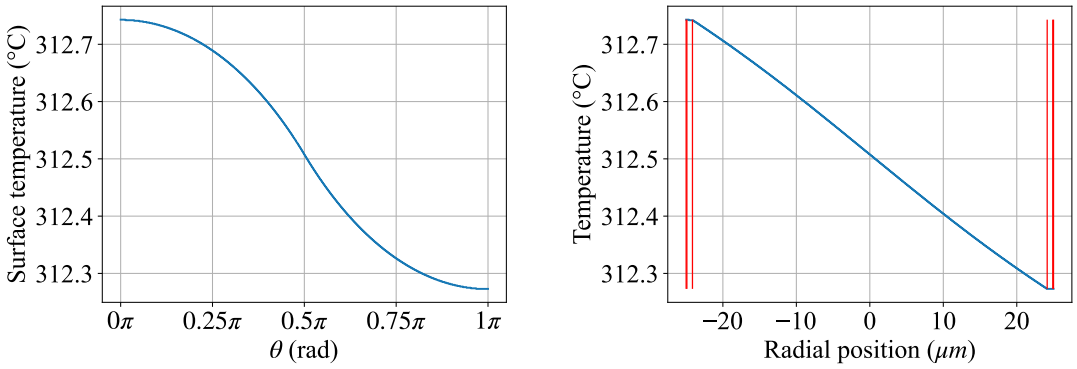
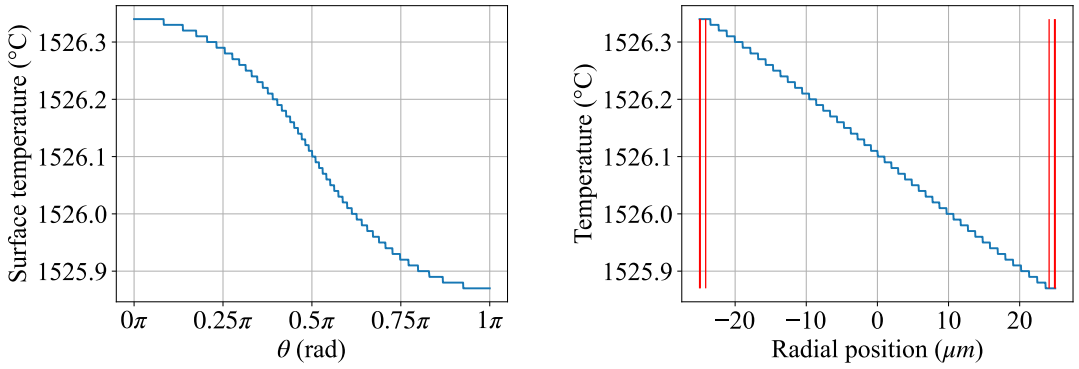


Figure 7.4: Simulated temperature distribution of shell interior from $-r$ to r. Shell layer boundaries indicated by the red vertical lines.



(a) (b)

Figure 7.5: (a) Simulated surface temperature distribution of shell under 10^4 Pa of pressure. (b) Internal shell temperature distribution.



(a) (b)

Figure 7.6: (a) Simulated surface temperature distribution of shell under 10^3 Pa of pressure. (b) Internal shell temperature distribution.

silver coating and possibly the inner glass wall which would lead to severe surface damage or complete destruction of the shell wall. Upward displacement of the shell in the beam focus would weaken the laser intensity incident on its surface until the forces are once again balanced now accounting for photophoretic contributions. It is possible heating is subdued to below damage threshold due to the lower intensity. However, the degree to which the heating would need to be reduced would be quite considerable. Instead, it is likely our previous simplifications assuming an almost stationary target or slow fluid flow regime is invalidated by photophoretic instability. The shell's motion through the air should induce forced convection currents to enhance heat transfer, drawing heat away from the surface, to the surroundings.

At 10^2 Pa and 1 Pa as an extreme case, we obtain a simulated surface temperatures of 1840 °C and 1874 °C respectively. These temperatures are, of course, too high to sustain shell trapping for reasons already discussed. Experimentally, although the shell's vertical position has settled, we see significant instability at 1×10^2 Pa and below, often leading to ejection of shells from the trap. We have only observed two instances of shell levitation at 1 Pa, however in both cases the shell was ejected before measurement could be taken.

As we continue to develop our understanding, we speculate on a number of possibilities to determine the origin of the instabilities observed at the tested pressures. Photophoretic instability due to high surface temperatures is highly likely as observations have been replicatable and align well with the changes in pressure-based interaction regimes described in Sec. 6.5. Natural resonances or instabilities from external noise sources may become more apparent due to the reduced damping under these conditions leading to greater shell oscillation amplitudes or ejection. Finally, the high shell temperatures predicted by the simulations could hold some truth as heat loss to the surroundings becomes increasingly reliant on radiation. A rapid increase in temperature could result in structural damage to the shell's walls. Alternatively, oxidation of the silver coating would diminish its reflectance or create changes to its thermal accommodation resulting in an imbalance of inertial forces.

7.1.3 Photophoresis: briefly revisited

We can use the simulation results to predict the magnitude of photophoretic forces acting on the shell at varying pressure. At $10^5\,\mathrm{Pa}$ we assume an average air temperature of $20\,^\circ\mathrm{C}$. We set $R = 8.314\,\mathrm{J/(mol\,K)}$, $M = 0.029\,\mathrm{kg/mol}$ so that the average gas velocity is $\bar{v} = 462.86\,\mathrm{m/s}$. We take the thermal creep to be $K_{TC} = 1.152$ so $D_g = 4.97 \times 10^{-5}$ which gives the photophoretic force in the continuous-flow regime acting on a $d = 50\,\mu\mathrm{m}$ shell to be $F_{pp}^{K_n<<1} = 1.62\,\mathrm{pN}$. This is ~ 130 times weaker than the weight of the shell ($mg = 210\,\mathrm{pN}$). We can repeat this for pressures $10^4\,\mathrm{Pa}$ and $10^3\,\mathrm{Pa}$. We must then scale $\bar{v}$, D_g and p^* accordingly. For simplicity, we assume the thermal creep coefficient to be constant as we remain in the $Kn << 1$ limit. Then $F_{pp}^{K_n<<1}|_{P=10^{-4}} = 16.2\,\mathrm{pN}$ and $F_{pp}^{K_n<<1}|_{P=10^{-3}} = 162\,\mathrm{pN}$. Interestingly, the force $F_{pp}^{K_n<<1}|_{P=10^{-3}}$ now begins to approach the force required to balance the weight of the shell, additional to the radiative pressure already supporting levitation. The result is a net force accelerating the shell upward.

The characteristic pressure p^* denotes the pressure at which the mean free path of the air equals the shells size. For our $50\,\mu\mathrm{m}$ shell this is when $p^* = 557\,\mathrm{Pa}$. The photophoretic force is maximised when $p = p^*$ giving $F_{ph}|_{P=557} = 290\,\mathrm{pN}$ - a force greater than the shell's weight. Then finally for completeness, we continue the photophoretic force calculations for $K_n > 1$ giving $F_{pp}^{K_n>1}|_{P=10^{-2}} = 52.2\,\mathrm{pN}$, a quarter of the shell's weight showing the downward descent of the shell to its original equilibrium.

7.2 Discrete Fourier analysis

Later in this chapter we will present the analysis of experimental shell position data. However, before we get to that stage, we first provide practical insights on how the data was processed.

Chap. 6 presented background on using Fourier analysis to model the expected behaviour of levitated shells. Transformation of the time varying position measurements allows us to reveal its frequency spectrum and inspect key properties such as resonant frequencies and other spectral features. In practice, the idealised continuous data stream is now replaced with discrete measurements in time and so we instead use the Discrete (-time) Fourier transform (DFT),

$$\tilde{a}_k = \sum_{m=0}^{N-1} a_m \exp\left(-2\pi i \frac{mk}{N}\right). \tag{7.3}$$

where $a_m = \exp(2\pi f m \Delta t)$. The time interval between consecutive samples is Δt and frequency f is the reciprocal quantity. The DFT can be efficiently calculated using fast-fourier transform (FFT) methods available in Python's NumPy [157] or similar packages. The DFT can be used to obtain the power spectrum (units: $\mu\mathrm{m}^2$), the power spectral density (units: $\mu\mathrm{m}^2/\mathrm{Hz}$) or their respective linear analogues (units: $\mu\mathrm{m}$ and $\mu\mathrm{m}/\sqrt{\mathrm{Hz}}$ respectively). Knowing what form of the DFT one requires and applying the appropriate normalisations can feel unintuitive at times and lead to some confusion. Therefore for

purposes of clarity, and to standardise notation for compatibility with future works, we will take some time go through definitions and terminology.

It can be seen from Eq. 7.3, increasing samples N, increases the amplitude of the frequency bins. This is problematic if trying to compared spectra of different lengths and so Eq. 7.3 must then be normalised so that it is not dependant on N. The normalisation depends on the type of spectrum required by the analysis. The total power in the original data a_m can be expressed in the following ways [158],

$$\sum_{m=0}^{N-1} a_m^2 \equiv \text{sum squared amplitude} \tag{7.4a}$$

$$\frac{1}{N}\sum_{m=0}^{N-1} a_m^2 \equiv \text{mean squared amplitude} \tag{7.4b}$$

$$\Delta t \sum_{m=0}^{N-1} a_m^2 \equiv \text{time-integral squared amplitude} \tag{7.4c}$$

We can then use Parseval's theorem to determine the appropriate normalisation to its Fourier counterparts. The theorem still holds for DFTs but is modified to accommodate discrete sampling,

$$\sum_{m=0}^{N-1} |a_m|^2 = \frac{1}{N}\sum_{k=0}^{N-1} |\tilde{a}_k|^2 \tag{7.5a}$$

$$\frac{1}{N}\sum_{m=0}^{N-1} |a_m|^2 = \frac{1}{N^2}\sum_{k=0}^{N-1} |\tilde{a}_k|^2 \tag{7.5b}$$

$$\Delta t \sum_{m=0}^{N-1} |a_m|^2 = \frac{\Delta t}{N}\sum_{k=0}^{N-1} |\tilde{a}_k|^2 \tag{7.5c}$$

We opted for the mean squared amplitude due to its intuitive result, computational simplicity and its generally preference in periodic signals processing resources. Another viable option could be the time-integral squared amplitude. It does not change with total measurement time nor with sampling rate for equal measurement time and so is suited to the factors relating to the measurement procedures we use. The time-integral form is usually used in the analysis of impulse or transient signals where the total energy over the measurement period is of interest rather than the average power. A change in the number of samples does however affect the frequency bin width and must be compensated when comparing two spectra of different lengths, and its relation to the power spectral density is less straightforward.

The power spectral density describes how the power is distributed in the frequency domain. If only the real parts of the DFT are considered as is often the case for physical systems, then we calculate the one-sided PSD. Parseval's theorem can be maintained by symmetry of the DFT power spectrum. We scale by a factor of 2 to account for the power lost in

the complex components of the DFT.

$$PSD_k = \frac{2|\tilde{a}_k|^2}{N f_s}, \quad k = 0, 1, ...N/2 \tag{7.6}$$

The PSD will show spectral sensitivity up to the Nyquist frequency, $f_{Nyq} = f_s/2$. The frequency bin width in the PSD is given by $\Delta f = f_s/N$. Although this form is dimensionally correct, further considerations may be required before it is used in analysis. This will be discussed in the next part.

7.2.1 Signal widowing

The DFT assumes the signal to be periodic, however typical finite time series data will resemble a small portion of a signal of seemingly infinite length. The ends of the data will have discontinuities that to not transition smoothly as would be expected of a true periodic signal. This leads to spectral leakage in the DFT spectrum resulting in a less accurate spectral representation of the signal. Window functions are applied to taper the edges to zero so that the data does in fact resembles a periodic signal. This minimizes the introduction of artificial high-frequency components and the power spectrum is concentrated more around the true frequencies. However this may be at the cost of reduced response amplitude in the frequency domain. Suppose a window, w_j, is applied to the initial signal, then the PSD is defined as [159],

$$PSD_k = \frac{2|\tilde{a}_k^w|^2}{N f_s W_{norm}}, \quad k = 0, 1, ...N/2 \tag{7.7}$$

where $\tilde{a}_k^w$ is the DFT of the windowed data. The sampling frequency f_s is scaled by the noise bandwidth of the analysis window. This step is necessary to ensure the PSD is independant of the specific analysis bandwidth used in its calculation. The window normalisation term for the PSD takes the form,

$$W_{norm} = \frac{1}{N} \sum_{m=0}^{N-1} w_m^2. \tag{7.8}$$

When no windowing is applied it is equivalent to applying a uniform/rectangular window length N. Then the noise bandwidth is the actual bandwidth of the system which is equal to the number of samples N, and W_{norm} is equal to 1 so the PSD is unchanged.

7.2.2 DFT summary: worked example

Suppose real position time series data, b_m, is obtained from a live experiment. Windowing is applied so that the data appears periodic to the DFT. We can apply a Hanning window, which is a weighted sum of cosines window, commonly used to reduce spectral leakage. It takes the form,

$$w_m = \frac{1 - cos(z)}{2}, \quad z = \frac{2\pi \cdot m}{N}, \text{ for } m = 0, 1, ..., N-1 \tag{7.9}$$

The DFT, $\tilde{b}_k^w$, is then calculated to transform the windowed position data into its frequency domain.

$$\tilde{b}_k^w = \sum_{m=0}^{N-1} b_m w_m \exp\left(-2\pi i \frac{mk}{N}\right), \quad k = 0, 1, ..., N-1$$

As we are only interested in the PSD, we may by-pass calculating the power explicitly and go straight to the PSD without further compensation,

$$PSD_k = \frac{2|\tilde{b}_k|^2}{N \cdot fs \cdot W_{norm}}, \quad k = 0, 1, ..., N/2$$

The Nf_s normalisations ensures sample length invariance, in line with the mean squared amplitude. Since a window was applied prior to the DFT calculation we must ensure that to is appropriately normalised using Eq. 7.8. For a Hanning window this comes out at $W_{norm} = 0.375$. Assuming the data to be stochastic, we can use the properties of its variance as a sanity check to ensure the calculations were performed correctly. Recall from Chap. 6 we can relate the variance in position to the sum of the PSD over the frequency domain.

$$\sigma^2(b_m) = \sum^{N/2} PSD_k \Delta f$$

The variance can be calculated directly from the position data and compared with the PSD sum provided. Minor discrepancies may arise due to the finite frequency resolution in the DFT.

7.3 Analysis of shell oscillations

An oscillating shell's position is tracked by imaging its scattered light onto a position detector (PD). Fig. 7.7 shows a photograph of the diagnostics layout consisting of the shell imaging and position sensing setups. The light was collected using a single 2" $f = 15\,\text{cm}$ aspheric lens (mounted inside the chamber) that provided a magnification of $1.5\times$. Position measurements were taken initially under atmospheric pressure using two linear PDs for the vertical and horizontal spatial axes.

Spatial distribution of an oscillating shell

The vertical PD operated at a Nyquist frequency of 4.7 kHz, collecting 10^6 samples in 106 s. The recorded position data is plotted as a time-series in Fig. 7.8(a). The measurement indicates asymmetry in the shell's motion evident by the sharp upper edge in the data - in contrast to the less well defined lower edge. The scatter signal produces an inverted image so negative vertical positions on the sensor correspond to a higher position inside the trap. The position data demonstrates the asymmetry in the vertical distribution of radiative pressure as downward displacement is restricted as the beam intensity increases lower in the trap. There is less resistance in the upward direction with only the weight of the shell and Stoke's drag counteracting any upward motion. This creates a weaker confinement boundary in the upward direction.

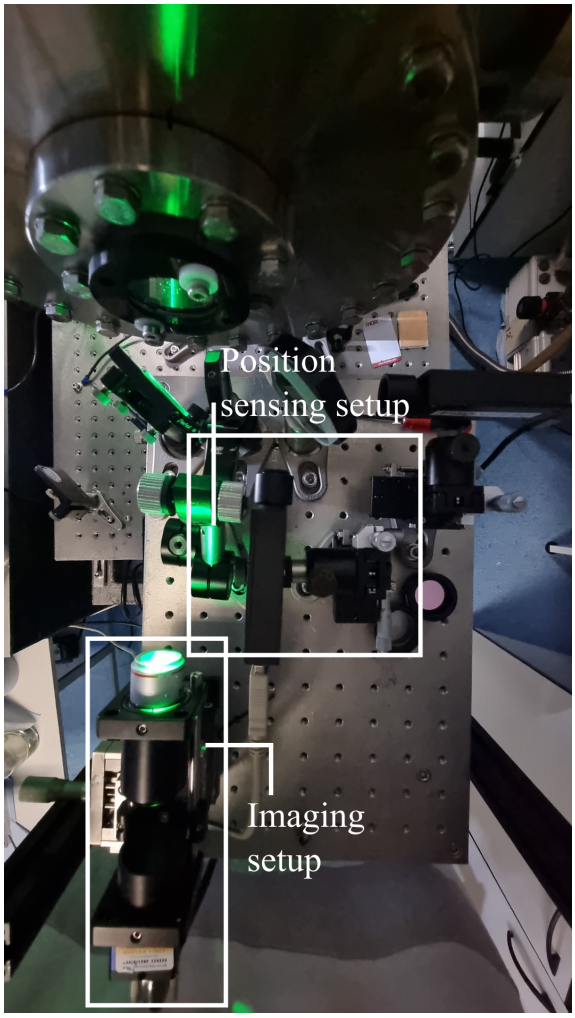


Figure 7.7: Diagnostics setup for the vacuum chamber levitation system. Imaging and position sensing arms were installed on a raised breadboard platform.

The spatial distribution of the shell's position measurement can be better visualised by the histogram shown in Fig. 7.8(b). Here we can see the equilibrium position at 0 µm and what resembles two distinct distributions. Video footage of the levitated shell showed relatively slow cyclic oscillations with large vertical displacement from its equilibrium position in line with the profile seen in Fig. 7.8. The pronounced asymmetry in its histogram is then likely due to these dynamics.

Brownian dynamics would dictate the distribution to be Gaussian-like. Rough Gaussian fits were applied to the respective histogram distributions shown in Fig. 7.9. The distributions are visualised in (a) linear-linear and (b) log-linear axes to inspect the quality of the fit particularly towards the limbs. The Gaussian profiles largely fit well, however there is noticeable deviation at the limbs indicating additional mechanisms that are currently unaccounted for.

Unlike the vertical position data, horizontal dynamics should not exhibit the same asymmetry since the force distribution is symmetric about its equilibrium. For the same lev-

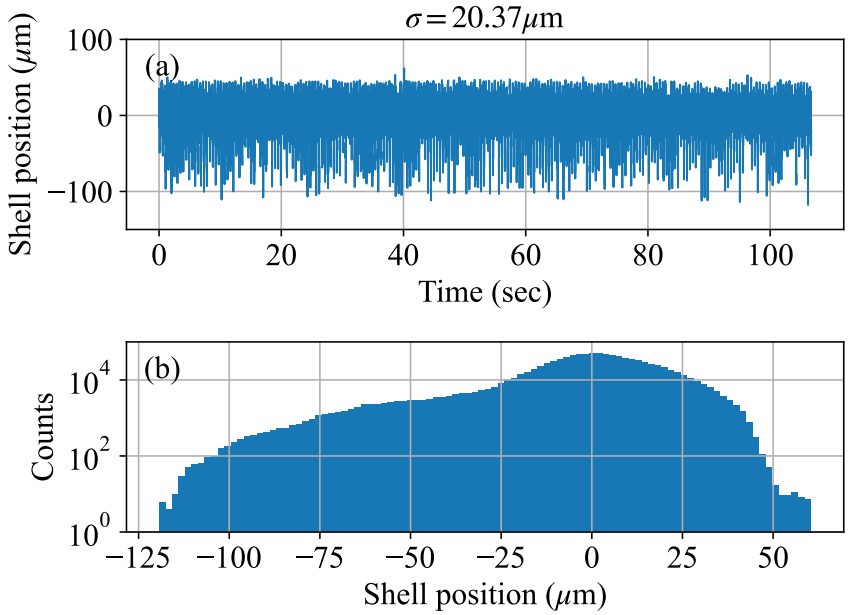


Figure 7.8: Vertical stability shown as (a) position time series data over 106 s duration and (b) position histogram for 37 µm shell.

itated shell as before, Fig. 7.10(a) shows the horizontal position time series to be much more evenly distributed about equilibrium. We so note a larger displacement amplitude than the vertical likely due to the weaker radial stiffness of the trap. Gaussian profiles were applied to the linear-log and log-log histograms, which show a more favorable fitting than before. The two-peak distribution is much more subtle possibly due to some horizontal coupling of the external driving forces.

Spectral analysis of an oscillating shell

To deepen our analysis we proceed to look at the Fourier spectrum of the previous spatial data. Fig. 7.12 plots the position PSD. The expected profile characteristic of Brownian-like motion is indicated in green. We have a flat low frequency region that begins to slope down at a corner frequency of around 100 Hz before hitting the high frequency noise floor. The brownian portion of the PSD plot was fitted using,

$$S(f) = \frac{4k_bT\Gamma_f}{(2\pi)^3 m^2} \cdot \frac{1}{(f_c^2 - f^2)^2 + f^2\beta_f^2} \tag{7.10}$$

which appropriately scales the $S(\omega) \to S(f)$ domain transformation. Additionally, Fig. 7.12 shows the lower frequencies to be dominated by external driving forces that aren't accounted for by the thermally driven oscillator model. These sharp spectral features are due to anomalous oscillations at 2 Hz frequency that were confirmed by comparing frames captured using a fast video camera operating at 159 frames/sec. Higher harmonics of the primary peak are also present due to additional components in the oscillation's Fourier

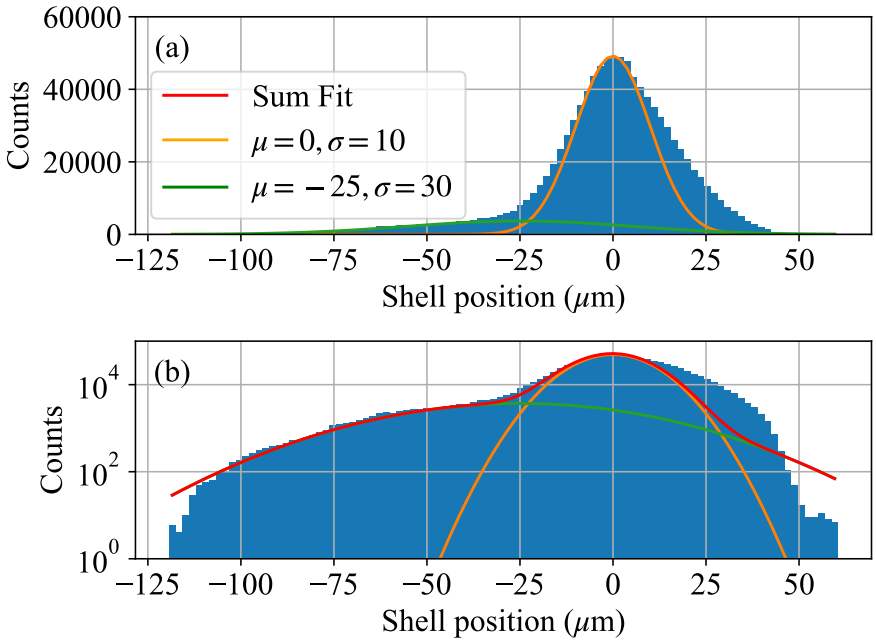


Figure 7.9: Vertical position distributions shown in (a) Linear-linear axes histograms with fitted Gaussians and (b) the same fittings plotted on Log-linear axes with an additional sum fit to show the combined profile contributions.

decomposition. The peaks were fit using a modified damping dependence that quadratically weakens with the harmonic order. This fitting was somewhat arbitrarily chosen as an attempt to understand the dependence of the fitting variables on the observed dynamics. Further investigation is required to better understand this behavior.

7.3.1 Spatial variance of an oscillating shell

We have three methods to determine the variance in shell position. The first is by Eq. 6.25 (restated here as $\sigma_x^2(t) = 4\pi k_b T\Gamma/\beta\omega_0^2 m^2$). This is the expected variance for a thermally driven oscillator as derived in Chap. 6. The second is directly from the position data as simply $var(x)$ for position x. We can then compare these quantities to confirm the stochastic nature of the position data, or lack thereof, in which case the result would allude to the presence of other driving mechanisms. The final method is from the sum of the PSD. Its agreement with $var(x)$ confirms whether the PSD was formed correctly from the position data with the appropriate normalisations.

The variance results for the vertical data are presented in Tab. 7.1. We find a stark difference between the expected and experimentally obtained results. This is not surprising given the anomalous profile of the shell's position distribution. Additionally, windowing the data appears to slightly worsen the variance result. This result is unexpected and may indicate a small error in the PSD pipeline. The total energy of the signal should be reduced because most windows scale the amplitude near the edges of the signal. The normalisation aims to compensate for this but it may be imperfect. This would result in

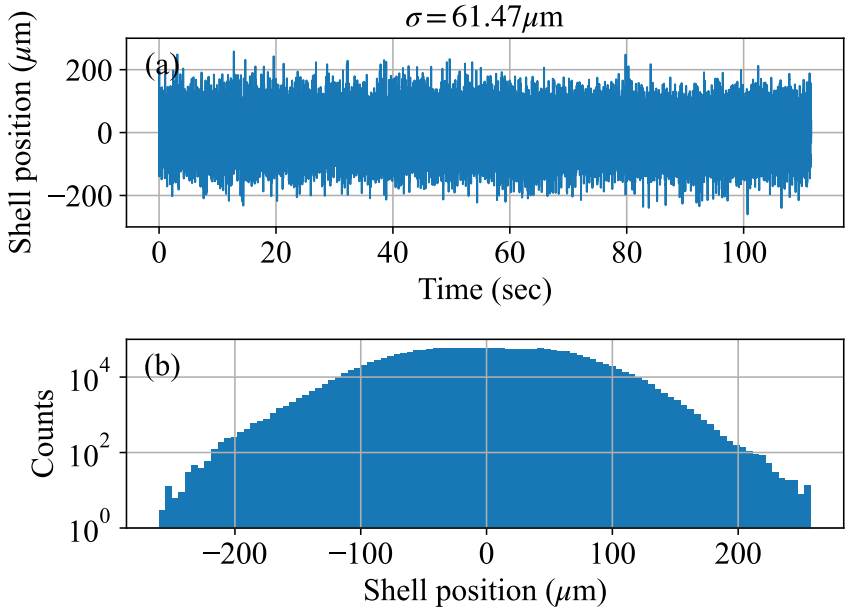


Figure 7.10: Horizontal stability shown as (a) position time series data over 106 s duration and (b) position histogram for 37 µm shell.

an under-estimation whereas we see an overestimate. Windowing is primarily applied to reduce spectral leakage, however applying it to sharp resonant features may smear the energy into neighbouring bins leading to an over-estimation in power and, as we see, the spatial variance. It is worth noting the period of the 2 Hz oscillation can be distributed as whole integer cycles within the 106 s measurement duration, and so it is possible the original data had little spectral leakage to begin with leading to an over-correction. This appears to be a quirk of this particular dataset and may not always be the case.

Tab. 7.2 again compares the expected and computed spatial variances, this time for the horizontal data. We see good agreement in the experimental methods but again significant deviation from the thermally driven oscillator expectations. This allows us to definitively conclude the driving mechanisms acting on this shell are dominated by factors other than thermal.

Table 7.1: Comparision of results for expected variance based on a thermally driven oscillator, variance computed directly from position data and variance computed from the sum of the PSD over the frequency domain. It is often more intuitive to work in terms of standard deviation and so corresponding values are included.

	$4\pi k_b T\Gamma/\beta\omega_0^2 m^2$	Var(position)	$\sum(PSD\Delta f)$	
			no-window	window
σ^2(µm^2)	0.0167	415	415	438
σ(µm)	0.13	20.37	20.37	20.94

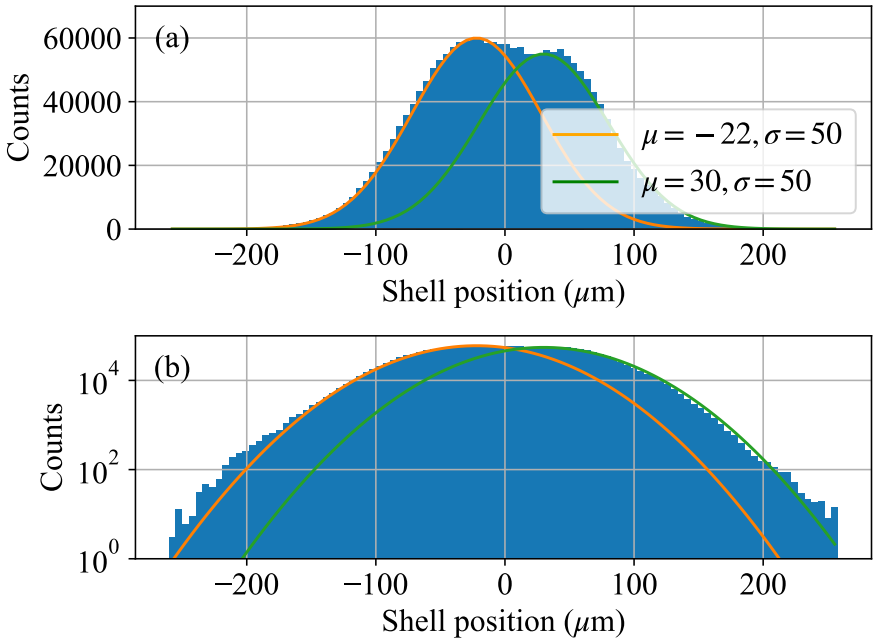


Figure 7.11: Horizontal position distributions in (a) Linear-linear axes histograms with fitted Gaussians. (b) The same fittings plotted on Log-linear axes.

Table 7.2: Similar to Tab. 7.1 the entries show the expected and computed spatial variance and standard deviation in the horizontal axis data.

	$4\pi k_b T\Gamma/\beta\omega_0^2 m^2$	Var(position)	$\sum(PSD\Delta f)$	
			no-window	window
$\sigma^2(\mu m^2)$	0.0138	3779	3779	3829
$\sigma(\mu m)$	0.12	61.47	61.47	61.88

7.4 Optical levitation at low pressure

A second levitation system was constructed inside a vacuum chamber for low pressure optical levitation. Fig. 7.13 shows the chamber installation with Fig. 7.14 showing a levitating shell inside the chamber.

Fig. 7.15 present results taken from a 90 µm shell optically levitated at lower pressure. The shell was initially captured at atmospheric pressure. The chamber was sealed shut and the pump was engaged to begin reducing the pressure. Stability measurements were taken at reduced static pressures. The motivation here was to demonstrate optical levitation at reduced pressures approaching the conditions appropriate for use as laser firing targets and to observe any changes in pressure-dependent behaviour such as spatial stability or changes to natural resonance. In most instances, the position data was shown to be Browinian-like with the exception of Fig. 7.15(b) and to an extent (e). The tail of the histogram in Fig. 7.15(e) corresponds to the large spikes seen around the 20 s mark in the time series data. In spite of these anomalies, the shell is shown to be highly stable at

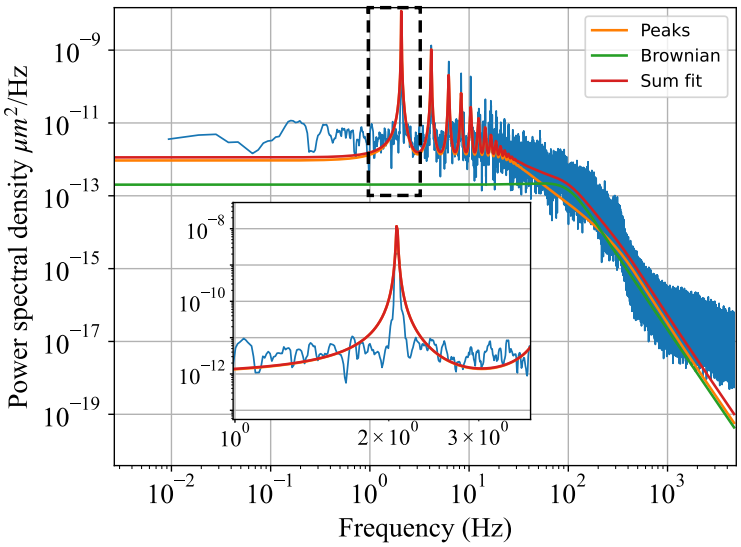


Figure 7.12: Power spectral density of 37 µm shell using 10^6 samples collected over 106 s. Brownian (green) and rough oscillatory motion (orange) modelled applied to fit the spectrum. Low frequency oscillations at 2 Hz oscillation with higher harmonics indicating complex oscillation structure.

the tested pressures with deviations being on the order of $< 8\,\%$ of the shell diameter. A common 30 Hz feature is present in the PSD plots attributed to laser fluctuations. The PSDs are largely featureless with estimated f_c on the hertz-level. In instances such as Fig. 7.15(b) and (c), the corner frequency may perhaps be sub-hertz, however the data resolution is insufficient to fit lower frequencies. To check this, the corner frequency of a 90 µm shell with $\sigma \sim 5\,\mu$m is expected to be on the mHz level assuming the oscillator is purely thermally driven.

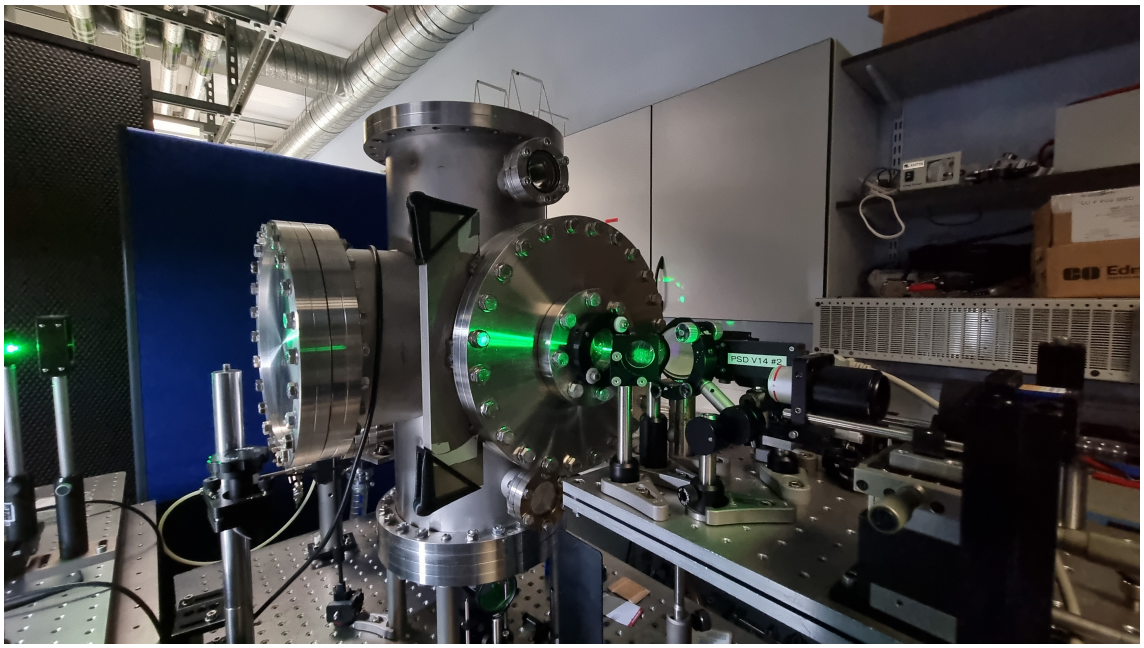


Figure 7.13: Vacuum chamber setup.

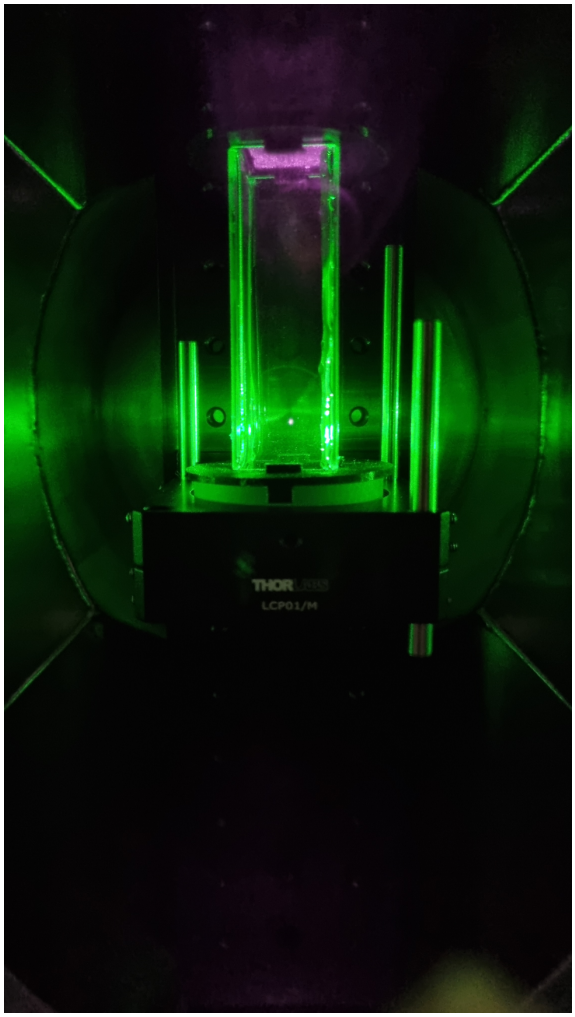
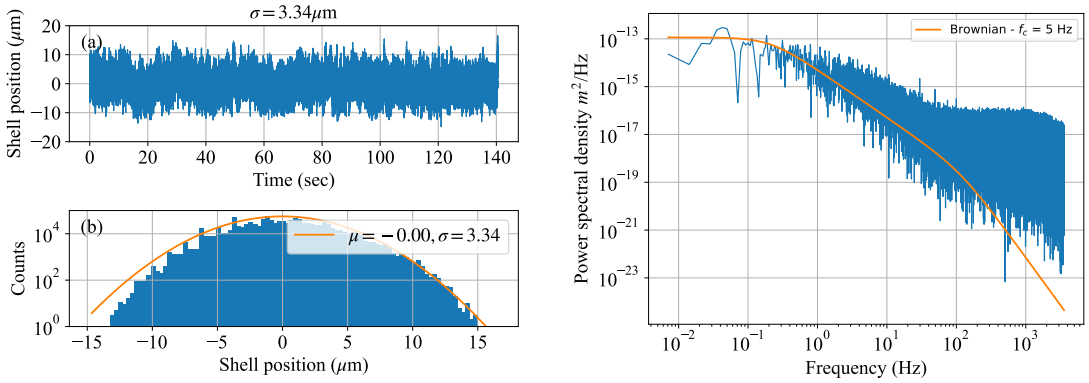
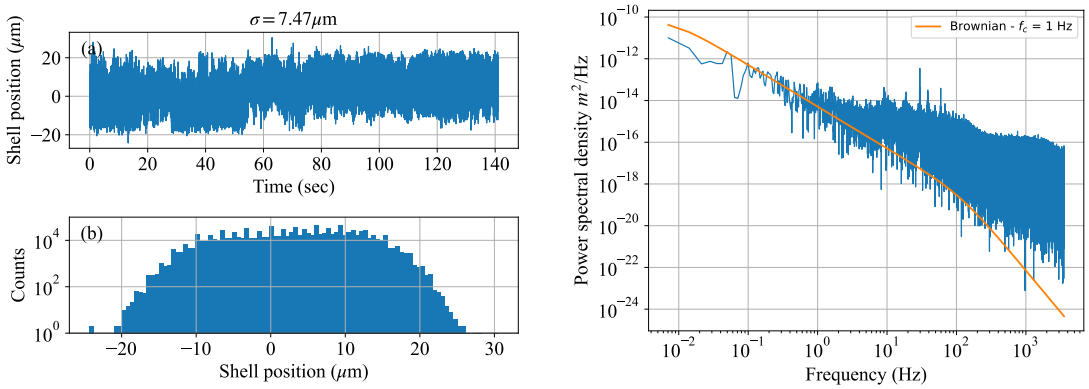


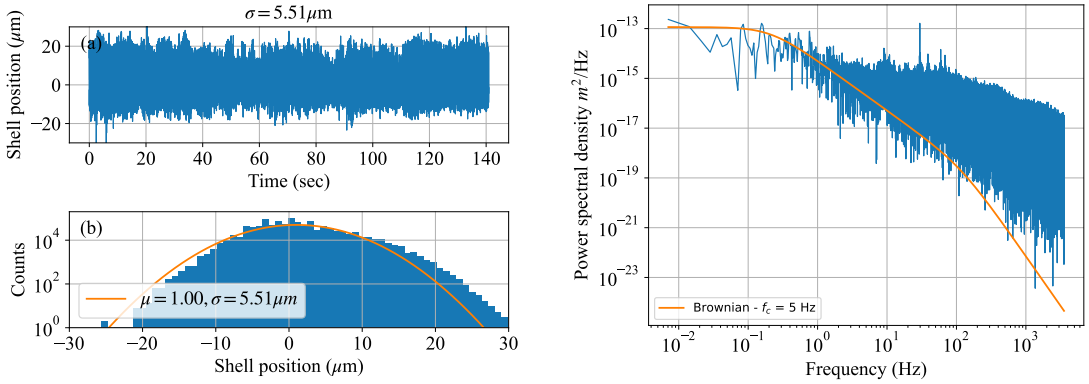
Figure 7.14: Levitating shell inside the draft collar of the vacuum chamber. The shell is back illuminated using a green LED.


σ = 3.34μm
(a)
Shell position (μm)
Time (sec)
(b)
Counts
μ = −0.00, σ = 3.34
Shell position (μm)
Brownian - f_c = 5 Hz
Power spectral density m^2/Hz
Frequency (Hz)

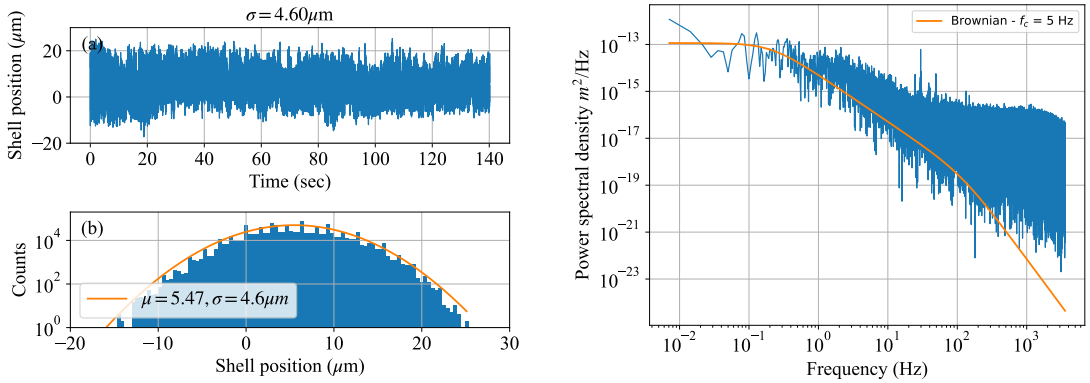
(a)


σ = 7.47μm
(a)
Shell position (μm)
Time (sec)
(b)
Counts
Shell position (μm)
Brownian - f_c = 1 Hz
Power spectral density m^2/Hz
Frequency (Hz)

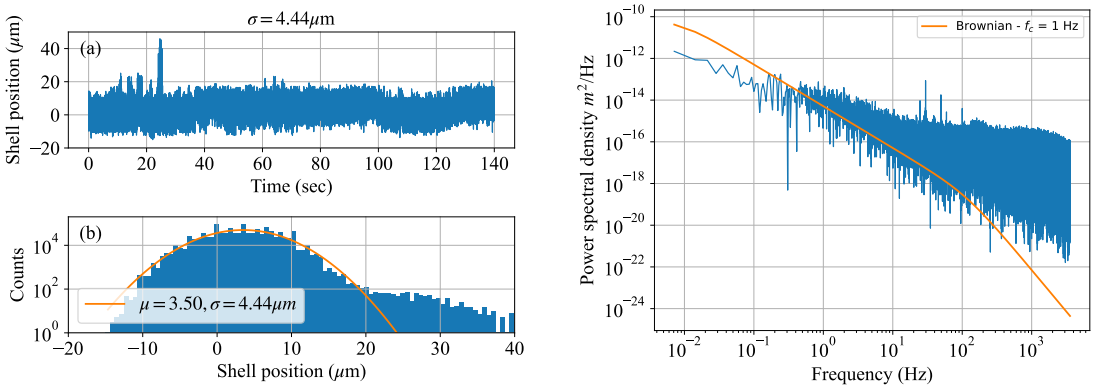
(b)


σ = 5.51μm
(a)
Shell position (μm)
Time (sec)
(b)
Counts
μ = 1.00, σ = 5.51μm
Shell position (μm)
Brownian - f_c = 5 Hz
Power spectral density m^2/Hz
Frequency (Hz)

(c)



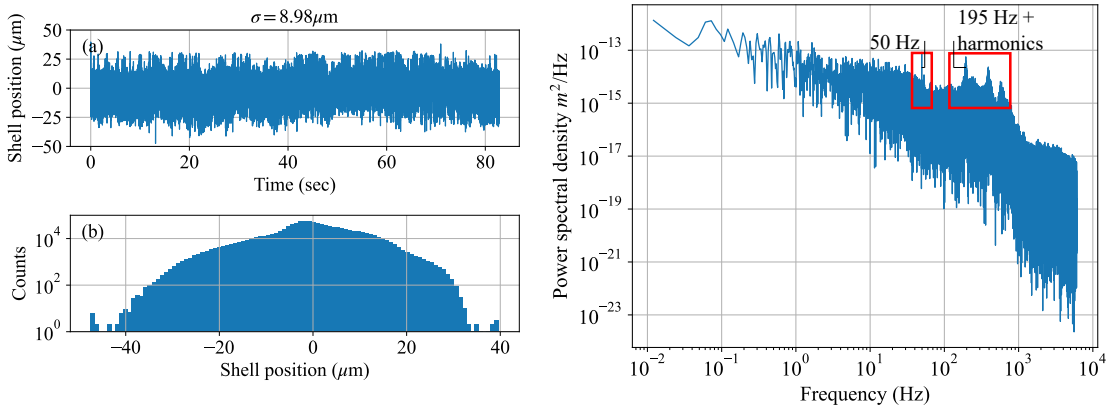
(d)



(e)

Figure 7.15: Position-histogram and PSD results for 90 µm shell levitated at (a) 10^5 Pa (b) 7×10^4 Pa (c) 4×10^4 Pa (d) 8×10^3 Pa (e) 1×10^3 Pa. 10^6 samples were obtained at a rate of $f_{Nyq} = 3.6$ kHz. In all cases the PSD fit shows f_c around the Hertz level or lower.

Where Fig. 7.15 shows results down to 1×10^3 Pa, stable levitation at lower pressures has also been demonstrated. Fig. 7.16 shows position data and the power density spectrum of a 80 µm shell levitating under 500 Pa. Additional spectral features are seen in at 195 Hz and its harmonics that do not correspond to the laser fluctuation lines seen in Fig. 7.15. Further yet, levitation of a 60 µm at pressures as low as 100 Pa have been observed. However it was loosely confined by comparison with $\sigma_v \sim 20$ µm.



(a) (b)

Figure 7.16: (a) Position-histogram and (b) PSD results for 80 µm shell levitated at 500 Pa pressure.

7.5 Vertical position stabilisation

Power modulated stabilisation was intended to be used as a general correction mechanism against vertical instability in the levitated shells. The methodology here is similar in principle to methods in parametric feedback cooling [142, 143]. Here, the trapping beam power is modulated based on the target's position inside the trap. Data is relayed from position sensors to external drivers to vary the trapping beam power based on the target's oscillation about it equilibrium. Constant phase correction of the modulation signal is required to coincide with the target's trajectory so that a kick can be applied to counter-act unwanted motion rather than to excite it. In our case, we expected fixed-phase single-frequency modulation so suffice. This is because the expected dynamics timescales for our targets trapped in air was expected to be sub-100 Hz while the modulation drivers can operate at the kHz level. Therefore, the target would only see an averaged effect. Successful demonstrations had been seen in previous MSc projects on oil droplets. Eventually further improvements were seen in implementing a variable modulation approach based on the target's trajectory. This was achieved by tracking the oil droplet's position using its scattered signal then using time interpolation methods to predict is trajectory over a small time interval and compute the change in power required to correct it.

The setup in Fig. 7.17 was used to modulate the trapping beam power. However, we ran into key systemic issues that made translating a direct copy of this technique to our system unachievable without modification of our position measurement technique, and so

the improvement to shell stability was not clear. This is because the shells were mostly stable by themselves up to the micron level and for most of the experiential time were near the resolution limit of the sensor's spatial sensitivity - sensor sensitivity was later improved. Position correction where the modulated power was adjusted to the shell's trajectory was later implemented, however this too was unsuccessful. This was due to the feedback loop correcting against erroneous position data due to rotational scattering being confused with vertical position change.

Previously, rotation could only be observed when a small defect or surface protrusion was visible. Otherwise it could sometimes be indicated in the position data as a highly periodic signal. However shells have also been observed to show strong oscillatory behaviour and so the nature and origin of the signal was not always clear. By removing the filter in the imaging microscope the scatter could more clearly be seen as being rotational even for shells that seemed to be perfectly spherical. This scattering was found to be more common than previously thought. However the strength of the signal varied case by case - sometimes not visible at all. Given this unpredictability, our method for stabilisation could not be implemented and required a rework of our detection proceedures.

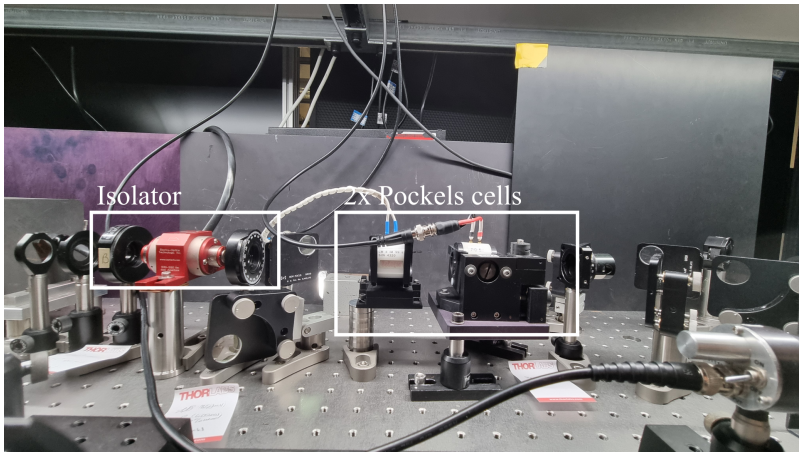


Figure 7.17: Power modulation setup. Due to low driving voltage range of the HV-drivers, two Pockels cells were used in series to get 10 % swing.

7.6 Trapping power modulation response

We have previously mentioned concerns in reliably predicting the spectral characteristics of our levitated shells' oscillations. Additionally, as discussed in the last section, the shells seemed to be robust against fixed frequency modulation or at least their effect was unclear. Assuming the undriven system is still harmonic, the lack of reliable measurement could be due the resonant power being too weak relative to the background to measure accurately, or that broadening effects acted to smooth its spectral prominence. To test this hypothesis, a frequency sweep was conducted by modulating the trapping beam power using a signal generator connected to Pockells cells via a high-voltage driver. The idea here is that when the modulation frequency coincides with resonance, the spectral features in Fourier-space

will be magnified due to self-excitation.

Modulation frequencies were driven from 20 Hz to 100 Hz. The peak amplitude of their respective power spectra was recorded. This is shown in Fig. 7.18. The trend shows a generally diminishing power share at the modulation frequency for increasing modulation frequency. The power amplitude doesn't appear to show signs of levelling off at the low frequency end. This could allude to the resonant frequency being below the range that was tested. Given the shell FFTs are sensitive to a magnitude or so below the Hertz level, there is scope to reduce the low end of the modulation frequencies for further testing. However care must be taken to select frequencies that aren't too slow so that the shell doesn't risk being dropped out of the trap. The FFTs also have reduced data resolution at low frequencies. Since sensitivity here is dependant on the integration time, longer measurement periods may be required to accurately sample these frequencies.

Fig. 7.18 shows a prominent feature at 50 Hz. It is possible the modulation is being magnified by self-excitation. The sensors have been shown to be resistant to mains and other electronic noises as confirmed from previous testing. The BNC cables connecting the electronics have been shown to pickup various RF sources from the lab and so it is possible the sensors are noise adverse yet the driving electronics are still susceptible to bleed through or antennae pick-up. Results at 40 Hz and 60 Hz appear to be positioned in line with the general trend.

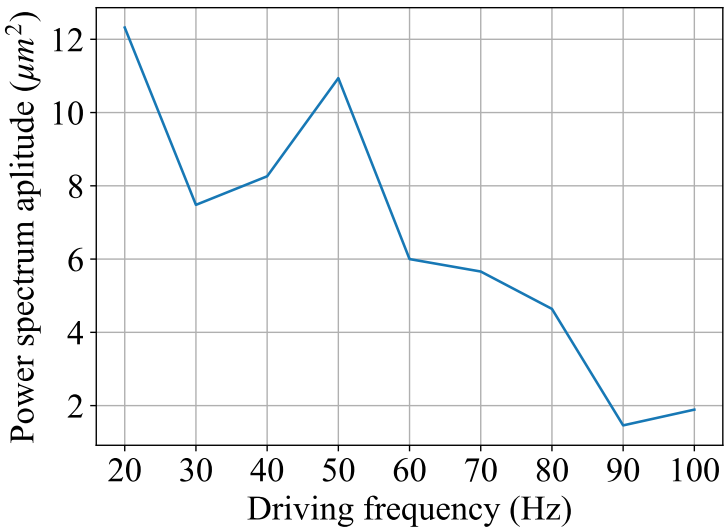


Figure 7.18: Peak oscillation amplitudes in the FFT power spectra of the respective modulation frequencies is plotted.

7.7 Multi-shell levitation

Our work so far has exclusively looked at spherical shell levitation. The symmetry of the annular beam and smooth shell surface geometry ensures a balanced distribution of optical

forces that facilitates stable levitation. However, on several occasions we have observed the levitation of multi-shell and non-spherical targets. In this section we showcase a few such examples. It is useful to note that future applications of levitated shells in high-intensity laser experiments could benefit from the ability to create arrays of targets which may boost the local-electric field in a plasmonic-like resonance structure.

7.7.1 Spatially separated shells

We have observed instances of spatially separated dual-shell levitation. Fig. 7.21 shows two 30 µm shells vertically displaced by 20 µm and stably trapped under continuous illumination. The lower shell fell out of the trap when exposed to fixed frequency power modulation - the upper shell remained trapped. Two 50 µm trapped shells have also been observed this time vertically separated by 15 µm. Unlike the previous case these were highly unstable with the upper shell exhibiting rapid oscillations while the lower was stationary. The two then combined to form a more stable arrangement but were observed to flip orientation several times over the observation period. The orientation changes were not continuous gradual changes but sudden and remained in this position until flipping again ($\sim 5-10$ min between flips). It is thought the flips were perhaps triggered by small fluctuations in the trap either due to the beam or environmental factors perturbing the shell cluster to position itself in to an alternative stable orientation. Stranger yet, Fig. 7.19 shows a peculiar instance of a two-shell cluster with a third shell that was both vertically and radially separated, likely indicating the creation of a secondary trapping region down-stream of the lower shell.

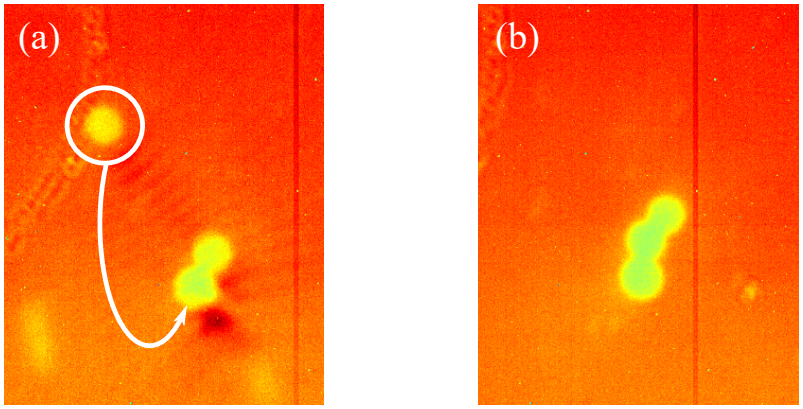


Figure 7.19: (a) Two 67 µm trapped shells with a third vertically and radially separated. Deep-red spots on the lower surfaces denote scattering of the trapping beam. (b) The lone shell was observed to loop underneath and attached itself to join the cluster.

The mechanism by which this type of trapping occurs is currently unclear. It is thought mutual interactions may be at play - static charge could build from the shell plume when loading into the trap or opto-thermal effects are likely to contribute [160, 147]. There may be a size preference for similar sized shells as seen in the above cases. Further investigation is required simulating the optical interactions to better understand the exact nature of the trapping mechanism.

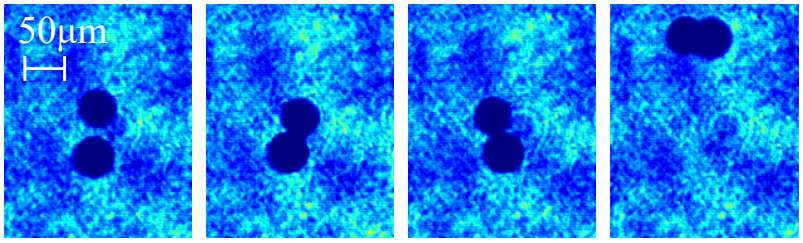


Figure 7.20: (Left to right) Images of two 50 µm shells initially separated by 15 µm then combine to form shell cluster. Cluster is observed to change orientation over time. When laying flat the shells sat higher in the trap.

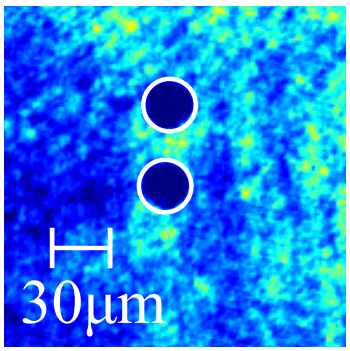


Figure 7.21: Two 30 µm levitating shells vertically separated by 20 µm

7.7.2 Shell clusters

The levitation of shell clusters was far more common, and could be somewhat reliably reproduced by introducing adhesive impurities into the shell samples such as oily finger prints. Additionally, the frequency of initially spatially separated levitating shells soon combining to form a cluster is undocumented but provides another route through which this can be achieved. Various clustering configurations have been observed ranging from simple vertically stacked shells to more complex structures. Examples are shown in Fig. 7.22. Not only are the shapes of these levitated targets peculiar but the combined mass that is being levitated is also remarkable. In the case of Fig. 7.22(c) the total mass is of order 100 ng. It was levitated with high positional stability with standard deviations measured to be 10.2 µm in the vertical and 4.3 µm in the horizontal. The mass here is equivalent to a 90 µm shell with a wall thickness and footprint of 60 µm. The stacked target arrangement then concentrates more mass into a smaller cross-sectional area. This possibly enhances stability as it experiences greater trap stiffness as it sits deeper in the trapping potential.

The possibility of levitating non-spherical targets opens an exciting avenue to explore the levitation of targets for applications where bespoke target arrangements of geometries may be required or beneficial. In the realm of high-intensity laser-target interactions, the proximity of metallic surfaces could increase the apparent field intensity through plasmonic enhancement [161, 162] facilitating the excitation of higher intensity interactions that the firing laser itself cannot directly probe.

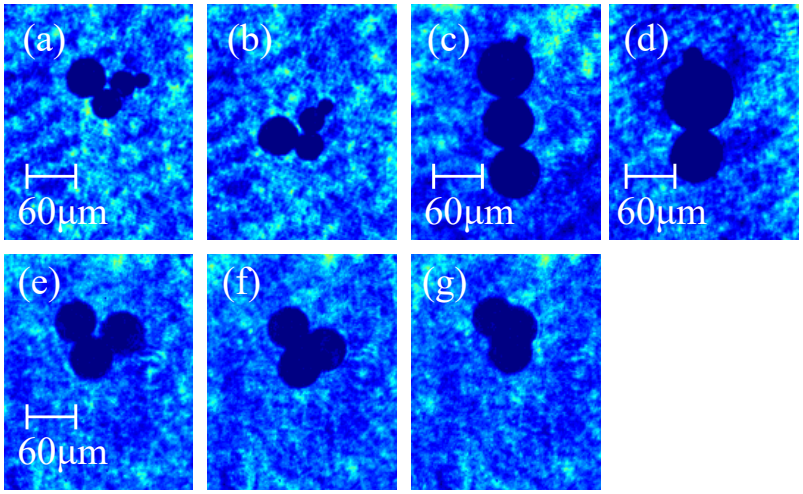


Figure 7.22: (a) Optically levitated 4-shell cluster (b) cluster rotated. (c) Vertical stack of three 60 µm shells. (d) Top-heavy stack. (e) The Mickey Mouse cluster comprised of three 43 µm shells (f-g) cluster rotated.

Applications may also be found in levitated sensors for gravitational wave detection [163]. The frequency scaling of these opto-mechanical systems is much more favourable than laser interferometric sensors as the former is limited by Brownian noise rather than shot noise. It is proposed that a 75 µm sphere in a 100 m cavity could extend the search volume of sources between 10-300 kHz by 10-10^3 times when compared with Advanced LIGO [164]. Additionally the projected force sensitivity is determined by the photon recoil limit and the scattering regime of the target as shown in Fig. 7.23 and improves with target size. Further enhancements have been proposed through the use of thin stacked discs or high aspect ratio prism targets [165] where theoretical studies have shown reduced heating effects and improve the search volume on the order of a magnitude [166]. However, prior to our work, little has been shown in the optical levitation of large high-mass targets such as ours in air or vacuum, and quantum ground state cooling in this size regime to achieve the required force sensitivities is yet to be demonstrated.

7.8 Summary

This chapter collects various results from our experiments in optical levitation. We begin by computing the beam intensity required to levitate a 50 µm shell. A thermal study was conducted investigating the extent of shell heating due to the absorbed laser power at static pressures from 10^5 Pa to 1 Pa. Heat transfer simulations considering only conduction and radiation heat loss showed surface temperatures reaching 1526 °C at 10^3 Pa, and 1840 °C at 10^2 Pa which would lead to severe damage or complete destruction of the levitating shell due to the melting point of its wall layers. Further investigation may be required to confirm these results as shell damage has not been observed under these pressures. Convective heat loss was not considered as we assumed static or slow fluid flow around the shell. We now find that perhaps a complete consideration of heat transfer mechanisms

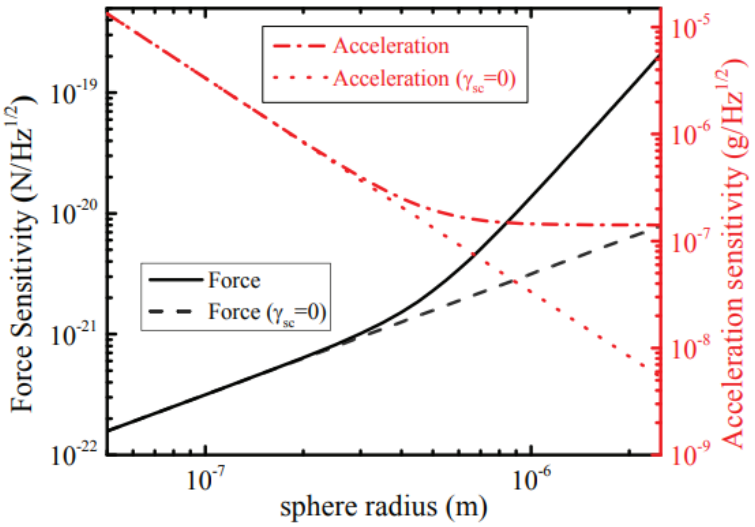


Figure 7.23: Plot taken from [164]. It compares force and acceleration sensitivity with radius of levitated silica particle at 1 kHz trap frequency. γ_{sc} denotes photon recoil heating

may be required to better model shell heating. However, the thermal simulations did allow us to get an estimate on the effective thermal conductivity of the shell to be 2.58 W m/K.

In experiment, we observe significant instability between 10^3 Pa and 10^2 Pa alluding to pressure dependent forces taking effect. The case for photophoretic forces is further strengthened using force calculations based on the shell's effective thermal conductivity obtained from the simulation results. We find the photophortic force balances the weight of the shell in magnitude at these pressures in addition to the already present radiative force which would result in the instability that has been observed.

We then shift our focus to the power spectral density analysis of a 34 µm levitating shell at atmospheric pressure. Here we described the procedure on how experimental position data was used to reveal spectral characteristics of an oscillating levitated shell and highlight features in the time-series, spatial distribution and Fourier data that showcase unexpected behaviour that our that was unaccounted for in our model. We repeat this for a seperate instance of a 90 µm levitating shell but under lower static pressures. We mostly found Gaussian spatial profiles and power density spectra that show agreement with our fitting models. However, the main takeaway here was the successful demonstration of a large levitating shell held with $\sim$ µm stability down to pressures of 10^3 Pa. In other instances, levitation at even lower pressures has been observed but with varying degrees of spatial stability.

To resolve these instabilities we attempted to implement active stabilisation methods firstly through fixed frequency power modulation and then by shell trajectory correction both of which were unsuccessful. The lack of success in the latter case revealed operational limitations in our position sensors which, at times, could not differentiate vertical position change with what is believed to be rotation induced scattering. Thus a redesign on the

sensing equipment is required to avoid operating off scatter light.

Finally, instances of non-spherical and multishell trapping are presented. This demonstrates the system does not require spherically symmetric target geometries but in fact allows complex target arrangements. This could have interesting applications in the levitation of bespoke application based target geometries.

Chapter 8

Conclusions & future works

8.1 Thesis conclusion

This thesis has presented research towards the development of a novel optical vortex (OV) laser along with demonstrations of its application in the optical levitation of reflective hollow shell targets at long focal range (40 mm) in air and low pressure.

The first half of this thesis focussed on aspects of OV generation. The concept of optical vortices was first introduced through the example of Laguerre-Gaussian (LG) beams, supported by a mathematical foundation for describing key properties in their helical phase structure and possession of orbital angular momentum (OAM). These properties can be used to discriminate OVs from other annular beams that may at first glance be similar in appearance. This is achieved by inspecting the propagation of the OV beam's spatial profile through a focus or diagnosing its OAM state through interferograms and modal decomposition.

While various OV generation devices exist today, we direct our focus to interferometric techniques, namely, in the non-standard use of the wedge-plate shearing interferometer (WPSI) as an OV mode conversion device. We describe how the interference of two TEM_{00} Gaussian beams can generate an LG_{01} OV in its output and apply this framework to the specific geometry of the WPSI. Operational guidelines for using the WPSI in a laboratory setting were provided, including a detailed breakdown of its configuration and key operating parameters. A notable limitation of the WPSI is found in its poor power conversion efficiency as the OV is produced through Fresnel reflection, thus converting $\sim 2\,\%$ of the incident TEM_{00} power.

To address this limitation, an intracavity implementation of the WPSI was explored, showing greater potential for power scalability for watt-level CW outout power. In this approach, the transmitted power is simply recycled back into the laser cavity while the face reflectance acts as the output coupling. By integrating the WPSI as a VOC, any standard laser cavity can, in principle, be augmented to be capable of OV output provided

the internal mode oscillates at the TEM_{00} mode with suitable coherence length. Two experimental demonstrations are presented for intracavity OV generation: a linear cavity configuration and a compact ring confuguration. The linear cavity suffered from spectral bandwidth issues resulting in improper mode conversion of the internal mode. This was found to be a specific limitation of this particular setup as other works have successfully demonstrated the linear cavity to work in this way [87]. These challenges were overcome through the use of a ring cavity where the unidirectional internal mode enhanced the incident power on the intracavity WPSI and surpressed the broad spectral emission to be single longitudinal mode. In this way we achieved watt-level OV output power with high LG_{01} purity (97.8 %) and beam quality ($M^2 = 1.94, 2.09$). Our work on intracavity OV generation has been published and can be found in Ref. [167].

The second part of this thesis applied this laser to generate an annular trapping beam for the capture and levitation of reflective hollow spherical (shell) targets. The optical design of the levitation system and the choice of target was motivated by possible applications in high-energy laser experiments, particularly in the generation of high-density plasmas, point X-ray sources, and charged-particle acceleration. The long focal length of the trapping region from the final focusing lens ensured such experiments can be performed away from damage-prone optics or potential coupling into a vacuum chamber. Through our collaborations, custom in-house built position sensors were developed intended for semi-disposable per-shot use and (relatively) inexpensive to replace as the high intensity EM-fields generated through these experiments can leave near by electronics such as sensing equipment prone to damage. In this aspect of the work, we aim to reduce the cost of replacing more expensive sensing equipment.

A vacuum envelope was used to house to the levitation system and early results at low-pressure levitation (down to 100-10 Pa) were documented. We have identified pressure instability zones where photophoretic forces dependent on the temperature distribution of the levitated shell surface and surrounding medium prevent us from achieving levitation as high-vacuum ($<10^{-3}$ Pa). A combined analytical and numerical study was conducted to provide deeper insight into these problematic photophoretic forces. Thermal simulations were performed to investigate laser induced heating of the shell surface and interior, and heat dissipation to the surrounding volume at pressures coinciding with our experimental explorations. The point at which the calculated photophortic forces became dominating against the laser driven radiative force supporting the shell were found to agree with the pressure instability zones seen in our experiments - further confirming the origin of these instabilities. Stabilisation mechanisms using active feedback have been devised to counteract these effects but require further development of the necessary hardware to fully implement. There is strong motivation to revisit this in future work. Our work on optical levitation has been presented at conferences [168] with the intention a of journal publication in the near future.

Alongside our experimental work, background theory drawn from similar studies in the

literature were collected to analyze the characteristic oscillations of our levitated shells. Given our unique combination of thin-walled reflective shell targets levitated using an annular beam in air and at low pressure, much of the expected dynamics were initially unexplored. Fourier-based analytical tools were employed to identify spectral features in the shell's oscillatory motion, which can be linked to trap characteristics such as stiffness, resonance and the degree of damping in the system and how this evolves with pressure. Assuming the shell's motion is stochastic, as in a thermally driven system exhibiting Brownian-like behaviour, the expected spatial variance can be derived from the power spectral density of the position time-series measurements. This variance serves as a benchmark to compare with theoretical models, enabling the validation of assumptions about the oscillator's driving mechanisms. Disagreement then reveals other possible sources such as laser noise or environmental factors such as vibrational instabilities which might then be amenable to active feedback control.

8.2 Future work

As is often the case with exploratory research, the road to developing new experimental capabilities is rarely straightforward. The path is littered with unforeseen challenges and intricate detours, which once navigated, can illuminate opportunities for refinement. Hindsight offers a valuable perspective, revealing areas for improvement and new avenues of inquiry that were not apparent at the outset. This chapter reflects on these insights and highlights aspects of the experiment that may benefit from revisitation and further development in future work.

8.2.1 Laser stability

The OV laser was initially constructed for the purpose of demonstrating the use of the WPSI as a VOC. Its technological requirements were to achieve watt-level output power, obtain high beam-quality and mode-purity comparable to previous demonstrations and operate in single-longitudinal mode to alleviate the coherence length issues seen in the linear cavity arrangement. These objectives were successfully demonstrated.

Power stability was characterised over 2.7 h of continuous use. Measurements after 1 h of warm-up time showed 3 % variation in peak-power and 0.6 % in average power. Trap life-times have since exceeded this by an order of magnitude and in some cases by two orders however laser stability over these time scales is not well known. Prolonged use may result in slow degradation in laser output due to thermal drift. Changes in mode profile have been observed over these long periods where the phase singularity of the OV has drifted off center. As shown in Chap. 3, the WPSI generated beam profile is coupled with the reflected power thus influencing long-term spatial stability in the trap. Although this is not an issue over the short interaction time-scales with high-intensity lasers, it is a concern for laser alignment purposes or potential applications of a "large" trapped object in a sensor application as knowledge of the trapping zone is required to spatial precision

equal to the firing laser's focal spot-size. A work around to the current system would be to introduce standard procedures requiring alignment checks prior to firing.

8.2.2 Active feedback stabilisation

Active feedback stabilisation methods were found to be unsuccessful due to unexpected limitations in our position measuring technique. Position measurements relied on the fact the scatter point from the shell surface would be a reliable indicator of its position, however this was found to not always be the case. Rotation in the levitated shells resulted in an additional strong periodic signal that the sensors confused for changes in vertical position. This could not be solved using our current approach.

An alternative approach is proposed by using a high spatial uniformity back-illuminated imaging setup similar to the shell imaging microscope. In this way, the position measurement would be insensitive to shell rotation unless there is a significant structural asymmetry in the shell. Then instead of tracking the scatter point, the position sensors would operate in reverse bias to track the shell's silhouette. This approach comes with a number of challenges. The first is the brightness sensitivity of the sensors to track a $\sim 50\,\mu m$ shadow against a bright background. Even with high magnification, tracking the image over the sensor's active region will be challenging. Of course equipment with better sensitivities can be acquired however, the development of our current sensors was motivated by the need for them to be inexpensive and disposable. We have recently addressed this by moving to an alternative ADC with both higher bit depth (16 compared to 12) and synchronous capture of multiple channels which further improves data integrity. Secondly, the noise level in this system will be dominated by brightness stability of the source. Greater suppression of vibrational noise may be required if other objects such as impurities in the beam path are illuminated as these may be mistaken for the shell or contribute to the signal imaged onto the sensor.

8.2.3 Levitation at low pressure

We demonstrated optical levitation at various static pressures earlier in Chap. 7. Although results have only been presented down to 100 Pa, we have observed levitation at pressures as low as $\sim 1\,Pa$ but were unable to record data. There is strong desire to demonstrate levitation at lower pressures approaching (ultra-) high vacuum ($<10^{-3}\,Pa$) to replicate the pressure conditions under which the shells will be used as firing targets for high-energy density experiments. However we are currently limited by instabilities below 100 Pa thought to be due to laser heating induced photophoretic forces and require stablisation to overcome.

In Chap. 7 we began to investigate the degree of heating experienced by a levitated shell and how this varies with pressure. We found that heating of the trapping volume results in photophoretic forces at pressures that match the pressure ranges in which we experimentally observe severe instability. This has limited our low-pressure levitation capabilities

and requires stabilisation methods to counteract these forces. Our simulations also showed significant heating of the shell surface and interior. Although we have observed shell falling out of the trap, the mechanism by which this occurs is not well documented in our case due to limited high-speed footage of shell ejection from the trap. Others have reported evaporation [169] and more severe forms of destruction such as burning [170]. Our simulations have shown the shell core to heat up to several 100 to >1000 °C. If the core of our shells is in fact gas filled, this could result in violent explosion of the thin-walled shells dependent on the rate at which it is heated. This is assuming the core hasn't already leaked diffusively overtime or through the negative pressure environment of the chamber.

8.2.4 High-intensity laser experiments

The previous three sections have detailed short-term performance goals aimed towards realising applications in high-intensity laser experimentation. Longer-term objectives are structured in terms of a developmental roadmap leading to the eventual installation of the levitation system at high-intensity laser facilities such as the Vulcan 2020 multi-PW system at the Rutherford Appleton Laboratory (RAL).

The current work serves as a bench-top demonstration of the optical levitation of thin-walled metallic targets that are highly desired in research area of its intended application. The next milestone will be to overcome the current technological challenges and produce a working system that can be deployed, or the blue-print transferred, to other University-scale laboratories that have access to high-power table-top laser systems such as Cerberus. Further development of the levitation system can take place once experimentation has begun with possible enhancements to trapping zone distance based on vacuum chamber constraints, efficient imaging and position sensing diagnostics layout dependent on the logistical constraints of the laboratory space, improved data acquisition routines, and possible tuning of beam size and power to accommodate other target types such as opaque absorbing targets or dielectric oil droplets. Once field deployable demonstrations have been successful, advanced prototyping may take place for transferal to facilities such as RAL for higher-power experimentation.

8.2.5 OAM transfer

Opto-mechanical rotators have reported record speeds exceeding 1 GHz in high-vacuum [171] achieved through SAM coupling. The transfer of OAM onto optically levitated objects has been reported in the literature [128, 172] and rotation in high vacuum has been reported at 6 MHz level [173]. We have observed rotation in our levitated shells but have not conclusively deduced whether this is due to OAM transfer from the OV trapping beam or thermally induced due to heating [174, 175]. The torque applied by a mode with indices p and l onto a surface is given by [176, 127]

$$\tau_r = \frac{P_{abs}}{\omega}\left[(l+\sigma_z)+\sigma_z\left(\frac{2kz_R}{2p+l+1}+1\right)^{-1}\right]. \tag{8.1}$$

where ω is the angular frequency of the light, $\sigma_z = \pm 1$ for circularly polarised light and $\sigma_z = 0$ for linear polarisation. Within the paraxial approximation we can remove the second σ_z term. The torque applied to spherical body or radius a acts against the torque drag τ_d due to the surrounding viscous medium,

$$\tau_d = 8\pi\mu a^3\Omega \tag{8.2}$$

When the torques are balanced, Ω is the angular velocity of the rotating body,

$$\Omega = \frac{P_{abs}\lambda l}{2\pi c}\frac{1}{8\pi\mu a^3} \tag{8.3}$$

In Chap. 7 we found a $d = 50\,\mu\text{m}$ shell is levitated by an incident power 31.56 mW. Adjusting for absorbed power this gives $\Omega = 7.45\,\text{mHz}$ which lies outside of the possible frequencies detected within our measurement duration. The low frequency signal resolution is dependent on our sampling that can be easily adjusted. The more pertinent limitation is our current diagnostics setup does not allow shell rotation to be measured easily and required a re-design or additional diagnostic capabilities. Nevertheless, the measurement of OAM transfer is still worthwhile. In the context of high-intensity laser interactions, this could then lead to investigations into the effect of rotating targets on plasma generation and its resulting dynamics.

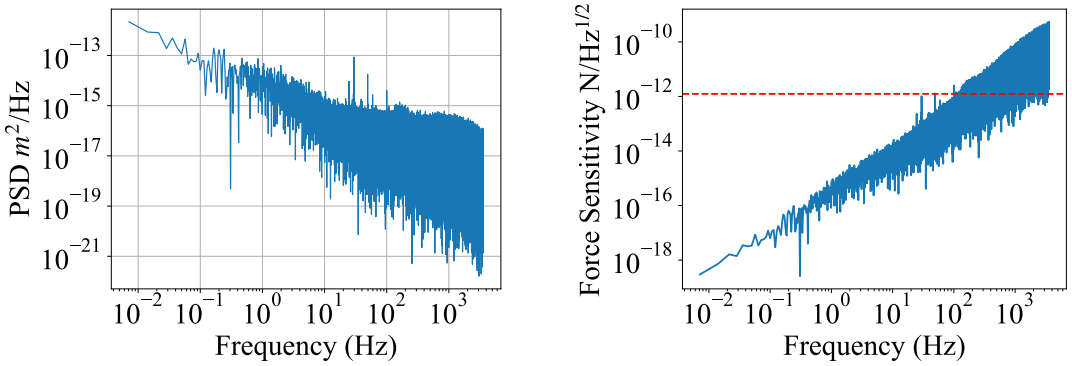
8.2.6 Force sensing applications

In recent years we have seen the development of levitated sensors for ultra-weak force sensing. Zeptonewton ($10^{-21}\,\text{N}$) force sensitivities have been demonstrated with integration times exceeding $10^5\,\text{s}$ (that is 28 h) [177]. Montiero *et al.* achieved similar sensitivity using 10 µm silica microsphere ($m = 95\,\text{ng}$) over 12 h measurement period [178]. Liang *et al.* first demonstrated yoctonewton ($10^{-24}\,\text{N}$) force sensitivity and with 2751 s of integration time (45 min) [90].

Our work has not yet explored force sensing capabilities however we can preform a rough calculation based on current performance. Through dimensional analysis we can relate the spatial power spectral density $S_x(f)$ (units: m^2/Hz) to a force sensitivity $S_F(f)$ (units: $N/Hz^{1/2}$) by the following,

$$S_F(f) = \sqrt{m^2(2\pi f)^4 S_x(f)} \tag{8.4}$$

Selecting Fig. 7.15 as a case study, we demonstrate the levitation of a large shell ($d = 90\,\mu\text{m}$ and $m = 100\,\text{ng}$) at low pressure. For reference, its PSD is shown again in Fig. 8.1(a). Applying Eq. 8.4 we obtain its force sensitivity spectrum shown in Fig. 8.1(b). It appears to show attonewton-level force sensitivity in the $f = 10^{-2}\,\text{Hz}$ region, however we must be wary of measurement limitatons before making conclusive performance claims. In the



(a) (b)

Figure 8.1: (a) Same as Fig. 7.15(d) it shows the PSD of a 90 µm shell levitating at a pressure of 10^3 Pa. (b) Corresponding force sensitivity as per Eq. 8.4. Red dotted line denote the thermal noise limit per measurement bandwidth.

Brownian noise limit the minimum measurable force is given by,

$$F_{min} = S_F^{th} b^{1/2} \tag{8.5}$$

where S_F^{th} is the thermal noise PSD as seen in Chap. 6 and b is the measurement bandwidth. Levitated sensors are resonant-type systems whose sensitivity peaks when the frequency of the incoming signal coincides with the resonance band of the oscillator [179]. The frequency scaling of the noise is dependent on the specific characteristics of the system and its limiting noise sources. In the above, the noise limit is set by thermal noise but this may be substituted for photon-recoil, laser shot noise or similar. A tutorial on various aspects of levitated sensors and their applications can be found in Ref. [180]. The OV laser in our work demonstrated sufficient stability for our intended application. For this system to be adapted for applications in optically-levitated force sensing, stabilisation of the levitation target and laser power is strongly recommended.

8.2.7 Final remarks

This thesis has presented work on OV laser development and its implementation in the optical levitation of reflective shell targets at long focal length. The OV laser deomonstrated excellent performance for our application meeting our requirements for target size and low vacuum stability with areas on immediate improvement already underway in the next generation of this work. The levitation system was successful in its objectives and shows great promise for further work.

References

[1] Ensieh Khalkhal et al. “The Evaluation of Laser Application in Surgery: A Review Article”. In: *Journal of Lasers in Medical Sciences* 10.5 (Dec. 2019), S104–S111. DOI: 10.15171/jlms.2019.S18.

[2] Heng Guo et al. “A review of ultrafast laser micro/nano fabrication: Material processing, surface/interface controlling, and devices fabrication”. In: *Nano Research* 17.7 (July 2024), pp. 6212–6230. DOI: 10.1007/s12274-024-6644-z.

[3] Hideaki Takabe and Yasuhiro Kuramitsu. “Recent progress of laboratory astrophysics with intense lasers”. In: *High Power Laser Science and Engineering* 9 (July 2021), e49. DOI: 10.1017/hpl.2021.35.

[4] B. Hidding et al. “Directions in plasma wakefield acceleration”. In: *Philosophical Transactions of the Royal Society A: Mathematical, Physical and Engineering Sciences* 377.2151 (Aug. 2019), p. 20190215. DOI: 10.1098/rsta.2019.0215.

[5] Wei-Min Wang et al. “Collimated ultrabright gamma rays from electron wiggling along a petawatt laser-irradiated wire in the QED regime”. In: *Proceedings of the National Academy of Sciences* 115.40 (Oct. 2018), pp. 9911–9916. DOI: 10.1073/pnas.1809649115.

[6] M. Schioppo et al. “Ultrastable optical clock with two cold-atom ensembles”. In: *Nature Photonics* 11.1 (Jan. 2017), pp. 48–52. DOI: 10.1038/nphoton.2016.231.

[7] W. F. McGrew et al. “Atomic clock performance enabling geodesy below the centimetre level”. In: *Nature* 564.7734 (Dec. 2018), pp. 87–90. DOI: 10.1038/s41586-018-0738-2.

[8] B. P. Abbott et al. “Observation of Gravitational Waves from a Binary Black Hole Merger”. In: *Physical Review Letters* 116.6 (Feb. 2016), p. 061102. DOI: 10.1103/PhysRevLett.116.061102.

[9] Arthur Ashkin. *Optical Trapping and Manipulation of Neutral Particles Using Lasers*. WORLD SCIENTIFIC, Dec. 2006. DOI: 10.1142/4208.

[10] T. H. MAIMAN. “Stimulated Optical Radiation in Ruby”. In: *Nature* 187.4736 (Aug. 1960), pp. 493–494. DOI: 10.1038/187493a0.

[11] A. Javan, W. R. Bennett, and D. R. Herriott. “Population Inversion and Continuous Optical Maser Oscillation in a Gas Discharge Containing a He-Ne Mixture”. In: *Physical Review Letters* 6.3 (Feb. 1961), pp. 106–110. DOI: 10.1103/PhysRevLett.6.106.

[12] F. J. McClung and R. W. Hellwarth. “Giant Optical Pulsations from Ruby”. In: *Journal of Applied Physics* 33.3 (Mar. 1962), pp. 828–829. DOI: 10.1063/1.1777174.

[13] E. Snitzer. “Proposed Fiber Cavities for Optical Masers”. In: *Journal of Applied Physics* 32.1 (Jan. 1961), pp. 36–39. DOI: 10.1063/1.1735955.

[14] Charles J. Koester and Elias Snitzer. “Amplification in a Fiber Laser”. In: *Applied Optics* 3.10 (Oct. 1964), p. 1182. DOI: 10.1364/AO.3.001182.

[15] L. Allen et al. “Orbital angular momentum of light and the transformation of Laguerre-Gaussian laser modes”. In: *Physical Review A* 45.11 (1992), pp. 8185–8189. DOI: 10.1887/0750309016/b1142c6.

[16] A. Cámara and T. Alieva. “Propagation of broken stable beams”. In: *Journal of Modern Optics* 58.9 (May 2011), pp. 743–747. DOI: 10.1080/09500340.2011.573589.

[17] Alois Mair et al. “Entanglement of the orbital angular momentum states of photons”. In: *Nature* 412.6844 (July 2001), pp. 313–316. DOI: 10.1038/35085529.

[18] Jonathan Leach et al. “Measuring the Orbital Angular Momentum of a Single Photon”. In: *Physical Review Letters* 88.25 (June 2002), p. 257901. DOI: 10.1103/PhysRevLett.88.257901.

[19] Graham Gibson et al. “Free-space information transfer using light beams carrying orbital angular momentum”. In: *Optics Express* 12.22 (2004), p. 5448. DOI: 10.1364/OPEX.12.005448.

[20] Jian Wang et al. “Terabit free-space data transmission employing orbital angular momentum multiplexing”. In: *Nature Photonics* 6.7 (July 2012), pp. 488–496. DOI: 10.1038/nphoton.2012.138.

[21] Dinesh N. Naik et al. “Ultrashort vortex from a Gaussian pulse-An achromatic-interferometric approach”. In: *Scientific Reports* 7.1 (2017), pp. 1–10. DOI: 10.1038/s41598-017-02613-3.

[22] Kohei Toyoda et al. “Using Optical Vortex To Control the Chirality of Twisted Metal Nanostructures”. In: *Nano Letters* 12.7 (July 2012), pp. 3645–3649. DOI: 10.1021/nl301347j.

[23] Gregory Foo, David M. Palacios, and Grover A. Swartzlander. “Optical vortex coronagraph”. In: *Optics Letters* 30.24 (Dec. 2005), p. 3308. DOI: 10.1364/OL.30.003308.

[24] D. Mawet et al. “Annular Groove Phase Mask Coronagraph”. In: *The Astrophysical Journal* 633.2 (Nov. 2005), pp. 1191–1200. DOI: 10.1086/462409.

[25] Linjie Li et al. “Achieving $\lambda/20$ Resolution by One-Color Initiation and Deactivation of Polymerization”. In: *Science* 324.5929 (May 2009), pp. 910–913. DOI: 10.1126/science.1168996.

[26] Timothy F. Scott et al. “Two-Color Single-Photon Photoinitiation and Photoinhibition for Subdiffraction Photolithography”. In: *Science* 324.5929 (May 2009), pp. 913–917. DOI: 10.1126/science.1167610.

[27] G. D’Aguanno et al. “Optical vortices during a superresolution process in a metamaterial”. In: *Physical Review A* 77.4 (Apr. 2008), p. 043825. DOI: 10.1103/PhysRevA.77.043825.

[28] M.W. Beijersbergen et al. “Helical-wavefront laser beams produced with a spiral phaseplate”. In: *Optics Communications* 112.5-6 (Dec. 1994), pp. 321–327. DOI: 10.1016/0030-4018(94)90638-6.

[29] J. Arlt et al. “The production of multiringed Laguerre–Gaussian modes by computer-generated holograms”. In: *Journal of Modern Optics* 45.6 (June 1998), pp. 1231–1237. DOI: 10.1080/09500349808230913.

[30] Sharon A. Kennedy et al. “Creation of Laguerre-Gaussian laser modes using diffractive optics”. In: *Physical Review A* 66.4 (Oct. 2002), p. 043801. DOI: 10.1103/PhysRevA.66.043801.

[31] L. Marrucci, C. Manzo, and D. Paparo. “Optical Spin-to-Orbital Angular Momentum Conversion in Inhomogeneous Anisotropic Media”. In: *Physical Review Letters* 96.16 (Apr. 2006), p. 163905. DOI: 10.1103/PhysRevLett.96.163905.

[32] L. Marrucci, C. Manzo, and D. Paparo. “Pancharatnam-Berry phase optical elements for wave front shaping in the visible domain: Switchable helical mode generation”. In: *Applied Physics Letters* 88.22 (May 2006). DOI: 10.1063/1.2207993.

[33] Yasunori Igasaki et al. “High Efficiency Electrically-Addressable Phase-Only Spatial Light Modulator”. In: *Optical Review* 6.4 (July 1999), pp. 339–344. DOI: 10.1007/s10043-999-0339-2.

[34] Alison M. Yao and Miles J. Padgett. “Orbital angular momentum: origins, behavior and applications”. In: *Advances in Optics and Photonics* 3.2 (2011), p. 161. DOI: 10.1364/aop.3.000161.

[35] J. B. Götte and S. M. Barnett. “Light beams carrying orbital angular momentum”. In: *The Angular Momentum of Light*. Cambridge University Press, Nov. 2012, pp. 1–30. DOI: 10.1017/CBO9780511795213.002.

[36] J. Durnin, J. J. Miceli, and J. H. Eberly. “Diffraction-free beams”. In: *Physical Review Letters* 58.15 (Apr. 1987), pp. 1499–1501. DOI: 10.1103/PhysRevLett.58.1499.

[37] J. C. Gutiérrez-Vega, M. D. Iturbe-Castillo, and S. Chávez-Cerda. “Alternative formulation for invariant optical fields: Mathieu beams”. In: *Optics Letters* 25.20 (Oct. 2000), p. 1493. DOI: 10.1364/OL.25.001493.

[38] M.W. Beijersbergen et al. “Astigmatic laser mode converters and transfer of orbital angular momentum”. In: *Optics Communications* 96.1-3 (Feb. 1993), pp. 123–132. DOI: 10.1016/0030-4018(93)90535-D.

[39] K. Sueda et al. “Laguerre-Gaussian beam generated with a multilevel spiral phase plate for high intensity laser pulses”. In: *Optics Express* 12.15 (2004), p. 3548. DOI: 10.1364/OPEX.12.003548.

[40] Etienne Brasselet et al. “Photopolymerized microscopic vortex beam generators: Precise delivery of optical orbital angular momentum”. In: *Applied Physics Letters* 97.21 (Nov. 2010). DOI: 10.1063/1.3517519.

[41] J. Courtial et al. “Measurement of the Rotational Frequency Shift Imparted to a Rotating Light Beam Possessing Orbital Angular Momentum”. In: *Physical Review Letters* 80.15 (Apr. 1998), pp. 3217–3219. DOI: 10.1103/PhysRevLett.80.3217.

[42] Andrew G. Peele et al. “Observation of an x-ray vortex”. In: *Optics Letters* 27.20 (Oct. 2002), p. 1752. DOI: 10.1364/OL.27.001752.

[43] S. Pancharatnam. “Generalized theory of interference, and its applications”. In: *Proceedings of the Indian Academy of Sciences - Section A* 44.5 (Nov. 1956), pp. 247–262. DOI: 10.1007/BF03046050.

[44] Michael Berry. “Quantal phase factors accompanying adiabatic changes”. In: *Proceedings of the Royal Society of London. A. Mathematical and Physical Sciences* 392.1802 (Mar. 1984), pp. 45–57. DOI: 10.1098/rspa.1984.0023.

[45] N. R. Heckenberg et al. “Laser beams with phase singularities”. In: *Optical and Quantum Electronics* 24.9 (Sept. 1992), S951–S962. DOI: 10.1007/BF01588597.

[46] Ram Oron et al. “Laser mode discrimination with intra-cavity spiral phase elements”. In: *Optics Communications* 169.1-6 (Oct. 1999), pp. 115–121. DOI: 10.1016/S0030-4018(99)00389-2.

[47] William R. Kerridge-Johns. “Intra-Cavity Spiral Phase Plate Laser with Non-Inverting Sagnac Mirror”. In: *2022 Conference on Lasers and Electro-Optics Pacific Rim (CLEO-PR)*. IEEE, July 2022, pp. 1–2. DOI: 10.1109/CLEO-PR62338.2022.10432138.

[48] Darryl Naidoo et al. “Controlled generation of higher-order Poincaré sphere beams from a laser”. In: *Nature Photonics* 10.5 (May 2016), pp. 327–332. DOI: 10.1038/nphoton.2016.37.

[49] Sandile Ngcobo et al. “A digital laser for on-demand laser modes”. In: *Nature Communications* 4.1 (Aug. 2013), p. 2289. DOI: 10.1038/ncomms3289.

[50] Akihiko Ito, Yuichi Kozawa, and Shunichi Sato. “Generation of hollow scalar and vector beams using a spot-defect mirror”. In: *Journal of the Optical Society of America A* 27.9 (Sept. 2010), p. 2072. DOI: 10.1364/JOSAA.27.002072.

[51] J.W. Kim and W.A. Clarkson. “Selective generation of Laguerre–Gaussian (LG0) mode output in a diode-laser pumped Nd:YAG laser”. In: *Optics Communications* 296 (June 2013), pp. 109–112. DOI: 10.1016/j.optcom.2013.01.046.

[52] William R. Kerridge-Johns and Michael J. Damzen. “Vortex laser from anti-resonant ring coupled cavities”. In: *Optics Express* 26.25 (2018), p. 32839. DOI: 10.1364/oe.26.032839.

[53] Xiaoxu Huang et al. “Direct Generation of Vortex Laser by Rotating Induced Off-Axis Pumping”. In: *IEEE Journal of Selected Topics in Quantum Electronics* 24.5 (Sept. 2018), pp. 1–6. DOI: 10.1109/JSTQE.2018.2814789.

[54] Guoping Lin et al. “Direct generation of a narrow-linewidth Laguerre–Gaussian vortex laser in a monolithic nonplanar oscillator”. In: *Optics Letters* 43.17 (Sept. 2018), p. 4164. DOI: 10.1364/OL.43.004164.

[55] Guoping Lin et al. “Spontaneous generation of orbital angular momentum crystals using a monolithic Nd:YAG nonplanar ring laser”. In: *Optics Letters* 44.2 (Jan. 2019), p. 203. DOI: 10.1364/OL.44.000203.

[56] Pravin Vaity, A. Aadhi, and R. P. Singh. “Formation of optical vortices through superposition of two Gaussian beams”. In: *Applied Optics* 52.27 (2013), pp. 6652–6656. DOI: 10.1364/AO.52.006652.

[57] W. R. Kerridge-Johns, J. W. T. Geberbauer, and M. J. Damzen. “Vortex laser by transforming Gaussian mode with an interferometric output coupler”. In: *Optics Express* 27.8 (2019), p. 11642. DOI: 10.1364/oe.27.011642.

[58] J. W. T. Geberbauer, W. R. Kerridge-Johns, and M. J. Damzen. “ >30 W vortex LG 01 or HG 10 laser using a mode transforming output coupler ”. In: *Optics Express* 29.18 (2021), p. 29082. DOI: 10.1364/oe.432674.

[59] William R. Kerridge-Johns, Jean-Benoît Jaillot, and Michael J. Damzen. “Sampling a vortex from a Gaussian beam using a wedge-plate shearing interferometer”. In: *Applied Optics* 60.12 (2021), p. 3510. DOI: 10.1364/ao.422625.

[60] Anthony E. Siegman. “New developments in laser resonators”. In: ed. by Dale A. Holmes. June 1990, p. 2. DOI: 10.1117/12.18425.

[61] A.E. Siegman and S.W. Townsend. “Output beam propagation and beam quality from a multimode stable-cavity laser”. In: *IEEE Journal of Quantum Electronics* 29.4 (Apr. 1993), pp. 1212–1217. DOI: 10.1109/3.214507.

[62] Mitsuo Takeda, Hideki Ina, and Seiji Kobayashi. “Fourier-transform method of fringe-pattern analysis for computer-based topography and interferometry”. In: *Journal of the Optical Society of America* 72.1 (Jan. 1982), p. 156. DOI: 10.1364/JOSA.72.000156.

[63] Philip Lacovara, Leon Esterowitz, and Roger Allen. “Flash-lamp-pumped Ti:Al_2O_3 laser using fluorescent conversion”. In: *Optics Letters* 10.6 (June 1985), p. 273. DOI: 10.1364/OL.10.000273.

[64] P. F. Moulton. “Spectroscopic and laser characteristics of Ti:Al_2O_3”. In: *Journal of the Optical Society of America B* 3.1 (Jan. 1986), p. 125. DOI: 10.1364/JOSAB.3.000125.

[65] J. E. Geusic, H. M. Marcos, and L. G. Van Uitert. “LASER OSCILLATIONS IN Nd-DOPED YTTRIUM ALUMINUM, YTTRIUM GALLIUM AND GADOLINIUM GARNETS”. In: *Applied Physics Letters* 4.10 (May 1964), pp. 182–184. DOI: 10.1063/1.1753928.

[66] T. Pollak et al. “CW laser operation of Nd:YLF”. In: *IEEE Journal of Quantum Electronics* 18.2 (Feb. 1982), pp. 159–163. DOI: 10.1109/JQE.1982.1071512.

[67] J. R. O’Connor. “UNUSUAL CRYSTAL-FIELD ENERGY LEVELS AND EFFICIENT LASER PROPERTIES OF YVO4:Nd”. In: *Applied Physics Letters* 9.11 (Dec. 1966), pp. 407–409. DOI: 10.1063/1.1754631.

[68] Vartan V. Ter-Mikirtychev. “Spectroscopic Properties of Nd3+-, Yb3+-, Er3+-, and Tm3+-Doped Fibers”. In: 2019, pp. 47–68. DOI: 10.1007/978-3-030-33890-9{_}5.

[69] R. Paschotta. “Vanadate Lasers - an encyclopedia article”. In: *RP Photonics Encyclopedia*. RP Photonics AG, 2023. DOI: 10.61835/1nd.

[70] R. Paschotta. “YAG Lasers - an encyclopedia article”. In: *RP Photonics Encyclopedia*. RP Photonics AG, 2005. DOI: 10.61835/7vp.

[71] D. Krennrich et al. “A comprehensive study of Nd:YAG, Nd:YAlO3, Nd:YVO4 and Nd:YGdVO4 lasers operating at wavelengths of 0.9 and 1.3 μm. Part 1: cw-operation”. In: *Applied Physics B* 92.2 (Aug. 2008), pp. 165–174. DOI: 10.1007/s00340-008-3069-4.

[72] D. Krennrich et al. “A comprehensive study of Nd:YAG, Nd:YAlO3, Nd:YVO4 and Nd:YGdVO4 lasers operating at wavelengths of 0.9 and 1.3 μm. Part 2: passively mode locked-operation”. In: *Applied Physics B* 92.2 (Aug. 2008), pp. 175–183. DOI: 10.1007/s00340-008-3070-y.

[73] L. Fornasiero et al. “Excited state absorption and stimulated emission of Nd 3+ in crystals. Part 2: YVO 4 , GdVO 4 , and Sr 5 (PO 4) 3 F”. In: *Applied Physics B: Lasers and Optics* 67.5 (Nov. 1998), pp. 549–553. DOI: 10.1007/s003400050543.

[74] Raphael Lavi et al. “Efficient pumping scheme for neodymium-doped materials by direct excitation of the upper lasing level”. In: *Applied Optics* 38.36 (Dec. 1999), p. 7382. DOI: 10.1364/AO.38.007382.

[75] V Lupei, N Pavel, and T Taira. “Highly efficient laser emission in concentrated Nd:YVO4 components under direct pumping into the emitting level”. In: *Optics Communications* 201.4-6 (Jan. 2002), pp. 431–435. DOI: 10.1016/S0030-4018(01)01720-5.

[76] A I Zagumennyĭ et al. “The Nd:GdVO 4 crystal: a new material for diode-pumped lasers”. In: *Soviet Journal of Quantum Electronics* 22.12 (Dec. 1992), pp. 1071–1072. DOI: 10.1070/QE1992v022n12ABEH003672.

[77] Glenn Christopher Bowkett. “Nd: YV04 Microchip Lasers and Amplifiers”. PhD thesis. Victoria University of Technology, 1999.

[78] Xin Ding et al. “High-efficiency Nd:YVO4 laser emission under direct pumping at 880nm”. In: *Optics Communications* 282.5 (Mar. 2009), pp. 981–984. DOI: 10.1016/j.optcom.2008.11.054.

[79] Theodore F. Ewanizky. “Ray-transfer-matrix approach to unstable resonator analysis”. In: *Applied Optics* 18.5 (Mar. 1979), p. 724. DOI: 10.1364/AO.18.000724.

[80] Herwig Kogelnik. “Imaging of Optical Modes - Resonators with Internal Lenses”. In: *Bell System Technical Journal* 44.3 (Mar. 1965), pp. 455–494. DOI: 10.1002/j.1538-7305.1965.tb01672.x.

[81] Vittorio Magni. “Resonators for solid-state lasers with large-volume fundamental mode and high alignment stability”. In: *Applied Optics* 25.1 (Jan. 1986), p. 107. DOI: 10.1364/AO.25.000107.

[82] Orazio Svelto. *Principles of Lasers*. Boston, MA: Springer US, 2010. DOI: 10.1007/978-1-4419-1302-9.

[83] F. R. Faxvog. “Modes of a unidirectional ring laser”. In: *Optics Letters* 5.7 (July 1980), p. 285. DOI: 10.1364/OL.5.000285.

[84] M. Hercher, M. Young, and C. B. Smoyer. "Traveling-Wave Ruby Laser with a Passive Optical Isolator". In: *Journal of Applied Physics* 36.10 (Oct. 1965), pp. 3351–3351. DOI: 10.1063/1.1702979.

[85] H. Abitan, H. Bohr, and C. F. Pedersen. "Fiber ring laser with a feedback mirror". In: *Applied Optics* 44.36 (Dec. 2005), p. 7802. DOI: 10.1364/AO.44.007802.

[86] P. C. Shardlow and M. J. Damzen. "20 W single longitudinal mode Nd:YVO4 retro-reflection ring laser operated as a self-intersecting master oscillator power amplifier". In: *Applied Physics B* 97.2 (Oct. 2009), pp. 257–262. DOI: 10.1007/s00340-009-3641-6.

[87] William R. Kerridge-Johns et al. "Red, orange, and dual wavelength vortex emission from Pr:WPFGF fiber laser using a microscope slide output coupler". In: *Optics Express* 31.10 (May 2023), p. 16607. DOI: 10.1364/OE.491867.

[88] Josep Mas et al. "Quantitative determination of optical trapping strength and viscoelastic moduli inside living cells". In: *Physical Biology* 10.4 (July 2013), p. 046006. DOI: 10.1088/1478-3975/10/4/046006.

[89] Swathi Sudhakar et al. "Germanium nanospheres for ultraresolution picotensiometry of kinesin motors". In: *Science* 371.6530 (Feb. 2021). DOI: 10.1126/science.abd9944.

[90] Tao Liang et al. "Yoctonewton force detection based on optically levitated oscillator". In: *Fundamental Research* 3.1 (Jan. 2023), pp. 57–62. DOI: 10.1016/j.fmre.2022.09.021.

[91] A. Ashkin, J. M. Dziedzic, and T. Yamane. "Optical trapping and manipulation of single cells using infrared laser beams". In: *Nature* 330.6150 (Dec. 1987), pp. 769–771. DOI: 10.1038/330769a0.

[92] G Thalhammer et al. "Optical macro-tweezers: trapping of highly motile micro-organisms". In: *Journal of Optics* 13.4 (Apr. 2011), p. 044024. DOI: 10.1088/2040-8978/13/4/044024.

[93] Philippe Cluzel et al. "DNA: An Extensible Molecule". In: *Science* 271.5250 (Feb. 1996), pp. 792–794. DOI: 10.1126/science.271.5250.792.

[94] Jeffrey T. Finer, Robert M. Simmons, and James A. Spudich. "Single myosin molecule mechanics: piconewton forces and nanometre steps". In: *Nature* 368.6467 (Mar. 1994), pp. 113–119. DOI: 10.1038/368113a0.

[95] Michael D. Perry and Gerard Mourou. "Terawatt to Petawatt Subpicosecond Lasers". In: *Science* 264.5161 (May 1994), pp. 917–924. DOI: 10.1126/science.264.5161.917.

[96] M. H. Key et al. "Hot electron production and heating by hot electrons in fast ignitor research". In: *Physics of Plasmas* 5.5 (May 1998), pp. 1966–1972. DOI: 10.1063/1.872867.

[97] E. L. Clark et al. "Measurements of Energetic Proton Transport through Magnetized Plasma from Intense Laser Interactions with Solids". In: *Physical Review Letters* 84.4 (Jan. 2000), pp. 670–673. DOI: 10.1103/PhysRevLett.84.670.

[98] R. D. Edwards et al. "Characterization of a gamma-ray source based on a laser-plasma accelerator with applications to radiography". In: *Applied Physics Letters* 80.12 (Mar. 2002), pp. 2129–2131. DOI: 10.1063/1.1464221.

[99] L. Rymell and H.M. Hertz. "Droplet target for low-debris laser-plasma soft X-ray generation". In: *Optics Communications* 103.1-2 (Nov. 1993), pp. 105–110. DOI: 10.1016/0030-4018(93)90651-K.

[100] M. Anand, C. P. Safvan, and M. Krishnamurthy. "Hard X-ray generation from micro-droplets in intense laser fields". In: *Applied Physics B* 81.4 (Aug. 2005), pp. 469–477. DOI: 10.1007/s00340-005-1899-x.

[101] P. P. Rajeev et al. "Metal Nanoplasmas as Bright Sources of Hard X-Ray Pulses". In: *Physical Review Letters* 90.11 (Mar. 2003), p. 115002. DOI: 10.1103/PhysRevLett.90.115002.

[102] E. T. Gumbrell et al. “Intense laser interactions with sprays of submicron droplets”. In: *Physics of Plasmas* 8.4 (Apr. 2001), pp. 1329–1339. DOI: 10.1063/1.1353186.

[103] T Sokollik et al. “Laser-driven ion acceleration using isolated mass-limited spheres”. In: *New Journal of Physics* 12.11 (Nov. 2010), p. 113013. DOI: 10.1088/1367-2630/12/11/113013.

[104] T. Paasch-Colberg et al. “New method for laser driven ion acceleration with isolated, mass-limited targets”. In: *Nuclear Instruments and Methods in Physics Research Section A: Accelerators, Spectrometers, Detectors and Associated Equipment* 653.1 (Oct. 2011), pp. 30–34. DOI: 10.1016/j.nima.2011.02.031.

[105] Lord Rayleigh. “On the equilibrium of liquid conducting masses charged with electricity”. In: *The London, Edinburgh, and Dublin Philosophical Magazine and Journal of Science* 14.87 (Sept. 1882), pp. 184–186. DOI: 10.1080/14786448208628425.

[106] C. J. Price et al. “An in-vacuo optical levitation trap for high-intensity laser interaction experiments with isolated microtargets”. In: *Review of Scientific Instruments* 86.3 (Mar. 2015). DOI: 10.1063/1.4908285.

[107] A. Maksimchuk et al. “Forward Ion Acceleration in Thin Films Driven by a High-Intensity Laser”. In: *Physical Review Letters* 84.18 (May 2000), pp. 4108–4111. DOI: 10.1103/PhysRevLett.84.4108.

[108] P. B. Johnson and R. W. Christy. “Optical Constants of the Noble Metals”. In: *Physical Review B* 6.12 (Dec. 1972), pp. 4370–4379. DOI: 10.1103/PhysRevB.6.4370.

[109] Yuanjie Yang et al. “Optical trapping with structured light: a review”. In: *Advanced Photonics* 3.03 (May 2021). DOI: 10.1117/1.AP.3.3.034001.

[110] N. B. Simpson et al. “Mechanical equivalence of spin and orbital angular momentum of light: an optical spanner”. In: *Optics Letters* 22.1 (Jan. 1997), p. 52. DOI: 10.1364/OL.22.000052.

[111] Syoji Ito et al. “Selective Optical Assembly of Highly Uniform Nanoparticles by Doughnut-Shaped Beams”. In: *Scientific Reports* 3.1 (Oct. 2013), p. 3047. DOI: 10.1038/srep03047.

[112] A. Ashkin. “Acceleration and Trapping of Particles by Radiation Pressure”. In: *Physical Review Letters* 24.4 (Jan. 1970), pp. 156–159. DOI: 10.1103/PhysRevLett.24.156.

[113] A. Ashkin and J. M. Dziedzic. “Optical Levitation by Radiation Pressure”. In: *Applied Physics Letters* 19.8 (Oct. 1971), pp. 283–285. DOI: 10.1063/1.1653919.

[114] A. Ashkin et al. “Observation of a single-beam gradient force optical trap for dielectric particles”. In: *Optics Letters* 11.5 (May 1986), p. 288. DOI: 10.1364/OL.11.000288.

[115] Spencer E. Olson et al. “Cold-atom confinement in an all-optical dark ring trap”. In: *Physical Review A - Atomic, Molecular, and Optical Physics* 76.6 (Dec. 2007), p. 061404. DOI: 10.1103/PhysRevA.76.061404.

[116] Takahiro Kuga et al. “Novel Optical Trap of Atoms with a Doughnut Beam”. In: *Physical Review Letters* 78.25 (June 1997), pp. 4713–4716. DOI: 10.1103/PhysRevLett.78.4713.

[117] S. Franke-Arnold et al. “Optical ferris wheel for ultracold atoms”. In: *Optics Express* 15.14 (July 2007), p. 8619. DOI: 10.1364/oe.15.008619.

[118] Xiaodong He et al. “Rotating single atoms in a ring lattice generated by a spatial light modulator”. In: *Optics Express* 17.23 (Nov. 2009), p. 21007. DOI: 10.1364/OE.17.021007.

[119] Mohamed Babiker, David L Andrews, and Vassilis E Lembessis. “Atoms in complex twisted light”. In: *Journal of Optics* 21.1 (Jan. 2019), p. 013001. DOI: 10.1088/2040-8986/aaed14.

[120] B. del Rosal et al. “Heat in optical tweezers”. In: ed. by Kishan Dholakia and Gabriel C. Spalding. Sept. 2013, 88102A. DOI: 10.1117/12.2027750.

[121] Alfonso Blázquez-Castro. “Optical Tweezers: Phototoxicity and Thermal Stress in Cells and Biomolecules”. In: *Micromachines* 10.8 (July 2019), p. 507. DOI: 10.3390/mi10080507.

[122] M. E. J. Friese et al. “Determination of the force constant of a single-beam gradient trap by measurement of backscattered light”. In: *Applied Optics* 35.36 (Dec. 1996), p. 7112. DOI: 10.1364/AO.35.007112.

[123] N. B. Simpson et al. “Optical tweezers with increased axial trapping efficiency”. In: *Journal of Modern Optics* 45.9 (Sept. 1998), pp. 1943–1949. DOI: 10.1080/09500349808231712.

[124] Anna T. O’Neil and Miles J. Padgett. “Axial and lateral trapping efficiency of Laguerre–Gaussian modes in inverted optical tweezers”. In: *Optics Communications* 193.1-6 (June 2001), pp. 45–50. DOI: 10.1016/S0030-4018(01)01198-1.

[125] Iker Gómez-Viloria et al. “On-Axis Optical Trapping with Vortex Beams: The Role of the Multipolar Decomposition”. In: *ACS Photonics* 11.2 (Feb. 2024), pp. 626–633. DOI: 10.1021/acsphotonics.3c01499.

[126] H. He et al. “Direct Observation of Transfer of Angular Momentum to Absorptive Particles from a Laser Beam with a Phase Singularity”. In: *Physical Review Letters* 75.5 (July 1995), pp. 826–829. DOI: 10.1103/PhysRevLett.75.826.

[127] M. E. J. Friese et al. “Optical angular-momentum transfer to trapped absorbing particles”. In: *Physical Review A* 54.2 (Aug. 1996), pp. 1593–1596. DOI: 10.1103/PhysRevA.54.1593.

[128] N. B. Simpson, L. Allen, and M. J. Padgett. “Optical tweezers and optical spanners with Laguerre–Gaussian modes”. In: *Journal of Modern Optics* 43.12 (Dec. 1996), pp. 2485–2491. DOI: 10.1080/09500349608230675.

[129] Anna T O’Neil and Miles J Padgett. “Three-dimensional optical confinement of micron-sized metal particles and the decoupling of the spin and orbital angular momentum within an optical spanner”. In: *Optics Communications* 185.1-3 (Nov. 2000), pp. 139–143. DOI: 10.1016/S0030-4018(00)00989-5.

[130] R. C. Gauthier and S. Wallace. “Optical levitation of spheres: analytical development and numerical computations of the force equations”. In: *Journal of the Optical Society of America B* 12.9 (Sept. 1995), p. 1680. DOI: 10.1364/JOSAB.12.001680.

[131] Ming Chen Wang and G. E. Uhlenbeck. “On the Theory of the Brownian Motion II”. In: *Reviews of Modern Physics* 17.2-3 (Apr. 1945), pp. 323–342. DOI: 10.1103/RevModPhys.17.323.

[132] William King. “Open source single molecule force spectroscopy”. PhD thesis. Drexel University, 2013.

[133] George Karniadakis, Ali Beskok, and Narayan Aluru. “Basic Concepts and Technologies”. In: *Microflows and Nanoflows*. New York: Springer-Verlag, pp. 1–48. DOI: 10.1007/0-387-28676-4{_}1.

[134] G A Bird. *Molecular Gas Dynamics And The Direct Simulation Of Gas Flows*. Oxford University PressOxford, May 1994. DOI: 10.1093/oso/9780198561958.001.0001.

[135] S. A. Beresnev, V. G. Chernyak, and G. A. Fomyagin. “Motion of a spherical particle in a rarefied gas. Part 2. Drag and thermal polarization”. In: *Journal of Fluid Mechanics* 219.-1 (Oct. 1990), p. 405. DOI: 10.1017/S0022112090003007.

[136] R Kubo. “The fluctuation-dissipation theorem”. In: *Reports on Progress in Physics* 29.1 (Jan. 1966), p. 306. DOI: 10.1088/0034-4885/29/1/306.

[137] G. E. Uhlenbeck and L. S. Ornstein. “On the Theory of the Brownian Motion”. In: *Physical Review* 36.5 (Sept. 1930), pp. 823–841. DOI: 10.1103/PhysRev.36.823.

[138] Tongcang Li and Mark G. Raizen. “Brownian motion at short time scales”. In: *Annalen der Physik* 525.4 (Apr. 2013), pp. 281–295. DOI: 10.1002/andp.201200232.

[139] Kirstine Berg-Sørensen and Henrik Flyvbjerg. "Power spectrum analysis for optical tweezers". In: *Review of Scientific Instruments* 75.3 (Mar. 2004), pp. 594–612. DOI: 10.1063/1.1645654.

[140] Jen-Feng Hs. "Cooling the center-of-mass motion of a diamond nanocrystal in a magneto-gravitational trap". PhD thesis. University of Pittsburgh, 2016.

[141] Jamie Vovrosh. "Parametric feedback cooling and squeezing of optically levitated particles". PhD thesis. University of Southampton, 2018.

[142] Jan Gieseler et al. "Subkelvin Parametric Feedback Cooling of a Laser-Trapped Nanoparticle". In: *Physical Review Letters* 109.10 (Sept. 2012), p. 103603. DOI: 10.1103/PhysRevLett.109.103603.

[143] Jamie Vovrosh et al. "Parametric feedback cooling of levitated optomechanics in a parabolic mirror trap". In: *Journal of the Optical Society of America B* 34.7 (July 2017), p. 1421. DOI: 10.1364/JOSAB.34.001421.

[144] G. Hettner. "Zur Theorie der Photophorese". In: *Zeitschrift fur Physik* 37.3 (Mar. 1926), pp. 179–192. DOI: 10.1007/BF01400195.

[145] Martin Li and Jochen Arlt. "Trapping multiple particles in single optical tweezers". In: *Optics Communications* 281.1 (Jan. 2008), pp. 135–140. DOI: 10.1016/j.optcom.2007.09.032.

[146] Brandon Redding et al. "Photophoretic trapping of airborne particles using ultraviolet illumination". In: *Optics Express* 23.3 (Feb. 2015), p. 3630. DOI: 10.1364/OE.23.003630.

[147] Souvik Sil et al. "Trapping multiple absorbing particles in air using an optical fiber by photophoretic forces". In: *Journal of Optics* 24.7 (July 2022), p. 074003. DOI: 10.1088/2040-8986/ac71b3.

[148] Hans Rohatschek. "Levitation of stratospheric and mesospheric aerosols by gravito-photophoresis". In: *Journal of Aerosol Science* 27.3 (Apr. 1996), pp. 467–475. DOI: 10.1016/0021-8502(95)00556-0.

[149] H. Rohatschek and H. Horvath. "Magneto-photophoresis and mesospheric particles". In: *Journal of Geophysical Research: Atmospheres* 115.D24 (Dec. 2010). DOI: 10.1029/2010JD014667.

[150] Hans Rohatschek. "Direction, magnitude and causes of photophoretic forces". In: *Journal of Aerosol Science* 16.1 (Jan. 1985), pp. 29–42. DOI: 10.1016/0021-8502(85)90018-7.

[151] Hans Rohatschek. "Semi-empirical model of photophoretic forces for the entire range of pressures". In: *Journal of Aerosol Science* 26.5 (July 1995), pp. 717–734. DOI: 10.1016/0021-8502(95)00011-Z.

[152] Larry D Reed. "Low Knudsen number photophoresis". In: *Journal of Aerosol Science* 8.2 (Mar. 1977), pp. 123–131. DOI: 10.1016/0021-8502(77)90073-8.

[153] M. H. Rosen and C. Jr. Orr. "The photophoretic force". In: *Journal of colloid science* 19 (1964), pp. 50–60.

[154] N.T Tong. "Photophoretic force in the free molecule and transition regimes". In: *Journal of Colloid and Interface Science* 43.1 (Apr. 1973), pp. 78–84. DOI: 10.1016/0021-9797(73)90349-4.

[155] Yu. I. Yalamov and A. S. Khasanov. "Photophoresis of coarse aerosol particles with nonuniform thermal conductivity". In: *Technical Physics* 43.4 (Apr. 1998), pp. 347–352. DOI: 10.1134/1.1258984.

[156] David J. S. Pereira and Miguel R. O. Panão. "Optimization Of Photophoretic Forces In Coated-Hollow Microspheres". In: *Proceedings of the International Symposium on the Application of Laser and Imaging Techniques to Fluid Mechanics* 21 (July 2024), pp. 1–14. DOI: 10.55037/lxlaser.21st.144.

[157] Charles R. Harris et al. “Array programming with NumPy”. In: *Nature* 585.7825 (Sept. 2020), pp. 357–362. DOI: 10.1038/s41586-020-2649-2.

[158] William Press et al. *Numerical Recipes in C: The Art of Scientific Computing*. 2nd. Cambridge University Press, 1992.

[159] G Heinzel, A Rudiger, and R Schilling. *Spectrum and spectral density estimation by the Discrete Fourier transform (DFT), including a comprehensive list of window functions and some new flat-top windows.* Tech. rep. Max-Planck-Institut fur ¨ Gravitationsphysik, 2002.

[160] R. Di Leonardo, F. Ianni, and G. Ruocco. “Colloidal Attraction Induced by a Temperature Gradient”. In: *Langmuir* 25.8 (Apr. 2009), pp. 4247–4250. DOI: 10.1021/la8038335.

[161] Th. Fennel et al. “Plasmon-Enhanced Electron Acceleration in Intense Laser Metal-Cluster Interactions”. In: *Physical Review Letters* 98.14 (Apr. 2007), p. 143401. DOI: 10.1103/PhysRevLett.98.143401.

[162] Shuichi Hashimoto, Daniel Werner, and Takayuki Uwada. “Studies on the interaction of pulsed lasers with plasmonic gold nanoparticles toward light manipulation, heat management, and nanofabrication”. In: *Journal of Photochemistry and Photobiology C: Photochemistry Reviews* 13.1 (Mar. 2012), pp. 28–54. DOI: 10.1016/j.jphotochemrev.2012.01.001.

[163] Asimina Arvanitaki and Andrew A. Geraci. “Detecting High-Frequency Gravitational Waves with Optically Levitated Sensors”. In: *Physical Review Letters* 110.7 (Feb. 2013), p. 071105. DOI: 10.1103/PhysRevLett.110.071105.

[164] ZHANG-QI YIN, ANDREW A. GERACI, and TONGCANG LI. “OPTOMECHANICS OF LEVITATED DIELECTRIC PARTICLES”. In: *International Journal of Modern Physics B* 27.26 (Oct. 2013), p. 1330018. DOI: 10.1142/S0217979213300181.

[165] George Winstone et al. “Optical Trapping of High-Aspect-Ratio NaYF Hexagonal Prisms for kHz-MHz Gravitational Wave Detectors”. In: *Physical Review Letters* 129.5 (July 2022), p. 053604. DOI: 10.1103/PhysRevLett.129.053604.

[166] Nancy Aggarwal et al. “Searching for New Physics with a Levitated-Sensor-Based Gravitational-Wave Detector”. In: *Physical Review Letters* 128.11 (Mar. 2022), p. 111101. DOI: 10.1103/PhysRevLett.128.111101.

[167] Abdul-Haseeb Munj and William R. Kerridge-Johns. “Unidirectional ring vortex laser using a wedge-plate shearing interferometer”. In: *Optics Express* 31.3 (Jan. 2023), p. 4954. DOI: 10.1364/OE.482849.

[168] Abdul-Haseeb Munj, Roland A. Smith, and William R. Kerridge-Johns. “Optical levitation using an LG01 vortex beam”. In: *Optical Manipulation and Structured Materials Conference*. Ed. by Takashige Omatsu, Síle N. Chormaic, and Kishan Dholakia. SPIE, Sept. 2023, p. 12. DOI: 10.1117/12.3008328.

[169] D. E. Chang et al. “Cavity opto-mechanics using an optically levitated nanosphere”. In: *Proceedings of the National Academy of Sciences* 107.3 (Jan. 2010), pp. 1005–1010. DOI: 10.1073/pnas.0912969107.

[170] A. T. M. A. Rahman et al. “Burning and graphitization of optically levitated nanodiamonds in vacuum”. In: *Scientific Reports* 6.1 (Feb. 2016), p. 21633. DOI: 10.1038/srep21633.

[171] René Reimann et al. “GHz Rotation of an Optically Trapped Nanoparticle in Vacuum”. In: *Physical Review Letters* 121.3 (July 2018), p. 033602. DOI: 10.1103/PhysRevLett.121.033602.

[172] Yijie Shen et al. “Optical vortices 30 years on: OAM manipulation from topological charge to multiple singularities”. In: *Light: Science & Applications* 8.1 (Oct. 2019), p. 90. DOI: 10.1038/s41377-019-0194-2.

[173] Fernando Monteiro et al. “Optical rotation of levitated spheres in high vacuum”. In: *Physical Review A* 97.5 (May 2018), p. 051802. DOI: 10.1103/PhysRevA.97.051802.

[174] Jinda Lin and Yong-qing Li. “Optical trapping and rotation of airborne absorbing particles with a single focused laser beam”. In: *Applied Physics Letters* 104.10 (Mar. 2014). DOI: 10.1063/1.4868542.

[175] Sudipta K. Bera et al. “Simultaneous measurement of mass and rotation of trapped absorbing particles in air”. In: *Optics Letters* 41.18 (Sept. 2016), p. 4356. DOI: 10.1364/OL.41.004356.

[176] Stephen M. Barnett and L. Allen. “Orbital angular momentum and nonparaxial light beams”. In: *Optics Communications* 110.5-6 (Sept. 1994), pp. 670–678. DOI: 10.1016/0030-4018(94)90269-0.

[177] Gambhir Ranjit et al. “Zeptonewton force sensing with nanospheres in an optical lattice”. In: *Physical Review A* 93.5 (May 2016), p. 053801. DOI: 10.1103/PhysRevA.93.053801.

[178] Fernando Monteiro et al. “Force and acceleration sensing with optically levitated nanogram masses at microkelvin temperatures”. In: *Physical Review A* 101.5 (May 2020), p. 053835. DOI: 10.1103/PhysRevA.101.053835.

[179] George Winstone et al. “High frequency gravitational wave detection with optically levitated nanoparticles: an update on LSD (levitated sensor detector)”. In: *Optical and Quantum Sensing and Precision Metrology II*. Ed. by Selim M. Shahriar and Jacob Scheuer. SPIE, Mar. 2022, p. 50. DOI: 10.1117/12.2610009.

[180] George Winstone et al. “Optomechanics of optically-levitated particles: A tutorial and perspective”. In: (July 2023).